Universitat Autònoma de Barcelona

Electrodeposition of novel nanostructured and porous materials for advanced applications: synthesis, structural characterization and physical/chemical performance

Jin Zhang

Universitat Autònoma
de Barcelona

Electrodeposition of novel nanostructured and porous materials for advanced applications: synthesis, structural characterization and physical/chemical performance

Jin Zhang

Tesi Doctoral

Programa de Doctorat en Ciència de Materials

Eva Pellicer Vilà (directora i tutora)

Jordi Sort Viñas (director)

Departament de Física

Facultat de Ciències

2016

Memòria presentada per aspirar al Grau de Doctor per

Jin Zhang

Vist i plau

Dra. Eva Pellicer Vilà	Dr. Jordi Sort Viñas
(directora i tutora)	(director)

Bellaterra, 17/06/2016

Universitat Autònoma
de Barcelona

Group of smart nanoengineered materials, nanomechanics and nanomagnetism

La **Dra. Eva Pellicer Vilà**, investigadora Ramón y Cajal del Departament de Física de la Universitat Autònoma de Barcelona,

i el **Dr. Jordi Sort Viñas**, professor ICREA del Departament de Física de la Universitat Autònoma de Barcelona,

CERTIFIQUEN:

Que **Jin Zhang** ha realitzat sota la seva direcció el treball d'investigació que s'exposa a la memòria titulada "*Electrodeposition of novel nanostructured and porous materials for advanced applications: synthesis, structural characterization and physical/chemical performance*" per optar al grau de **Doctor per la Universitat Autònoma de Barcelona**.

Que el disseny dels experiments, síntesi de mostres, llur caracterització, l'anàlisi dels resultats, la redacció dels articles i d'aquesta memòria són fruit del treball d'investigació realitzat per Jin Zhang.

I perquè així consti, signen el present certificat,

Dra. Eva Pellicer Vilà

Dr. Jordi Sort Viñas

Bellaterra, 17 de juny de 2016

Acknowledgement

To start, I would like to thank my supervisors Dr. Eva Pellicer and Prof. Jordi Sort, for their guidance, support and their advices, which have helped me a lot regarding presentation skill, academic writing, and experimental skills. Especially, thanks them for broadening my views on materials science and electrodeposition.

I would like to give a special appreciation to Prof. Maria Dolors Baró for sharing me her life experiences when I was confused about life. I will always remember her constant help during my PhD study.

I am grateful to all co-authors of the articles I have published or submitted so far.

I would also like to thank all the lab mates that have share the lab life with me: Jordina, Pau, Alberto, Miquel, Irati, Feng, Fan, Vassil, Santi, Pablo, Patxi, Alex, Doga, and Evangeria. I would also like to thank former colleagues Anna and Sebastiá for their advices and friendship.

It is a great pleasure to acknowledge the support and help coming from the technicians from the Microscopy Servei, X-ray Diffraction, ICMAB, University of Barcelona and ICN 2 for their assistance in SEM, TEM, XRD, and contact angle measurements.

Thanks to my grant China scholarship council. Without that, I wouldn’t have the chance to pursue my PhD study in UAB.

I would like to thank my Chinese friends Huiyan, Lijuan, Xuhui for their help and support.

Thanks to my family, mother, father, sister, brother in low and my nephew. My love has always been here for all of you.

I would like to thank Daniel for his love and support. I started to realized that how brave I can be and the energy holding inside me.

In the end, I will need to thank myself. Thank you for being always persistent and patient. I hope you could be the person you want to be and do the things you want to do. I would like to finish the acknowledgement with a sentence I always use to warn me for the ups and downs:

Be patient, life has to go step by step.

Abstract

This Thesis dissertation covers the electrochemical synthesis of advanced metallic materials in two different configurations, namely porous films and segmented nanowires (NWs). Porous films are prepared by hydrogen bubble-assisted electrodeposition (macroporous Ni and Cu-Ni systems) and self-organized template (block-copolymer P123) assisted electrodeposition (nanoporous Ni). The Cu-Ni films exhibit a hierarchical porosity (they consist of micron-sized roughly spherical pores and nanodendritic walls), superhydrophobic character and ferromagnetic properties at room temperature (due to the occurrence of phase separation during deposition). Furthermore, they are electrocatalytically active toward hydrogen evolution reaction in alkaline media, outperforming pure Cu and Ni porous films prepared under similar conditions.

Meanwhile, segmented CoPt/Cu/Ni and CoPt/Ni NWs with controlled segment lengths are prepared by electrodeposition in polycarbonate (PC) membranes. Due to the dissimilar ferromagnetic properties of CoPt and Ni segments (hard- and soft-ferromagnetic character, respectively), it is possible to achieve an antiparallel alignment of the magnetization of the segments if their lengths are properly tuned. This would make it possible to minimize aggregation of the NWs once released from the PC template. These findings have been validated by analytical calculations.

The macroporous Cu-Ni and Ni films are used as scaffolds for the fabrication of novel nanocomposite layers, namely ZnO@CuNi, Al_2O_3@Ni and Co_2FeO_4@Ni, by applying sol-gel coating and atomic layer deposition techniques. The latter allows a nanometer-thick conformal coating of the metallic host. The resulting nanocomposites combine the properties coming from the metallic matrix and those arising from the coating (photoluminescence and photocatalytic properties in the case of ZnO, changes in the wettability for Al_2O_3 and Co_2FeO_4).

Finally, the nanomechanical properties of nanoporous Ni films are evaluated and a thickness-dependence of both the Young’s modulus and the yield strength with the maximum applied force during nanoidentation is disclosed, due to the graded porosity of these films.

Abstract

Resum

Aquesta tesi doctoral comprèn la síntesi electroquímica de materials metàl·lics avançats en dues configuracions diferents, capes poroses i nanofils segmentats. Les capes poroses s'han preparat per electrodeposició fent ús de les bombolles d'hidrogen que es generen durant el procés com a plantilles (sistemes de Ni i Cu-Ni macroporós) i també per electrodeposició en presència del polímer P123 que actua com a plantilla autoorganitzada (Ni nanoporós). Les capes de Cu-Ni presenten una porositat jeràrquica (estan formades per microporus esfèrics i les partes de porus són nanodendrítiques), caràcter superhidrofòbic i propietats ferromagnètiques a temperatura ambient (gràcies a la separació de fases que s'aconsegueix durant el procés de deposició). A més, aquestes capes són electroquímicament actives vers la reacció d'evolució d'hidrogen en medi alcalí, bo i presentant millor resposta que les capes de Cu i Ni poroses preparades en condicions similars.

D'altra banda, s'han fabricat nanofils segmentats de CoPt/Cu/Ni i CoPt/Ni amb un control acurat de la llargada dels segments en membranes de policarbonat (PC). Gràcies al fet que els segments de CoPt i Ni presenten propietats ferromagnètiques distintes (l'un és magnèticament dur i l'altre magnèticament tou), es pot aconseguir un alineament antiparal·lel de la magnetització de saturació dels segments si llurs llargades es dissenyen de forma apropiada. Això faria possible minimitzar-ne la seva aglomeració un cop els nanofils fossin alliberats de la membrana de PC. Les troballes experimentals han estat validades mitjançant càlculs analítics.

S'han utilitat les capes macroporoses de Cu-Ni i Ni com a matrius per a la fabricació de noves làmines de nanocompòsit, en particular ZnO@CuNi, Al_2O_3@Ni i Co_2FeO_4@Ni, mitjançat processos de sol-gel i deposició de capa atòmica (en anglès, ALD). L'ALD permet la formació d'un recobriment conformal de gruix nanomètric en l'esquelet metàl·lic porós. Els nanocompòsits resultants combinen les propietats de la matriu metàl·lica i les del recobriment (fotoluminescència i propietats fotocatalítiques en el cas del ZnO, canvis en la mullabilitat en el cas de Al_2O_3 i Co_2FeO_4).

Finalment, s'han avaluat les propietats nanomecàniques de films de Ni nanoporós i s'ha vist que existeix una dependència tant del mòdul de Young com del límit d'elasticitat amb la força màxima aplicada durant els assaigs de nanoindentació, atès que aquetes capes presenten una gradació de la porositat en funció del gruix.

Table of contents

Table of contents

List of Figures

List of Tables

List of Tables

Departament de Física

1. Introduction

Chapter 1: Introduction

Research in nanostructured materials generates considerable interest in the scientific community because of their novel and enhanced properties endowed by confining the dimensions of such materials. Nanostructured materials, whose structural or constituent elements –clusters, crystallites or molecules– have dimensions in the range of 1 to 100 nm, are currently synthesized by a wide variety of physical, chemical and mechanical methods. Among them, magnetic nanostructured materials, more precisely ferromagnetic materials, are the subject of myriad theoretical and experimental investigations since they combine a nanostructured morphology with the intriguing magnetic features emerging at the nanoscale. They find great uses in information storage devices, such as computers, cell phones and non-volatile memories, as well as in biomedical and biotechnological applications, such as direct detection of antibodies in biological samples and stimuli responsive drug delivery systems, to name a few.

1.1 Template assisted electrodeposition of nanostructured materials

Synthesis and processing of nanostructured metallic and ceramic materials have been reviewed by several authors[1-4]. Compared to physical fabrication techniques, such as sputtering, evaporation, molecular beam epitaxy, focused ion beam, etc., electrodeposition offers various advantages. Firstly, electrodeposition does not require vacuum conditions; it can work at ambient pressure and room temperature. Secondly, substrates with a wide variety of shapes can be coated, which is particularly useful for template-assisted electrodeposition approaches. Thirdly, high deposition rates are attainable. Last, relatively thick dense and porous coatings (up to several hundreds of micrometers in thickness) can be obtained. All these features make electrodeposition a fast and cost-effective technique for the production of nanostructured materials.

1.1 Template assisted electrodeposition of nanostructured materials

Template-assisted electrodeposition[5] methods allow synthesizing low-dimensional materials (nanoparticles, nanowires, nanotubes, nanorods) with controlled shape and size. They involve the use of either dynamic, self-organized, or restrictive templates as a cathode in the electrochemical cell. The template can be removed after the electrodeposition step by calcination or etching, depending on the demands of the synthesis as well as the nature of the templates. General features of each approach are described below.

1.1.1 Dynamic template-assisted electrodeposition

In aqueous solutions and at sufficiently large cathodic overpotentials, H^+ is easily reduced to H_2. Hydrogen co-evolution was an unwanted issue for many years, because the produced bubbles disrupt the normal growth of metal deposits. However, H_2 bubbles can actually be utilized as a dynamic template during electrodeposition to fabricate porous materials[6]. Typically, macropores in the micron size range are caused by the growth of the metal or alloy around the bubbles generated on the cathode surface. The intensively evolved H_2 bubbles change the hydrodynamic conditions near the electrode surface, profoundly affecting the morphology and structure of the deposits. Nanodendrites and foams are a consequence of both the H_2 evolution and the applied high overpotential. This preparation technique is clean and efficient as it affords access to porous morphologies without the need for additional organic or inorganic templates. The main advantage of dynamic templates is that they are automatically detached from the growing porous layer during the deposition process.

Several groups have exploited the concept of H_2 co-evolution accompanying cations discharge to prepare a large variety of porous metals or alloys. A number of different electrodeposition modes have been utilized, namely pulse [7,8], constant potential[9,10] (potentiostatic) and constant current[11,12] (galvanostatic) methods, which broadly speaking produce similar morphologies. Monometals such as Ni[13], Cu[12,14,15], Bi[16], Pd[17], Pt[18], Sn[19], Co[20], Ru[21] and bimetallic systems containing Ni (NiSn[22], NiCo[23], NiCu[24]), Pd (AgPd[25], PdNi[26]) Pt (PtPd[27], AuPt[28], CuPt[29]) and Cu (CuAg[30], CuAu[31]) have been prepared by hydrogen bubble template-assisted electrodeposition. The first detained studies on porous magnetic materials produced in this way focused on Ni[32,33]. Recent developments have led to the production of porous magnetic films including Ni[13], CuNi[24], CoNi[23], CuFe[34] alloy, bimetallic Cu-Ni[35], and even NiCoFe.[36]

Besides H_2 bubbles, ions can also serve as a dynamic template during electrodeposition in some cases. For example, Cl^- and $ZnCl^+$ can cyclically function as dynamic templates during the electrodeposition of ZnO when grown under a triangular potential waveform signal. [37] During the cathodic step, $ZnCl^+$ adsorbs on the substrate, thus providing a blocking effect which inhibits ZnO from being deposited inside the pores. During the anodic step, Cl^- exerts a pinning effect, which prevents the as-grown ZnO deposits from dissolution. Although this approach has not been applied to deposit porous metallic films so far, it highlights the opportunity to use ions as a dynamic template in electrodeposition.

1.1.2 Self-organized template-assisted electrodeposition

Self-organized templates allow the electrodeposition of a range of materials featuring regular arrays of uniform pores from submicrometer to nanometer sizes. There are mainly two types of self-organized templates[38]: lyotropic liquid crystalline (LLC) phases and close-packed arrays of spherical colloidal beads.

LLC phases produce materials with regular arrays of pores in the 2-10 nm size range with wall thicknesses typically of the same order. These phases are formed by dissolving high concentrations of surfactant in water[39]. Surfactant molecules are typically amphiphilic in character, i.e., they possess hydrophilic and hydrophobic regions, having a long hydrocarbon tail and a relatively small ionic or polar head group. The simplest liquid crystalline phase is spherical micelles, for which the hydrophobic groups are oriented toward the inner part of the micelles and the hydrophilic groups are oriented toward the outer part of the micelles (i.e., they are in contact with water). At higher amphiphile concentration, the micelles fuse to form cylindrical aggregates of indefinite length, and these cylinders arrange into a long-range hexagonal lattice. By continuous increasing the concentration of the surfactant, the so-called “lamellar phase” is formed. In order to use these phases as templates for the growth of nanoporous metallic deposits, appropriate metal salts are dissolved in the aqueous domain of the electrolyte. Using block copolymers as surfactants affords films with larger pores. Besides, block copolymer systems also form similar phases when used in ternary systems with water and an organic solvent such as ethanol. This approach is an attractive route to prepare porous metals, semimetals, metal oxides, or alloy materials, such as, Pd[40], Ni[41], Pt[42], MnO_2[43], NiCoFeB[44] or PtRu[45]. Well-defined mesostructures can be formed depending on the temperature and composition of the mixture.

Colloidal templates can be utilized as matrices to produce porous films featuring close-packed arrays of interconnected spherical pores from 20 nm to over 1 μm in diameter. Spherical colloidal particles (e.g. latex beads) can be assembled as colloidal crystalline layers on conducting substrates by various methods such as electrophoresis, centrifugation, sedimentation, or evaporation. With careful control of the conditions, it is possible to deposit high quality (single crystalline) materials over large areas (> 1 mm^2)[46]. The voids left behind the colloidal spheres can be filled with the target materials by electrodeposition. Electrodeposition possesses significant advantages over other deposition approaches. First of all, it ensures that the deposits distribute as a “negative copy” of the template, and thus shrinkage of materials does not take place when the template is removed. The resulting porous film is a true cast of the template structure and the pore size of the deposits is directly determined by the size of the colloidal spheres. This method is very flexible because both aqueous and non-aqueous electrolytes can be utilized, and the colloidal templates are compatible with a wide range of deposition conditions. Porous metals[47,48] and alloys[49], polymers[50], oxides[51] and semiconductors[52] have been successfully obtained by electrodeposition through colloidal templates. In general, electrodeposition allows fine control over the thickness of the resulting macroporous and nanoporous films by controlling the charge passed through the system.

1.1.3 Restrictive template-assisted electrodeposition

Nanowires and nanotubes of diverse materials can be synthesized by electrodeposition into the cylindrical pores or channels of an inert, non-conductive nanoporous electrode material. Track-etch polymeric [53] and porous alumina[54] membranes are archetypical materials used for such purposes. Nevertheless, other nanoporous structures including conductive polymers[55], semiconductors[56], carbons[57] and other solid materials[58,59] can also serve as templates to synthesize nanometer-sized particles, fibrils, rods and tubules. Nanoindented holes produced on purpose on a substrate are also used for electrodeposition purposes.[60] The experimental set-up of electrodeposition using restrictive templates is schematically shown in Figure 1.1. The template acts as the cathode, and it is brought into contact with the electrolyte. The anode is placed inside the electrolyte as well, facing the cathode. Polymeric membranes constitute an important class of porous materials, in which (I) pores are randomly distributed; (II) pores with different geometry can be fabricated; (III) pore size can be adjusted between 10 nm and a few micrometers. The maximal pore density is 10^{10} pores/cm^2. They are typically used in low temperature (20-200 ^{o}C) syntheses and in large-scale routine applications. Ceramic templates, like anodized aluminum oxide (AAO) membranes, are usually more fragile, more expensive, and harder to fabricate. On the other hand, ceramic membranes tend to withstand harsher synthetic conditions (e.g., high temperature, solvent, andcorrosive or fouling-favoring environments). Pores in AAO templates are mostly cylindrical and often arranged in a hexagonal fashion. Maximal pore density can reach up to 10^{11} pores/cm^2. Carbon membranes are based on appropriate polymeric or pitch precursors, and they are intermediate (both in character and properties) between polymeric and ceramic membranes. The properties of carbon membranes are closer to the properties of their ceramic counterparts: high temperature and chemical stabilities (except in oxidative environments at temperatures > 350-400 ^{o}C). Besides the desired pore geometry, pore density or size distribution, templates must meet certain requirements: (I) they must be compatible with the processing conditions; (II) they should be chemically inert during the synthesis; (III) the internal pore walls must be wettable by the electrolyte; (IV) it should be possible to dissolve them in order to release the electrodeposited material (nanowires, nanorodos, nanotubes).

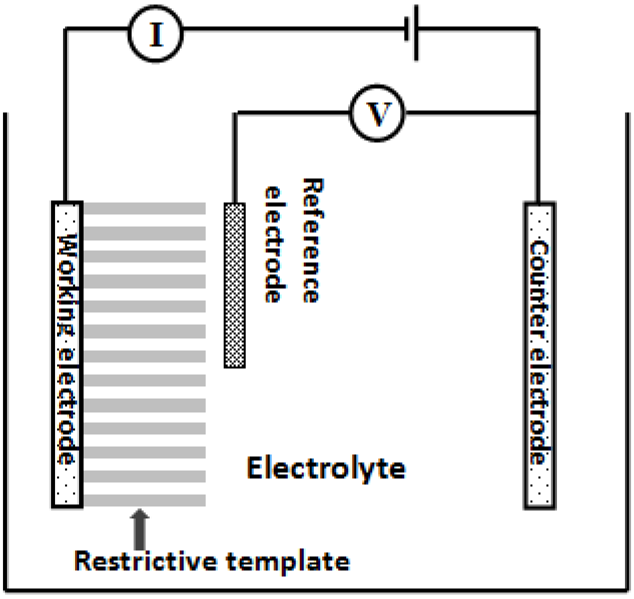

Figure 1.1: Schematic electrode arrangement for the synthesis of nanowires and nanotubes through restrictive template-assisted electrodeposition.

1.2 Porous nanocomposites

The field of nanocomposites involves the study of multiphase materials for which at least one of the constituent phases has one dimension less than 100 nm. The promise of nanocomposites lies in their multifunctionality and the possibility of realizing unique combinations of properties unachievable with traditional single-phase materials. Nanocomposites[61] can be considered as solid structures with nanometer-scale dimensional repeat distances between the different phases that constitute the structure. Classical nanocomposite materials are made of an inorganic (host) solid containing an organic (guest) component or vice versa. Alternatively, they can consist of two or more inorganic/organic phases in some combinatorial form with the constraint that at least one of the phases or features is in the nanosize domain. The nanostructure phase present in nanocomposites can be 0-dimensional (0D) (e.g. embedded clusters), 1D (e.g. nanotubes), 2D (nanoscale coating) and 3D (embedded networks). Extreme cases of nanocomposites are porous media, colloids, gels and copolymers.

Apart from the properties of individual components in nanocomposite systems, interfaces play an important role in either enhancing or limiting the overall properties of the system. A shining example is the mechanical behavior of nanotube-filled polymer composites. Placing nanotubes inside polymers can improve the mechanical properties of the latter. However, if non-interacting interfaces are created, then weak regions in the nanocomposite exist, which do not result in an enhancement of its mechanical properties. Contrarily, if robust interfaces are created, mechanical properties do improve. Such improvement can be exacerbated in the case of porous nanocomposites. Due to their high surface area, interfaces in porous nanocomposites constitute a relatively large volume fraction. As a consequence, their intriguing properties often arise from the interaction of their constituent phases at the interface. In general, porous nanocomposites exhibit several properties (mechanical, electrical, optical, catalytic, and structural-related properties) at once. Each of the properties is either brought by their components or achieved though synergies created between them.

1.2.1 Methods to prepare porous nanocomposites

In recent years, porous membranes and networks have been used to produce porous nanocomposites by the incorporation (through partial filling or coating) of a material into the porous matrix. Two extreme examples are shown in Figure 1.2. On the one hand, a thin layer can be deposited as a negative copy of the porous matrix (Figure 1.2a). The pores are coated or partially filled (nonsaturated state). On the other hand, the porous matrix can be completely filled (saturated state) (Figure 1.2b).

Pore size in porous networks or membranes can range from a few nanometers to several micrometers. The porous matrix provides support and mechanical strength to the final nanocomposite, and sometimes it has its own functionality. Both simple and complex approaches to create porous nanocomposites based on porous matrices are available. A practical dual-phase porous system, such as nanowires embedded in AAO membrane, can be prepared simply by electrodeposition of metals or alloys into the AAO channels[62]. On the other hand, incorporating materials in 3D porous metallic films, which often display hierarchical porosity (i.e., macro- or mesopores with ramified walls), entail several difficulties. Indeed, proper processing techniques must be chosen to avoid oxidation and collapse of these metallic foams. In general, porous nanocomposites can be prepared through several methods, ranging from chemical to vapor phase deposition routes. Some examples of techniques used to partially fill or coat porous matrices are given below:

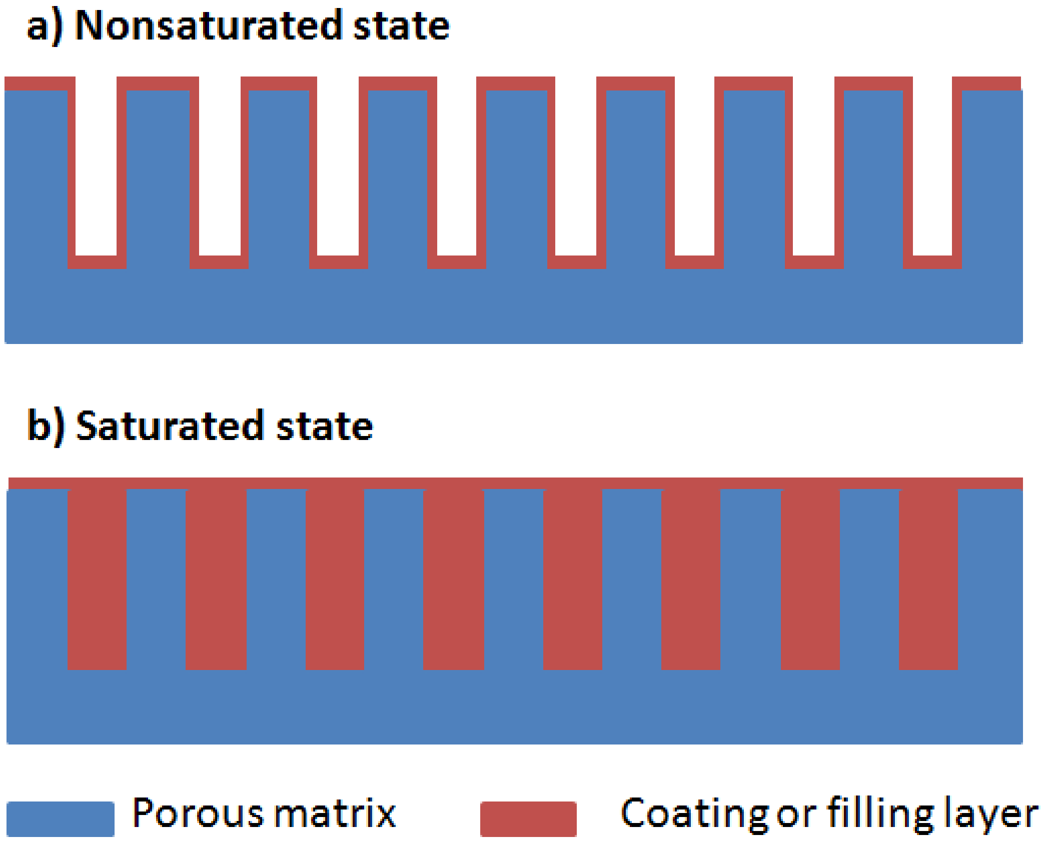

Figure 1.2: Schematic representation of two extreme porous nanocomposites. a) nonsaturated state: the porous matrix is coated or partially filled; b) saturated state: the porous matrix is completely filled.

A. Atomic layer deposition (ALD)

ALD[63] is a thin film deposition technique based on the sequential use of a gas phase chemical process. During coating, two or more chemical vapors or gaseous precursors react sequentially on the substrate surface, producing a solid thin film.

The gas phase precursors could have access to all spaces independent of the substrate geometry and the line-of-sight to the substrate. ALD possesses several advantages over alternative chemical and physical vapor deposition methods, such as precise control of film thickness at the nanometer scale, and the possibility to produce pinhole-free and conformal coatings. In addition, it is a highly repeatable and scalable process.

ALD has been proven successful to grow a wide range of materials[64-68]. These include metals, insulators and semiconductors in both crystalline and amorphous phase. The main limitation of extending ALD to other materials is the limited selection of effective reaction pathways. The selection is further restricted by the availability of reactants. Two main groups of metal reactants are used in ALD: inorganic and metal organic reactants. There is also a selection of counter reactants that are appropriately suited to the metal reactants. For example, NH_3 and H_2S[68,69] are commonly used as counter reactions for depositing nitrides and sulfides. Oxygen counter reactants include O_2[70], H_2O[71], O_3[72], H_2O_2[73] and O· from a plasma source[74], among which O_3 and O· are very reactive and therefore they can be used for low temperature ALD. In spite of its lower reactivity, H_2O is another commonly used oxygen source for oxide, because it is gentle to substrate surface. ALD has been used to deposit materials onto particles, nanotubes, nanorods, high-aspect ratio structures including porous AAO membranes and porous polycarbonate membranes[75-79]. Yet, successful ALD onto porous metallic films is rather challenging and still under investigation. The growth of a conformal coating onto a substrate (e.g. porous metallic film) without worsening the morphological and compositional features of the underlying material (i.e., the porous film) largely depends on the deposition conditions.

B. Magnetron sputtering

Magnetron sputtering[80] is a plasma vapor deposition process in which a target (or cathode) plate is bombarded by energy ions generated in glow discharge plasma, situated in front of the target. The bombardment process causes the removal, i.e., sputtering, of target atoms, which may then condense on a substrate as a thin film. This technique has become a good choice for the deposition of a wide range of industrially relevant coatings. Examples include hard, wear-resistant coatings, low friction coatings, corrosion resistant coatings, decorative coatings and coatings with specific optical or electrical properties.

C. Electrodeposition

Restrictive template-assisted electrodeposition is another effective approach to produce coatings on an electrically conducting surface, as explained in section 1.1.3. It is generally used for the growth of metals, alloys, conducting metal oxides, some metal hydroxides and a few polymers. Both thickness and morphology of the coating can be precisely controlled by adjusting the electrochemical parameters.

D. Suspension infiltration

Suspension infiltration[81] is a method that involves infiltrating an aqueous suspension containing nanoparticles into porous membranes or networks. After infiltration, the liquid-filled porous matrices are freeze-dried to remove the water while retaining a uniform distribution of nanoparticles. Afterwards, soft sintering is applied to firmly bond the nanoparticles to the membrane without altering their original shape. This method is rather straightforward and it is environmentally friendly. In addition, the size and number of nanoparticles can be altered to precisely control the specific surface area of the resulting porous nanocomposites. Finally, the method can be also carried out under controlled air-dry or vacuum dry instead of freeze-dry process. Therefore, it can be readily extended to a wide range of starting porous materials which cannot stand harsh freeze conditions.

E. Sol-gel coating

Sol-gel[82] process is essentially a method for producing solid materials, mainly metal oxides, from small molecules. The process involves the conversion of monomers into a colloidal solution (sol) which acts as the precursor for an integrated network (or gel) of either discrete particles or network polymers. It can be used to prepare thin films, fibers, spheres, powders, aerogels, xerogels and glasses.

In fact, many techniques currently used for fabricating porous nanocomposites are based on sol-gel approaches. Suitable precursors can be added during the sol-gel processing of the material. Sol-gel mixtures can be deposited on a substrate by dip coating process[83], spin coating process[84], spray coating techniques[85] or hydrothermal methods[86] to produce porous nanocomposites. Both dip-coating and spin-coating using sol-gel mixtures as precursors entail limitations when applied to large substrates or substrates with micron-size features. Moreover, using the aforementioned deposition techniques, coatings thicker than 1 μm can only be obtained by repeating coating/calcinations cycles. The development of coating techniques based on sol-gel, especially on relatively large porous metallic foam films, is still in its infancy.

Apart from these exemplary techniques, there are other coating methods available to fabricate nanocomposites based on porous matrices. Coatings can be applied as liquids, gases or solids, depending on the nature of the base porous material.

1.2.2 Classification of porous nanocomposites materials

According to the matrix materials, porous nanocomposites can be classified in three different categories: porous ceramic nanocomposites, porous polymer nanocomposites, and porous metal nanocomposites.

A. Porous ceramic nanocomposites

Porous ceramics are promising candidates for a large variety of applications, such as catalyst supports, energy storage devices, microelectronics, filtration and tissue engineering scaffolds. Pores can offer insulating properties at high temperature, capture impurities in filtration process, as well as providing the architecture for hosting another material. A very useful example of porous ceramic nanocomposites is nanowires or nanotubes electrodeposited into porous AAO[87]. The dimensions and chemical composition of nanowires and nanotubes can be tuned on-demand by adjusting the electrodeposition parameters. Multilayer[88] or core-shell nanowires[89], consisting of different materials along the wire length, can also be synthesized by electrochemical means. The advantage of template-based synthesis of nanowires over other approaches is that the former offers the possibility to grow well-separated individual nanowires with adjustable diameters. Some disadvantages can be the poor crystallinity of the deposited materials (as it is a low-temperature deposition process) and contamination with impurities from electrochemical baths.

Other examples of porous ceramic nanocomposites that have been created out of ceramic scaffolds are Kaolinite-silica and diatomite-based silicalite-1. Kaolinite-silica with controllable specific surface area and strength has been prepared via suspension infiltration method[81]. Likewise, diatomite-based silicalite-1 hierarchical porous nanocomposites were fabricated through a facile *in situ* process[90].

B. Porous polymer nanocomposites

Porous polymers are essential for catalysis, separation, absorption, ion exchange, insulation, drug delivery, and tissue engineering, to name a few. They can be utilized as templates for the deposition of inorganic nanoparticles onto their surface by simply dipping the polymer into a colloidal solution or by vacuum deposition of a volatile metal oxide precursor. In both cases, the polymer needs to withstand both the solvent in which the nanoparticles are suspended and the temperature applied during vacuum evaporation of it. Etch ion-track polymeric membranes, such as polycarbonate membrane (PC), polyethylene terephthalate (PET), polyimide (PI), can serve as templates for electrodepositon to fabricate porous polymer nanocomposites. Details were already provided in section 1.1.3.

C. Porous metal nanocomposites

Porous metals and alloys are also available as matrix materials to form porous metal nanocomposites. An important example of a porous metallic matrix is silver-palladium[91] utilized for separation and purification of hydrogen. The synthesis of chemically homogeneous metal or alloy porous structures by chemical or physical methods is typically challenging because material homogeneity (including composition, pore size, and pore arrangement) is not straightforwardly controlled. To date, template-assisted electrodeposition has been proven successful to fabricate 3D porous metallic films, as described in section 1.1. Depending on the chosen template (e.g. hydrogen or LLC phases), these 3D porous metallic films can have pore sizes ranging from a few nanometers to hundreds of micrometers.

For some specific cases, one-step electrodeposition of porous metal-ceramic nanocomposites in the presence of surfactants is possible. For instance, Bi/Bi_2O_3[92] composites films, with a thickness of 130 µm, have been obtained galvanostatically from an electrolyte containing a nonionic surfactant Triton X-100. Mesoporous Ni/Ni-oxide[93] was electrodeposited from aqueous Ni(II) acetate dissolved in the lyotropic liquid crystalline phases of Brij 56 and Brij 78 surfactant templates.

1.3 Magnetic properties of nanostructured materials

1.3.1 Theoretical background

A. Magnetic behavior of materials

Magnetism is a macroscopic phenomenon, which is due to the existence of magnetic moments in the atoms associated either with the movement of electrons around the atomic nucleus (orbital moment) or electron rotation around their own axis (spin moment). Materials can be classified into different categories depending on the response to an applied external field, *H*:

- **Diamagnetism (DM).** The change in orbital motion in response to an applied field is known as the diamagnetic effect, and it occurs in all atoms. It manifests as a linear relationship between the magnetization and the applied field, with a small negative slope. Actually, diamagnetism only shows up in atoms with no net magnetic moment. In other materials diamagnetism is overshadowed by much stronger contributions, such as ferromagnetism or paramagnetism. Diamagnetic materials do not present permanent magnetic moment upon removal of the applied external field (i.e., no remanent magnetization). Hence, they do not exhibit any hysteresis.
- **Paramagnetism (PM).** In paramagnetic materials, the magnetic moments are virtually uncoupled to each other and thermal energy causes random alignment of the magnetic moments of each atom, as shown in Figure 1.3a. In other words, the magnetic exchange interactions between neighboring atoms are negligible. Nevertheless, when a magnetic field is applied, the magnetic moment starts to align, but only a small fraction becomes actually

oriented along the field direction, thus resulting in a small linear positive slope in the magnetization versus field curve, but without hysteresis.

- **Ferromagnetism (FM).** In ferromagnetic materials, the spins of neighboring atoms are oriented parallel each other since they are coupled via positive exchange interactions. Upon application of an external magnetic field, the moments tend to orient along the field direction, as depicted in Figure 1.3b. When the field is removed, magnetic domains form and a certain fraction of the saturation magnetization is retained, giving rise to a remanent magnetization. As a result, the magnetization versus field curve shows a hysteretic behavior, which means that the material “remembers” the direction of the previously applied magnetic field. Temperature plays an important role in ferromagnetic materials. When the material is heated to above the Curie temperature (T_c), the thermal energy is high enough to overcome the cooperative ferromagnetic ordering and, as a consequence, ferromagnetic materials become paramagnetic.
- **Antiferromagnetism (AFM).** In antiferromagnetic materials, the interaction between the magnetic moments tends to align adjacent moments antiparallel to each other, as shown in Figure 1.3c. This is the result of negative exchange interactions. Because of this antiparallel alignment, the net moment in absence of an external magnetic field is zero. When a magnetic field is applied, the magnetization versus field curve shows a linear behavior with a positive slope, as for the case of paramagnetic materials. Similar to ferromagnetic materials, antiferromagnetism disappears when temperature is larger than the so-called Néel temperature (T_N), where thermal energy transforms the antiferromagnetic material into a paramagnetic one.
- **Ferrimagnetism:** Similar to antiferromagnetic materials, the exchange interactions between neighboring atoms are also negative in ferrimagnetic materials (antiparallel alignment), but the net magnetic moment is not zero because the magnetization of one sublattice is greater than that of the oppositely oriented sublattice (Figure 1.3d). From a phenomenological point

of view, ferrimagnetic materials behave similarly to ferromagnetic ones, with a clear hysteresis loop.

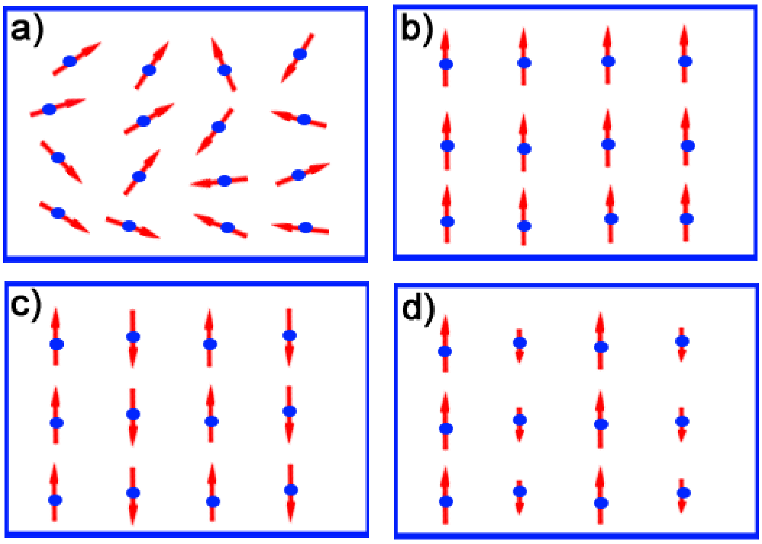

Figure 1.3: Schematic representation of the magnetic moments configuration for: a) paramagnetic, b) ferromagnetic, c) antiferromagnetic, d) ferrimagnetic materials.

B. Magnetization curves

The fundamental motivation behind the study of nanostructured magnetic materials is the dramatic change in the magnetic properties observed when the critical length governing a given phenomenon is comparable to the nanocrystal or nanomaterial size. Effects related to the surface or the interface are stronger in particulate systems than in thin films due to the larger amount of exposed surface.

In classical ferromagnets, the magnetization does not fall to zero when the applied magnetic field is removed. To get familiarized with commonly measured magnetic parameters, Figure 1.4 schematically illustrates the typical hysteresis loop (magnetization versus field) displayed by a ferromagnetic material. The application of a magnetic field causes the spins to progressively align with the field. At sufficiently high fields, the magnetization levels off and reaches a constant value, called saturation magnetization, M_s. When the magnitude of the applied field is reduced back to zero, the magnetization retains a positive value, termed remanent magnetization, M_r. The ratio of the remanent magnetization to saturation magnetization, M_r/M_s, is called squareness ratio and it varies from 0 to 1. The remanent magnetization can be removed by reversing the magnetic field strength to a value equal to the coercivity, H_c. When the reversed magnetic field is increased further, saturation is achieved in the reversed direction.

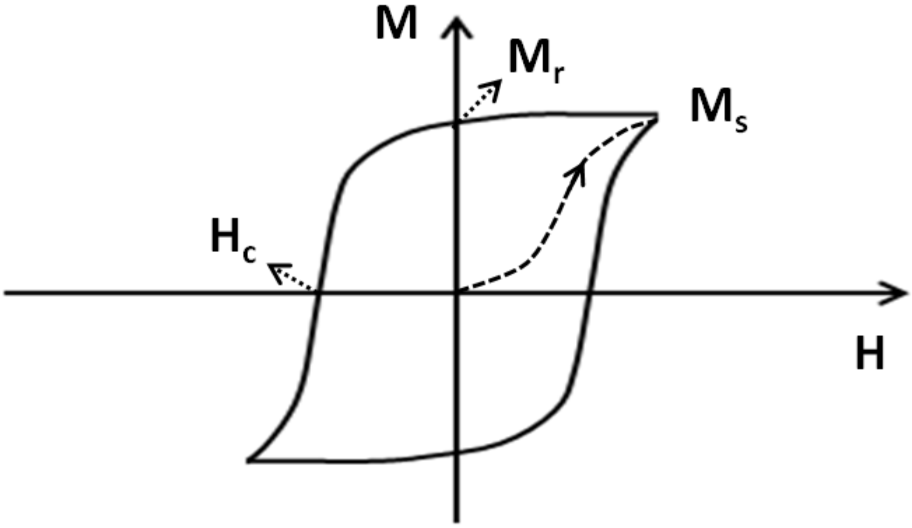

Figure 1.4: Schematic representation of a hysteresis loop in a ferromagnetic material. The saturation magnetization, $M_{S,}$ remanent magnetization, M_r and coercivity, H_c, are indicated. The dashed curve depicts the non-linear magnetization path described by the material when it is initially magnetized from a zero field value.

The hysteresis loop shows the "history dependent" nature of magnetization for a ferromagnetic material. The suitability of nanostructured ferromagnetic materials for a particular application is largely determined by the characteristics of their hysteresis loops. Nanostructured magnetic materials show a wide variety of unusual magnetic properties compared to the bulk materials. In case of bulk defect-free materials, their intrinsic magnetic properties only depend on the chemical and crystallographic structure. The size and shape of studied bulk samples are not crucially important, i.e., for instance, M_s, H_c and T_c values of small and big cobalt samples are all equal. However, magnetic characteristics of nanostructured materials are strongly influenced by the so-called finite-size and surface effects. Finite-size effects, in the strict sense of word, come from quantum confinement of the electrons. Surface effects are related, in the simplest case, to the symmetry breaking of the crystal structure at the boundary of each particle, but it can also be due to different chemical and magnetic structures of internal (“core”) and surface (“shell”) parts of nanostructured materials.

C. FM materials: soft and hard

Because of their “memory effect”, FM materials are really important for widespread technological applications. Ferromagnetic materials tend to organize spontaneously in small volumes called domains, wherein the magnetic moments of each atom are oriented parallel to each other along a certain direction, different than that from neighboring domains. In the absence of magnetic field, the overall domain arrangement minimizes the external energy and the bulk material appears demagnetized. When a magnetic field is applied the domains oriented favorably with respect to the applied field direction grow at the expenses of unfavorably oriented ones, until all moments in the material are parallel to the applied field, reaching the saturation magnetization (M_s). Magnetic domains are responsible for the magnetic hysteresis exhibited by FM materials since the domain configuration at remanence (after saturation and removal of the external field) is no longer isotropic, but gives rise to a certain remanent magnetization (M_r). The negative magnetic field that needs to be applied to return the net magnetization back to zero is called coercivity (H_C). FM materials are characterized by a T_c above which thermal agitation destroys the magnetic exchange coupling, transforming the material into paramagnetic.

Iron, cobalt, nickel, and their alloys, some manganese compounds, and some rare-earth compounds show FM response. They can be further classified as soft or hard according to the shape of their hysteresis loops. Some examples of soft FM materials are Fe, Ni, permalloy and CuNi alloys. Soft FM materials are characterized by low values of coercivity (H_c), often lower than 10 Oe, and large values of M_s, usually higher than 100 emu/g. Hence, they feature a narrow hysteresis loop (see Figure 1.5a). Hard ferromagnetic materials, also known as permanent magnets, strongly resist demagnetization once magnetized. They are used, for example, in motors, loudspeakers or meters, and have high value of H_c, typically larger than 350 Oe, and smaller values of M_s compared to soft materials. Accordingly, they show wide hysteresis loops (Figure 1.5b).

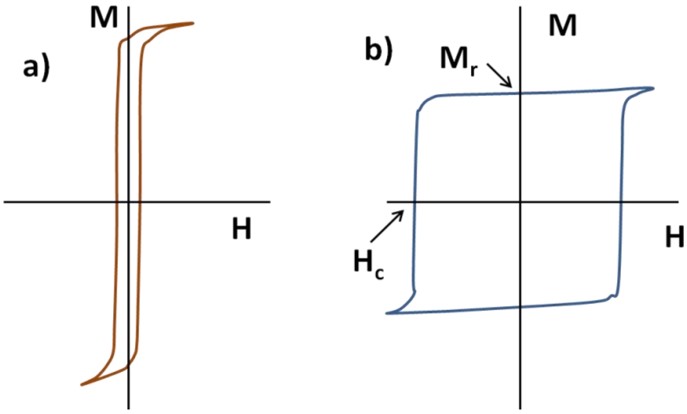

Figure 1.5: Typical hysteresis loops for a) soft- and b) hard-ferromagnetic materials.

D. Magnetic anisotropy

The term "magnetic anisotropy" refers to the dependence of the magnetic properties on the direction along which they are measured. The strength and type of magnetic anisotropy affect the shape of the hysteresis loops. As a result, magnetic anisotropy greatly determines the suitability of a magnetic material for a given application. The most common types of magnetic anisotropy are (1) magnetocrystalline anisotropy, (2) shape anisotropy, (3) surface anisotropy, (4) stress anisotropy and (5) exchange anisotropy (for example by the interface coupling with an antiferromagnet)[94]. Among them, magnetocrystalline anisotropy and shape anisotropy are most often discussed when dealing with nanostructured materials. In a first approximation, anisotropy can be modeled as uniaxial in character and, then, it is simply represented by

$$E = KV\sin^2\theta \qquad \text{[Eq. 1.1]}$$

Here E stands for the anisotropy energy; K is the effective uniaxial anisotropy energy per unit volume, θ is the angle between the moment and the easy axis, and V is the particle volume.

Magnetocrystalline anisotropy arises from spin-orbit coupling and energetically favors alignment of the magnetization along a specific crystallographic direction. It can be defined as the tendency for the magnetization to align itself along a preferred crystallographic direction, i.e. the easy magnetization axis of the materials. The crystalline anisotropy is specific to certain materials and operates independently of the particle shape. For example, at room temperature, cobalt crystallizes in the hexagonal close packed structure, being the hexagonal (*c*) axis the easy axis. In the cubic systems, symmetry creates multiple easy axes. Face-centered cubic Ni has <111> direction as its easy axis. Meanwhile, for Fe, which possesses body-centered cubic crystallographic structure, the easy axis is <100>. In most materials the spin-obit coupling is fairly weak, and therefore the crystalline anisotropy is not particularly strong. High-anisotropy materials always contain heavy elements in their composition, such as rare-earth elements. For these materials, a large field must be applied in the direction opposite to the magnetization in order to overcome the anisotropy and reverse the magnetization. Hence, materials containing rare-earth elements are attractive candidates for high-coercivity applications.

Although most materials show some crystallographic anisotropy, a polycrystalline sample with no preferred grain orientation has no net crystal anisotropy. A spherically- shaped material will be magnetized by the same field to the same extent in every direction. However, if the material is not spherical, then it will become easier to be magnetized along its long axis. This phenomenon is known as shape anisotropy. Shape anisotropy is predicted to produce the largest coercivity. For single-domain Fe particles, an increase of the aspect ratio from 1.1 to 1.5 with the easy axis aligned along the field results in a four-fold increase of coercivity. An increase in the aspect ratio to 5 additionally doubles the coercivity.

Anisotropy can also be induced by a treatment, such as annealing in the presence of a magnetic field, by plastic deformation or ion beam irradiation. Most materials in which magnetic anisotropy can be induced are polycrystalline alloys. Stress anisotropy results from external or internal stress generated upon rapid cooling, external pressure, etc. Exchange anisotropy occurs when a ferromagnet is in close contact to an antiferromagnet or a ferrimagnet. A preferential direction in the ferromagnetic phase can be created due to the occurrence of a magnetic coupling at the interface.

E. Influence of particle size on coercivity. Single domain particles

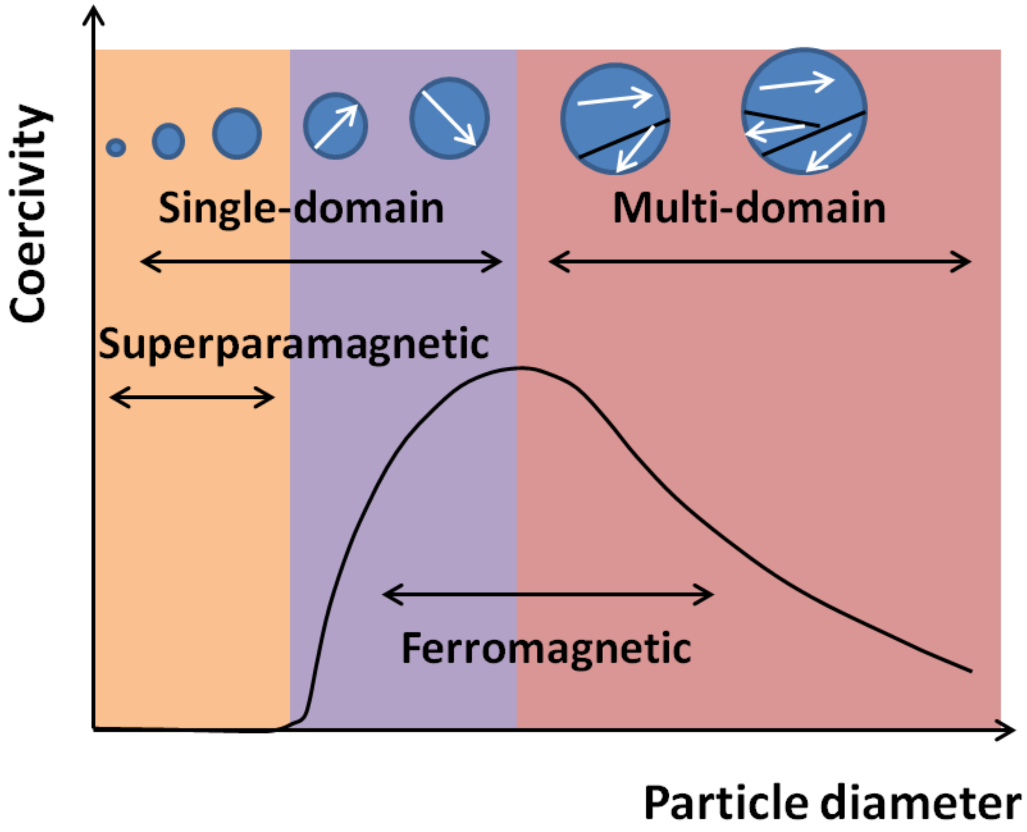

Figure 1.6: Size dependence of coercivity in magnetic nanoparticles.

Magnetic domains—defined, as aforementioned, as small regions of material comprising groups of spins aligned parallel to each other and acting cooperatively—are separated by domain walls, which have a characteristic width and formation energy. Experimental investigations[95] on the dependence of coercivity on the particle size or volume of studied ferromagnetic material show a behavior similar to the one schematically illustrated in Figure 1.6. In large particles, the formation of domain walls is energetically favorable. As particle size is reduced and approaches the critical particle size, D_c, the formation of domain walls becomes unfavorable and the particle is referred to a “single domain particle”. Changes of magnetization can no longer occur through domain wall propagation and magnetization reversal occurs by coherent rotation, resulting in a maximum coercivity value. Thereafter, when the particle size is further reduced below the single domain size, spins become strongly influenced by the thermofluctuations and the coercivity falls to zero, since thermal energy overcomes the anisotropy energy. This occurs at the so-called superparamagnetic limit. Reviews on single domain particles were published by Bean and Livingston[96], Brown[97], Wohlfarth[98], Jacobs and Kneller[99], etc. Theoretical predictions were made by Frenkel and Dorfman[100].

F. Types of magnetic nanocomposites and overview of their magnetic properties

Depending on the physical mechanisms responsible for the magnetic behavior in nanostructured materials, different "nanostructured morphologies" can be distinguished. This classification was proposed by Rieke[101]. There are two extreme regimes. On the one hand, one can find systems consisting of isolated magnetic particles with nanoscale diameter embedded in a non-magnetic medium (type *a* systems, Figure 1.7a). These non-interacting systems derive their unique magnetic properties strictly from the reduced size of the components, with no contribution from interparticle interactions. To avoid these interactions, the particles need to be well dispersed in the matrix. On the other hand, there are bulk nanostructured magnetic materials with nanoscale structure (type *d* in Figure 1.7d), in which a significant fraction (up to 50%) of the sample volume is composed of grain boundaries and interfaces. Contrary to type *a* systems, magnetic properties here are dominated by the interactions. The length scale of the interactions can span many grains and it is critically dependent on the character of the interface. The predominance of interactions and grain boundaries in type *d* nanostructures means that their magnetic behavior cannot be predicted simply by applying theories used for polycrystalline materials with reduced length scales but, instead, their magnetic response is more complex.

The magnetic behavior of most experimentally realizable systems is the sum of contributions of both interaction and size effects. Classification of materials according to dimensionality is useful from the viewpoint of structural-related properties. However, an alternative classification is suggested to properly describe magnetic materials. Figure 1.7 schematically shows four categories of nanostructured magnetic materials ranging from non-interacting particles (type *a*) for which the magnetization is determined strictly by size effects, to fine-grained bulk structures, in which interactions dominate the magnetic properties. Two forms of each of these types are indicated: the ideal type *a* material is one in which the particles are separated from each other and can be treated as non-interacting. Ferrofluids, in which long surfactant molecules provide separation of particles, are a subset of type *a*. Type *d* materials may be single phase, in which both the crystalline and the noncrystalline fractions of the material are chemically identical, or they may consist of multiple phases. Intermediate forms include ultrafine particles with core-shell morphology (type *b*), as well as nanocomposite materials (type *c*) in which two chemically dissimilar materials are combined. In type *b* particles, the presence of a shell can help prevent particle-particle interactions, but often at the cost of interactions between the core and the shell. In many cases, the shells are formed via oxidation and may themselves be magnetic. Type *c* nanocomposites consist of magnetic particles distributed throughout a matrix, and the magnetic interactions are determined by the volume fraction of the magnetic particles and the character of the matrix.

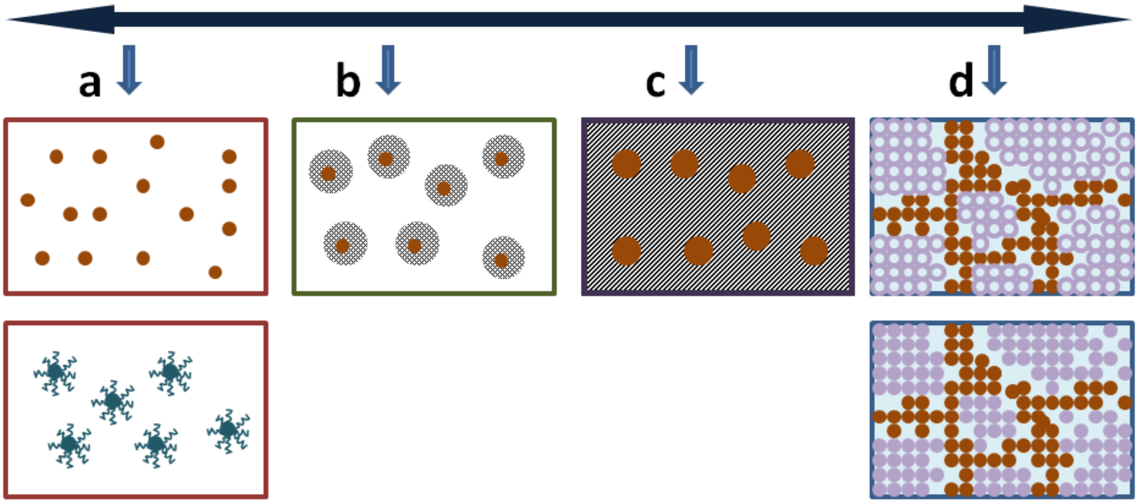

Figure 1.7: Schematic representation of the different types of magnetic nanostructured materials.

1.3.2 Applications

Over the years, magnetic materials have found a wide range of technological applications, some of them very well-known (permanent magnets in loudspeakers and headphones, hard disks of computers, cores of electric transformers, etc.), and others less well-known (such as drug delivery systems, wirelessly actuated robotic platforms, beam guides in synchrotrons, etc.). Here emphasis is put on two different applications that are representative of the types of materials studied in this Thesis: magnetic targeted drug delivery systems and magnetic recording.

A. Magnetic targeted drug delivery system

The concept of “drug delivery” was first proposed by Freeman[102] who stated that fine iron particles can be transported through the vascular system and be concentrated at a particular region of the body with the aid of an external magnetic field. In this way, nanostructured magnetic materials can be used to deliver drugs or antibodies to the organs or tissues altered by diseases. The process of drug localization using magnetic delivery systems is based on the competition between forces exerted on the nanostructured magnetic materials by blood compartment (dragging forces), and magnetic forces associated with torques generated by the magnets. Controlled drug delivery systems can be specially designed to obtain the desired effects on target sites by combination of carrier materials and carried drugs, thus avoiding the serious concerns associated with generalized chemotherapy.

Many drug carriers[103-108] including dendrimers, micelles, emulsions, organic and inorganic micro- and nanoparticulated systems, nanowires, nanotubes, liposomes, virosomes, metal-organic frameworks (MOF), hydrogels, and polyelectrolyte multilayer, have been described in the literature. Many of them can be engineered to contain multiple tags (chromophores, optical or magnetic responsive nanoparticles, to name a few) together with the carried drug for both imaging/cell trafficking and therapy. Porous materials[109] can serve as drug carriers as well. Their large inner surface areas, high surface-to-volume ratio, large pore volumes, tunable pore size and well-known possibilities of pore-wall functionalization allow them to host in their interior a wide variety of drugs and molecules. The large inner surface area permits the adsorption of large amounts of drugs or biomolecules because adsorption is a surface-based phenomenon. Moreover, these structured porous materials can be configured as micro- and nanoparticulated systems, fibers, monoliths, coatings, etc., hence opening up their application in diverse medical fields. Moreover, new developments in nanodrug delivery suggest that nanowires[110] coated with drugs could effectively deliver drugs into cells or organs. These nanowires could even penetrate intracellularly and, in some cases, be delivered into a biological system for cell repair or therapeutic activities.

Nanostructured magnetic materials for drug delivery applications must possess some specific characteristics[111]. The first requirement is often to display a superparamagnetic behavior. Superparamagnetism is preferred because once the external magnetic field is removed, magnetization disappears (negligible remanence and coercivity), and thus agglomeration (and therefore possible problems like embolization or thrombosis of capillary vessels) can be avoided. Another key requirement is the biodegradability or intact excretion of the magnetic drug carrier. For non-biodegradable cases, a specific coating is needed to avoid exposure and leach of the magnetic drug carrier and to facilitate intact excretion through the kidney, so that the half-life of the agent in the blood is determined by the glomerular filtration rate.

B. Magnetic recording

Magnetic materials have long served as dependable media for digital data storage and have efficiently served as basis for audio and video recording. Magnetic recording technology has constantly evolved to achieve consistent areal density growth. As longitudinal recording has reached its limit, perpendicular recording technology has taken over[112-113]. At really high densities, tight control of the media microstructure, especially grain size, grain size dispersion, and chemical isolation to avoid exchange and dipolar interactions are necessary, in order to keep the media noise within acceptable limits. Materials with high uniaxial magnetocrystalline anisotropy are attractive for ultra-high-density magnetic recording applications because they allow smaller, thermally stable media grains while circumventing the superparamagnetic limit. Indeed, the search for higher magnetic recording densities pursues particle sizes that are < 10 nm. With such small particle size, high magnetocrystalline anisotropy is needed to avoid thermal and field fluctuations that can destroy the magnetization in recorded locations. Particle-dispersed recording systems are also possible targets for future magneto-optical data storage. For the particulates, high magnetization is crucial, because it determines the strength of the magnetic stray field detected during read processes. Alloys have advantages in this regard and encapsulation in medium (matrix) can solve several problems associated with chemical stability of the particulates. Nanocomposites, e.g., metal/carbon, metal/oxide, or immiscible metal/metal mixtures, are prospective routes toward generating < 10 nm granular structures, which are needed for ultrahigh density recording. Much work has been reported on nanocrystalline rare-earth transition-metal films, most prominently Co_5Sm- and $Co_{17}Sm_2$- based films.

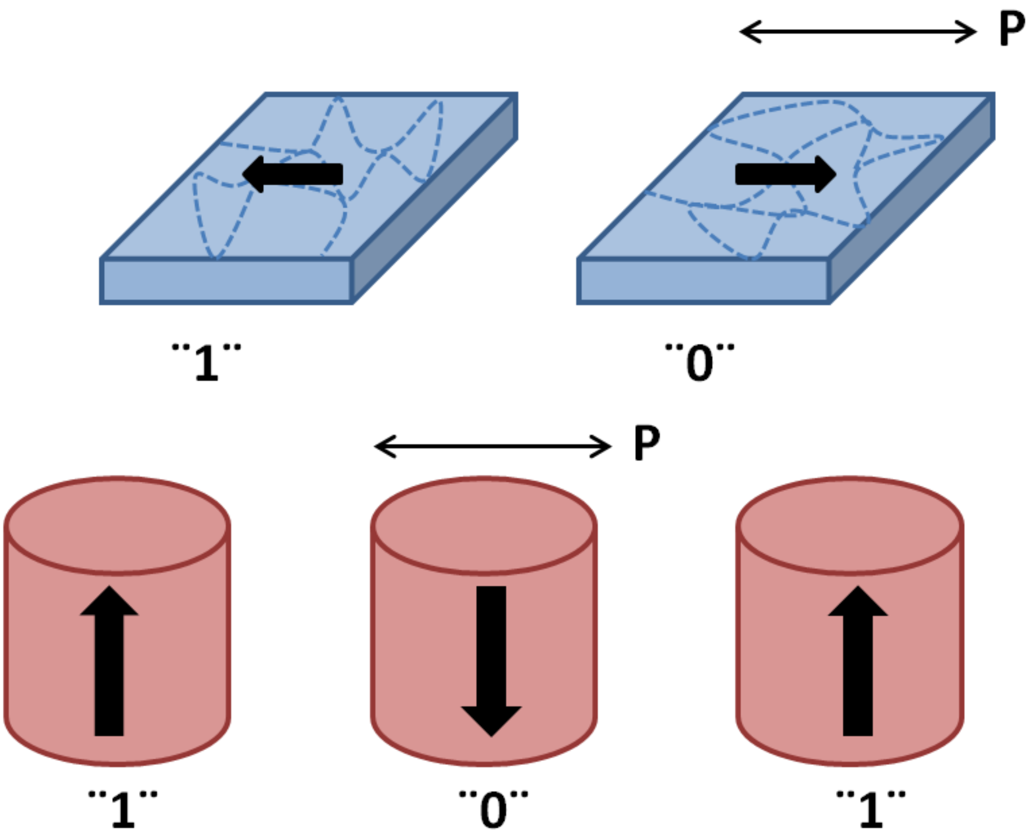

Figure 1.8: a) Patterned medium with in-plane magnetization. The single-domain bits are defined with lateral size “p”. They can be polycrystalline (as indicated by dotted lines) with exchange coupling, or single crystal. b) patterned medium with perpendicular magnetization. Binary “1” and “0” are shown.

Patterned media[114], in which data is stored in an array of single-domain magnetic particles is necessary to overcome the thermal instability and to enable recording densities of up to 1 Tbit in^{-2}. Schematically shown in Figure 1.8 is a patterned recording medium that consists of a regular array of magnetic elements, each of which has uniaxial magnetic anisotropy. The easy axis can be oriented parallel or perpendicular to the substrate. Each element stores one bit, depending on the direction of its magnetization state. Unlike thin film media, the grains within each patterned element are coupled so that the entire element behaves as a single magnetic domain. Particle arrays with deep sub-micron feature sizes are too small to be fabricated using conventional optical lithography. Instead, a range of nanolithography techniques has been used to make prototype structures, including electron-beam, X-ray, imprint, and interference lithographies. Arrays of magnetic particles can also be synthesized by using self-organized templates. These templates can possess an ordered structure whose period may be smaller than that achievable through lithography. The template is then used as a mask for the etching of a magnetic material or as a mold for deposition of magnetic material. Same deposition techniques can be applied for lithography and template growth techniques. Self-assembly methods have also been developed in which magnetic particles are synthesized chemically and assembled as a close-packed monolayer on a surface. Structures with period of order 10 nm can be made, a feature size that is beyond that of most lithography techniques.

1.4 Surface related properties

1.4.1 Wettability

Wettability is the ability of a liquid to maintain contact with a solid surface. It is governed by the occurrence of intermolecular interactions when the two are brought together. The degree of wettability is determined by a force balance between adhesive and cohesive forces. The topic of wettability has received tremendous interest from both fundamental and applied points of view. It plays an important role in many industrial processes, such as oil recovery, lubrication, liquid coating, printing, and spray quenching[115-119]. Wettability involves the three phases of matter: gas, liquid and solid. In recent years, there has been an increasing interest in the study of superhydrophobic surfaces, due to their potential applications in self-cleaning, nanofluidics, and electrowetting[120-124]. Wettability studies usually involve the measurement of contact angles as the primary data, which indicate the degree of wetting when a solid and liquid interact.

A. Contact angle and surface tension

Contact angle is the angle that a liquid creates with a solid surface or the capillary walls of a porous material when both materials come in contact together. Adhesive forces between liquid and solid make the liquid drop to spread across the solid surface. Likewise, cohesive forces within the liquid make the drop to ball up and to avoid contact with the surface. Consider a liquid drop resting on a flat, horizontal solid surface (Figure 1.9). A small contact angle is observed when the liquid spreads on the surface, while a large contact angle is observed when the liquid beads on the surface. More specifically, a contact angle below 90° indicates that wetting of the surface is favorable, and the fluid will spread over a large area on the surface. Meanwhile a non-wetting liquid creates a contact angle between 90° and 180° with the solid surface and forms compact liquid droplets. For example, complete wetting occurs when the contact angle is 0°, as the droplet turns into a flat puddle. For superhydrophobic surfaces, water contact angles are usually greater than 150°, showing almost no contact between the liquid drop and the surface, which can be rationalized by the "lotus effect"[125]. Furthermore, contact angles are not limited to the liquid or vapor interface on a solid; they are also applicable to the liquid-liquid interface on a solid.

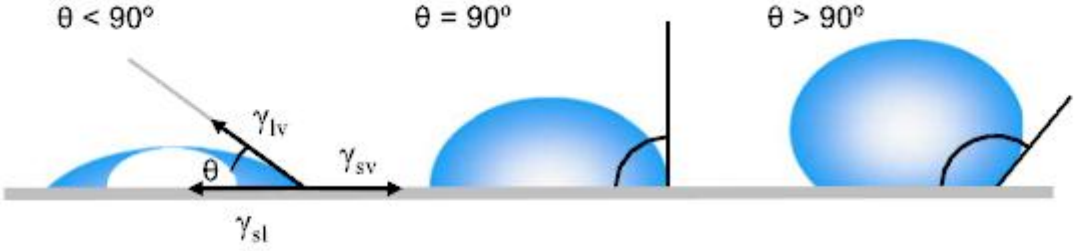

Figure 1.9: Schematic illustrations of the contact angle formed by sessile liquid drops on a smooth homogeneous solid surface. (Taken from *Surface Science Techniques,* Springer Series in Surface Science 51, DOI: 10.1007/978-3-642-34243.1_1, 2013)

The cohesive forces between liquid molecules are responsible for the phenomenon known as surface tension. Ideally, it determines the shape of a liquid. In a pure liquid, each molecule in the bulk is pulled equally in every direction by neighboring liquid molecules, resulting in a zero net force. However, the molecules exposed at the surface do not have neighboring molecules in all directions to provide a balanced net force. Instead, they are pulled inward by the neighboring molecules (Figure 1.10), creating an internal pressure. As a result, the liquid voluntarily contracts its surface area to maintain the lowest surface free energy. Small droplets and bubbles are usually spherical, which will minimize the surface area for a fixed volume. The intermolecular force is called surface tension, and it is responsible for the shape of the liquid droplets. In practice, the contact angle is determined by a combination of surface tension and external force (usually gravity)[126].

Figure 1.10: Surface tension is caused by the unbalanced forces of liquid molecules at the surface. (Taken from *Surface Science Techniques,* Springer Series in Surface Science 51, DOI: 10.1007/978-3-642-34243.1_1, 2013)

B. High-energy and low-energy surfaces

Traditionally, solid surfaces have been divided into high-energy solids and low-energy solids. The relative energy of a solid has to do with the bulk nature of the solid itself. Solids such as metals, glasses, and ceramics are known as “hard solids”, because the chemical bonds that hold them together (metallic, covalent or ionic) are very strong. Thus, it takes a large input of energy to break these solids. They are termed as “high-energy” solids. Most molecular liquids achieve complete wetting with high-energy surfaces.

The other type of solids is weak molecular crystals (e.g. fluorocarbons, hydrocarbons, etc.) where the molecules are held together essentially by physical forces, such as van de Waals and hydrogen bonds. Therefore these materials are termed as “low-energy” solids. Depending on the type of liquid chosen, low-energy surfaces can permit either complete or partial wetting[127]. It is possible to predict the wettability of a surface if the critical surface tension of the solid is known. Besides, wettability is also determined by the outermost chemical groups of the solid. Differences in wettability between surfaces that are similar in structure are due to differences in the packing of atoms. For instance, if a surface has branched chains, it will have poorer packing than a surface with straight chains.

C. Contact angle measurement of rough surfaces

The wetting behavior of rough surfaces is a complex phenomenon, since contact angle varies with porosity, roughness and wall morphology. The relationship between roughness and wettability was described by Wenzel[128] in 1936, who stated that any change in wettability caused by increasing surface roughness depends on the chemical nature of the surface. For example, ”spontaneous” liquid penetration might occur if the actual solid favors wetting. The liquid fills the voids beneath and thus occupies larger surface area (Figure 1.11). In cases where the liquid does not penetrate into the grooves, the Wenzel’s theory cannot be applied. A liquid drop in Cassie[129] state, as illustrated in Figure 1.11, rests upon the asperities with gas pockets trapped in the voids. In turn, the contact surface area is lower than it would be for a droplet of the same volume on either a flat or a rough surface in Wenzel state. It has been found that a real Cassie state can be achieved, i.e. no penetration of liquid into the voids, if surface morphology is carefully designed [130].

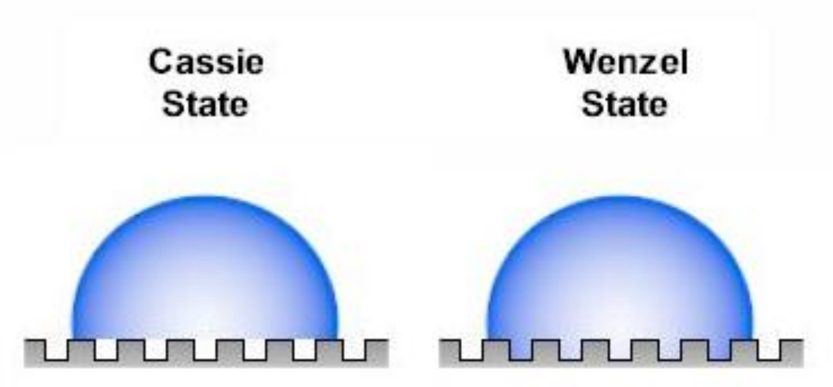

Figure 1.11: Schematic representation of a liquid droplet on a rough surface, following the Cassie state and Wenzel state. (Taken from *Raméhart instrument* website)

1.4.2 Electrocatalysis

Hydrogen evolution reaction (HER) on different metals in acidic or alkaline media is one of the most investigated reactions in the field of electrochemistry. HER is currently receiving considerable attention because: i) hydrogen is an interesting candidate as an energy carrier for future fuel cells applications, ii) it is one of the main reaction products in chlorine production, iii) HER supplies highly pure hydrogen.

For the case of HER in acidic or neutral electrolyte, processes that occur at the surface of electrodes are described as follows[131]:

Cathode: $4H_3O^+ + 4e^- \rightarrow 4H_2O + 2H_2$ [Eq. 1.2]

Anode: $6H_2O \rightarrow 4H_3O^+ + O_2 + 4e^-$ [Eq. 1.3]

Net: $2H_2O \rightarrow 2H_2 + O_2$ + Heat [Eq. 1.4]

When the process takes place in an alkaline electrolyte, electrochemical reactions occurring at the cathode and anode are[132]:

Cathode: $2H_2O + 2e^- \rightarrow 2OH^- + H_2$ [Eq. 1.5]

Anode: $2OH^- \rightarrow ½O_2 + H_2O + 2e^-$ [Eq. 1.6]

Of course the sum will lead to the same net reaction as that described in acidic media. The reaction rate has been proven to be faster in acidic electrolyte than in alkaline solution, due to the higher facility to extract hydrogen atoms from H_3O^+ (acid solution) than H_2O (alkaline solution). However, for the specific case of alkaline electrolyte, where a strong base is used, hydroxide anions are transported from the electrolyte to the anode surface, where they lose electrons. Although Pt and Pt alloys are by far the best HER catalysts, the high price of Pt ores has persuaded the research community to look for cheaper and more abundant alternatives. For example, Ni[133] and its alloys are popular choices for HER in alkaline solution because of their low-cost, good activity and availability. To enhance conductivity, the electrolyte usually consists of high-mobility ions. Potassium hydroxide is normally used, which in turn avoids corrosion problems caused by acid electrolytes.

A. Porous bimetallic catalysts for HER

For HER, bimetallic electrodes are normally employed. Electrode materials selected should have good corrosion resistance, high conductivity, high catalytic effect, and low price[134]. Endowing bimetallic materials with high surface area is of paramount importance for HER applications. He and co-workers[135] studied the influence of electrolyte concentration and temperature on the HER behavior of porous Ni_3Al bimetallic electrodes. Lu et al.[136] successfully synthesized nanoporous Cu-Ti bimetallic electrocatalyst, which is able to produce hydrogen from water under a mild overpotential at more than twice the rate of the carbon-supported Pt catalyst. García-Anton and co-workers[137] compared the HER behavior of porous CoNi with Ni in alkaline solution. It was shown that the presence of Co improves the intrinsic catalytic behavior of electrode, especially at high temperature. Tungsten and molybdenum[138] were also individually combined with Ni to evaluate the synergy effect of these metals (i.e., Ni-W and Ni-Mo) in the HER activity. In any case, it is difficult to predict the HER activity of bimetallic porous materials. Research in the HER electrodes development has focused on several areas of interest: i) intrinsic nature of the reaction, ii) electrode composition, iii) surface morphology (including surface area), iv) structure, chemical and electronic properties, and v) physical, chemical and electrochemical activation treatments.

1.4.3 Photoluminescence

The photoluminescence (PL) technique has been widely used to investigate the structure and properties of the active sites on the surface of metal oxides and zeolites. Compared to other characterization techniques, PL possesses high sensitivity and it is non-destructive. Also, PL technique has been applied to the photocatalysis field for understanding surface processes occurring on semiconductors. Information such as surface oxygen vacancies and defects, efficiency of charge carrier trapping, migration and transfer can be obtained from PL measurements in order to describe the electronic structure, optical and photochemical properties of semiconductor materials. It is well-known that PL signals in semiconductor materials result from the recombination of photo-induced charge carriers. In general, the lower the PL intensity, the lower the recombination rate of photo-induced electron-hole pairs, and the higher the photocatalytic activity of semiconductor photocatalysts.

A. PL mechanism of semiconductor materials

Semiconductors are characterized by an electronic band structure in which the highest-occupied energy band, called valence band (VB), and the lowest-occupied energy band, called conduction band (CB), are separated by a band gap, i.e. region of forbidden energies[139-141]. Figure 1.12 shows the main photophysical processes for a semiconductor excited by light with an energy value not less than the band gap energy. Here, only the PL phenomena of excited energy higher or equal to the band gap energy of semiconductor are represented. Four main processes occur[142]. Process I is the photo-excited process in which the electrons from the VB are promoted to the CB to reach different excited states, with simultaneous generation of holes (h^+) in the VB under irradiation. However, the excited electrons in the CB easily come back to the VB via a certain path to recombine with holes, since they are very unstable. During the recombination process, a certain amount of chemical energy can be released, which would further transform possibly to heat or to light energy. The light energy can be dissipated as radiation, which results in a luminescence emission of semiconductor materials, called the PL phenomenon. In fact, the excited with different energy levels in the CB easily transfer firstly to the CB bottom via non-radiative transitions; subsequently, processes II, III, IV will possibly occur. Process II is the band-band PL process in which the electron transitions from the CB bottom to the VB top can take place, with simultaneous release of energy as radiation. Process III is the excitonic PL process in which the non-radiative transitions of excited electrons from the CB bottom to different sub-bands (or surface states) occur first, and subsequent radiative transitions from the sub-band to the VB top can take place. In addition, the excited electrons at the bottom of the CB can come back to the VB directly or indirectly by non-radiative transitions, this being process IV. In fact, only photophysical process II and III can give rise to PL phenomena. The former is attributed to the band-band PL, and the latter is attributed to the excitonic PL. According to PL attributes, the band-band PL spectrum can directly reflect the separation situation of photo-induced charge carriers, viz. the stronger the band-

band PL signal, the higher the recombination rate of photo-induced carriers. The excitonic PL spectrum cannot directly reflect the separation situation of photo-induced carriers. Instead, it provides some important information about surface defects, oxygen vacancies and surface states, which can strongly affect photocatalytic reactions.

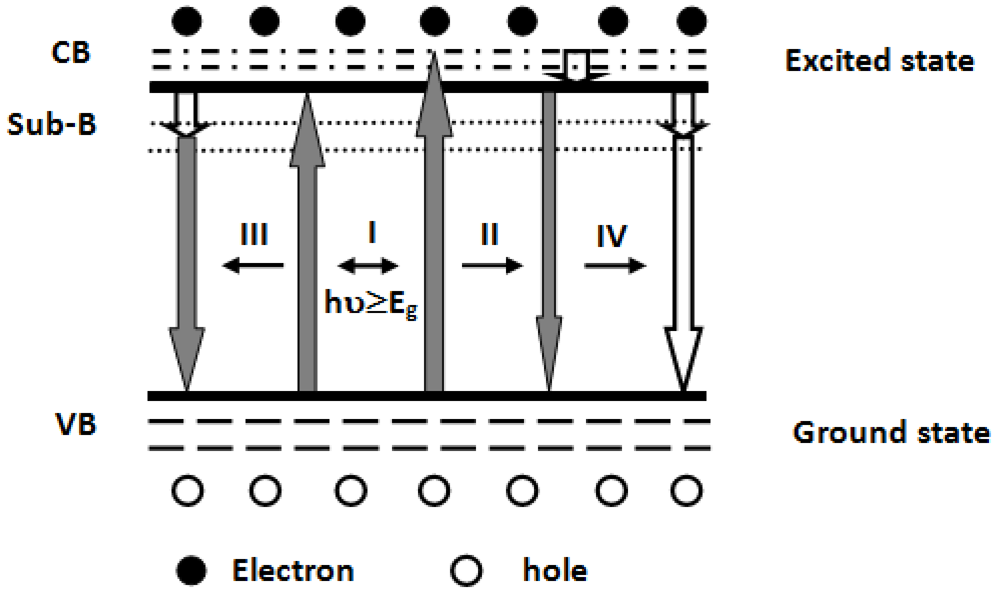

Figure 1.12: Main photophysical processes of a semiconductor excited by light with equal or higher energy than the band gap energy (I–photo-excited process; II–band-band PL process; III–excitonic PL process; IV–non-radiative transition process).

1.4.4 Photocatalysis

Photocatalysis is the science of employing catalysts utilized for speeding up chemical reactions that require or engage light. A photocatalyst is capable of absorbing light, producing electron-hole pairs that enable chemical transformations of the reaction participants and regenerate its chemical composition after each cycle of such interactions. The main attributes of a photocatalytic system are a suitable band gap and morphology, high surface area, stability and reusability. Semiconductors such as TiO_2, ZnO, WO_3, CdS, ZnS, $SrTiO_3$, SnO_2, WSe_2, Fe_2O_3, etc. are commonly used as photocatalysts. When a semiconductor is irradiated with light of energy higher or equal to the band gap energy, an electron from the VB is excited to the CB with simultaneous generation of a h^+ in the VB. The e_{cb}^- and h_{vb}^+ can recombine on the surface or in the bulk of the particle in a few nanoseconds, or can be separated under the built-in electric field to transfer to different positions on the surfaces to react with donor (D) or acceptor (A) species adsorbed on or close to the surfaces. Thereby, subsequent anodic and cathodic redox reactions can be initiated. Figure 1.13 shows the schematic diagram of the photocatalytic reaction on an illuminated semiconductor particle. The photoelectron, which has a strong reducing power, is easily trapped by electronic acceptors like adsorbed O_2, to further produce superoxide radical anion (O_2^{-}). The more negative is the energy level of the CB bottom, the stronger is the reducing power of photo-induced electrons. However, the photo-induced holes have a strong oxidizing power, which make them to be easily trapped by electronic donors, such as organic pollutants. As a result, these organic pollutants oxidize. The more positive the energy level of the VB top, the stronger the oxidizing power of photo-induced holes. The photocatalytic reaction is a kind of special photochemical process. The separation and recombination of the photo-induced charge carriers are in competing processes, and the photocatalytic reaction is effective only when photo-induced electrons and holes are trapped on the surface. Therefore, the dynamic behaviors of photo-induced charge carriers, such as transfer, capture, separation and recombination, can greatly affect photocatalytic activity of semiconductor materials.

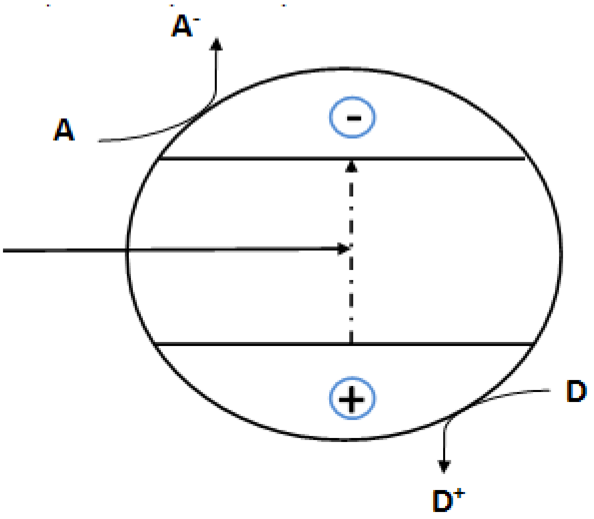

Figure 1.13 Schematic diagram of photocatalytic reaction on an illuminated semiconductor particle.

1.5 State-of-the art on electrodeposited magnetic Ni–containing porous films and multi-segmented nanowires

1.5.1 Electrodeposited Ni-containing porous films

As aforementioned, evolution of hydrogen gas accompanying electrodeposition can be used to produce porous deposits. A pioneering work exploiting this concept was presented by Marozzi and Chialvo, dating back to 2000-2001[32,33]. These authors prepared porous Ni films by electrodeposition, and demonstrated that the morphology of the Ni films was greatly determined by hydrogen co-evolution. Several research groups then sought to extend the concept to other materials. In 2003, Liu and Shin[143] synthesized 3D nanoramified Cu and Sn porous films using hydrogen bubbles as a source of porosity. A similar work on porous Cu films from the same group[144] proved that surfactants and additives critically affect hydrogen bubble behavior. Acetic acid was utilized as a bubble stabilizer, and chloride ions, current density, and acidity were shown to modify the morphology to some extent. Detailed overviews on the formation of porous Cu were published by Nikolic and co-workers[145,146]. Co-deposition of Cu and Ni over a wide range of Cu/Ni ratios was performed by Mattarozzi and Cattarin[147,148]. However, both magnetic and wettability properties of the resulting deposits were overlooked.

Porous Ni was also electrodeposited into the voids of a microporous polymer matrix template[149]. Subsequent heat treatment eliminated the polymer, leaving the microporous Ni film behind. The preparation of nanoporous magnetic films using LLC phases as template has been much less explored. Brij 56 and Pluronic P123 surfactants were used by Treiner and Chevalet[150] to produce nanoporous Ni by electrodeposition.

An interesting variation of this idea was proposed by Xia et al.,[151,152] who coated a porous Ni film with a porous silica network by magnetron sputtering. Other systems involving porous Ni as a matrix to host secondary materials include Ni/Co(OH)$_2$ and Ni/Fe$_3$O$_4$. Pérez-Herranz et al.[153] deposited Ni on top of porous Cu films. In these three cases, the porous framework (porous Cu and Ni) provided sufficient mechanical strength to support the coating layer. Yet, the conformal deposition of a thin layer on top of this type of porous structures has not been reported.

1.5.2 Electrodeposited magnetic multi-segmented nanowires

Since the discovery of giant magnetoresistance (GMR) in Fe/Cr multilayer films[154,155], many efforts have been directed toward the synthesis of magnetic/non-magnetic multilayers. Advances in the field of magnetic multilayer films electrodeposition have to be mostly attributed to Yahalom and Zadok[156]. Soon after the electrodeposition of nanowires made of magnetic metals and alloys became a reality, electroplaters sought to fabricate nanowires featuring multiple segments. In 1994, Blondel et al.[157] electrodeposited Co/Cu multi-segmented nanowires into track-etched membranes, thus favoring the GMR technology welcome to 1D nanostructures. Almost simultaneously, Liu et al.[158] reported on the GMR properties of Co/Cu multi-segmented nanowires. In both Blondel and Liu’s works, control over the segments lengths was accomplished by tuning the electrodeposition time. Another work related to Co/Cu multi-segmented nanowires was published by Tang and co-workers[159], in which the deposited charge rather than the deposition time was used to tune segments length. Since then, many other bi-segmented nanowires have been synthesized by pulse electrodeposition method, referred to as potential modulated multilayer deposition (PMMD)[160]. Systems in the $A_{1-x}B_x$/B form, for which B is more noble than A, can be electrodeposited from the same electrolyte, as the B ions are discharged more easily[160]. This occurs when the difference in equilibrium potentials of A and B is sufficiently large (typically > 0.4 V) and the concentration of the more noble metal ions is significant lower. Multi-segments with a bilayer repeat unit of the form A_xB_{1-x}/A_yB_{1-y} can also be synthesized from a single electrolyte[161]. Systems include Ni/Cu[162], CoNi/Cu[163], NiFe/Cu[164], Ag/Co[165], Fe/FeAu[166], Co/$CoPt_3$[167] and others. Later on, trisegmented nanowires Ni/NiO/Co[168] were fabricated to study the magnetic tunnel junctions. A quick anodization of Ni segment was carried out in alkaline solution to obtain the oxide layer and tunneling magnetoresistance was observed. In 2007, Co/Cu/Co[169] nanowires were electrodeposited in an alumina nanoporous template to study the spin momentum transfer effects. The same year, a group from University of

California San Diego showed the fabrication of soft/hard composite nanowire arrays of Ni/CoPt[170] using AAO template-assisted electrodeposition. In this case, Ni and CoPt segments were strongly magnetically coupled.

In spite of the literature related to electrodeposition of magnetic multi-segmented nanowires, studies on the synergy and interfacial interaction effects between the different segments are still limited, so there is much room to explore. Also, once released from the template or detached from the substrate, agglomeration and robustness of these multi-segmented nanowires need to be seriously taken into consideration for practical uses. A study on the quality of Co/Au[171] was published in 2014, in which Au/Co/Au nanowires were electrodeposited in AAO template using two different electrolytes (dual-bath electrodeposition). The texture and crystalline structure of Co segments was shown to greatly determine the quality of the junctions.

1.6 Objectives

Electrochemical processing methods and Ni-containing materials are at the core of this Thesis. On the one hand, Ni-containing materials with novel geometries and configurations (e.g. spongy films and segmented nanowires) are prepared and characterized, with special emphasis on their magnetic properties. On the other hand, this Thesis also seeks to demonstrate that electrodeposition can be smartly combined with other techniques to produce exotic nanocomposites which are not straightforward through other processing techniques.

The goals of this Thesis can be summarized as follows:

(I) *Growth of Cu-Ni magnetic metallic foams by hydrogen bubble-assisted electrodeposition in an acidic electrolyte.* The main purpose is to establish the correlations among chemical composition, morphology, and crystallographic structure of the prepared spongy Cu-Ni films with their magnetic behavior, wettability and catalytic activity toward hydrogen evolution reaction in alkaline media.

(II) *Electrodeposition of multi-segmented magnetic nanowires consisting of two ferromagnetic segments (CoPt and Ni) with dissimilar coercivity separated by a nonmagnetic spacer (Cu)*. The main purpose is to modify on-demand the relative length of the soft (Ni) and hard magnetic (CoPt) segments in order to assess their impact on the room-temperature magnetic properties. The influence of the crystallographic texture of each segment on the quality of the junctions is also investigated. Another goal is to evaluate from a theoretical point of view the degree of magnetic dipolar interactions between neighboring nanowires and to establish the most suitable conditions to minimize their agglomeration in bodily fluids and their eventual use for multibit magnetic recording.

(III) *Coating of electrodeposited magnetic porous Ni-containing films with transition metal oxides*. The main objective is to coat electroplated 3D porous magnetic Ni-containing films achieved in (I) with transition metal oxides using either gas or liquid precursors. The possibility to cover porous pure Ni and CuNi films with ZnO, Al_2O_3

and cobalt ferrite by either simple (sol-gel) or more sophisticated (atomic layer deposition) methods is investigated. The second goal is to explore the physical (e.g. magnetic) and physicochemical (e.g. photocatalytic activity, wettability) properties of the resulting nanocomposites, achieved through the synergetic combination of the properties of the Ni-based scaffold and the coated layer.

(IV) *Preparation of nanoporous pure Ni films with graded porosity through self-organized template-assisted electrodeposition and characterization of their nanomechanical properties*. The main goal is to investigate the thickness dependent nanomechanical performance of nanoporous Ni films prepared from a block-copolymer containing electrolyte.

References

[1] G. Cao, D. Liu, *Adv. Colloid Interface Sci*. **2008**, *136*, 45.

[2] A. Huczko, *Appl. Phys. A* **2000**, *70*, 365.

[3] K. S. Shankar, A. K. Raychaudhuri, *Mater. Sci. Eng. C* **2005**, *25*, 738.

[4] V. Rajendran, Engineering Physics. New Delhi: Tata McGraw-Hill, **2009**.

[5] D. Bera, S. C. Kuiry, S. Seal, *JOM* **2004**, *56*, 49.

[6] B. J. Plowman, L. A. Jones, S. K. Bhargave, *Chem. Commun*. **2015**, *51*, 4331.

[7] N. D. Nikolic, G. Brankovic, *Mater. Lett.* **2012**, *70*, 11.

[8] N. D. Nikolic, G. Brankovic, V. M. Maksimocic, *J. Electroanal. Chem*. **2011**, *661*, 309.

[9] N. D. Nikolic, K. I. Popov, L. J. Pavlovic, M. G. Pavlovic, *J. Solid State Electrochem*. **2007**, *11,* 667.

[10] N. D. Nikolic, K. I. Popov, L. J. Pavlovic, M. G. Pavlovic, *Surf. Coat. Technol*. **2006**, *201*, 560.

[11] H. Zhang, Y. Ye, R. Shen, C. Ru, Y. Hu, *J. Electrochem. Soc*. **2013**, *160*, D441.

[12] H. C. Shin, M. Liu, *Chem. Mater*. **2004**, *16*, 5460.

[13] F. Yang, K. Cheng, X. Xue, J. Yin, G. Wang, D. Cao, *Electrochim. Acta* **2013**, *107*, 194.

[14] K. I. Popov, M. G. Pavlovic, M. D. Maksimovic, S. S. Krstajic, *J. Appl. Electrochem*. **1978**, *8*, 503.

[15] K. I. Popov, M. D. Maksimovic, D. T. Lukic, M. G. Pavlovic, *J. Appl. Electrochem*. **1980**, *10*, 299.

[16] M. Yang, *J. Mater. Chem*. **2011**, *21*, 3119.

[17] S. Cherevko, N. Kulyk, C. H. Chung, *Nanoscale* **2012**, *4*, 103.

[18] J. Liu, L. Cao, W. Huang, A. Li, *J. Electroanal. Chem*. **2012***, 686*, 38.

[19] J. H. Jeun, D. H. Kim, S. H. Hong, *Sens. Actuators B* **2012**, *161*, 784.

[20] V. D. Jovic, V. Maskimovic, M. G. Pavlovic, K. I. Popov, *J. Solid State Electrochem*. **2005**, *10*, 373.

[21] D. K. Oppedisano, L. A. Jones, T. Junk, S. K. Bhargava*, J. Electrochem. Soc*. **2014**, *161*, D489.

[22] K. Zhuo, M. G. Jeong, C. H. Chung, *J. Power Sources* **2013**, *244*, 601.

[23] L. D. Rafailovic, D. M. Minic, H. P. Karnthaler, J. Wosik, T. Trisovic, G. E. Nauer, *j. Electrochem. Soc*. **2010**, *157*, D295.

[24] L. Mattarozzi, S. Cattarin, N. Comisso, R. Gerbasi, P. Guerriero, M. Musiani, L. V. Gómez, E. Verlato, *ECS Electrochem. Lett*. **2013**, *2*, D58.

[25] M. Jin, H. Ma, *Russ. J. Electrochem*. **2013**, *49*, 1081.

[26] R. Li, H. Mao, J. Zhang, T. Huang, A. Yu*, J. Power Sources* **2013**, *241*, 660.

[27] X. Niu, H. Zhao, C. Chen, M. Lan, *ChemCatChem*, **2013**, *5*, 1416.

[28] J. Liu, L. Cao, W. Huang, Z. Li, *ACS Appl. Mater. Interfaces* **2011**, *3*, 3552.

[29] S. Cherevko, N. Kulyk, C. H. Chung, *Nanoscale* **2012,** *4*, 568.

[30] I. Najdovski, P. R. Selvakannan, A. P. O´Mullane, *RSC Adv*. **2014**, *4*, 7207.

[31] I. Najdovski, P. R. Selvakannan, S. K. Bhargava, A. P. O´Mullane, *Nanoscale* **2012**, *4*, 6298.

[32] C. A. Marozzi, A. C. Chialvo, *Electrochim. Acta* **2001**, *46*, 861.

[33] C. A. Marozzi, A. C. Chialvo, *Electrochim. Acta* **2000**, *45*, 2111.

[34] G. A. Lange, S. Eugénio,R. G. Duarte, T. M. Silva, M. J. Carmezim, M. F. Montemor, *J. Electroanal. Chem*. **2015**, *737*, 85.

[35] I. H. Cardona, E. Ortega, L. V. Gómez, V. P. Herranz, *Int. J. Hydrogen Energy* **2012**, *37*, 2147.

[36] N. D. Nikolic, G. Brankovic, *Mater. Lett.* **2012**, *70*, 11.

[37] F. Hu, K. C. Chan, T. M. Yue, C. Surya, *J. Phys. Chem. C* **2000**, *114*, 5811.

[38] P. N. Bartlett, *Electrochem. Soc. Interface* **2004**, *13*, 28.

[39] D. J. Mitchell, G. J. T. Tiddy, L. Waring, T. Bostock, M. P. Mcdonald, *J. Chem. Soc.*, *Faraday Tran. 1* **1983**, *79,* 975.

[40] P. N. Bartlett, B. Gollas, S. Guerin, J. Marwan, *Phys.Chem. Chem. Phys*. **2002**, *4*, 3835.

[41] H. Luo, L. Sun, Y. Lu, Y. Yan*, Langmuir* **2004**, *20*, 10218.

[42] G. S. Attard, P. N. Bartlett, N. R. B. Coleman, J. M. Elliott, J. R. Owen, J. H. Wang, *Science* **1997**, *278*, 838.

[43] B. Dong, T. Xue, C. Xu, H. Li, *Microporous Mesoporous Mater*. **2008**, *112*, 627.

[44] Y. Yamauchi, M. Komatsu, M. Fuziwara, Y. Nemoto, K. Sato, T. Yokoshima, H. Sukegawa, K. Inomata, K. Kuroda, *Angew. Chem. Int. Ed*. **2009**, *48*, 7792.

[45] Y. Liang, Y. Juan, K. Lu, U. Jeng, S. Chen, W. Chuang, C. Su, C. Liu, C. Pao, J. lee, H. Sheu, J. Chen, *J. Phys. Chem. C* **2012**, *116*, 21149.

[46] M. Bardosova, R. H. Tredgold, *J. Mater. Chem*. **2002**, *12*, 2835.

[47] P. N. Bartlett, P. R. Birkin, M. A. Ghanem, *Chem. Common*. **2000**, *17*, 1671.

[48] J. E. G. J. Wijnhoven, S. J. M. Zevenhuizen, M. A. Hendriks, D. Vanmaekelbergh, J. J. Kelly, W. L. Vos, *Adv. Mater*. **2000**, *12,* 888.

[49] F. Ke, L. Huang, J. Cai, S. Sun, *Electrochim. Acta* **2007**, *52*, 6741.

[50] X. Luo, A. J. Killard, A. Morrin, M. R. Smyth, *Chem. Common*. **2007**, 3207.

[51] P. N. Bartlett, T. Dunford, M. A. Ghanem, *J. Mater. Chem*. **2002**, *12*, 3130.

[52] Y. Lee, T. Kuo, C. Hsu, Y. Su, C. Chen, *Langmuir*, **2002**, *18*, 9942.

[53] J. C. Hulteen, C. R. Martin, *J. Mater. Chem*. **1997**, *7*, 1075.

[54] M. Platt, R. A. W. Dryfe, E. P. L. Robert, *Electrochim. Acta* **2003**, *48*, 3037.

[55] G. A. Tsirlina, O. A. Petrii, T. Y. Safonova, I. M. Papisov, S. Y. Vassiliev, A. E. Gabrielov, *Electrochim. Acta* **2002**, *47*, 3758.

[56] G. Fasol, K. Runge, *Appl. Phys. Lett*. **1997**, *70*, 2467.

[57] B. M. Quinn, C. Dekker, S. G. Lemay, *J. Am. Chem. Soc*. **2005**, *127*, 6146.

[58] T. M. Whitney, J. S. Jiang, P. C. Searson, C. L. Chien, *Science* **1993**, *261*, 1316.

[59] D. Wang, W. L. Zhou, B. F. McCaughy, J. E. Hampsey, X. Ji, Y. Jiang, H. Xu, J. Tang, R. H. Schmehl, C. O´Connor, C. J. Brinker, Y. Lu, *Adv. Mater*. **2003**, *15*, 130.

[60] J. Carrey, K. Bouzehouane, J. M. George, C. Ceneray, T. Blon, M. Bibes, A. Vaurès, S. Fusil, S. Kenane, L. Vila, L. Piraux, *Appl. Phys. Lett*. **2002**, *81*, 760.

[61] P. M. Ajayan, L. S. Schadler, P. V. Braun, Nanocomposite Science and Technology. Wiley-Vch Verlag GmhH Co. KGaA: Weinheim, **2003.**

[62] A. M. Lindo, E. Pellicer, M. A. Zeeshan, R. Grisch, F. Qiu, J. Sort, M. S. Sakar, B. J. Nelson, S. Pané, *Phys. Chem. Chem. Phys*. **2015**, *17*, 13274.

[63] S. M. George, *Chem. Rev*. **2010**, *110*, 111.

[64] H. Kim, J. Vac. Sci. *Technol. B: Microelectron. Nanometer Struct*. **2003**, *21*, 2231.

[65] M. Leskelä, M. Ritala, *Thin Solid Film* **2002**, *409,* 138.

[66] T. J. Knisley, L. C. Kalutarage, C. H. Winter, Coord. *Chem. Rev*. **2013**, *257*, 3222.

[67] J. R. Bakke, K. L. Pickrahn, T. P. Brennan, S. F. Bent, *Nanoscale* **2011**, *3*, 3482.

[68] V. Miikkulainen, M. Leskelä, M. Ritala, R. L. Puurunen, *J. Appl. Phys*. **2013**, *113*, 021301.

[69] R. L. Puurunen, *J. Appl. Phys*. **2005**, *97*, 121301.

[70] M. Schuisky, J. Aarik, K. Kukli, A. Aidla, A. Harsta, *Langmuir* **2001**, *17*, 5508.

[71] S. Y. Lee, H. K. Kim, J. H. Lee, I. Yu, J. Lee, C. S. Hwang, *J. Mater. Chem. C* **2014**, *2*, 2558.

[72] S. C. Ha, E. Choi, S. H. Kim, J. S. Roh, *Thin Solid Films* **2005**, *476*, 252.

[73] M. Choi, H. Park, D. S. Jeong, J. H. Kim, J. Kim, S. K. Kim, *Appl. Surf. Sci*. **2014**, *301*, 451.

[74] W. Zafiropoulo, Oxygen Radical Enhanced Atomic-layer Deposition Using Ozone Plasma. US 20150279665A1 Oct. 1, **2015**.

[75] D. M. King, J. A. Spencer II, X. Liang, L. F. Hakim, A. W. Weimer, *Surf. Coat. Technol*. **2007**, *201*, 9163.

[76] M. G. Willinger, G. Neri, A. Bonavita, G. Micali, E. Rauwel, T. Herntrich, N. Pinna, *Phys. Chem. Chem. Phys*. **2009**, *11*, 3651.

[77] J. Song, S. Lim, *J. Phys. Chem. C* **2007**, *111*, 596.

[78] J. W. Elam, G. Xiong, C. Y. Han, H. H. Wang, J. P. Birrell, U. Welp, J. N. Hryn, M. J. Pellin, T. F. Baumann, J. F. Poco, J. H. Satcher Jr, *J. Nanomater*. **2006**, *2006*, 1.

[79] G. Triani, P. J. Evans, D. J. Attard, K. E. Prince, J. Bartlett, S. Tan, R. P. Burford. *J. Mater. Chem*. **2006**, *11*, 1355.

[80] P. J. Kelly, R. D. Arnell, *Vacuum* **2000**, *56*, 159.

[81] W. Li, K. Lu, J. Y. Walz, *Langmuir* **2012**, *28*, 16423.

[82] S. M. Attia, J. Wang, G. Wu, J. Shen, J. Ma, *J. Mater. Sci, Technol*. **2002**, *18*, 211.

[83] K. Thongsuriwong, P. Amornpitoksuk, S. Suwanboon, Adv. *Powder Technol.* **2013**, *24*, 275.

[84] E. Redel, S. Petrov, Ö. Dag, J. Moir, C. Huai, P. Mirtchev, G. A. Ozin, *Small* **2012**, *8*, 68.

[85] S. A. Mahadik, D. B. Mahadik, M. S. Kavale, V. G. Parale, P. B. Wagh, H. C. Barshilia, S. C. Gupta, N. D. Hegde, A. V. Rao, *J Sol-Gel Sci. Technol*. **2012**, *63*, 580.

[86] V. G. Velderrain, Y. O. López, J. S. Guitiérrez, A. L. Ortiz, V. H. C. Martinez, *Green Sustainable Chem*. **2014**, *4*, 120.

[87] N. Tasaltin, S. Öztürk, N. Kilinç, H. Yüzer, Z. Z. Öztürk, *Nanoscale Res. Lett*. **2010**, *5*, 1137.

[88] S. Valizadeh, L. Hultman, J. M. George, P. Leisner, *Adv. Funct. Mater*. **2002**, *12*, 766.

[89] S. Ghost, J. E. Hujdic, A. V. Bedolla, E. J. Menke, *J. Phys. Chem. C* **2011**, *115*, 17670.

[90] W. Yuan, P. Yuan, D. Liu, W. Yu, L. Deng, F. Chen, *Microporous Mesoporous Mater*. **2015**, *206*, 184.

[91] J. B. Hunter, Silver-Palladium Film for Separation and Purification of Hydrogen, US 2773561 A May 2, **1955**.

[92] R. D. Roca, D. Esqué-de los Ojos, M. Guerrero, E. Pellicer, M. D. Baró, S. Suriñach, J. Sort, *Mater. Sci. Eng. A* **2015**, *626*, 150.

[93] P. A. Nelson, J. M. Elliott, G. S. Attard, J. R. Owen, *Chem. Mater*. **2002**, *14*, 524.

[94] B. D. Cullity, C. D. Graham, Introduction to Magnetic Materials, 2nd Edition, Wiley-IEEE Press: Hoboken, **2008**.

[95] N. Kurti, Selected Works of Louis Néel, Gordon and Break Science Publishers: New York, **1988**.

[96] C. P. Bean, J. D. Livingston, *J. Appl. Phys*. **1959**, *30*, S120.

[97] W. F. Jr. Brown, Micromagnetics, Wiley-Interscience: New York, **1963**.

[98] E. P. Wohlfarth, in Magnetism, R. T. Rado, H. Suhl, Eds, Academic Press, New York, **1963**, III, 351.

[99] I. S. Jacobs, C. P. bean, Fine Particles, Thin Films and Exchange Anisotropy (Effects of Finite Dimensions and Interfaces on the Basic Properties of Ferromagnets). In: Magnetism, R. T. Rado, H. Suhl, Eds, Academic Press, New York, **1963**, III, 271.

[100] J. Frenkel, J. Dorfman, *Nature* **1930**, *126*, 274.

[101] R. D. Rieke, *Chem. Mater*. **1996**, *8*, 1770.

[102] M. W. Freeman, A. Arrott, J. H. L. Watson, *J. Appl. Phys.* **1960**, *31*, S404.

[103] H. Kobayashi, S. Kawamoto, T. Saga, N. Sato, A. Hiraga, T. Ishimori, J. Konishi, K. Togashi, M. W. Brechbiel, *Magn. Reson. Med*. **2001**, *46*, 781.

[104] D. Kirn, R. L. Martuza, J. Zwiebel, *Nat. Med*. **2001**, *7*, 781.

[105] E. Kim, J. Kim, H. Shin, H. Lee, J. M. Yang, J. Kim, J. Sohn, H. Kim, C. Yun, *Hum. Gene. Ther*. **2003**, *14*, 1415.

[106] W. Shenton, T. Douglas, M. Young, G. Stubbs, S. Mann, *Adv. Mater*. **1999**, *11*, 253.

[107] N. W. S. Kam, T. C. Jessop, P. A. Wender, H. Dai, *J. Am. Chem. Soc*. **2004**, *126*, 6850.

[108] E. Strable, J. E. Johnson, M. G. Finn, *Nano Lett*. **2004**, *4*, 1385.

[109] M. Arruebo, *Wiley Interdiscip. Rev.: Nanomed. Nanobiotechnol*. **2012**, *4*, 16.

[110] K. M. Pondman, N. D. Bunt, A. W. Maijenburg, R. J. A. van Wezel, U. Kishore, L. Abelmann, J. E. ten Elshof, B. ten Haken, *J. Magn. Magn. Mater*. **2015**, *380*, 299.

[111] M. Arruebo, R. F. Pacheco, M. R. Ibarra, J. Santamatía, *Nano Today* **2007**, *2*, 22.

[112] S. Iwasaki, *J. Magn. Magn. Mater*. **2005**, *287*, 9.

[113] H. N. Bertram, H. Zhou, R. Gustafson, *IEEE Trans. Magn.* **1998**, *34*, 1845.

[114] C. A. Ross, Annu. *Rev. Mater. Res*. **2001**, *31*, 203.

[115] X. Zhao, M. J. Blunt, J. Yao, *Pet. Sci. Technol. Eng*. **2010**, *71*, 169.

[116] K. N. Prabhu, P. Fernandes, G. Kumar, *Mater. Des*. **2009**, *30*, 297.

[117] Y. Q. Wang, H. F. Yang, Q. G. Han, L. Fang, S. R. Ge, *Adv. Mater. Res*. **2010**, *154-155*, 1019.

[118] Y. Son, C. Kim, D. H. Yang, D. J. Ahn, *Langmuir* **2008**, *24*, 2900.

[119] M. Sakai, T. Yanagisawa, A. Nakajima, Y. Kameshima, K. Okada, *Langmuir* **2009**, *25*, 13.

[120] H. Yang, P. Jiang, *Langmuir* **2010**, *26,* 12598.

[121] B. Bhushan, Y. C. Junk, K. Koch, *Langmuir* **2009**, *25*, 3240.

[122] M. Raucher, S. Dietrich, *Annu. Rev. Mater. Sci*. **2008**, *38*, 143.

[123] K. Fei, C. P. Chiu, C. W. Hong, *Microfluid. Nanofluid*. **2008**, *4*, 321.

[124] Z. K. Motamed, L. Kadem, A. Dolatabadi, *Microfluid. Nanofluid*. **2010**, *8*, 47.

[125] A. Lafuma, D. Queue, *Nat. Mater*. **2003**, *2*, 457.

[126] Y. Yuan, T. R. Lee, Surface Science Techniques, G. Bracco, B. Holst, Eds, Springer Berlin Heidelberg: Berlin **2013**.

[127] P. G. de Gennes, *Rev. Mod. Phys*. **1985**, *57*, 827.

[128] R. N. Wenzel, *Ind. Eng. Chem*. **1936**, *28*, 988.

[129] A. B. D. Cassie, S. Baxter, *Trans. Faraday. Soc*. **1944**, *40*, 546.

[130] A. Tuteja, W. Choi, M. Ma, J. M. Mabry, S. A. Mazzella, G. C. Rutledge, G. H. Mckinley, R. E. *Cohen, Science* **2007**, *318*, 1618.

[131] O. Savadoga, *Hem. Ind*. **2000**, *54*, 95.

[132] F. Safizadeh, E. Ghali, G. Houlachi, *Int. J. Hydrogen Eng*. **2015**, *40*, 256.

[133] G. Lu, P. Evans,G. Zangari, *J. Electrochem. Soc*. **2003**, *150*, A551.

[134] C. G. M. Guio, L. A. Stern, X. Hu, *Chem. Soc. Rev*. **2014**, *43*, 6555.

[135] H. Dong, T. Lei, Y. He, N. Xu, B. Huang, C. T. Liu, *Int. J. Hydrogen Eng*. **2011**, *36*, 12112.

[136] Q. Lu, G. S. Hutchings, W. Yu, Y. Zhou, R. V. Forest, R. Tao, J. Rosen, B. T. Yonemoto, Z. Cao, H. Zheng, J. Q. Xiao, F. Jiao, J. G. Chen, *Nature Common*. **2014**, *6*, 6567.

[137] I. Herraiz-Cardona, C. González-Buch, E. Ortega, V. Pérez-Herranz, J. García-Antón, *Int. J. Chem. Mol. Nuc. Mater. Metal. Eng.* **2012**, *6*, 823.

[138] C. G. Buch, I. H. Cardona, E. M. Ortega, J. G. Antón, V. P. Herranz, *Chem. Eng. Trans.* **2013**, *32*, 865.

[139] A. L. Linsebigler, G. Lu, J. T. Yates, *Chem. Rev*. **1995**, *95*, 735.

[140] M. R. Hoffmann, S. T. Martin, W. Choi, D. W. Bahnemann, *Chem. Rev*. **1995**, *95*, 69.

[141] M. I. Litter, *Appl. Catal. B* **1999**, *23*, 89.

[142] L. Jing, Y. Qu, B. Wang, S. Li, B. Jiang, L. Yang, W. Fu, H. Fu, J. Sun, *Sol. Energy Mater. Sol. Cells* **2006**, *90*, 1773.

[143] H. C. Shin, J. Dong, M. Liu, *Adv. Mater*. **2003**, *15*, 1610.

[144] H. C. Shin, M. Liu, *Chem. Mater*. **2004**, *16*, 5460.

[145] N. Nikolic, Modern Aspects of Electrochemistry, S. S. Djokic, Ed, Springer, US, **2012**, 187-249.

[146] N. Nikolic, K. I. Popov, Modern Aspects of Electrochemistry, S. S. Djokic, Ed, Springer, New York, **2010**, 1-70.

[147] L. Mattarozzi, S. Cattarin, N. Comisso, R. Gerbasi, P. Guerriero, M. Musiani, L. V. Gomez, E. Verlato, *ECS Electrochem. Lett*. **2013**, *2*, D58.

[148] L. Mattarozzi, S. Cattarin, N. Comisso, A. Gambirasi, P. Guerriero, M. Musiani, L. V. Gomez, E. Verlato, *Electrochem. Acta* **2014**, *140*, 337.

[149] I. J. Brown, S. Sotiropoulos, *J. Appl. Electrochem*. **2000**, *30,* 107.

[150] R. Campbell, M. G. Bakker, C. Treiner, J. Chevalet, *J. Porous Mater*. **2004**, *11,* 63.

[151] Y. Q. Zhang, X. H. Xia, X. L. Wang, Y. J. Ma, S. J. Shi, Y. Y. Tang, C. G. Gu, J. P. Tu, *J. Power Sources* **2012**, *213*, 106.

[152] X. H. Xia, J. P. Tu, Y. Q. Zhang, Y. J. Ma, X. L. Wang, C. D. Gu, X. B. Zhao, *J. Phys. Chem. C* **2011**, *115*, 22662.

[153] I. H. Cardona, E. Ortega, L. V. Gomez, V. P. Herranz, *Int. J. Hydrogen Energy* **2012**, *37*, 2147.

[154] M. N. Baibich, J. M. Broto, A. Fert, F. N. van Dau, F. Petroff, *Phys. Rev. Lett*. **1988**, *61*, 2472.

[155] G. Binasch, P. Grüberg, F. Saurenbach, W. Zinn, *Phys. Rev. B* **1989**, *39*, 4828.

[156] J. Yahalom, O. Zadok, *J. Mater. Sci*. **1987**, *22*, 499.

[157] L. Pirauz, J. M. George, J. F. Despres, C. Leroy, E. Ferain, R. Legras, K. Ounadjela, A. Fert, *Appl. Phys. Lett*. **1994**, *65*, 2484.

[158] A. Blondel, J. P. Meier, B. Doudin, J. P. Ansermet, *Appl. Phys. Lett*. **1994**, *65*, 3019.

[159] X. T. Tang, G. C. Wang, M. Shima, *J. Appl. Phys*. **2006**, *99*, 033906.

[160] M. Chen, C. L. Chien, P. C. Searson, *Chem. Mater*. **2006**, *18*, 1595.

[161] J. Yahalom, O. Zadok, *J. Mater. Sci*. **1987**, *22*, 499.

[162] P. Cojocaru, A. Leserri, L. Magagnin, M. Vázquez, G. Carac, *ESC Trans*. **2011**, *33*, 43.

[163] X. Tang, G. Wang, M. Shima, *J. Magn. Magn. Mater*. **2007**, *309*, 188.

[164] S. Esmaili, M. E. Bahrololoom, K. L. Kavanagh, *Mater. Charact*. **2011**, *62*, 204.

[165] C. H. Peng, T. Y. Wu, C. C. Hwang, *Sci. World J.* **2013**, *2013*.

[166] S. Lucatero, W. H. Fowle, E. J. Podlaha, *Electrochem. Solid-State Lett*. **2009**, *12*, D96.

[167] Y. Su, J. Tang, H. Yang, Z. Cheng, *Nanoscale*, **2013**, *5*, 9709.

[168] A. Sokolov, I. F. Sabirianov, E. Y. Tsymbal, B. Doudin, X. Z. Li, J. Redepenning, *J. Appl. Phys*. **2003**, *93*, 7029.

[169] T. Blon, M. M. Tempfli, S. M. Tempfli, L. Piraux, S. Fusil, R. Guillemet, K. Bouzehouane, C. Deranlot, V. Cros, *J. Appl. Phys*. **2007**, *102*, 103906.

[170] A. I. Gaplin, X. R. Ye, L. H. Chen, D. Hong, S. Jin, *IEEE Trans. Magn*. **2007**, *43*, 2151.

[171] B. Jang, E. Pellicer, M. Guerrero, X. Chen, H. Choi, B. J. Nelson, J. Sort, S. Pané, *ACS Appl. Mater. Interfaces* **2014**, *6*, 14583.

Departament de Física

2. Experimental techniques

Chapter 2 Experimental techniques

In this chapter we describe the fundamentals of the main techniques used to study the morphology, structure, physical (magnetic, mechanical) and (electro)chemical (wettability, electrocatalytic hydrogen evolution) properties of the as-prepared materials.

2.1 Electrochemical set-up

2.1.1 Apparatus

Electrochemical experiments (mostly involving materials electrodeposition and HER tests) were carried out on a PGSTAT302N Autolab potentiostat/galvanostat (Ecochemie) controlled with GPES software, which is shown in Figure 2.1.

Figure 2.1: PGSTAT302N Autolab potentiostat/galvanostat. (Taken from *Metrohm Autolab* website)

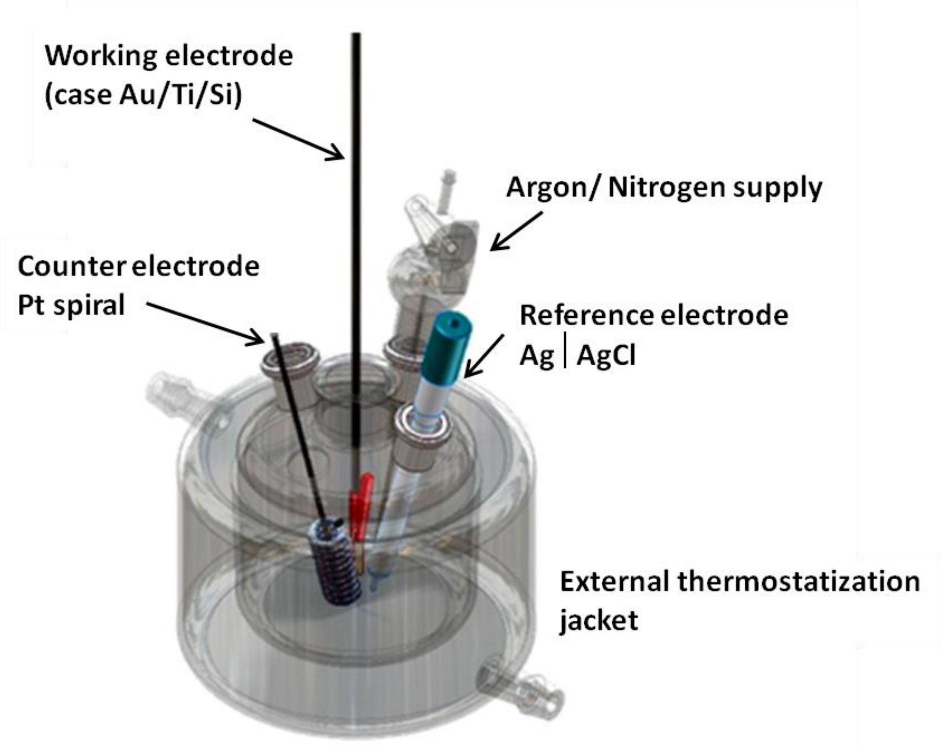

Figure 2.2: Electrochemical cell in three-electrode configuration (courtesy of Dr. S. Pané).

2.1.2 Cell and electrodes

All experiments were performed in a single-compartment, double-jacket glass electrochemical cell (Figure 2.2). To thermo-stabilize the electrochemical cell, JULABO refrigerated and heating circulators were used to heat and cool the electrochemical cell on-demand.

A double junction Ag│AgCl 3M KCl electrode (E = + 0.210 V *versus* standard hydrogen electrode (SHE)) was utilized as the reference electrode. The outer solution was changed according to the electrolyte used. All potentials are referred to this electrode. A platinum wire was utilized as counter electrode, which was positioned vertically facing the working electrode.

Depending on the electrochemical experiment, different working electrodes were selected. Each type of electrode has been treated and/or cleaned following a specific procedure in order to achieve reproducibility of experiments. The working electrodes used are:

Au(125 nm)/Ti(25 nm)/Si substrates (Figure 2.3) of 5 mm x 10 mm. Ti and Au work as adhesion and seed layers, respectively. Before each deposition, the Au seed layer was cleaned with acetone, followed by diluted sulphuric acid and finally rinsed in water. The working area was always 0.25 cm^{-2}, which was controlled by wrapping the unexposed surface with Teflon tape.

Track-etched polycarbonate (PC) membrane (Nuclepore, Whatman) had an average nominal pore size of 30 nm (Figure 2.4a). This kind of membrane is hydrophilic in nature and was used for nanowires deposition. First, a thin conductive layer was sputtered onto one side of the PC to render it conductive. The PC was put in contact with a copper plate through the sputtered conductive thin film and held inside a plastic stationary holder (Figure 2.4b). A circular area of 3.14 cm^2 was exposed to the electrolyte for deposition. Before deposition, the PC membrane was placed in an ultrasonicator for a couple of minutes to remove the air trapped inside the channels.

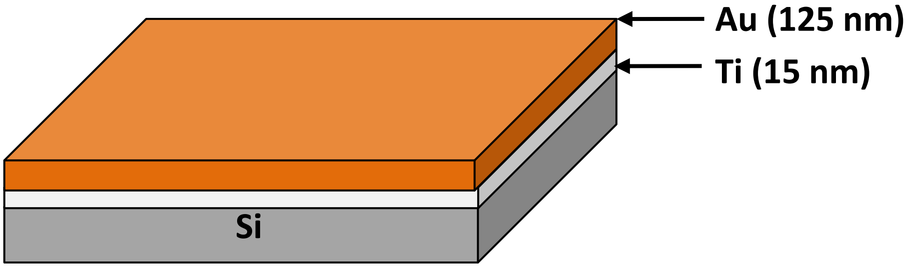

Figure 2.3: Schematic representation of Au (125 nm)/Ti (15 nm)/Si (100) electrode.

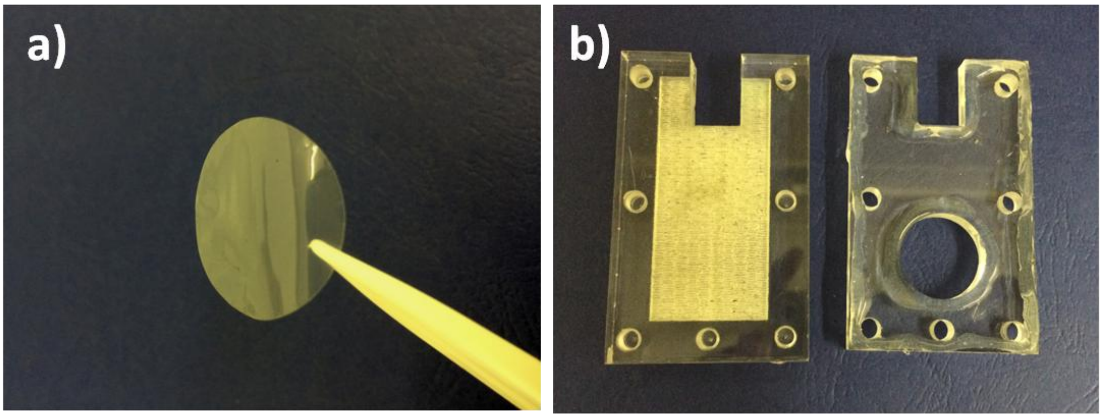

Figure 2.4: a) PC membrane, b) plastic holder for PC membrane

2.1.3 Electrochemical techniques

A. Cyclic voltammetry (CV)

CV is an electrochemical technique which involves measuring the current that develops in an electrochemical cell cyclically under conditions where potential exceeds the value predicted by the Nernst equation. In our case, CV was used to investigate the activity of Cu-Ni magnetic metallic foams towards HER. CVs were performed by cycling the potential between -1.0 V and -2.0 V at 50 mV s^{-1}. 50 cycles of CV were run in order to assess materials' stability.

B. Linear sweep voltammetry (LSV)

LSV is very similar to CV. In LSV, a fixed potential range is employed much like potential step measurements. Typically, in LSV the potential is scanned from a lower limit to an upper limit as shown in Figure 2.5a. The current response is plotted as a function of potential rather than time (Figure 2.5b). Both CV and LSV are really useful in electrochemistry. In some cases LSV is better suited. For example, in irreversible reactions CV will not give any additional data that LSV would show us.

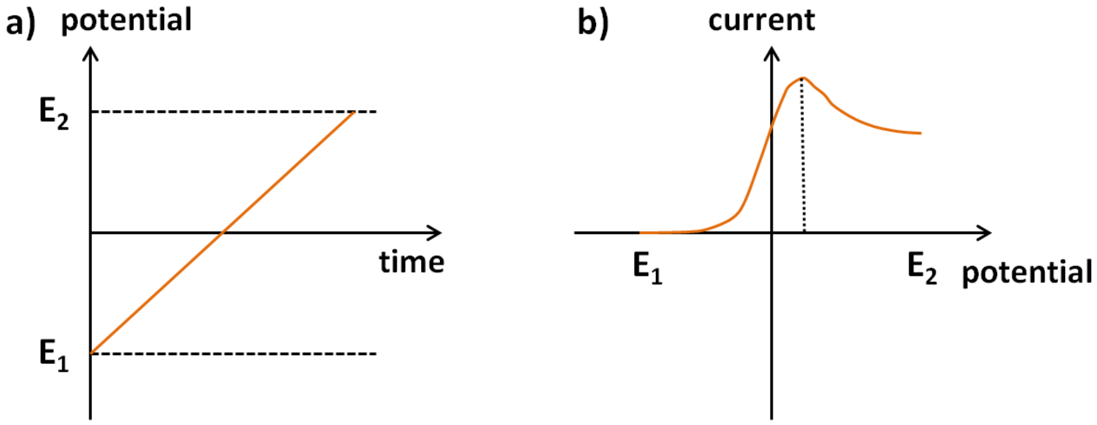

Figure 2.5: a) linear potential sweep, b) typical current-potential curve.

2.2 Structural and morphological analysis techniques

2.2.1 Scanning electron microscopy (SEM)

SEM uses a focused beam of high-energy electrons to generate a variety of signals at the surface of solid specimens. The signals that derive from electron-sample interactions reveal information about the sample including external morphology, chemical composition, and crystalline structure and orientation of materials composing the sample (Figure 2.6)[1]. In most applications, data are collected over a selected area of the surface of the sample, and a 2-dimensional image is generated that displays spatial variations in these properties. SEM is also capable of performing analyses of selected point locations on the sample; this approach is especially useful in qualitatively or semi-quantitatively determining chemical compositions (using energy dispersive X-ray analyses -EDX), crystalline structure, and crystal orientations (using backscattered electrons).

Morphological characterization of the nanostructured materials obtained was done on a HR-SEM Zeiss Merlin microscope equipped with EDX analysis data acquisition system (INCA). The observation of alloy deposits on Au/Ti/Si substrates was performed directly (no special preparation of specimens for observation was required). In the case of PC membrane based electrodeposition, specimens were prepared via drop-casting a droplet of the as-grown nanowires previously suspended in chloroform onto an aluminum foil, and subsequently dried in air.

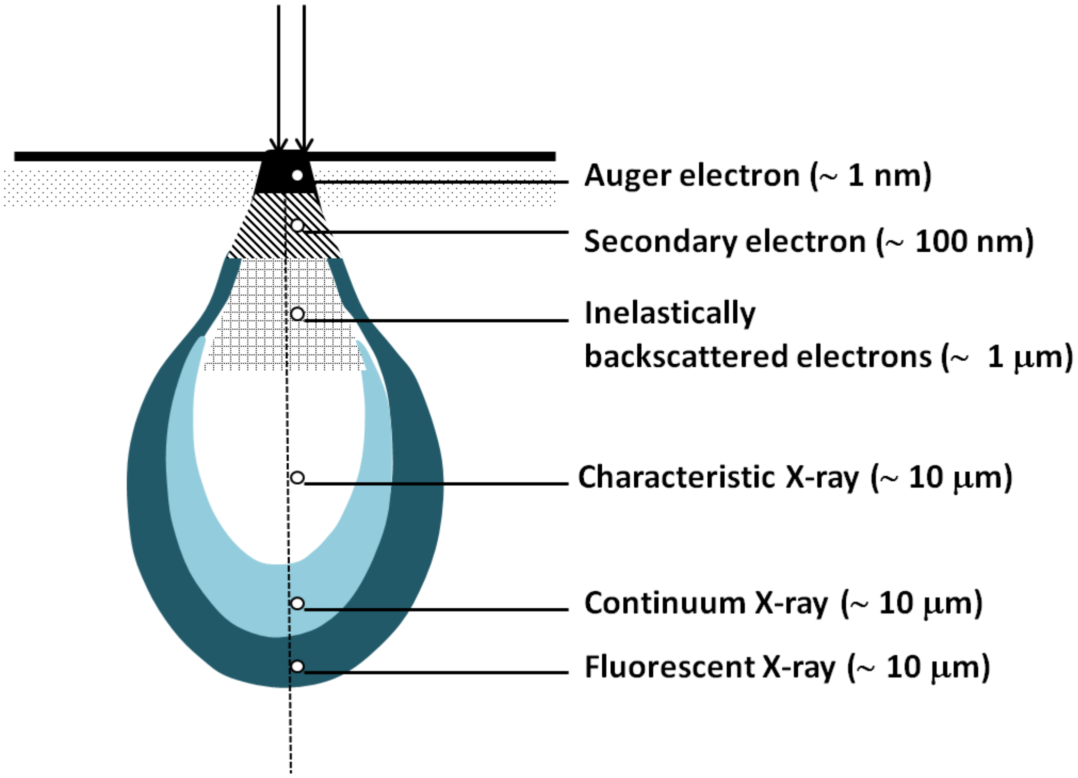

Figure 2.6: Types of electrons and radiation generated inside the sample in a scanning electron microscope.

2.2.2 Transmission electron microscope (TEM)

TEM is a microscopy technique in which a beam of electrons is transmitted through an ultra-thin specimen, interacting with the specimen as it passes through it. The interactions (Figure 2.7) between the electrons and the atoms can be used to observe features such as the crystal structure and features in the structure itself like dislocations and grain boundaries. TEM can also be used to perform chemical analysis, to study the growth of layers, their composition, and defects in semiconductors. High resolution can be used to analyze the quality, shape, size and density of quantum wells, wires, and dots.

Electrons interact strongly with atoms by elastic and inelastic scattering. The specimens must therefore be very thin depending on the density and elemental composition of the specimen and the resolution desired. Like SEM, specimen preparation procedures are usually required like mechanical thinning, ion milling, etc. In our work, the diameter of the nanowires is rather small (100 nm) so that they were straightforwardly observed after dispersing them in chloroform in an ultrasonicator and depositing them onto a TEM grid. The TEM utilized in this study for nanowires characterization was a Jeol-JEM 2011 system with a field emission gun operating at 200 kV, located in the *Serveis Cientificotècnics* of *Universitat de Barcelona*. Electron energy loss spectra (EELS) were acquired in the 650-1150 eV energy loss range. In the case of porous Ni supported Al_2O_3 and Co_2FeO_4, samples was firstly embedded in a polymer and then small pieces were cut using a microtome apparatus. Finally, the thin slices were drop-casted onto a TEM grid. The TEM utilized in this case was a Tecnai F20 HRTEM/STEM microscope, located at *Institut Català de Nanociència i Nanotecnologia*.

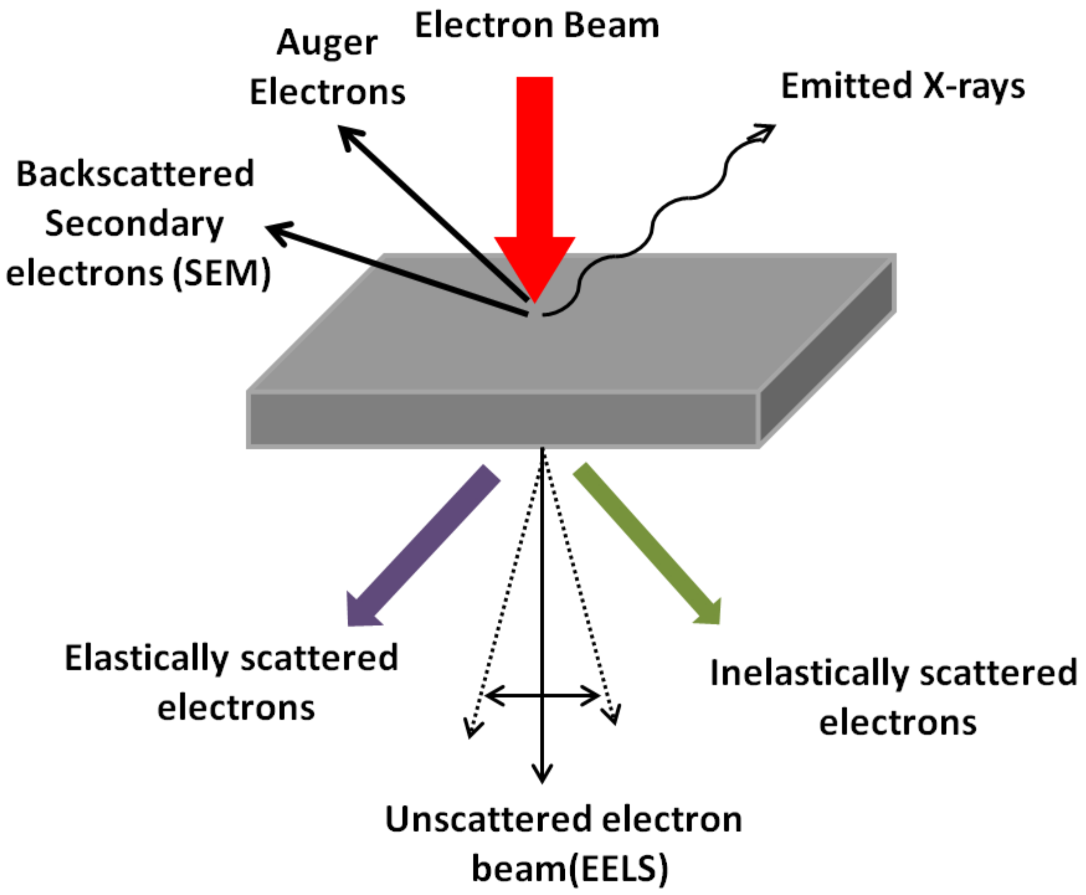

Figure 2.7: Scheme of the generation of the electrons signal in TEM (bottom part).

2.2.3 X-ray diffraction (XRD)

XRD analysis is based on constructive interference of monochromatic X-rays and a crystalline sample. The X-rays are generated by a cathode ray tube, filtered to produce monochromatic radiation, collimated to concentrate, and directed toward the sample. The interaction of the incident X-rays with the sample produces constructive interference (and a diffracted beam) when conditions satisfy the Bragg's Law:

$$n\lambda = 2d \sin\theta \qquad \text{[Eq. 2.1]}$$

This law relates the wavelength of electromagnetic radiation to the diffraction angle and the lattice spacing in a crystalline sample. The characteristic X-ray diffraction pattern generated in a typical XRD analysis provides a unique "fingerprint" of the crystals present in the sample. When properly interpreted, by comparison with standard reference patterns and measurements, this fingerprint allows identification of the crystalline phases.

X-ray diffraction patterns have been recorded on a Philips X´Pert diffractometer in Bragg-brentano geometry using Cu K_α radiation with wavelength proportion of I ($K_{\alpha 1}$)/I ($K_{\alpha 2}$) = 0.5 ($\lambda(K_{\alpha 1}) = 1.5406$ Å, $\lambda(K_{\alpha 2}) = 1.5443$ Å). XRD patterns of Cu-Ni magnetic metallic foams were recorded in the range of 39-56° 2θ range (step size = 0.03°, step time = 2s). 2θ range for CoPt/Cu/Ni and CoPt/Ni nanowires were 30-100° (step size = 0.026°, step time = 2000 s). Finally, the 2θ range for porous Ni supported Al_2O_3 and Co_2FeO_4 was 30-55° 2θ range (step size = 0.026°, step time = 1200 s).

2.3 Vibrating sample magnetometry (VSM)

VSM is a scientific instrument that measures magnetic properties. It was invented in 1955 by Simon Foner at Lincoln laboratory MIT[2]. The principle of this magnetometer is to measure the electromotive force induced by a ferromagnetic sample when it is vibrating at a constant frequency, under the presence of static and uniform magnetic field. A VSM operates by first placing the sample to be studied in a constant magnetic field. If the sample is magnetic, this constant magnetic field will magnetize it by aligning the magnetic domains, or the individual magnetic spins, with the field. The stronger the constant field, the larger the magnetization will be. The magnetic dipole moment of the sample will create a magnetic field around the sample, i. e. magnetic stray field. Since the sample is moving up and down, this magnetic stray field is changing as a function of time and can be sensed by a set of pick-up coils.

The variations of the magnetic flux will cause an electric field in the pick-up coils according to Faraday's law of induction. This current will be proportional to the magnetization of the sample. The greater the magnetization, the higher the induced current. The induction current is amplified by a transimpedance amplifier and lock-in amplifier. Using controlling and monitoring software, the system provides the value of the magnetization of the sample and its dependence on the strength of the magnetic field. A typical measurement of a sample is performed as follows:

- The strength of the constant magnetic field is set
- The sample begins to vibrate
- The signal received from the probe is translated into a value for the magnetic moment of the sample
- The strength of the constant magnetic field changes to a new value
- The strength of the constant magnetic field reaches its new value
- The signal from the probe again gets translated into a value for the magnetization of the sample
- The constant magnetic field varies over a given range, and a plot of magnetization (M) versus magnetic field strength (H) is generated.

Samples of porous Cu-Ni magnetic metallic foams and CoPt/Cu/Ni and CoPt/Ni nanowires were measured in an Oxford Instruments 1.2 VSM. The magnetic field was generated by an electromagnet, with poles of 177 mm in diameter. The gap between the two poles was of approximately 40 mm. Magnetic properties of porous Ni supported Al_2O_3 and Co_2FeO_4 samples were measured in a VSM from Micro-Sense at room temperature. Magnetic hysteresis loops were carried out up to 2 T.

2.4 Nanoindentation

Nanoindentation tests allow extracting elastic modulus and hardness of the specimen material from load-displacement measurements. In general, the test involves a sequencial procedure of loading and unloading; both load (*P*) and displacement (*h*) of the tip are recorded during the test (Figure 2.8). This technique can applied to thin films or micro- and nanometric structures, in which the mechanical properties are derived directly from the loading-displacement curves at the beginning of the unloading segment using the method of Oliver and Pharr[3]. From the initial unloading slope, the contact stiffness, *S*, is determined as:

$$s = \frac{\mathrm{d}P}{\mathrm{d}h} \qquad \text{[Eq. 2.2]}$$

The value of *S* is evaluated based on its relationship with the contact area, *A*, and the reduced Young´s modulus, E_r:

$$s = \beta \frac{2}{\sqrt{\pi}} E_r \sqrt{A} \qquad \text{[Eq. 2.3]}$$

Here, β is a constant that depends on the geometry of the indenter (for Berkovich indenter, $\beta = 1.034$)[4] and E_r is related to the Young's moduli of the sample and the tip through:

$$\frac{1}{E_r} = \frac{1-v^2}{E} + \frac{1-v_i^2}{E_i} \qquad \text{[Eq. 2.3]}$$

Where E and v denote, repectively, Young´s modulus and Poisson´s ratio of the sample, and the E_i and v_i are the corresponding values for the indenter. Note that for diamond tip, E_i = 1140 GPa and v_i = 0.07[4]. Hardness is calcuted from the following expression:

$$H = \frac{P_{Max}}{A} \qquad \text{[Eq. 2.4]}$$

Where P_{Max} is the maximum load applied during nanoindentation. As shown from Eq. 2.4, the determination of contact area (*A*) if of paramount importance to calculate *H* and *E* values.

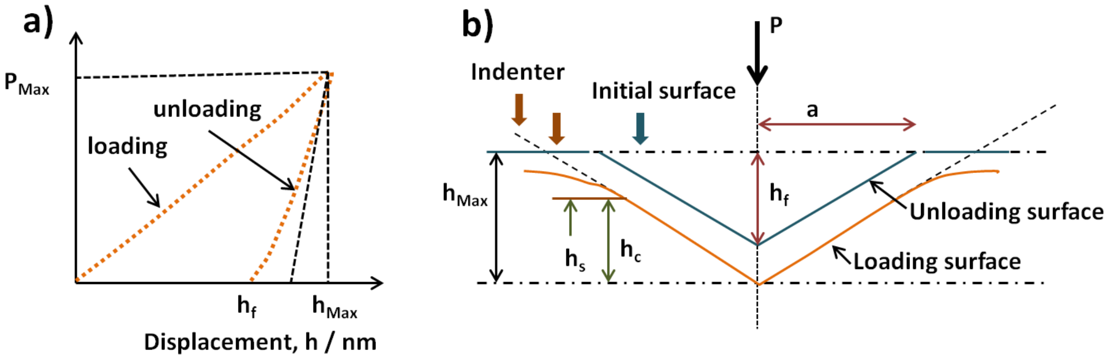

Figure 2.8: a) Typical load-displacement nanoindentation curve. b) Schematic illustration of the indenter and specimen surface at full load and unload and the parameters characterizing the contact geometry[4].

Nanoindentation experiments were performed in load-control mode, using a *Ultra-Micro Indentation System* (UMIS) instrument from Fischer-Cripps Laboratories equipped with a Berkovich pyramidal-shaped diamond tip. The maximum applied load ranged from 2 to 25 mN. The thermal drift during the nanoindentation was kept below 0.05 nm s^{-1}. At least 10 indents were performed at each maximum applied load to verify the accuracy of the indentation data. Corrections for the contact area (calibrated with a fused quartz specimen), instrument compliance, and initial penetration depth were applied.

References

[1] J. Goldstein, Scanning electron microscopy and X-ray microanalysis. Plenum Publisher: New York **2003**

[2] S. Foner, *Rev. Sci. Instrum*. **1959**, *30*,548.

[3] W. C. Oliver, G. M. Pharr, *J. Mater. Res*. **1992**, *7*, 1564.

[4] A. C. Fischer-Cripps, Nanoindentation, F. F. Ling, Ed., Springer, New York, **2004**.

References

Departament de Física

3. Results: compilation of articles

Chapter 3: Results: Compilation of Articles

In the following, the results derived from the thesis work are presented as a compilation of articles. An extended abstract is included before each of these articles. A general discussion of the results can be found in the articles themselves.

3.1 Electrodeposition of magnetic, superhydrophobic, non-stick, two-phase Cu-Ni foam films and their enhanced performance for hydrogen evolution reaction in alkaline water media

In this article we report on the electrodeposition of hierarchical micro/nanoporous two-phase Cu-Ni films, with tuneable composition and morphology, by taking advantage of hydrogen co-evolution as a source of porosity (i.e., hydrogen bubbles act as a dynamic template during electrodeposition). Cu and Ni deposit within the interstices left by the hydrogen bubbles. This results in porous films with highly interconnected nanodendritic walls. The influence of some deposition parameters on films' morphology (by SEM), their composition (by EDX), and their structure (by XRD) are investigated. In turn, the resulting effects on their magnetic behavior (by VSM), wettability and electrocatalytic properties are explored.

Morphological analyses reveal that the porous structure, including pore topology and spatial arrangement, is largely affected by the current density, the stirring rate, the total metal concentration and the molar ratio of cations in solution. Cu-Ni magnetic metallic foams with Ni contents ranging from 15 at% to 35 at% have been achieved by varying the current density. EDX mapping images show that Ni is mostly concentrated at the inner wall of the pores, while Cu forms the porous skeleton itself. XRD analyses indicate clear phase separation, which can be explained on the basis of: I) the low concentration of complexed cations in solution; II) difference in the nucleation rates of Cu and Ni; III) the existence of a miscibility gap; IV) lower free energy of Ni-rich regions compared with CuNi solid solution. Due to the occurrence of phase separation, the as-deposited Cu-rich films display a ferromagnetic behavior, with saturation magnetization (and coercivity) values that progressively increase (decrease) with the Ni content.

Contact angle values beyond 150° are observed for aqueous NaCl droplets, likely due to the rough porous structure of the Cu-Ni films created by the hydrogen bubble template. In addition, when a NaCl droplet is slowly deposited onto the Cu-Ni foam film's surface, it does not spread out the coating neither penetrates into it. Instead, it comes in contact with the outermost surface of the film, the syringe not being able to completely extrude the liquid. Afterwards the whole droplet departs without any visual water residual left.

To study the electrocatalytic activity of the deposited Cu-Ni foams towards HER, polarization curves are recorded in 1 M Ar-purged KOH solution at a sweeping rate of 50 mV s^{-1}. For the sake of comparison, the electrocatalytic behavior of pure porous Cu and Ni metals are also tested. The as-prepared Cu-Ni foam films exhibit lower onset potentials and higher current densities than pure Cu and Ni coatings. Furthermore, the $Cu_{85}Ni_{15}$ sample shows the most promising hydrogen evolution properties, i.e. the smallest overpotential and the highest current density among all the samples. It is conjectured that the migration of H-adatoms from the Ni to the Cu centers and the subsequent desorption of molecular hydrogen desorption is favoured for this sample, partly because the size of their Ni clusters is smaller and thereby the distance between the adsorption and desorption sites is shorter.

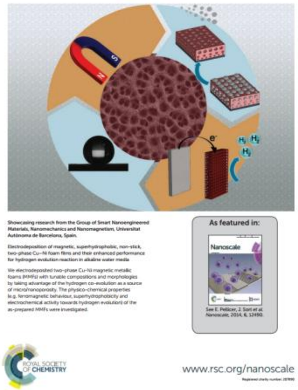

Showcasing research from the Group of Smart Nanoengineered Materials, Nanomechanics and Nanomagnetism, Universitat Autònoma de Barcelona, Spain.

Electrodeposition of magnetic, superhydrophobic, non-stick, two-phase Cu–Ni foam films and their enhanced performance for hydrogen evolution reaction in alkaline water media

We electrodeposited two-phase Cu-Ni magnetic metallic foams (MMFs) with tunable compositions and morphologies by taking advantage of the hydrogen co-evolution as a source of micro/nanoporosity. The physico-chemical properties (e.g. ferromagnetic behaviour, superhydrophobicity and electrochemical activity towards hydrogen evolution) of the as-prepared MMFs were investigated.

As featured in:

See E. Pellicer, J. Sort et al. Nanoscale, 2014, 6, 12490.

www.rsc.org/nanoscale

Electrodeposition of Magnetic, Superhydrophobic, Non-stick, Two-phase Cu-Ni Foam Films and Their Enhanced Performance for Hydrogen Evolution Reaction in Alkaline Water Media

J. Zhang[a], *M. D. Baró*[a], *E. Pellicer*[a,*], *J. Sort*[a, b, *]

[a] Departament de Física, Facultat de Ciències, Universitat Autònoma de Barcelona, E-08193 Bellaterra, Spain.

[b] Institució Catalana de Recerca i Estudis Avançats (ICREA) and Departament de Física, Universitat Autònoma de Barcelona, E-08193 Bellaterra, Spain.

*To whom correspondence should be addressed:

Prof. Jordi Sort, Dr. Eva Pellicer

E-mail: Jordi.Sort@uab.cat, Eva.Pellicer@uab.cat

(Back inside cover of the issue)

ABSTRACT

Two-phase Cu-Ni magnetic metallic foams (MMFs) with tunable composition have been prepared by electrodeposition taking advantage of hydrogen co-evolution as a source of porosity. It is observed that Ni tends to deposit inside the porous network defined by the Cu building blocks. Contact angle measurements reveal that the prepared porous films show a remarkable superhydrophobicity (contact angle values larger than 150°) and a non-sticking property to aqueous droplets. This behavior is predominately ascribed to the morphology of the films – hierarchical micro/nanoporosity, wall thickness, and spatial arrangement. The electrochemical activity and stability towards hydrogen evolution reaction of the Cu-Ni MMFs has been investigated by cyclic voltammetry in 1 M KOH at 298 K, and the optimal Ni content is found to be 15 at%. Furthermore, all the foam-like films exhibit ferromagnetic behaviour due to the presence of the Ni-rich phase, with coercivity values ranging from 114 Oe to 300 Oe. From the technological point of view, the Cu-Ni MMFs are promising candidates for magnetically-actuated micro/nano-electromechanical systems (MEMS/NEMS) and micro/nanorobotic platforms with a large surface-area to volume ratio or in magnetic sensors or separators.

1. Introduction

Metallic foams (MFs) have received considerable attention within the scientific community because they show a number of interesting properties compared to fully dense materials: large surface area, light weight, higher catalytic activity, and absorbability of mechanical impacts, amongst others.[1,2] This has prompted the use of MFs in several applications like electrocatalysts[3], fuel cells[4], batteries[5], supercapacitors[6], sensors[7] and biomedical implants[8]. During the past few decades, tremendous efforts have been directed towards developing synthetic strategies for MFs with well controlled composition, morphology and spatial arrangement, such as de-alloying, modified polyol process, hard-templating, combustion synthesis and sol-gel method.[1,2] Strictly speaking, MFs are cellular structures made of a solid material, typically aluminum, that show a large porosity (75-95 % of the volume are voids).

The pores can be sealed (closed-cell foam) or can form an interconnected network (open-cell foam). Although the term ‘metallic foam’ was traditionally applied to a special class of cellular metals that originate from liquid-gas mixtures[9], the term has expanded its meaning to cover porous metallic layers of any composition produced by other means. Electrodeposition using hydrogen bubbles as a dynamic template has attracted significant attention within the MF community since three-dimensional (3D) self-supported metallic foams with highly porous walls can be straightforwardly obtained. Hydrogen is chosen not only because of its role as a ‘soft’ template, but also due to its low cost, low toxicity and, most importantly, needless of template removal, as typically required in other synthetic strategies. In fact, the hydrogen template assisted electrodeposition is a one-step method because hydrogen is automatically detached from the growing porous layer during the deposition process. Recent developments in the use of hydrogen evolution as a dynamic template have led to the production of several porous metals including Sn[10], Cu[11], Ni[12], Ag[13], Pt[14] and Au[15], intermetallic compounds like Cu_6Sn_5[16] or other bi-metallic systems like Cu/Pd[17]. Interestingly, the rough porous structure created by the hydrogen bubble template provides a novel approach to build up hydrophobic or even superhydrophobic surfaces that mimic the lotus leaves in the nature word. For example, 3D porous Cu films with tunable hydrophobicity were successfully sculptured by Xia and co-workers via changing the pore size and the wall thickness.[11]

Advanced synthetic routes to engineer magnetic materials with different nanoarchitectures has fostered the discovery of new magnetic phenomena and, in turn, expanded the range of applications of magnetic materials. In this context, magnetic MFs (MMFs) have shown to be appealing for magnetic micro/nano-electromechanical systems (MEMS/NEMS) and in micro/nanorobotic platforms. For example, MMFs can navigate through wastewaters under the action of external magnetic fields and absorb a variety of oils from polluted water[18]. So far, a few ferromagnetic metals and alloys have been produced by electrodeposition using hydrogen bubbles as a source of porosity. For example, Tu[19] and co-workers succeeded in the fabrication of 3D porous nano-Ni supported Si composite film using hydrogen bubbles as scaffold. Mattarozzi[20] et al. produced Cu-Ni alloy layers with interconnected porosity at large current density (–3 A cm^{-2}) to promote vigorous hydrogen evolution, while Eugénio et al. fabricated phase-separated Cu-Ni films with non-interconnected rounded pores[21]. In these works, emphasis was laid on the electrochemical performance of the material (i.e., nano-Ni supported Si composite was applied in lithium-ion batteries and porous Cu-Ni was used in the reduction of nitrate ions in alkaline media and as electrode in supercapacitors). The magnetic properties of these MFs have been overlooked.

Besides eventual ferromagnetic behavior, Cu-Ni system shows a number of interesting functional properties such as high corrosion resistance, improved malleability, excellent ductility and solderability[22]. In particular, the corrosion resistance of Cu-Ni alloys with 35-50 wt % Ni (referred to as Constantan) in chloride-containing media is very high. This makes Cu-Ni material attractive for protective coatings in marine environments[23-25]. In addition, Cu-Ni exhibits antibiofouling[25] and electrocatalytic properties[26]. For all these reasons, Cu-Ni has attracted the interest of electroplaters for more than 100 years[27]. The electrodeposition of either single-phase or two-phase non-porous Cu-Ni deposits has been demonstrated in different electrolytic solutions[28-31]. From the magnetic point of view, Cu-Ni alloys show a paramagnetic-to-ferromagnetic transition. The threshold for ferromagnetism at room temperature is ca. 61 at% Ni[29]. Compared to fully dense (i.e., non-porous) Cu-Ni films, the preparation of porous Cu-Ni by electrodeposition has been much less investigated[20,21]. Searson[32] and co-workers have successfully developed porous core/shell Cu-Ni thin films by electrodeposition. The films featured columnar structures consisting of a Ni-rich shell and a Cu-rich core. They further proved that the driving force for phase separation was the miscibility gap and the different nucleation and growth rates of Cu and Ni[33]. Other strategies not relying on the direct electrosynthesis of Cu-Ni have been also pursued. Choi et al. prepared Cu-Ni foams with dendritic walls by electrodeposition onto nonconductive alumina coated with electroless Cu[34]. After heat-treatment in vacuum, the Cu layer was electrochemically etched. Very recently, a Cu-Ni foam was produced by Ni electrodeposition onto Cu-coated foamed polyurethane followed by electrophoretic deposition of graphene nanosheets[35]. After thermal treatment, a material useful as a shield against electromagnetic interference was obtained. Nevertheless, although the synthesis of Cu-Ni MFs has been already attempted, their magnetic properties have not been studied hitherto.

From the aforementioned reasons, it is envisaged that the development of Cu-Ni MMFs combining tunable porosity (and in turn, superhydrophobicity) with tailored magnetic response emerges as a challenging engineering subject that could trigger the development of novel technological applications based on the multifunctional character of the Cu-Ni system. Compared to fully dense Cu-Ni, the porous networks make the material better suited as electrocatalyst and sensor whereas the magnetic properties could allow wireless actuation in magnetic MEMS/NEMS (e.g. self-cleaning magnetic separators) or robotic platforms[36,37].

Herein, we present the synthesis of ferromagnetic Cu-Ni MFs by one-step galvanostatic electrodeposition from acidic electrolytic solutions containing Cu (II) and Ni (II) sulfate salts and acetic acid as hydrogen bubble stabilizer. The hydrogen bubble template is found to confine the nucleation events resulting in phase-separated Cu-Ni MMFs. The effect of current density, [Cu(II)]/[Ni(II)] ratio in solution, and stirring rate on the alloy morphology and composition are systematically investigated. It is also shown that the Cu-Ni surfaces are superhydrophobic, with contact angle values greater than 150°. Furthermore, we demonstrate that the as-prepared Cu-Ni MMFs exhibit improved electrocatalytic activity and high stability towards hydrogen evolution reaction (HER) in alkaline media.

2. Experimental procedure

2.1 Synthesis of Cu-Ni MMFs

All depositions were carried out in a single-compartment, double-jacketed glass electrochemical cell. Si/Ti (25 nm)/Au (125 nm) substrates (working area 0.25 cm^2) were used as cathode. Prior to deposition, the substrates were cleaned with acetone, followed by diluted sulphuric acid and finally rinsed in water. A platinum sheet served as the counter electrode, and a double junction Ag|AgCl 3 M KCl electrode (*E*

= + 0.210 V *versus* standard hydrogen electrode (SHE)) was utilized as the reference electrode. For Cu-Ni MMFs electrodeposition, a constant current density ranging from –0.7 A cm^{-2} to –4 A cm^{-2} was applied by using a PGSTAT120N Autolab potentiostat/galvanostat (Ecochemie). The electrolyte consisted of $CuSO_4·5H_2O$ (0.01-0.02 M), $NiSO_4·6H_2O$ (0.15-0.3 M), H_2SO_4 (1 M), CH_3COOH (0.1 M), HCl (50 mM), and sodium citrate tribasic dehydrate (0.2 M). All chemicals are of analytical grade and used as received without further purification. Electrolyte solution was prepared from ultrapure water. Argon was bubbled through the solution to get rid of oxygen before each deposition. Unless otherwise stated, all deposition processes were carried out at 25℃ and under stirring (800 rpm) using a magnetic stirrer bar. Pure Ni MMFs were synthesized from a different electrolyte reported elsewhere[19].

2.2 Characterization

Scanning electron microscopy (SEM) images and energy-dispersive X-ray spectroscopic (EDX) analyses were performed on a Merlin Zeiss microscope operated at 3 kV and 15 kV, respectively. X-ray diffraction patterns of the MMFs were recorded with a Philips X'Pert diffractometer in the 39-56° 2θ-range (step size = 0.03°, step time = 2 s) using Cu K_α radiation (λ = 0.154178 nm). Average crystallite size and phase percentages were estimated using the Rietveld full-pattern fitting procedure ("Materials Analysis using diffraction" MAUD software). Room temperature hysteresis loops were collected using a vibrating sample magnetometer (VSM) from Oxford Instruments, with a maximum applied magnetic field of 0.3 T. A surface analyzer (Smartdrop, Femtofab) was used to determine the contact angles for the porous surfaces (sessile drop technique). The liquid utilized for the measurements was 7 µL droplets of 5 wt% NaCl solution at room temperature. The reported contact angle values correspond to the average obtained from two independent measurements.

2.3 Electrocatalytic activity towards HER

The electrochemical activity of the Cu-Ni MMFs towards HER was measured in the same three-electrode system used for the deposition of the MMFs. The Cu-Ni MMFs deposited on Si/Ti/Au substrate were used as the working electrode. Polarization curves were recorded in a de-aerated 1 M KOH solution by cycling the potential between –1.0 V and –2.0 V at 50 mV s^{-1}. The onset potential and current density values of Cu-Ni MMFs were compared with those of pure Ni MMFs and pure Cu MFs. 50 cycles of cyclic voltammetry (CV) were run in order to assess material stability. The temperature of the cell was set at 25 ℃.

3. Results and discussion

3.1 Morphology and structure of Cu-Ni MMFs

Two-phase Cu-Ni MMFs were successfully fabricated on Si/Ti/Au substrates by electrodeposition using hydrogen bubble as a dynamic template. Compared with the Au surface, the electrodeposited Cu-Ni MMFs possess higher overpotential towards hydrogen evolution in highly acidic media. Therefore the hydrogen bubbles, which mainly evolve from the water electrolysis on Au surface, create a dynamic bubble template for Cu-Ni deposition. This makes the Cu and Ni discharge events to be mostly confined within the interstices left by the hydrogen bubbles. The scheme of the process for fabricating Cu-Ni MMFs is illustrated in Fig. 1. Hydrogen is automatically detached from the growing porous layer, acting as a dynamic template for Cu-Ni deposition.

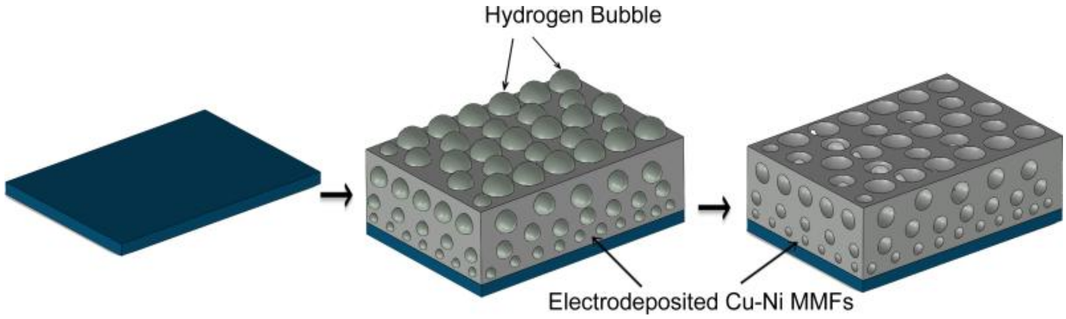

Fig. 1 Schematic diagram illustrating the fabrication of Cu-Ni MMFs. Numerous gas bubbles, evolved at different locations on the substrate, act as a dynamic template during metal growth. Deposition mainly occurs at bubbles interstices.

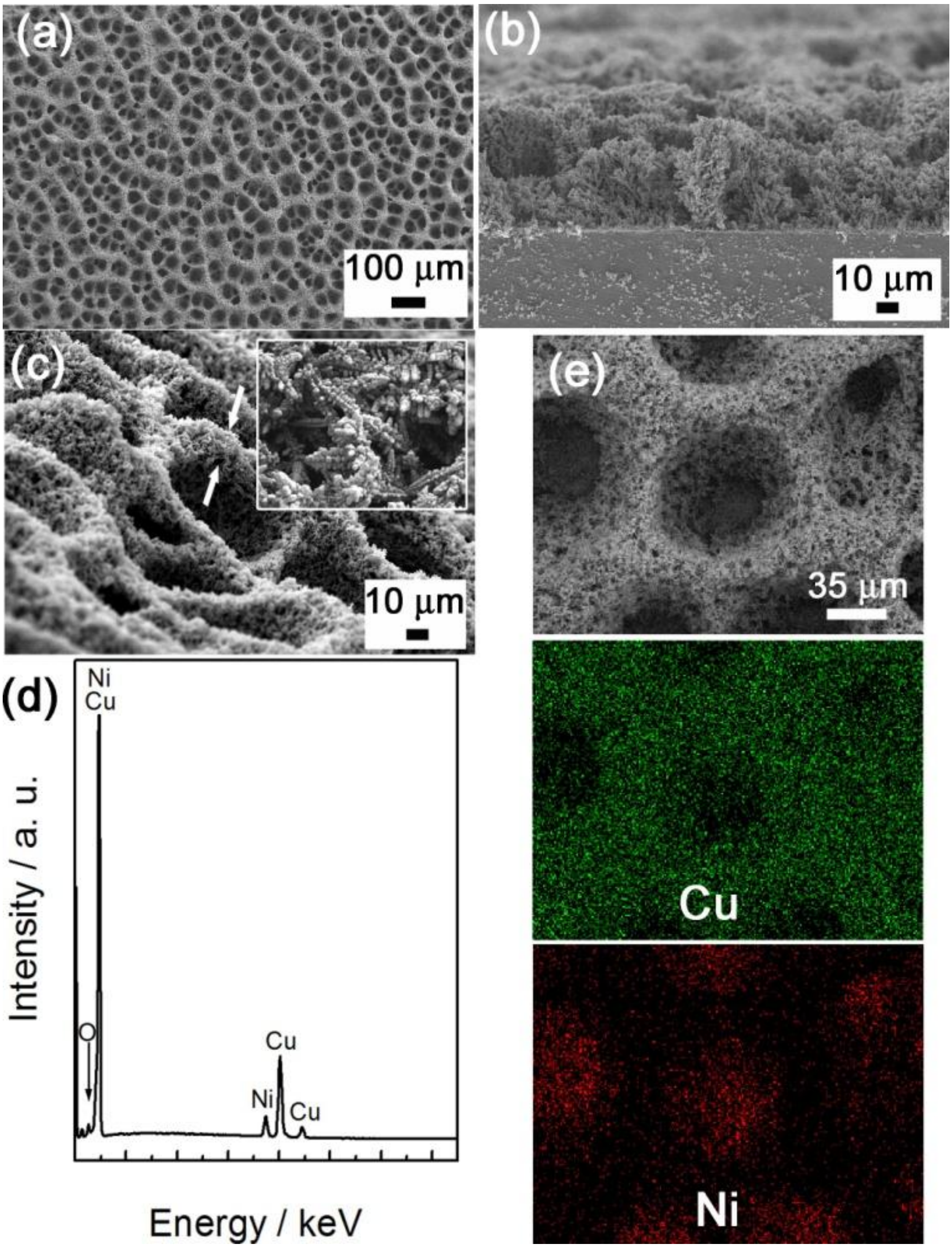

Fig. 2 SEM images: (a) top, (b) cross-sectional and (c) oblique-sectional (insert, magnified) views of Cu-Ni MMFs deposited at an applied current density of –1 A cm^{-2} for 300 s. (d) Corresponding EDX spectrum (80 at% Cu) and (e) EDX mapping images of the zoomed SEM image shown on top. Concentrations of metal salts in the bath were 0.02 M $CuSO_4·5H_2O$ and 0.3 M $NiSO_4·6H_2O$ ([Ni(II)]/[Cu(II)]: 15).

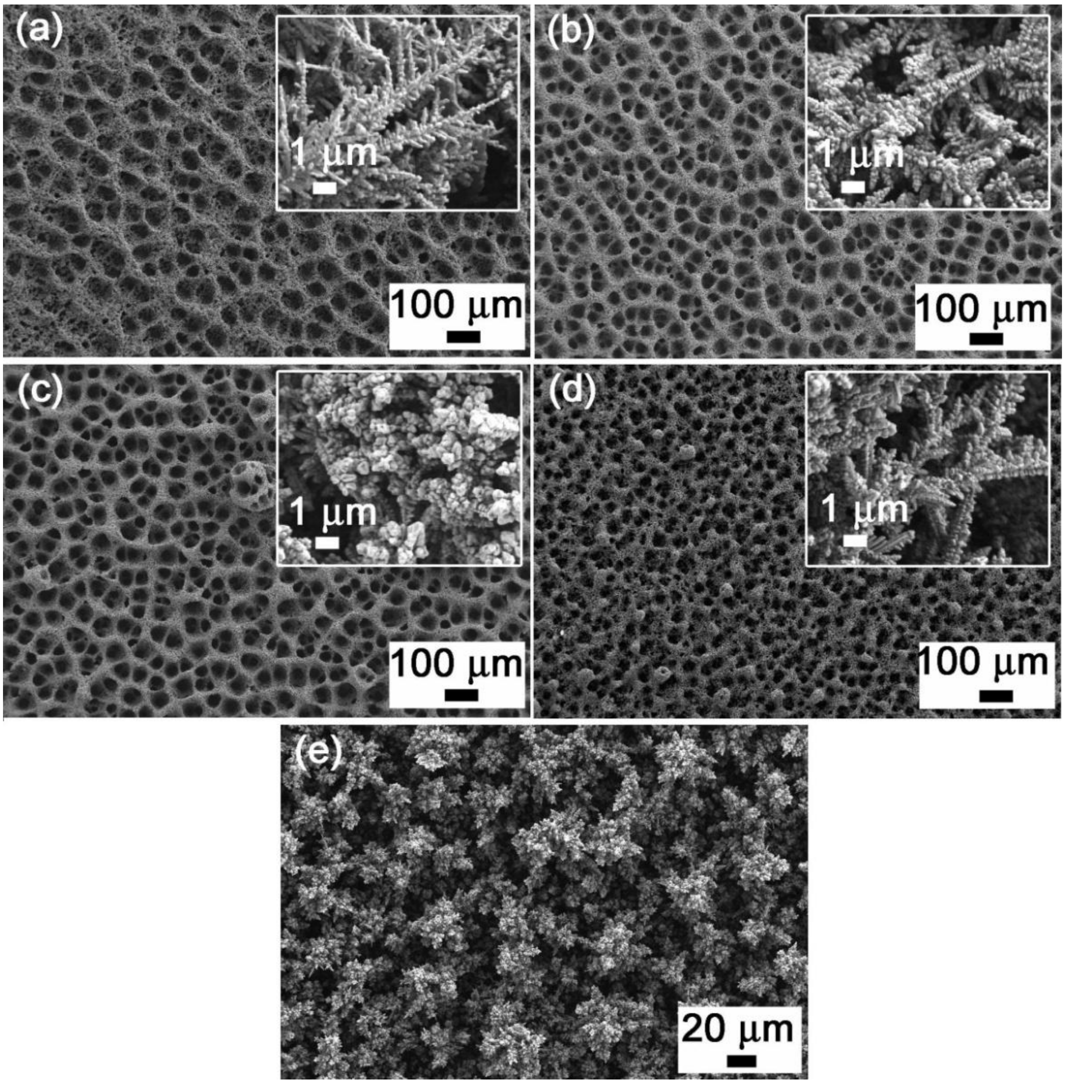

Fig. 3 Low and high (inserts) magnification SEM images of Cu-Ni MMFs deposited at different current densities: (a) –0.7 A cm^{-2} ($Cu_{85}Ni_{15}$), (b) –1 A cm^{-2} ($Cu_{80}Ni_{20}$), (c) –2 A cm^{-2} ($Cu_{75}Ni_{25}$), (d) –3 A cm^{-2} ($Cu_{65}Ni_{35}$) and (e) –4 A cm^{-2} ($Cu_{60}Ni_{40}$). Concentrations of metal salts in the bath were 0.02 M $CuSO_4{\cdot}5H_2O$ and 0.3 M $NiSO_4{\cdot}6H_2O$ ([Ni(II)]/[Cu(II)]: 15).

Fig. 2 depicts typical SEM images of Cu-Ni MMFs grown by electrodeposition at a constant current density of –1 A cm^{-2} for 300 s from a bath containing 0.02 M $CuSO_4{\cdot}5H_2O$ and 0.3 M $NiSO_4{\cdot}6H_2O$ as metal salts. The SEM micrographs clearly show that the as-prepared Cu-Ni MMFs exhibit 3D interconnected porous structure with pore sizes ranging from 20 μm to 50 μm (Fig. 2a) and thickness of 60 μm (Fig. 2b). Here, acetic acid was very efficient in preventing hydrogen bubbles from coalescence, thus favoring the construction of a template with smaller dynamic pores. Acetic acid is chosen not only because of its strong bubble stabilizing effect, but also because it contains no metallic ions in its structure/formula that could interfere with the deposition process and be incorporated in the deposits[38,39]. Moreover, oblique-sectional image (Fig. 2c and insert) shows that the wall thickness is about 10 µm and that the wall is made of numerous loosely packed nanodendrites. Hence the films display hierarchical porosity (roughly around 50-70%). A representative energy dispersive X-ray spectrum of the Cu-Ni MMFs is shown in Fig. 2d. Cu and Ni elements, together with a very low oxygen signal, are detected. This proves that the porous layers are almost entirely metallic. EDX mapping images (Fig. 2e) show that Ni is mostly concentrated at the inner wall of the pores, while Cu forms the porous skeleton itself. In other words, Ni is distributed as a 'negative copy' of the Cu framework. The EDX mapping indicates that phase separation occurs during the electrodeposition of Cu-Ni MMFs.

Once the synthesis of two-phase Cu-Ni MMFs was proven to be successful, a series of Cu-Ni films with different network morphology and composition were prepared by applying the following current densities: –0.7, –1, –2, –3, and –4 A cm^{-2} (Fig. 3). The porous character and the dendritic walls were preserved in most cases. The composition varies as a function of the applied current density, with the Ni content ranging from 15 at% to 60 at%, indicating that Ni electrodeposition is charge-transfer controlled[40]. Herein, the pore size together with the composition could be modulated to some extent. At low current densities (between –0.7 and –2 A cm^{-2}) (see Fig. 3a-c), the network features are evident. The corresponding films show the morphology typical of a ´metal sponge´ owing to the interconnected pores[9]. When the applied current density is made more negative within this range, the hydrogen bubbles start to generate not only from the Au surface but also from the freshly deposited Cu-Ni MMFs. As a result the branch length of the dendrites decreases and the features become less sharp or, in other words, more rounded (*cf*. inserts of Fig. 3a-c). The intensively evolved hydrogen bubbles change the hydrodynamic conditions near the electrode surface, and likely hinder the diffusion-control necessity for dendritic growth. When the cathodic current density is further increased to –3 A cm^{-2} (see Fig. 3d), the typical dendritic morphology develops again and over-grown spherical particles are observed throughout the porous film. Note that the agitation provided by both hydrogen bubble and magnetic stirring is not sufficient to guaranty the supply of metal ions to the cathode (Si/Ti/Au substrate).[21] Since the deposition rate increases with the increase of applied current density, the electrodeposition process becomes mass-transfer controlled and the dendritic growth is in turn favored. Besides, the formation of hydrogen bubbles is also accelerated, which creates a vigorous local turbulence of the electrolyte. This suppresses bubble coalescence, resulting in smaller hydrogen bubbles for the formation of the MMFs skeleton, thus causing a decrease of the pore size[11]. These results are in accordance with EDX elemental mapping analysis (Fig. 2e) i.e., the morphology of the electrodeposited film is governed by the Cu content. Namely, Ni tends to deposit at the inner wall of the pores defined by the Cu building blocks. At -4 A cm^{-2}, the resulting film (60 at% Ni) displays a porous flower-like pattern, as shown in the SEM image of Fig. 3e. In this case, no interconnected pores are observed. The film is porous but the morphology is completely different from that of the layers produced at relatively lower current densities.

Fig. 4 shows the X-ray diffraction patterns in the 39°-56° 2θ range of Cu-Ni MMFs deposited at current densities from -0.7 to -4 A cm^{-2}. For all the samples, four diffraction peaks corresponding to Cu (111), Ni (111), Cu (200), and Ni (200) reflections of face-centered cubic (fcc) structure are detected. The significant peak splitting further confirms the phase separation and hence the formation of two-phase Cu-Ni MMFs. The position of the Cu (111) reflection is shifted *ca*. 0.05° toward higher angles with respect to the tabulated position (43.298°). Likewise, the position of the Ni (111) reflection is shifted nearly the same amount toward lower angles with respect to the tabulated position (44.505°).

Hence, the films consist of Cu-rich and Ni-rich phases (*i.e.*, some Ni is dissolved into α_1 Cu phase while some Cu is dissolved into α_2 Ni phase). In addition, the relative intensity of the reflections associated with Ni-rich phase increases as the applied current density is made more negative, which indicates the presence of an increasingly larger volume fraction of the Ni-rich phase. Finally, the width of the XRD peaks corresponding to the Ni-rich phase is larger for lower Ni content (*e.g.* $Cu_{85}Ni_{15}$), suggesting that the size of the Ni-rich clusters is smaller in this case.

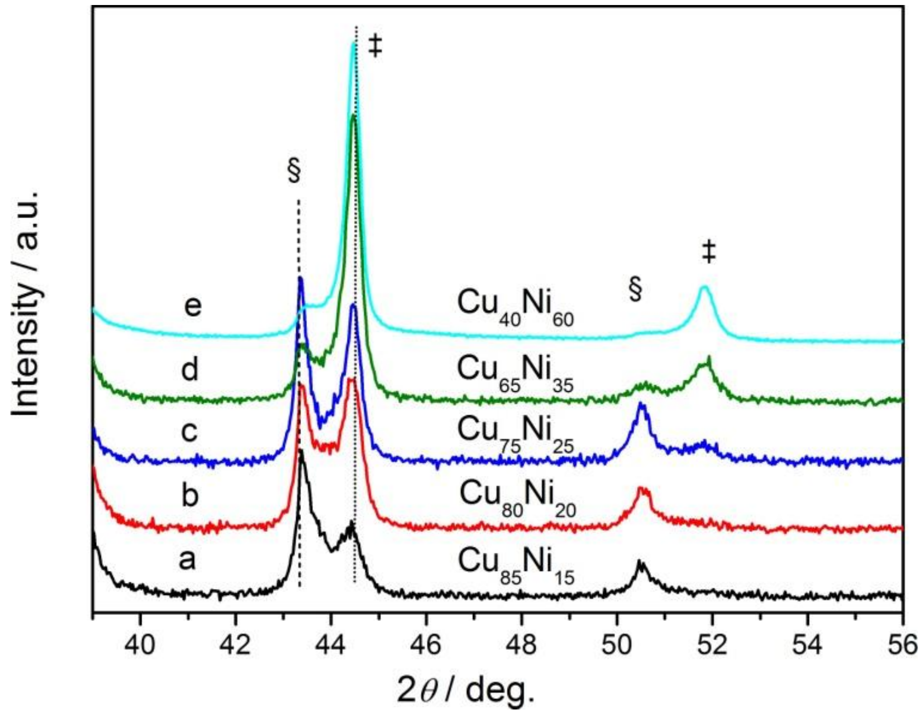

Fig. 4 XRD patterns of Cu-Ni MMFs deposited at different current densities: (a) –0.7 A cm^{-2}, (b) –1 A cm^{-2}, (c) –2 A cm^{-2}, (d) –3 A cm^{-2} and (e) –4 A cm^{-2}. Peaks denoted by § and ‡ belong to Cu-rich and Ni-rich phases, respectively. The dashed and dotted lines indicate the position of tabulated pure fcc (111) Cu and fcc (111) Ni, respectively. Concentrations of metal salts in the bath were 0.02 M $CuSO_4\cdot5H_2O$ and 0.3 M $NiSO_4\cdot6H_2O$ ([Ni(II)]/[Cu(II)]: 15).

To further determine the key experimental factors enabling the formation of porous films with ramified walls, a series of controlled experiments were carried out. Firstly, it was found that the concentration of Cu and Ni salts in the electrolyte (*i.e.*, degree of dilution) has a remarkable influence on the film morphology. Namely, when the concentration of Cu and Ni salts decreases to 0.01 M and 0.15 M, respectively, while the rest of conditions remain unchanged, the as-prepared Cu-Ni MMFs show an irregular foam-like morphology with randomly distributed spherical pores (*c.f.* Fig. S1a and b). The [Ni(II)]/[Cu(II)] ratio in the electrolyte also plays an important role in modulating the composition and the morphology of the Cu-Ni MMFs. For example, the porous network structure is no longer evident when the [Ni(II)]/[Cu(II)] is increased to 30. As shown in Fig. S2a, although the resulting sample is rough, no porous network is visible. Sample morphology changes from non-uniform foam with over-grown particles to a high-quality porous network film (*c.f.* Fig. S2b and c) as the [Ni(II)]/[Cu(II)] decreases from 20 to 15. Such a decrease of the [Ni(II)]/[Cu(II)] ratio in solution is also linked to an increase of the Cu percentage in the Cu-Ni MMFs. Further decrease of the [Ni(II)]/[Cu(II)] to 1 results in pure Cu layers with clear network-like porous structure (Fig. S2d). This observation confirms that Cu deposition promotes the porous architecture.

The stirring rate also has an influence on the composition and morphology of Cu-Ni MMFs. When electrodeposition is conducted under relatively gentle stirring (600 rpm) using a magnetic stirrer bar, the products mainly consist of poor foam-like materials with a Cu content at around 70 at% (Fig. S3a). An increase of the stirring rate from 600 rpm to 800 rpm favors the growth of a porous network film with higher Cu content (80 at%), suggesting that mass-transfer rate is a critical factor in determining the composition and network structure (see Fig. S3b). This phenomenon occurs because Cu is typically discharged under mass-transfer control, while Ni deposition is under charge-transfer control over a wide potential range[40]. When the agitation rate is sufficiently vigorous, Cu deposition governed by ion diffusion increases and the porous network is achieved, confirming the importance of Cu on the coating architecture.

On the basis of these results, the following considerations can be made on the deposition behavior of phase-separated Cu-Ni. The tendency towards phase separation is considered to be associated with the degree of mutual solubility of Ni and Cu elements. In our conditions, the concentration of sodium citrate is lower than the total metal ion concentration. The deposition of Cu-Ni MMFs is supposed to mostly proceed according to the following reactions[41]:

$$Cu^{2+} + 2e^{-} \leftrightarrows Cu \qquad (1)$$

$$Ni^{2+} + 2e^{-} \leftrightarrows Ni \qquad (2)$$

$$H^{+} + e^{-} \leftrightarrows \tfrac{1}{2} H_2 \qquad (3)$$

$$H_2O + e^- \leftrightarrows \tfrac{1}{2} H_2 + OH^- \qquad (4)$$

The formation of a Cu-Ni solid solution (*i.e.*, an alloy) typically requires the presence of a complexing agent in solution to favour the codeposition of the two metals[42]. Although citrate was present in the bath, the concentration of complexed metal ions is extremely low because citrate mostly exists in its protonated form and cannot thus complex the cations in solution. Hence, Ni and Cu discharge mainly occurs from uncomplexed Cu and Ni ions (1) and (2). Simultaneously, a large fraction of the current supplied is used to reduce the protons in solution (3) (along with water reduction (4)). Moreover, Cu^{2+} reduces much faster than Ni^{2+}, leading to the formation of low-density large Cu islands during the initial stages of reduction process. When the surface becomes depleted in Cu ions, Ni nucleation is promoted in the vicinity of Cu islands[32,33.] The miscibility gap in the composition range likely provides the driving force for phase separation. The atomic fraction of Ni in the Cu-Ni MMFs where the phase separation is observed is in the range from 15 at% to 35 at%, coincident with the miscibility gap existing in the Cu-Ni system[43,44], as shown in Fig S4. Nevertheless, according to the local environment model, another explanation could be that the total free energy of the MMFs becomes lower if the Ni atoms segregate to form Ni-rich magnetic clusters, compared to the Cu-Ni solid solution[45,46]. Further experimental proof is nevertheless still necessary to gain deeper knowledge on the formation mechanism of the two-phase Cu-Ni MMFs, especially taking into account that metastable phases not predicted by the phase diagrams are available by electrodeposition.

3.2 Magnetic Properties

The hysteresis loops corresponding to the Cu-Ni MMFs deposited at varying current densities are shown in Fig. 5. Although all films contain a Ni percentage below 61 at% and would therefore be in principle non-ferromagnetic[29], well-defined hysteresis loops are obtained even when the Ni percentage is only 15 at%. This observation confirms that phase separation actually takes place during electrodeposition, so that Ni-rich regions (with Ni percentage above 61 at%) coexist or are embedded in a non-ferromagnetic Cu-rich matrix. This microstructure is in good agreement with the SEM-EDX observations (Fig. 2e) and XRD analysis (Fig. 4). As expected, the saturation magnetization, M_S, of these MMFs increases with the Ni content. However, the increase is not linear but it becomes steeper for Ni percentages above 20 at%, where the amount of Ni-rich regions starts to be significant (~40, 60 and 80 vol% of Ni-rich phase in the samples with atomic compositions $Cu_{75}Ni_{25}$, $Cu_{65}Ni_{35}$ and $Cu_{40}Ni_{60}$, respectively). The porosity degree is not taken into account in the normalization of the magnetization (M) of the films (the volume is considered from the real thickness of the films, including both the pores and the Cu-Ni walls). Hence, M_s would be much larger if the actual volume of Cu-Ni (without the pores) had been used to normalize M. The hysteresis loops also reveal that the coercivity, H_c, tends to slightly increase with the decrease of Ni content in the MMFs. Assuming that the Ni-rich (ferromagnetic) regions are surrounded by non-ferromagnetic Cu-rich regions, such dependence of H_c can be understood from the interplay between different factors. First, a progressive decrease of the effective ferromagnetic particle size with the decrease of the Ni content could be expected since interconnection between ferromagnetic clusters would be precluded if the Ni content is exceedingly low. XRD reveals that the crystallite size *(i.e.*, average coherent diffraction length) of the Ni-rich phase decreases from 80 to 60 nm as the Ni content in the samples decreases from 60 at% to 15 at%). It is well known that, in general, H_c is inversely proportional to the particle size, as magnetization reversal changes from multi-domain (propagation of domain walls) to mono-domain (coherent rotation) states[47]. Secondly, and for the same reason, the strength of magnetic dipolar interactions is supposedly larger for higher Ni contents, as the average distance between neighboring magnetic regions becomes smaller. Dipolar interactions promote cooperative reversal of the ferromagnetic clusters and tend to decrease H_c[48]. Finally, the fact that Ni is prone to concentrate at the inner walls of the porous structure (Fig. 2e) suggests that these MMFs could be suitable for trapping small ferromagnetic particles inside the porous frameworks. Therefore, this material could find applications as magnetic sensor or separator.

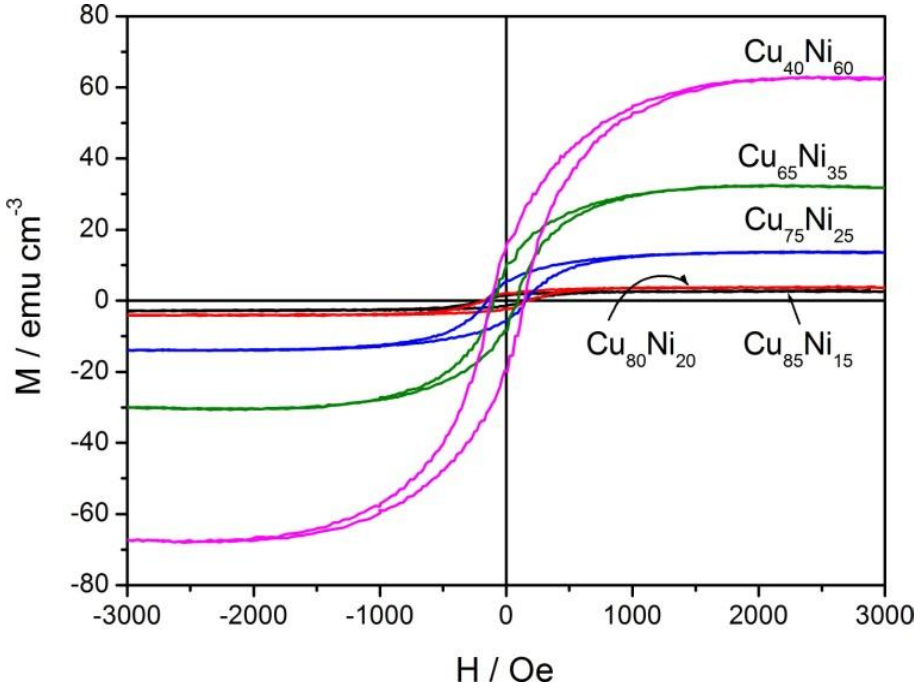

Fig. 5 Room temperature hysteresis loops of the Cu-Ni MMFs.

3.3 Wettability

The wettability of the Cu-Ni MMFs was characterized by the sessile drop technique, using 7 µL of 5 wt% NaCl droplets. Fig. 6 shows that all porous coatings exhibit contact angles larger than 150°, *i.e*. they show superhydrophobic behavior, although the values fluctuate slightly with the change in the applied current density. The wettability of a solid surface is governed by the intrinsic surface nature as well as by the geometrical microstructure. The 3D interconnected porous structure together with the dendritic walls results in the increase of the surface roughness, which in turn significantly decreases the surface area in contact with the NaCl droplets. Moreover, air is trapped in the grooves of such a rough surface, allowing the NaCl droplets to be in contact only with the outermost features of the surface. As a result, superhydrophobic surfaces with large contact angle are achieved. The slight differences in the contact angle values may be ascribed to the experiment uncertainty[49]. Nevertheless, it is challenging to measure the contact angle even for smooth homogeneous surfaces. As observed by Panchagnula and Vedantam[50], the contact angle is determined not only by the area fraction, but also by the conditions near the contact line. The contact angle may vary with regard to the contact line topology, even though the area fraction along the contact line is kept constant[51,52].

To further explore the superhydrophobic character of the Cu-Ni MMFs, NaCl droplets were slowly deposited onto film surface and removed from the Cu-Ni MMFs to assess the non-wetting behavior. Fig. 7 depicts a sequence of images showing *contact* of the droplet onto the Cu-Ni surface, *extrusion* exerted by the syringe and withdrawal (*departure*) of the droplet from the surface. It can be clearly seen that the NaCl droplet does not penetrate into or spread out the coating. Instead, it comes in contact with the outermost surface with the syringe not being able to completely extrude the liquid and afterwards the whole droplet departs without visual water residual left. This result indicates that the adhesive force between the droplet and the syringe is much higher than that between the droplet and the Cu-Ni surface. This phenomenon is similar to that recently reported by Su[53] and Liang[54], who also demonstrated the non-sticking property in their cases. As-prepared superhydrophobic, non-stick coatings are expected to have potential applications in self-cleaning[55], anti-corrosion[56], anti-icing[57], oil-water separation[58] and drag-reduction[59].

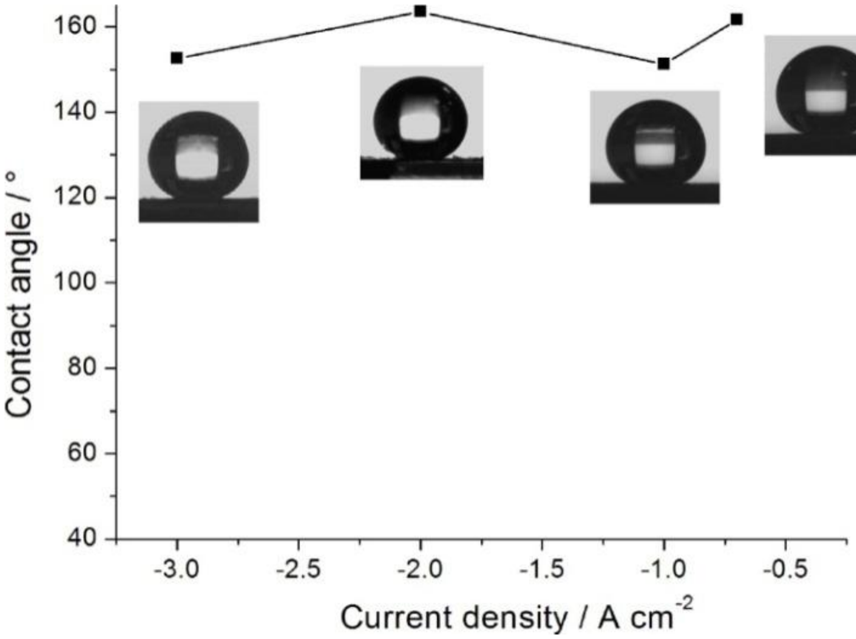

Fig. 6 Contact angles of Cu-Ni MMFs prepared at different current densities. The pictures show the shape of the 5 wt% NaCl droplet on the surface of the as-prepared films.

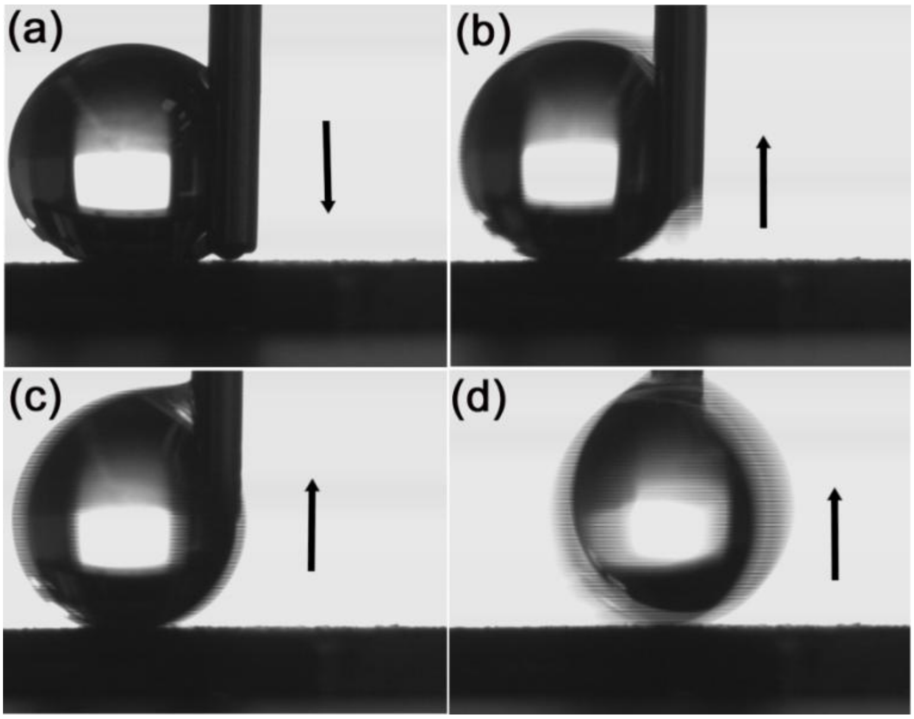

Fig. 7 The process of *contact* (a), *extrusion* (b and c), and *departure* (d) observed between a 5 wt% NaCl droplet and the surface of $Cu_{80}Ni_{20}$ MMF obtained at –1 A cm^{-2}. The arrows represent the moving direction of the syringe.

3.4 Electrocatalytic activity

Recently, nickel-based catalysts have been found to have intriguing electrocatalytic HER performance[60-64]. In view of their highly porous morphology, the as-obtained Cu-Ni MMFs are expected to be suitable candidates for HER. Fig. 8 shows the polarization curves (*j*-*V* plots) of the various Cu-Ni catalysts in 1 M Ar-purged KOH solution at a sweeping rate of 50 mV s^{-1}. For comparison, the behavior of the pure porous metals were also tested and used as reference materials. Porous Ni was electrodeposited from a solution reported elsewhere[19] (Fig. S5) since attempts to produce a Ni film with high-quality porous network from our bath were proven unsuccessful. Instead, pure Cu films with adequate morphology could be obtained from our bath when the [Ni(II)]/[Cu(II)] was made 1:1 (Fig. S2d). From their respective HER polarization curves, the as-prepared Cu-Ni MMFs exhibit lower onset potentials and higher current densities than pure Cu and Ni coatings. Moreover, the onset potential of the $Cu_{85}Ni_{15}$ sample is positively shifted in the polarization curves, indicating the smallest overpotential (η) (of about –1.2 V) among all Cu-Ni MMFs. The enhanced HER activity of $Cu_{85}Ni_{15}$ is mainly due to the synergistic effect of the two metals. In HER, two main reactions are involved[65]. The first step accounts for the interaction of water molecules with the metal (M) whereas the second step is the desorption of freshly generated hydrogen molecules from M. On the one hand, the H_2O-M interaction should be strong enough to promote the discharge of water molecules. On the other hand, weak binding between H and M favors hydrogen desorption. As for the H_2O-M interaction is concerned, the proton absorption bonding is apparently controlled by the number of *d*-electrons[66]. Metals with more unpaired electrons in the *d*-band interact strongly with electron-donating adatoms or molecules. For Ni, with d^8-orbitals, the proton can enter the lattice and the electron from the hydrogen becomes collectivized with the metallic electrons. However, if there are no available un-paired *d*-electrons (case of Cu), *i.e*. high *d*-character according to Pauling's concept, then there are no available sites for absorption. Therefore, Ni atoms display much higher HER activity than Cu atoms. For the hydrogen desorption step, the H-adatoms generated on the Ni sites migrate toward the neighboring Cu atoms where recombination of the H-adatoms occurs and molecular hydrogen releases from the traps. It is conjectured that the release of molecular hydrogen from Cu is favored (with respect to that from Ni) because the hydrogen binding energy (BE_H) of Cu (–2.39 eV) approaches the thermoneutral H_2 (g) dissociation (–2.28 eV)[67]. It is believed that since the feature size of Ni-clusters in the $Cu_{85}Ni_{15}$ MMF is smaller than for the other compositions (in accordance with the XRD and magnetic results), the distance between the generation centers and the desorption traps is shortened. As a result, the migration of H-adatoms from the Ni to the Cu centers becomes easier and the molecular hydrogen desorption is promoted more efficiently, thus enhancing the HER.

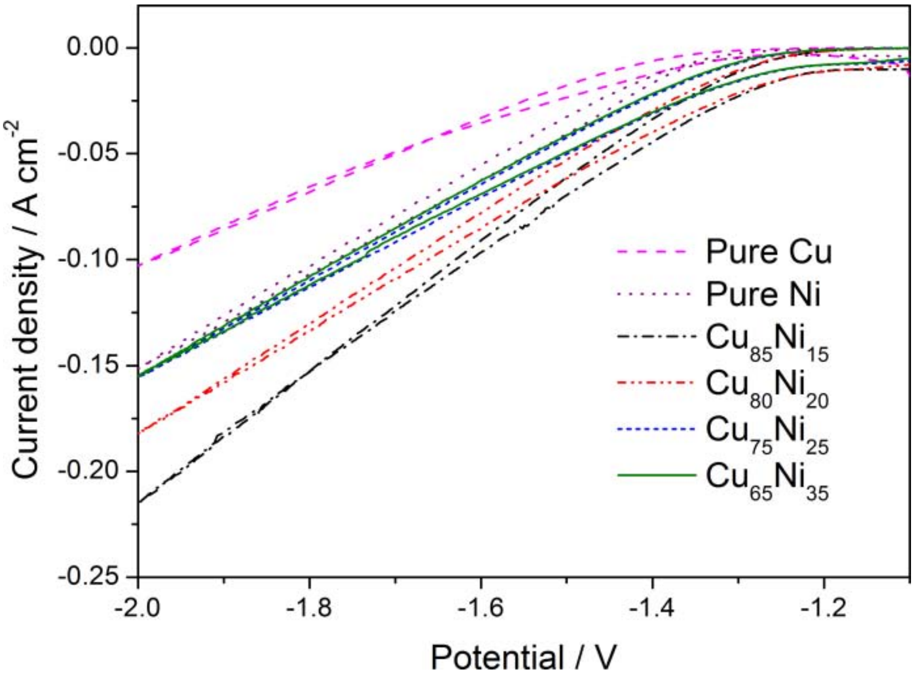

Fig. 8 Polarization curves recorded in Ar-saturated 1 M KOH electrolyte for Cu-Ni MMFs with different composition. The response of pure porous Cu and Ni films is shown for comparison. Scan rate: 50 mV s^{-1}.

In electrocatalysis processes, catalysts may suffer from deformation of the structure, poisoning and thus loss of the catalytic activity[68]. In order to examine the catalytic durability, Cu-Ni MMFs with different composition were subjected to 50 cycles in 1 M KOH electrolyte within the potential range from –1.0 V to –1.6 V. As shown in Fig. 9, the HER current densities of the Cu-Ni MMFs have the highest value at the 1st cycle, and then decrease during the subsequent cycles. This phenomenon is attributed to the formation of the hydrogen bubble on the catalyst surface, which results in the decrease of the available active surface area for HER. After 20th cycle, the current densities are maintained and stable CV curves are observed with an equilibrium state of surface tension and buoyancy force. The morphology of $Cu_{80}Ni_{20}$ MMF before and after the cycling test was analyzed by SEM, indicating that no apparent worsening of the foam morphology occurred (see Fig. S6).

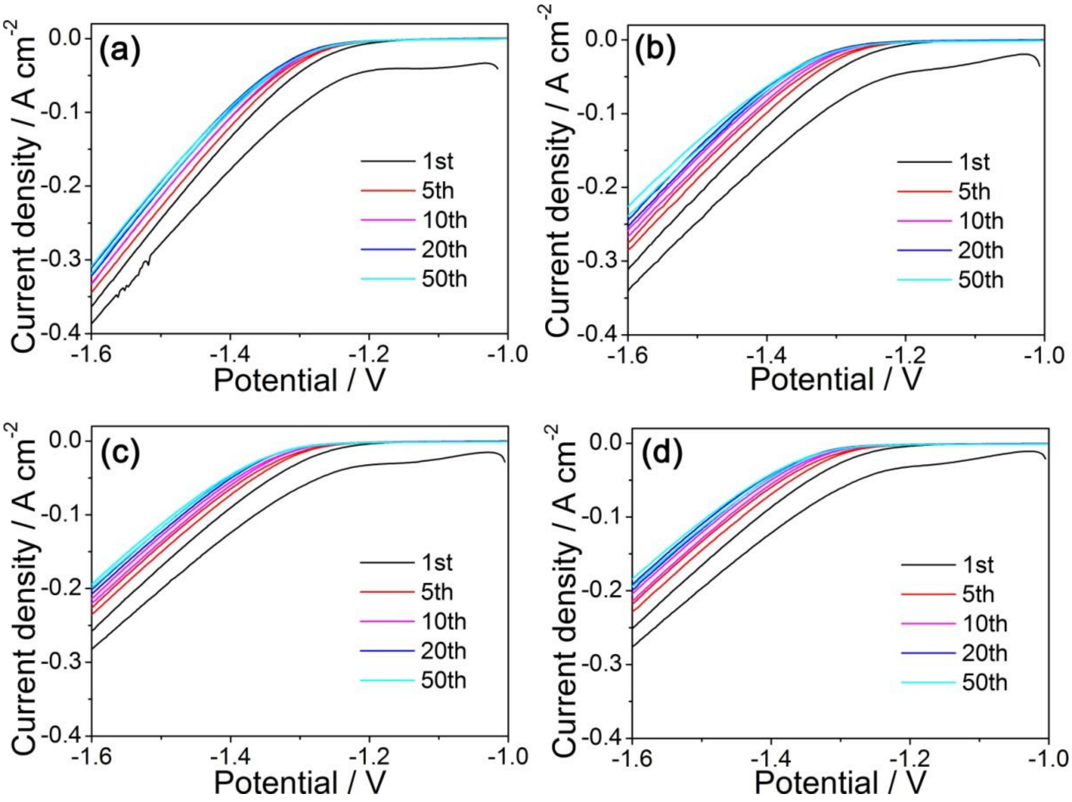

Fig. 9 CV curves of Cu-Ni MMFs with different composition in Ar-saturated 1 M KOH solution: (a) $Cu_{85}Ni_{15}$, (b) $Cu_{80}Ni_{20}$, (c) $Cu_{75}Ni_{25}$, and (d) $Cu_{65}Ni_{35}$.

4. Conclusion

In summary, Cu-Ni MMFs consisting of Ni-rich and Cu-rich phases have been successfully synthesized by the hydrogen bubble template electrodeposition method. Cu and Ni are deposited within the interstices left by the hydrogen bubbles, yielding porous films with highly interconnected nanodendritic walls. The current density has been varied to adjust the network morphology and the Cu/Ni ratio in the films.

Namely, Cu-Ni MMFs with Ni contents ranging from 15 at% to 35 at% and tunable pore topologies have been obtained. The stirring rate, the total metal concentration (dilution degree), and the molar ratio of cations in solution exert a remarkable influence on the composition, morphology and spatial arrangement of Cu-Ni MMFs. XRD analyses indicate clear phase separation that can be understood on the basis of: the low concentration of complexed cations in solution and hence the difference in the nucleation rates of Cu and Ni, the existence of a miscibility gap, and the lower free energy of Ni-rich regions compared with a Cu-Ni solid solution. Due to such phase separation, even the films rich in Cu display a ferromagnetic behavior, with saturation magnetization (and coercivity) values that progressively increase (decrease) with the Ni content. All the Cu-Ni MMFs show superhydrophobicity behavior with contact angles greater than 150°. Furthermore, these MMFs exhibit superior stability and enhanced composition-dependent electrocatalytic activity towards HER over pure Cu and Ni porous films. In particular, the $Cu_{85}Ni_{15}$ MMF shows the highest specific activity. Owing to this combination of properties, these foams are promising inexpensive candidates for widespread technology applicants, such as magnetic micro/nano-electromechanical systems (MEMS/NEMS) and robotic platforms, magnetic separators and sensors.

Acknowledgement

Jin Zhang is grateful to the China Scholarship Council (CSC) for the PhD grant. The authors would like to acknowledge the Spanish MINECO MAT2011-27380-C02-01 and the Catalan DGR 2014-SGR-1015. E.P. is grateful to the Spanish MINECO for the 'Ramón y Cajal' contract (RYC-2012-10839). M.D.B. was partially supported by an ICREA Academia award. Technical support from the Microscopy Service at UAB and from ICMAB for the sessile drop technique measurements is highly appreciated.

Supporting information

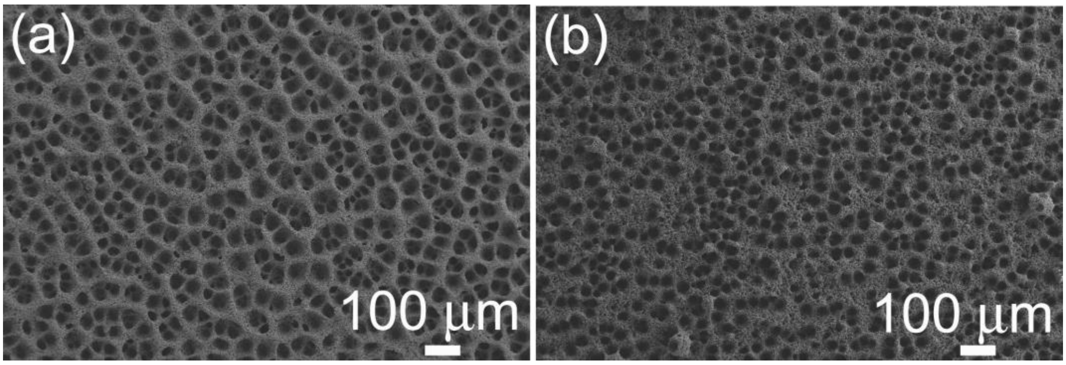

Fig. S1 SEM images of Cu-Ni MMFs electrodeposited at –1 A cm^{-2} for 300 s in electrolytes containing the following metal salts concentrations: (a) 0.02 M $CuSO_4·5H_2O$ + 0.3 M $NiSO_4·6H_2O$, (b) 0.01 M $CuSO_4·5H_2O$ + 0.15 M $NiSO_4·6H_2O$.

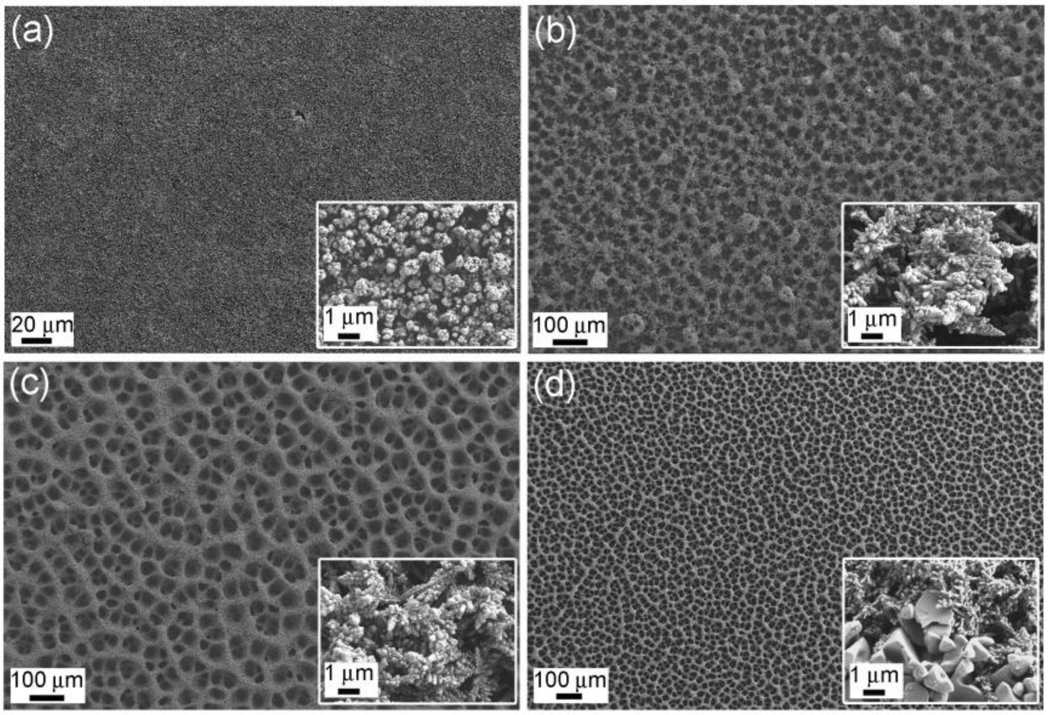

Fig. S2 SEM images of Cu-Ni MMFs electrodeposited at –1 A cm^{-2} for 300 s in electrolytes with varying [Ni (II)]/[Cu (II)] ratios: (a) 30, (b) 20, (c) 15, (d) 1.

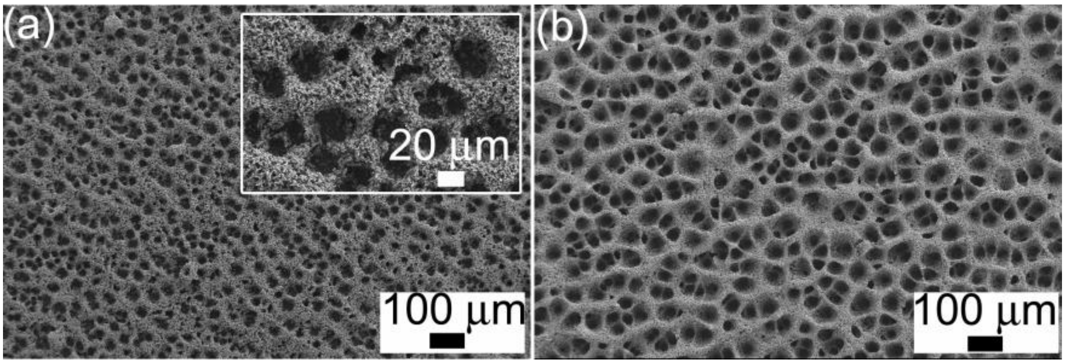

Fig. S3 SEM images of Cu-Ni MMFs were electrodeposited at –1 A cm^{-2} for 300 s under different stirring rates: (a) 600 rpm, (b) 800 rpm.

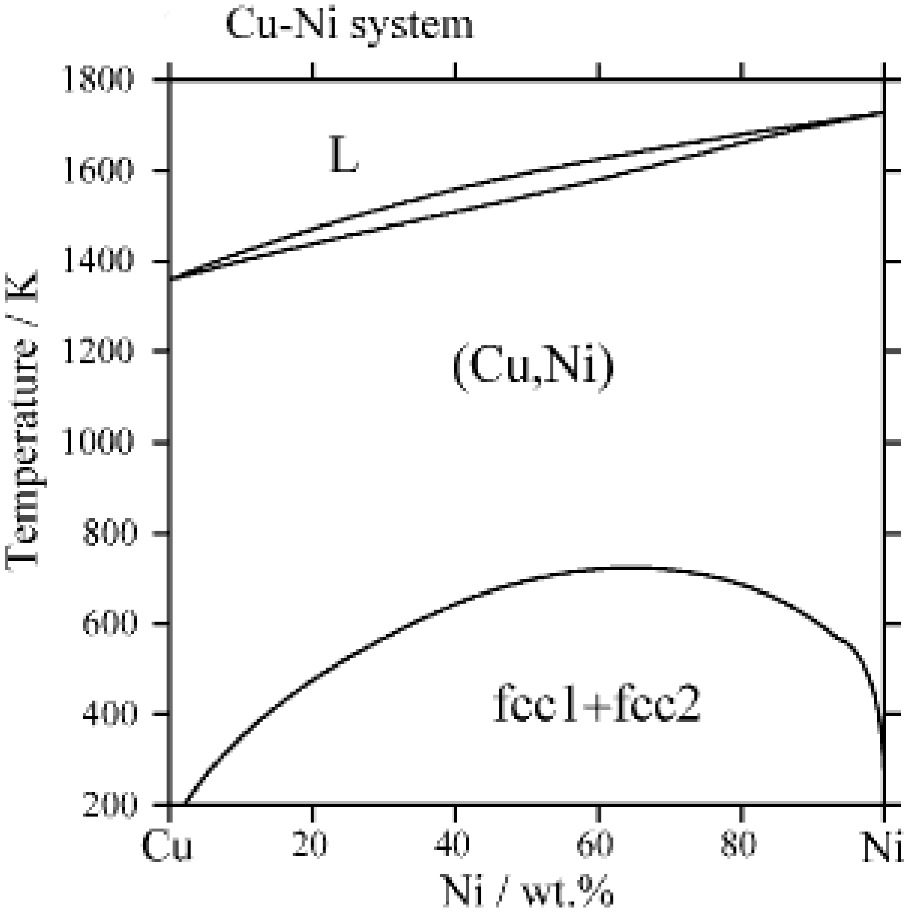

Fig. S4 Calculated phase diagram of the Cu-Ni binary system [44]. (*J. Phys. Chem. Solids*, 2005, **66**, 256–260).

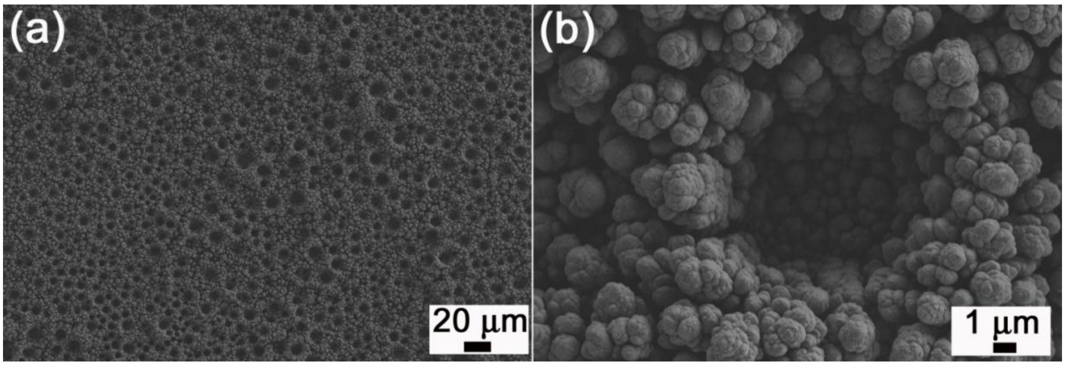

Fig. S5 SEM images of porous pure Ni films prepared according to reference [19]. (*J. Power Sources* 2012, **213**, 106).

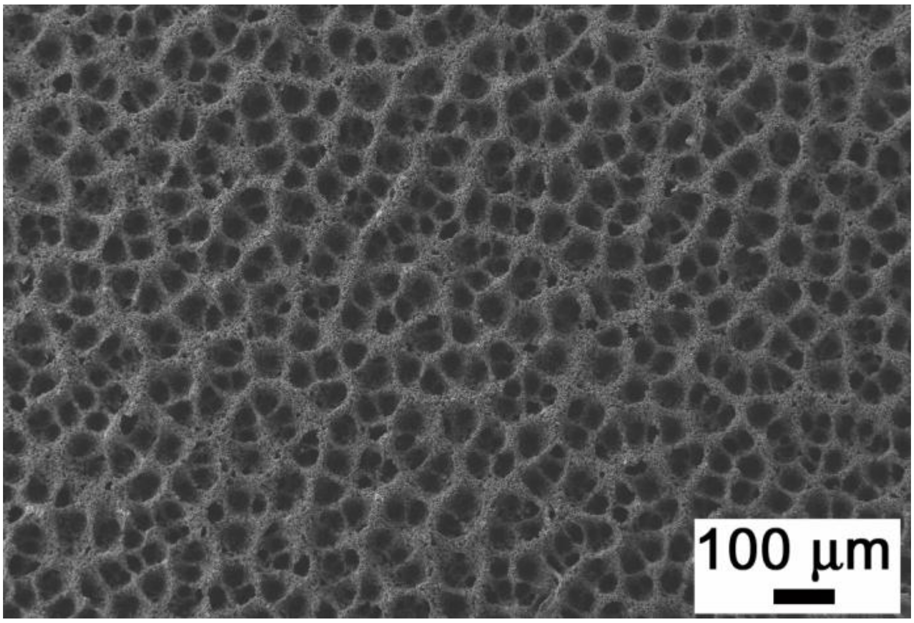

Fig. S6 SEM image of $Cu_{80}Ni_{20}$ film after 50 consecutive cycles in 1 M KOH (Figure 9). No apparent changes in morphology are observed, suggesting that the Cu-Ni MMFs are stable.

Reference

1. L. P. Lefebvre, J. Banhart and D. C. Dunand, *Adv. Eng. Mater.,* 2008, **10**, 775–787.
2. B. C. Tappan, S. A. Steiner and E. P. Luther, *Angew. Chem. Int. Ed.,* 2010, **49**, 4544–4565.
3. Z. Yin and F. Chen, *Electrochim. Acta,* 2014, **117**, 84–91.
4. F. Yang, K. Cheng, X. Xue, J. Yin, G. Wang and D. Cao, *Electrochim. Acta*, 2013, **107**, 194–199.
5. Q. Xiong, J. Tu, Y. Lu, J. Chen, Y. Yu, X. Wang and C. Gu, *J. Mater. Chem.*, 2012, **22**, 18639-18645.
6. X. H. Xia, J. P. Tu, Y. Q. Zhang, Y. J. Mai, X. L. Wang, C. D. Gu and X. B. Zhao, *J. Phys. Chem. C*, 2011, **115**, 22662–22668.
7. X. Sun, H. Ji, X. Li, S. Cai and C. Zheng, *J. Alloys Compd.*, 2014, **600**, 111–117.
8. H. Hsu, S. Wu, S. Hsu, T. Chang and W. Ho, *J. Alloys Compd.*, 2014, **582**, 793–801.
9. J. Banhart, *JOM*, 2000, **52**, 22–27.
10. H. Shin, J. Dong and M. Liu, *Adv. Mater.*, 2003, **15**, 1610–1614.
11. Y. Li, W. Jia, Y. Song and X. Xia, *Chem. Mater.*, 2007, **19**, 5758–5764.
12. I. H. Cardona, E. Ortega, L. V. Gómez and V. P. Herranz, *Int. J. Hydrogen Energy*, 2012, **37**, 2147-2156.
13. S. Cherevko, X. Xing and C. Chung, *Electrochem. Commun.*, 2010, **12**, 467–470.
14. A. Ott, L. A. Jones and S. K. Bhargava, *Electrochem. Commun.*, 2011, **13**, 1248–1251.
15. T. N. Huan, T. Ganesh, K. S. Kim, S. Kim, S. Han and H. Chung, *Biosens. Bioelectron.*, 2011, **27**, 183–186.

16. H. Shin and M. Liu, *Adv. Funct. Mater.*, 2005, **15**, 582–586.

17. I. Najdovski, P. R. Selvakannan, A. P. O'Mullane and S. K. Bhargava, *Chem. Eur. J.*, 2011, **17**, 10058–10063.

18. N. Chen and Q. Pan, *ACS Nano*, 2013, **7**, 6875–6883.

19. Y. Q. Zhang, X. H. Xia, X. L. Wang, Y. J. Mai, S. J. Shi, Y. Y. Tang, C. G. Gu and J. P. Tu, *J. Power Sources*, 2012, **213**, 106–111.

20. L. Mattarozzi, S. Cattarin, N. Comisso, R. Gerbasi, P. Guerriero, M. Musiani, L. Vazquez-Gome, and E. Verlato, *ECS Electrochem. Lett.*, 2013, **2**, D58–D60.

21. S. Eugénio, T. M. Silva, M. J. Carmezim, R. G. Duarte and M. F. Montemor, *J. Appl. Electrochem.*, 2013, **44**, 455–465.

22. R.W. Cahn, P. Hassen and E. J. Kramer, 'Materials Science and Technology, A Comprehensive Treatment, Vol. 8, Structure and Properties of Non-Ferrous Alloys' (VCH, New York, 1996).

23. A. M. Beccaria, Y. Z. Wang and G. Poggi, *Surf. Interf. Anal.*, 2004, **21**, 442-446.

24. G. Kear, B. D. Barker, K. Stokes and F. C. Walsh, *J. Appl. Electrochem.*, 2004, **34**, 659–669.

25. M. Metikoš-Huković, R. Babić, I. Škugor Rončević and Z. Grubač, *Desalination*, 2011, **276**, 228–232.

26. X. Tian, X. Zhao, L. Zhang, C. Yang, Z. Pi and S. X. Zhang, *Nanotechnology*, 2008, **19**, 215711–215716.

27. A. Green, A. E. Russell and S. Roy, *J. Electrochem. Soc.*, 1998, **145**, 875–881.

28. L. C. Melo, P. Lima-Neto and A. N. Correia, *J. Appl. Electrochem.*, 2010, **41**, 415–422.

29. E. Pellicer, A. Varea, S. Pané, B. J. Nelson, E. Menéndez, M. Estrader, S. Suriñach, M. D. Baró, J. Nogués and J. Sort, *Adv. Funct. Mater.*, 2010, **20**, 983–991.

30. C. Bonhte and D. Landolt, *Electrochim. Acta*, 1997, **42**, 2407–2417.

31. M. Ishikawa, H. Enomoto, M. Matsuok and C. Iwakura, *Electrochim. Acta*, 1995, **40**, 1663–1668.

32. Z. Liu, L. Guo, C. Chien and P. C. Searson, *J. Electrochem. Soc.*, 2008, **155**, D569–D574.

33. Z. Liu, G. Xia, F. Zhu, S. Kim, N. Markovic, C. Chie and P. C. Searson, *J. Appl. Phys.*, 2008, **103**, 064313–06438.

34. W.-S. Choi, H.-R. Jung, S.-H. Kwon, J.-W. Lee, M. Liu, and H.-C. Shin, *J. Mater. Chem.*, 2012, **22,** 1028-1032.

35. K. Ji, H. Zhao, Z. Huang and Z. Dai, *Mater. Lett.*, 2014, **122**, 244–247.

36. M. A. Zeeshan, S. Pané, S. K. Youn, E. Pellicer, S. Schuerle, J. Sort, S. Fusco, A. M. Lindo, H. G. Park and B. J. Nelson, *Adv. Funct. Mater.*, 2013, **23**, 823–831.

37. M. A. Zeeshan, R. Grisch, E. Pellicer, K. M. Sivaraman, K. E. Peyer, J. Sort, B. Ozkale, M. S. Sakar, B. J. Nelson and S. Pané, *Small*, 2014, **10**, 1284–1288.

38. H. Shin and M. Liu, *Chem. Mater.*, 2004, **16**, 5460–5464.

39. V. S. J. Craig, B. W. Ninham and R. M. Pashley, *J. Phys. Chem.*, 1993, **97**, 10192–10197.

40. A. Ollivier, L. Muhr, S. Delbos, P. P. Grand, M. Matlosz and E. Chassaing*, J. Appl. Electrochem.*, 2009, **39**, 2337–2344.

41. R. Y. Ying, P. K. Ng, Z. Mao and R. E. White, *J. Electrochem. Soc.*, 1988, **135**, 2964–2971.

42. E. J. Podlaha and C. H. E. Te, *Electrochim. Acta*, 1994, **39**, 2649–2657.

43. ASM, Binary Alloy Phase Diagrams, ASM International, Materials Park, OH, 1996.

44. C. P. Wang, X. J. Liu, M. Jiang, I. Ohnuma, R. Kainuma and K. Ishida, *J. Phys. Chem. Solids*, 2005, **66**, 256–260.

45. A. Amamou, F. Gautier and B. Loegel, *J. Phys. F: Metal Phys.*, 1974, **35**, C4–217 – C4–222.

46. M. J. Fesharaki, L. Péter, T. Schucknecht, D. Rafaja, J. Dégi, L. Pogány, K. Neuróhr, É. Széles, G. Nabiyouni and I. Bakonyi, *J. Electrochem. Soc.*, 2012, **159**, D162-D171.

47. G. C. Hadjipanayis, *J. Magn. Magn. Mater.*, 1999, **200**, 373–391.

48. R. Skomski and J. M. D. Coey, "*Permanent Magnetism*", Institute of Physics, Bristol, 1999.

49. H. B. Eral, D. J. C. M. ’t Mannetje and J. M. Oh, *Colloid Polym. Sci.*, 2013, **291**, 247–260

50. M. V. Panchagnula, S. Vedantam, *Langmuir*, 2007, **23**, 13242–13242.

51. L. Gao and T. J. McCarthy, *Langmuir*, 2007, **23**, 3762–3765.

52. L. Gao and T. J. Mccarthy, *Langmuir*, 2007, **23**, 13243–13243.

53. F. Guo, X. Su, G. Hou and P. Li, *Appl. Surf. Sci.*, 2012, **258**, 4906–4910.

54. J. Liang, D. Li, D. Wang, K. Li, and L. Chen, *Appl. Surf. Sci.*, 2014, **293**, 265–270.

55. D. Quéré, *Rep. Prog. Phys.*, 2005, **68**, 2495–2532.

56. L. Zhao, Q. Liu, R. Gao, J. Wang, W. Yang and L. Liu, *Corros. Sci.*, 2014, **80**, 177–183.

57. T. Kako, A. Nakajima, H. Irie, Z. Kato, K. Uematsu, T. Watanabe and K. Hashimoto, *J. Mater. Sci.*, 2004, **39**, 547–555.

58. J. Zhang and S. Seeger, *Adv. Funct. Mater.*, 2011, **21**, 4699–4704.

59. C. H. Choi and C. J. Kim, *Phys. Rev. Lett.,* 2006, **96**, 066001–066004.

60. M. Wang, L. Chen and L Sun, *Energy Environ. Sci.*, 2012, **5**, 6763-6778.

61. S. H. Ahn, H. Park, I. Choi, S. J. Yoo, S. J. Hwang, H. Kim, E. Cho, C. W. Yoon, H. Park, H. Son, J. M. Hernandez, S. W. Nam, T. Lim, S. Kim and J. H. Jang, *Int. J. Hydrogen Energy*, 2013, **38**, 13493–13501.

62. R. Solmaz, A. Döner and G. Kardaş, *Int. J. Hydrogen Energy*, 2009, **34**, 2089–2094.

63. F. Bonet, S. Grugeon, L. Dupont, R. Herrera Urbina, C. Guéry and J. M. Tarascon, *J. Solid State Chem.*, 2003, **172**, 111–115.

64. R. Solmaz, A. Döner and G. Kardaş, *Electrochem. Commun.*, 2008, **10**, 1909–1911.

65. F. Rosalbino, G. Scavino and M. Actis Grande, *J. Electroanal. Chem*., 2013, **694**, 114–121.

66. M. M. Jaksic, *Int. J. Hydrogen Energy*, 1987, **12**, 727–752.

67. J. Greeley and M. Mavrikakis, *Nature Mater.*, 2004, **3**, 810–815.

68. Y. Xu, Y. Yuan, A. Ma, X. Wu, Y. Liu and B. Zhang, *Chemphyschem*, 2012, **13**, 2601–2609.

Table of contents graphic

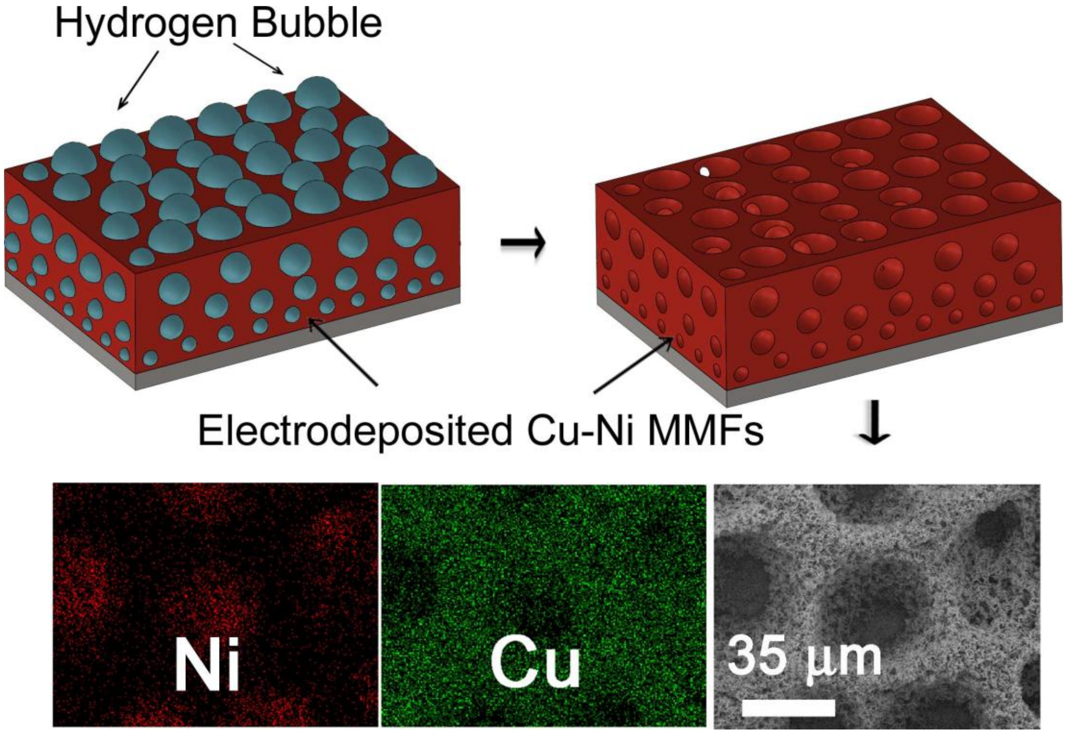

3.2 Room temperature synthesis of three-dimensional porous ZnO@CuNi hybrid magnetic layers with photoluminescent and photocatalytic properties

In this article a novel synthetic approach to prepare three-dimensional (3D) porous ZnO@CuNi hybrid films at room temperature, without need of any heat treatment, is presented. The synthetic procedure consists of a few steps. First, CuNi foams with two different compositions are prepared by electrodeposition. In parallel, ZnO nanoparticles are prepared by sol-gel method. Then, a dispersion containing the ZnO nanoparticles is deposited drop-wise onto the CuNi porous films. Such nanoparticles impregnate the interior of the CuNi pores, forming a smooth continuous shell, as the solvent is left to evaporate. In this way, truly 3D porous ZnO@CuNi composite films are obtained.

The obtained composite materials exhibit an interesting combination of ferromagnetic, photoluminescent and photocatalytic properties, stemming from the different constituent phases assembled in a core-shell fashion. The multifunctional character of this hybrid porous material is possible for several reasons: (i) although the pristine CuNi alloys are rich in Cu and should not be therefore ferromagnetic since the overall Ni content is below 70 at%, phase separation into Cu-rich and Ni-rich phases (the latter being ferromagnetic) occurs during electrodeposition in acidic pH; (ii) the possibility to fill/coat the metallic parent template with ZnO at room temperature (with no need of an annealing treatment) allows preserving the inherent macroporosity of the pristine CuNi films (i.e., thermally-induced collapse of the porous structure is precluded), thus rendering films with a high surface-area-to-volume ratio; (iii) no oxidation of the porous CuNi films takes place during the room-temperature impregnation step (i.e., no loss of magnetization occurs with respect to the pristine CuNi).

A photoluminescent signal appears across the entire thickness of the porous layer. It is slightly more intense at 30 µm depth and decays at higher depth (i. e. at the region closer to the substrate surface). These results indicate that ZnO penetrates into the entire CuNi network. The as-prepared ZnO@CuNi hybrid porous layers show some activity towards the aqueous degradation of Rhodamine B under the UV-Vis light irradiation. After being irradiated for 3h, no apparent detachment of the ZnO nanoparticles from the CuNi substrate is observed. The solution becomes transparent and no considerable worsening of the morphology occurs. Moreover, the procedure can be easily extrapolated to other systems, thus paving the way for the preparation of novel hybrid materials for multifunctional solid-state devices.

Room Temperature Synthesis of Three-Dimensional Porous ZnO@CuNi Hybrid Magnetic Layers with Photoluminescent and Photocatalytic Properties

Miguel Guerrero[a]**‡*, *Jin Zhang*[a‡]*, Ainhoa Altube*[b]*, Eva García-Lecina*[b]*, Mònica Roldan*[c]*, Maria Dolors Baró*[a]*, Eva Pellicer*[a]** and Jordi Sort*[d]

[a]Departament de Física, Facultat de Ciències, Universitat Autònoma de Barcelona, E-08193 Bellaterra, Spain.

[b]Surfaces Division, IK4-CIDETEC, Paseo Miramón, 196, E-20009 San Sebastián, Spain.

[c]Servei de Microscòpia, Universitat Autònoma de Barcelona, E-08193 Bellaterra, Spain.

[d]Institució Catalana de Recerca i Estudis Avançats (ICREA) and Departament de Física, Universitat Autònoma de Barcelona, E-08193 Bellaterra, Spain.

†*These authors have equally contributed to this work*

*To whom correspondence should be addressed:

Dr. Eva Pellicer; Dr. Miguel Guerrero

Email: Miguel.Guerrero@uab.cat; Eva.Pellicer@uab.cat

Abstract

A facile synthetic approach to prepare porous ZnO@CuNi hybrid films is presented. Initially, magnetic CuNi porous layers (consisting of phase separated CuNi alloys) are successfully grown by electrodeposition at different current densities using H_2 bubbles as a dynamic template to generate the porosity. The porous CuNi alloys serve as parent scaffolds to be subsequently filled with a solution containing ZnO nanoparticles previously synthesized by sol-gel. The dispersed nanoparticles are deposited dropwise onto the CuNi frameworks and the solvent is left to evaporate while the nanoparticles impregnate the interior of the pores, rendering ZnO-coated CuNi 3D porous structures. No thermal annealing is required to obtain the porous films. The synthesized hybrid porous layers exhibit an interesting combination of tunable ferromagnetic and photoluminescent properties. In addition, the aqueous photocatalytic activity of the composite is studied under UV–visible light irradiation for the degradation of Rhodamine B. The proposed method represents a fast and inexpensive approach towards the implementation of devices based on metal-semiconductor porous systems, avoiding the use of post-synthesis heat treatment steps which could cause deleterious oxidation of the metallic counterpart, as well as collapse of the porous structure and loss of the ferromagnetic properties.

1. Introduction

The advances in the synthetic pathways to produce porous semiconducting materials (PSM) with controllable pore size and composition have boosted a wealth of applications in a number of different fields such as solar fuel production,[1] gas-sensing,[2,3] or environmental healing,[4,5] where materials with a high surface area are essential. Different PSM architectures including particles, rods, wires and films (the latter with porosity ranging from the macro- to the nanoscale) have been engineered in the last years.[6] Depending on the end application, PSMs have been manufactured either alone or in combination with other materials.

In general, the ability to use three-dimensional (3D) porous scaffolds as parent templates to be filled or coated with second phase materials (e.g., oxide semiconductors) has been shown to trigger new functionalities stemming from the synergy created between the host and the guest (or the matrix and the filler) components.[7] For example, in the case of metal-oxide ceramic composites, one can take advantage of the large hardness of the ceramic counterpart and the high ductility of the metal to design microstructures with optimized mechanical performance.[8,9] Magnetic exchange-interactions in certain metal-oxide nanocomposites have also triggered interesting applications in the field of nanomagnetism, as a means to enhance the coercivity of the resulting material.[10]

One of the main challenges to produce hybrid composite materials using polymeric or metallic porous scaffolds as templates, particularly when the second phase is intended to be an oxide, is that a high-temperature heat-treatment, often in the presence of an O_2-containing atmosphere, is required.[11] Such treatment can cause carburization of the polymer or oxidation of the parent metallic template, and can eventually provoke the collapse of the porous network. These issues need to be tackled when growing a metal oxide as the second phase by atomic layer deposition or colloidal templating (which typically involves subsequent heat-treatment in air).[11] Thus, new methodologies to fill or coat porous templates with suitable second-phase materials at temperatures close to room temperature are highly needed.

Zinc oxide (ZnO), one of the most important n-type II-VI semiconductor materials with a wide band gap of 3.2 eV, possesses unique electrical and optical properties including good transparency, high electron mobility, and strong room-temperature luminescence.[12] Therefore, ZnO has recently attracted enormous attention due to its potential applications in integrated optoelectronics and laser technology[13] or photocatalysis.[14,15] Additionally, the piezo/pyroelectric properties of ZnO make it a smart candidate for sensors and other types of micro/nano-electromechanical systems (MEMS/NEMS).[16,17] There are several synthetic techniques for the growth of ZnO-based materials. These include vapor deposition,[18] hydrothermal synthesis,[19] sol-gel method,[20] or mechanochemical approach.[21] Depending on the deposition process conditions, different structural, electrical and optical properties are obtained. Pulsed laser deposition,[22] chemical vapor deposition[23] or spray pyrolysis[24] can be used to prepare dense ZnO immobilized films. The synthesis of porous ZnO films is typically more challenging. Dip-coating methods are receiving attention since they enable the low-cost deposition of ZnO films, eventually in porous form.[25,26] Other approaches to synthesize porous metal oxide films on a substrate include spin-coating of sol-gel[27], template-assisted electrostatic spray deposition[28], and hydrothermal methods.[29] Both dip-coating and spin-coating of sol-gel mixtures show significant limitations when they are faced with large substrates and/or substrates with micrometer-sized feature. Moreover, film thickness typically achieved in a single coating step is in the range of about 100-400 nm depending on coating conditions, whereas a film thicker than 1 µm can be obtained only by repeated coating/calcinations cycles.[28] For the precise control of the film thickness, pore size and porosity degree, the use of pre-fabricated polymeric or metallic porous templates is often preferred. Nevertheless, in most cases, one or more post-synthesis heat treatment steps at temperatures ranging from 250°C to 900°C are necessary to convert the solution precursors into ZnO.[30,31] As aforementioned, this can be a serious shortcoming when the porous scaffold is not intended to be eliminated but to remain unaffected (and hence keep the initial features like the composition, overall porosity and physical properties) after the heat treatment.

In this work, a novel approach to coat the interior of the pores of a CuNi 3D porous film scaffold with a ZnO shell at room temperature is presented. CuNi films are obtained by hydrogen-bubble assisted electrodeposition, which has proven to be a convenient technique to produce networked macroporous films of some compositions.[32] The Cu/Ni ratio is adjusted in order to deliver room-temperature ferromagnetic properties, which are not typically available in single-phase semiconductor materials. Thus, the obtained hybrid porous composites maintain the magnetic properties of the CuNi foams while exhibiting new functionalities (e.g. photoluminescence, photocatalytic activity) stemming from the presence of the ZnO semiconducting second phase. In particular, the aqueous photocatalytic activity of this composite system under UV-visible light irradiation for the degradation of Rhodamine B (RhB) is demonstrated. The multifunctional character of this composite material is possible because (i) the macro-porosity of the initial CuNi alloy foam is preserved and (ii) oxidation of the CuNi parent template is also avoided because of the low temperature used in all the synthetic steps.

2. Experimental section

2.1 Synthesis of the CuNi metallic foams

Two-phase CuNi metallic foams (MF) were successfully obtained by electrodeposition at different current densities on Ti/Si/Au substrates using H_2 as a dynamic template (Figure 1a and 1b). All chemicals were of analytical grade and were used as received without further purification. Electrolyte solution was prepared from ultrapure water. Si/Ti (25 nm)/Au (125 nm) substrates (working area of 0.25 cm^2) were employed as cathodes. Given the low roughness of the Au surface, surface conditioning (e.g. polishing) was not required. All depositions were carried out in a single-compartment, double-jacketed glass electrochemical cell. A platinum sheet served as the counter electrode, and a double junction Ag|AgCl 3 M KCl electrode (E = +0.210 V versus standard hydrogen electrode (SHE)) was utilized as the reference electrode. For CuNi MF electrodeposition, a constant current density of -1 A cm^{-2} and 300 s ($Cu_{80}Ni_{20}$) or -3 A cm^{-2} and 100 s ($Cu_{65}Ni_{35}$) was applied by using a PGSTAT302N Autolab potentiostat/ galvanostat (Ecochemie, Utrecht, Netherlands). The deposition charge for the growth of CuNi MFs was kept constant in order to achieve a similar thickness (ca. 60 µm). The electrolyte consisted of $CuSO_4{\cdot}5H_2O$ (0.01 M), $NiSO_4{\cdot}6H_2O$ (0.15 M), H_2SO_4 (1 M), CH_3COOH (0.1 M), HCl (50 mM), and sodium citrate tribasic dehydrate (0.2 M). All deposition processes were carried out at 25 °C and under stirring (800 rpm) using a magnetic stirrer bar.

2.2 Synthesis of the ZnO nanoparticles

Into a flask containing 20 mL of methanol were added 0.090 g of zinc acetate ($[Zn(CH_3COO)_2]{\cdot}2H_2O$ Aldrich, 98%) and 25 µL of deionized water. The solution was heated to 60 °C under magnetic stirring. Later, a solution of 0.050 g of potassium hydroxide (KOH, Aldrich, 85%) and 20 mL of methanol heated to 60 °C was dropwise added to the zinc solution. During this step, ZnO nanoparticles (NPs) were formed by sol-gel (ZnO NPs mean size = 7.3 nm). When the reaction was finished (24 h), the upper fraction of the reaction solution was withdrawn. Next, 40 mL of methanol were added to the solution and stirred for 15 min. Again, the upper fraction of the solution was discarded after 15 min. The methanol washing process was repeated twice. The isolated ZnO NPs were suspended in 40 mL of methanol, leading to a concentration of ca. 0.83 g ZnO L^{-1}.

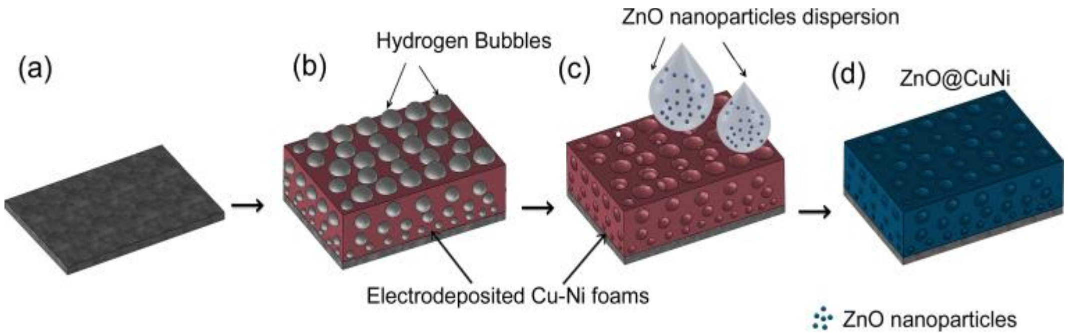

Figure 1. Schematic flow of the synthesis of the ZnO@CuNi hybrid porous layers. From (a) to (b) hydrogen bubble-assisted electrodeposition of porous CuNi MF and from (c) to (d) impregnation of the CuNi scaffold with ZnO NPs suspension.

2.3 Synthesis of the hybrid ZnO@CuNi porous film

As shown in Figure 1(c) and 1(d), 15 µL of the previously synthesized ZnO NPs suspension were dropwise added onto the surface of the CuNi MF. Next, the impregnated CuNi MF was placed inside a vacuum desiccator (0.5 mbar) for 120 s at room temperature. The impregnation process was consecutively repeated 6 times to yield ZnO@CuNi porous films with increasingly higher ZnO coverage. Samples were investigated after three and six consecutive impregnations (*middle* and *final* coverage, respectively). Samples were done in triplicate in order to ensure reproducible results.

2.4 Morphological and structural characterization

The morphology and structure of the porous films were studied by field emission scanning electron microscopy (FE-SEM), high resolution transmission electron microscopy (HRTEM) and X-ray diffraction (XRD). HRTEM characterisation was carried out on a JEOL JEM-2011 microscope operated at 200 kV. For HRTEM observations, a portion of the film was scratched off with a metallic spatula and the powder released was dispersed in ethanol. The dispersion was then sonicated on a SELECTA Ultrasounds 230 V – 40 kHz apparatus (JP Selecta, Barcelona, Spain) for 10 s in order to break up big aggregates. Afterwards, one or two drops of the suspension were placed dropwise onto a holey carbon-coated Cu TEM grid. The chemical composition of the films was determined by energy dispersive X-ray spectroscopy (EDX). The stoichiometry of the Cu-Ni MFs is given in at%. XRD patterns were recorded on a Philips X'Pert diffractometer (Panalytical, Madrid, Spain) using the Cu K_{α} radiation, in the 20°-90° 2ϑ range (0.03° step size, 8 s holding time). A full-pattern fitting procedure (Rietveld method, MAUD software)[33] was used to extract microstructural parameters from the XRD patterns.

2.5 Magnetic characterization

Room temperature hysteresis loops were collected at room temperature using a vibrating sample magnetometer (VSM) from Oxford Instruments (Abingdon), with a maximum applied magnetic field of 0.3 T. The field was applied parallel to the film plane.

2.6 Confocal imaging

The photoluminescence (PL) properties of the films were studied by confocal scanning laser microscopy (CSLM). The samples were mounted on Ibidi culture dishes (Ibidi GmbH, Martinsried, Germany). For 3D analysis, the samples were visualized with a TCS-SP5 CSLM microscope (Leica Microsystems CMS GmbH Mannheim, Germany) using a Plan Apochromat 10x / 0.4 (dry) objective. The ZnO@CuNi nanocomposites were excited with a blue diode laser (405 nm) and the autofluorescence was detected in the 420-580 nm range. Because the CuNi MF matrices are non-fluorescent, they were imaged using reflected light mode from an argon laser (488 nm) and subsequently detected in the 480-495 nm range. Stacks of 50 sections were collected at every 3 µm along the material's thickness. The three-dimensional images were processed by using Surpass Module in Imaris X64 v. 6.2.0 software (Bitplane; Zürich, Switzerland).

The emission signal of the specimens was excited at 405 nm with a blue diode laser, and its fluorescence intensity was recorded generating a lambda stack (69 images) with emission wavelength ranging from 425 to 750 nm, at 10 nm intervals. A set of 10 regions of interest (ROIs) of 400 μm^2 each was used to analyze the mean fluorescence intensity (MFI) of the samples in relation to emission wavelength. For each ROI, a graph plotting mean pixel intensity and emission wavelength of the lambda stack was generated.

Finally, photostability experiments were performed to monitor long time-lapse experiments. A defined region of interest (ROI: 620 µm x 620 µm) was photo-bleached at full laser power of 50 mW of blue diode 405 nm (100% power, 100% transmission). Fluorescence signal was detected in the range from 420 nm to 580 nm. Confocal time series were recorded with intervals of 1 frame / 850 ms for a period of 10 min. Data from all studies was analyzed using the LAS AF software 2.4.1 (Leica Microsystems) obtaining the variation of the MFI (normalized fluorescence values) as a function of irradiation time.

2.7 Evaluation of photocatalytic activity

The photocatalytic activity of the uncoated CuNi and hybrid ZnO@CuNi porous layers was evaluated by decolorization of a 5 ppm RhB aqueous solution (Alfa Aesar, Germany, 98%, without further treatment). The solutions were prepared by introducing the layers to be tested in 10 mL of the RhB solution. For each experiment, a blank RhB solution was used as a control and reference test. The reaction cells were placed in a SwiftCure IB irradiation cabin (Peschl Ultraviolet GmbH from Mainz, Germany) equipped with a mercury lamp. Cut-off filters were used to limit the wavelength radiation and to avoid direct photolysis of the dye (ISO 10678:2010 standard). The average light intensity used was 220 W and the wavelength ranged from 320 to 500 nm. The photocatalytic experiments were conducted under continuous magnetic stirring at a constant temperature of 29 °C.

After conditioning the suspensions for 60 min in dark to reach adsorption-desorption equilibrium, the light was turned on to initiate the reaction. Experiments were then carried out under ultraviolet-visible (UV-vis) irradiation for an overall time of 180 min. The red color of the solution faded gradually with time due to the decomposition of RhB. Aliquots (4 mL) were withdrawn regularly (at 0, 15, 30, 60, 120, and 180 min) from the reaction. The supernatant solutions were then tested with a UV-vis spectrophotometer (Shimadzu UV-1603, Shimadzu Corporation, Kyoto, Japan) by measuring absorption spectra of RhB (λ= 554 nm) as a function of the irradiation time. Following the measurement, the aliquot was immediately retured to the reaction vessel to continue the reaction. Thus, the final volume marginally decreased (approximately 5%). Photocatalytic activity of the catalysts was calculated as (C/C_o), where C_o is the concentration of the test solution of RhB before irradiation and C is the concentration of RhB after UV-vis irradiation.

3. Results and Discussion

3.1 Morphological and structural characteristics of the porous layers

XRD analyses were carried out to investigate the crystallographic structure of the prepared films. XRD patterns in the 30-60° 2ϑ range of $Cu_{65}Ni_{35}$ (fabricated with j = -3 A cm^{-2}) and $Cu_{80}Ni_{20}$ (fabricated with j = -1 A cm^{-2}) samples before the ZnO deposition are shown in Figure 2. All the samples show four diffraction peaks corresponding to Cu/Ni (111) and Cu/Ni (200) reflections (# and ×, respectively), proving the occurrence of two face-centered cubic (fcc) structures, one enriched in Cu and the other in Ni. The occurrence of two-phase CuNi films was anticipated considering the electrodeposition conditions. Namely, in order to favour intensive hydrogen co-evolution during electrodeposition, a highly acidic electrolyte was employed. In these conditions, citrate has negligible complexing capacity because it exists mostly in its protonated form. As a result, the co-deposition of Cu and Ni cations (and hence, the formation of a solid solution) is severely hindered, which results in heterogeneous nucleation (and hence, the occurrence of phase-separated deposits). From the magnetic viewpoint, formation of phase-separated CuNi films is desirable since room-temperature ferromagnetic properties are then accessible for almost any Ni content. If a single-phase alloy were formed, the ferromagnetic behaviour would hold only for Ni percentages above 70 at%. Below this value, alloy layers would be paramagnetic.[34] The average crystallite size of the CuNi parent templates, determined using the MAUD software, ranges between 10 nm and 13 nm for both Cu-rich and Ni-rich phases. By applying the Bragg's and Vegard's laws on the (111) reflection, the amount of the Cu- and the Ni-rich phases was estimated to be 85 at% and 15 at%, respectively, for the $Cu_{80}Ni_{20}$ film, and 73 at% and 27 at%, respectively, for the $Cu_{65}Ni_{35}$ film. The precise stoichiometry of the Cu-rich and Ni-rich phases is given in the Supporting Information (Table S1). The XRD patterns of the hybrid ZnO@CuNi porous layers show, apart from the reflections coming from the metallic Cu-Ni, three additional diffraction peaks at 31.81°, 47.60°, and 56.69°, corresponding to (100), (102) and (110) crystalline planes, respectively, of ZnO in its wurtzite hexagonal phase (JCPDS 36-1451). These peaks are considerably broader, evidencing the nanocrystalline nature of the ZnO coating. Its crystallite size is around 7 nm, as estimated from the Rietveld refinements. Notice that the structural properties of the porous CuNi templates do not become altered after the coating with ZnO, as expected from the room temperature conditions used for ZnO deposition onto CuNi MF.

The evolution of surface morphology from the pristine CuNi MF film upon ZnO impregnation was studied by FE-SEM at different magnifications. As an example, representative FE-SEM images of the uncoated $Cu_{80}Ni_{20}$ MF and the corresponding film after being coated with ZnO (three and six impregnation steps or, in other words, *middle* and *final* coverages) are shown in Figure 3. At low magnification, a uniform distribution of 3D interconnected spherical pores of around 50 µm in diameter, was observed over the entire surface of the uncoated MF (Figure 3(a)). In close-up observations, the pore walls (about 20 µm in thickness) were found to be inherently porous (they are built up from numerous nanodendrites, see Figure S1), hence displaying a hierarchical porosity. The size of the 50 µm macropores directly correlates with the size of the H_2 bubbles. In the present work, acetic acid was added to the bath to prevent from bubble coalescence and, hence, formation of bigger pores. Instead, the porosity of the walls is likely due to the fast deposition rate. CuNi grains cannot stack in a dense manner (as would occur under lower deposition rates) and dendrites are formed. Due to the fractal architecture of such dendrites, numerous 'nano' voids are generated during growth.

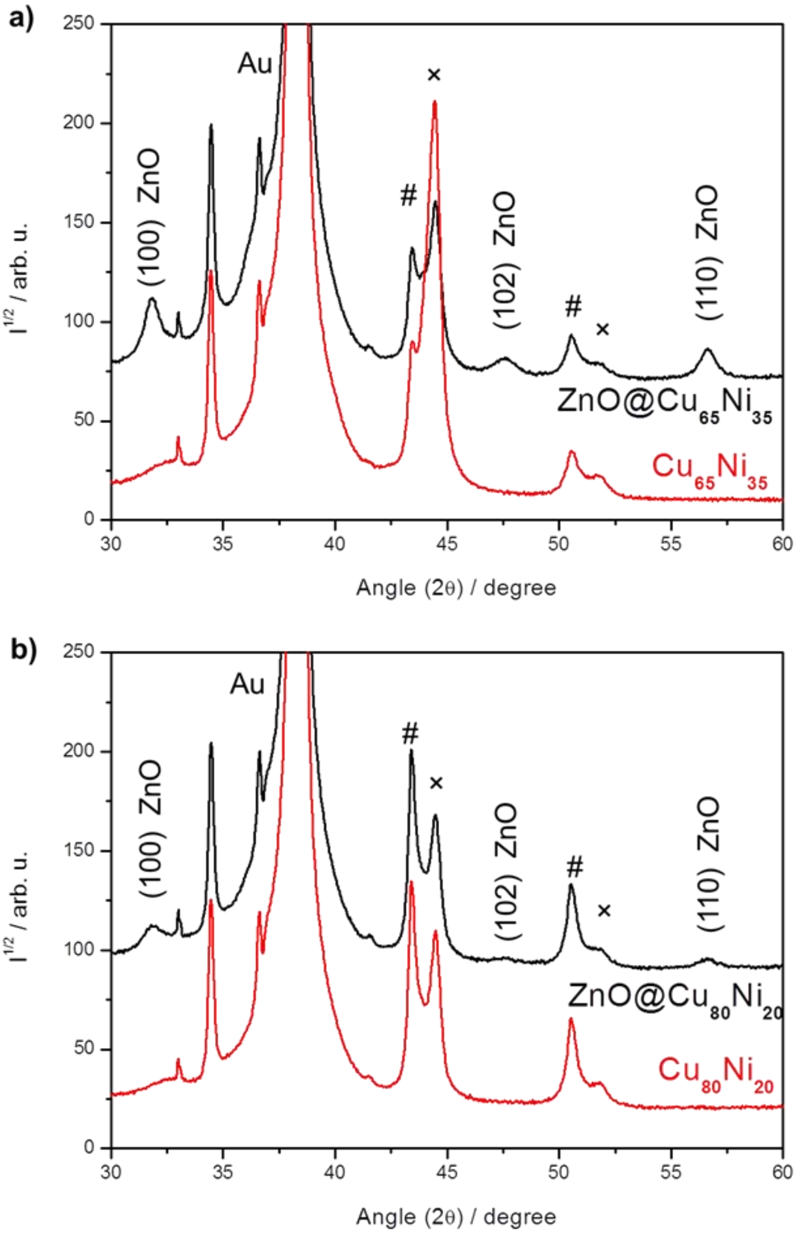

Figure 2. XRD of (a) $Cu_{65}Ni_{35}$ (red) and $ZnO@Cu_{65}Ni_{35}$ (black) and (b) $Cu_{80}Ni_{20}$ (red) and $ZnO@Cu_{80}Ni_{20}$ (black). Peaks denoted by # and × belong to Cu-rich and Ni-rich phases, respectively. Two diffraction peaks at 33.06° and 34.36° belong to (100) Si and (100) α-Ti crystalline planes, respectively, of the substrate. Abbreviation: au = arbitrary units.

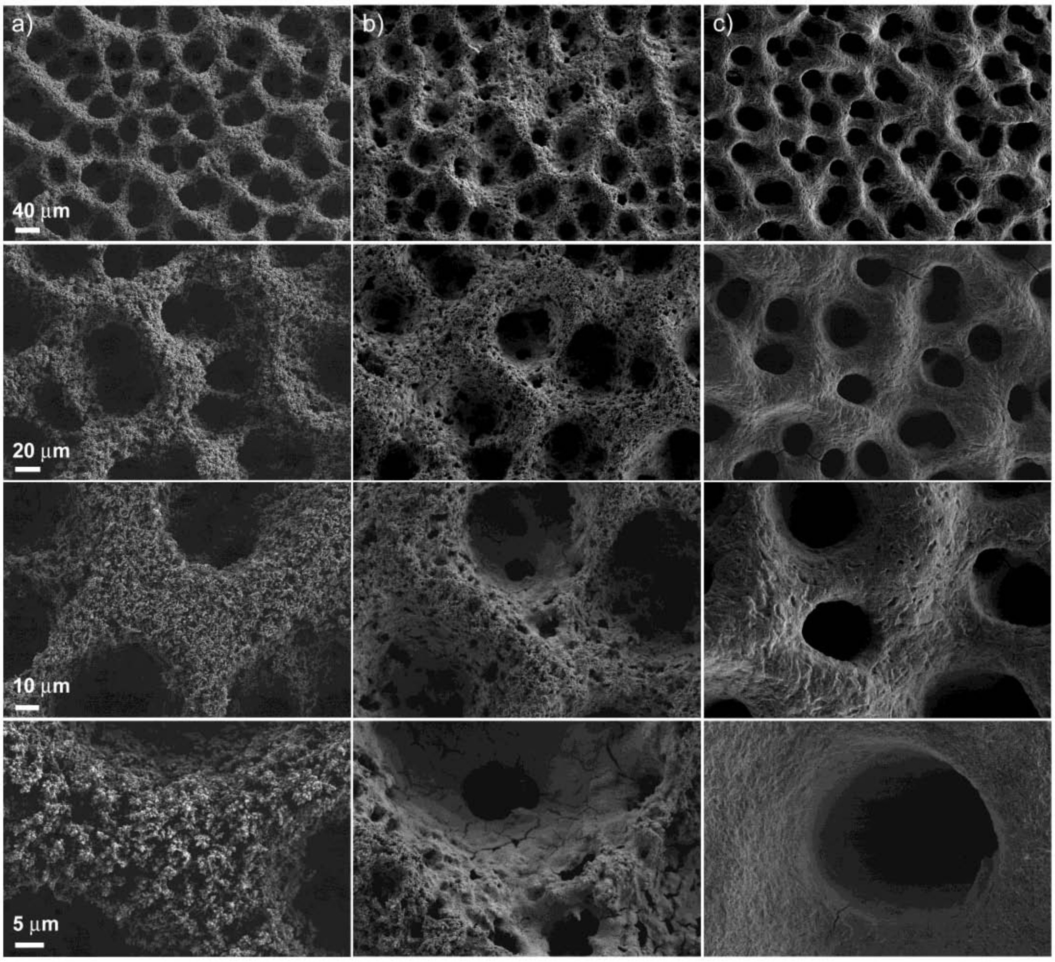

Figure 3. FE-SEM images of (a) the uncoated $Cu_{80}Ni_{20}$ MF and the ZnO-coated $Cu_{80}Ni_{20}$ after (b) three consecutive impregnations (*middle* coverage) and (c) six consecutive impregnations (*final* coverage). In each column different magnifications of the three materials are shown.

Upon ZnO impregnation, the nanodendrites become less apparent and finally are no longer visible (Figures 3(b) and 3(c)). As a result, the pore walls show a smoother appearance. Nonetheless, the macro-porosity is preserved along the coating process. These macropores become smaller in size (from about 50 µm in $Cu_{80}Ni_{20}$ to about 30 µm in $ZnO@Cu_{80}Ni_{20}$) as expected from the increasingly thicker ZnO shell which conformally coats the CuNi network. Representative images of $ZnO@Cu_{65}Ni_{35}$ film are shown in Figure S2. In this case, the ZnO shell is less uniform than for $ZnO@Cu_{80}Ni_{20}$, which is in part due to the less regular morphology of the CuNi foams featuring larger Ni contents.[35] This is because there is strong dependence of the Ni content on the CuNi morphology. Cu deposition typically promotes the formation of a uniform foam-like architecture. With increasing the Ni content, pore interconnectivity worsens. EDX mapping images prove that Zn is well-distributed among the CuNi MF (Figure S3). It is envisaged that the 3D interconnected macroporous structure of the ZnO@CuNi framework could be advantageous for catalytic applications. In particular, an enhanced surface diffusion of the reactant adatoms, ad-ions or molecules through the porous channels and subsequent desorption of the products could positively impact the kinetics of the reaction.

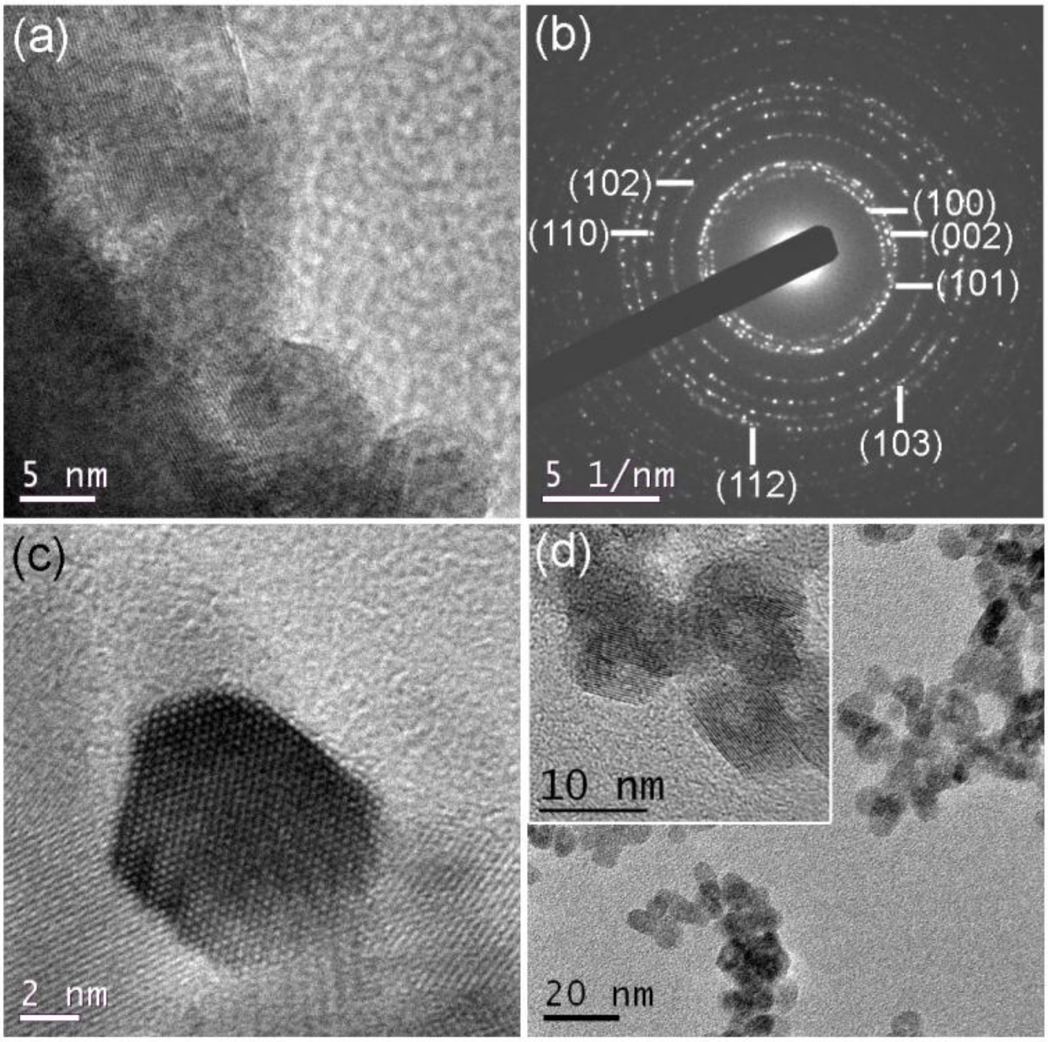

Figure 4. (a) High-Resolution TEM image of ZnO@$Cu_{80}Ni_{20}$ hybrid porous layer; (b) the SAED pattern of the ZnO NPs stacked on the CuNi layer. (c) High-Resolution TEM image of an individual ZnO NP. (d) TEM image of as-prepared ZnO nanoparticles. magnified in the inset.

Figure 4 depicts HR-TEM images of the ZnO@$Cu_{80}Ni_{20}$ hybrid porous layer taken at the oxide-metal edge. Figure 4(a) shows that the nanocomposite consists of a rather continuous shell of ZnO NPs well attached to the CuNi MF surface even after sonication of the sample (Figure S4). The selected area electron diffraction (SAED) pattern showed in Figure 4(b) displays spotty rings. Since the spot size was around 200 nm, the beam is actually embracing several small crystals with different orientations. This further confirms the nanocrystalline structure of the ZnO, in agreement with XRD analyses. Furthermore, in a zoomed detail of a single ZnO NP (Figure 4(c)) the lattice planes are sharply defined, thus confirming the high crystallinity of the ZnO in the ZnO@$Cu_{80}Ni_{20}$ nanocomposite. Interestingly, this synthetic methodology preserves the morphology as well as the high crystallinity of the as-prepared ZnO NPs (Figure 4(d)).

3.2 Magnetic properties of the porous layers

Well-defined hysteresis loops corresponding to the $Cu_{80}Ni_{20}$ MFs as well as ZnO@$Cu_{80}Ni_{20}$ are shown in Figure 5(a). It is known that CuNi single-phase alloys are ferromagnetic at room temperature for Ni contents above 70 % at.[34,36] Hence, the occurrence of ferromagnetism in spite of the low Ni content is a further indication that the CuNi MF are not single phase but, instead, Ni-rich clusters (ferromagnetic) co-exist together with a non-ferromagnetic Cu-rich matrix, in agreement with XRD results (Figure 2). To further explore the influence of the Ni content on the magnetic response of the layers, uncoated and ZnO-coated $Cu_{65}Ni_{35}$ films were also investigated. The $Cu_{65}Ni_{35}$ MF and its homologous ZnO@$Cu_{65}Ni_{35}$ porous film (Figure 5(b)) exhibit higher saturation magnetization (M_S) in comparison to $Cu_{80}Ni_{20}$ based films due to the higher Ni content. The hysteresis loops also reveal that the coercivity, H_c, tends to slightly decrease with the increase of the Ni content in the nanocomposites, in agreement with our previous work on uncoated CuNi porous films.[35] Remarkably, for both compositions the presence of the ZnO shell does not alter the magnetic response of the CuNi matrix as M_S remains the same before and after the ZnO coating. This indicates that the metallic character of the pristine CuNi MF is maintained during ZnO impregnation (i.e., no oxidation occurs).

Hence, this synthetic approach can be of high interest in applications where it is necessary to retain the initial magnetic properties of the MF. Since the ZnO coating over the $Cu_{65}Ni_{35}$ MF was defective (Figure S1) or, at least, less conformal than over the $Cu_{80}Ni_{20}$ MF, the latter was selected for the subsequent analysis of the optical and catalytic properties.

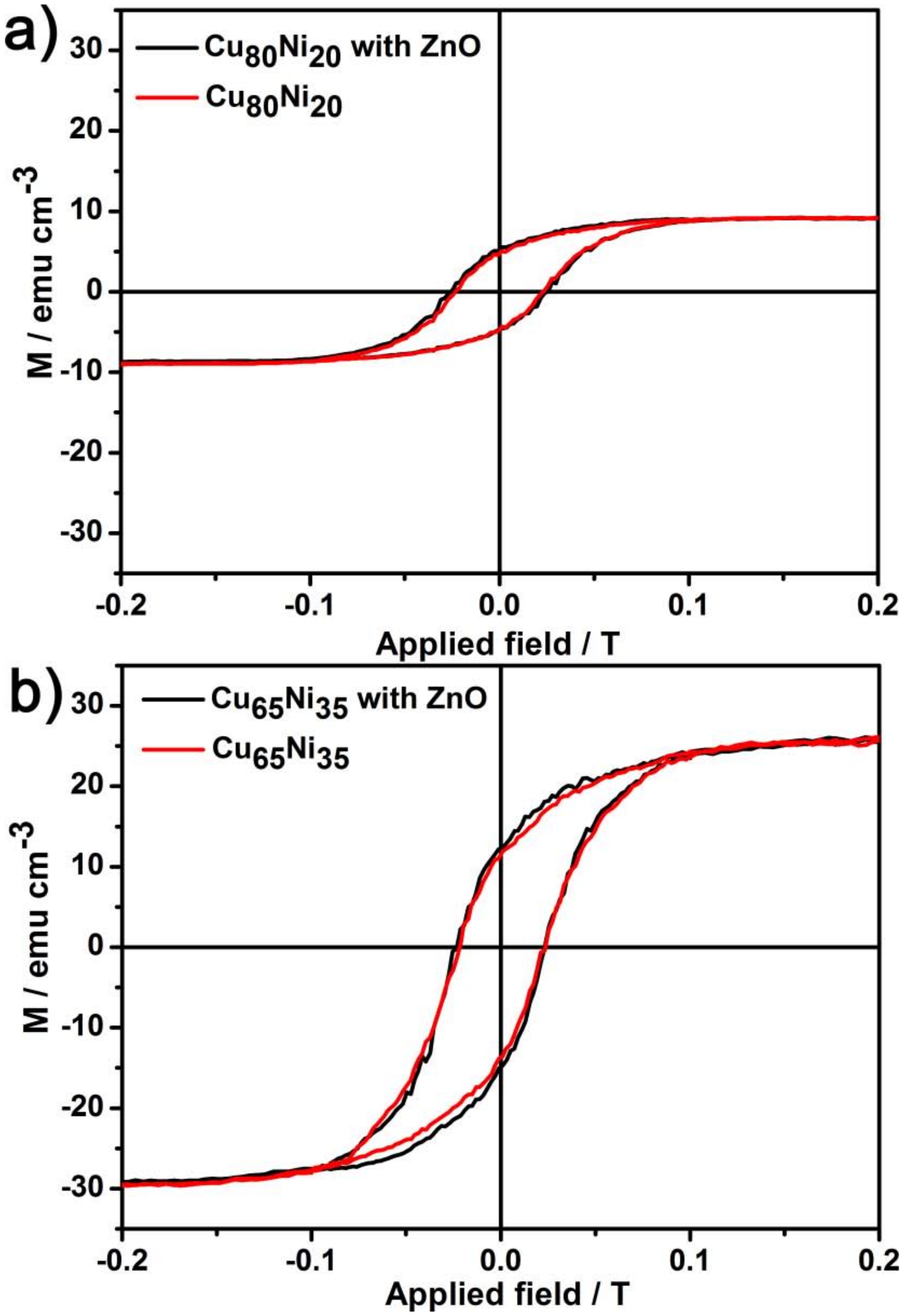

Figure 5. Room temperature hysteresis loops of the (a) $Cu_{80}Ni_{20}$ and $ZnO@Cu_{80}Ni_{20}$ and (b) $Cu_{65}Ni_{35}$ and $ZnO@Cu_{65}Ni_{35}$ samples.

3.3 Optical properties of the hybrid layers

3D image reconstruction and confocal methodologies offer great advantages for studying complex nanocomposites without mechanical distortions, providing valuable 3D information. Figure 6(a) shows the isosurface module of Imaris 3D photoluminescence (3D-PL, green) and structural (reflection mode, gray) image of the porous ZnO@$Cu_{80}Ni_{20}$ porous nanocomposite film. The full dataset was surveyed to determine the range of intensities (gray values) within the volume (0–255; black-white). An isovalue (intensity) was chosen and the software constructed a map of all the chosen values in the volume. After segmentation, isosurfacing produces simplified hollow objects (or 3D surfaces), which are accurate simplified representations of the original shape of segmented structure. This surface model was extremely helpful to study the 3D shape and spatial relationship with different layers of the hybrid nanocomposite. Notice that the green (arising from the ZnO) and the gray (arising from the CuNi) colors indicate a homogeneous distribution of ZnO within the CuNi matrix. Particularly, the PL response (Figure 6(b)) consists of broad-band emission which covers the entire visible range (in the wavelength interval 425-750 nm) and has a maximum of around 595 nm. In general, a broad green fluorescence in ZnO is attributed to oxygen defects.[37] Moreover, the PL signal is recovered across the entire thickness of the porous layer as can be observed in Figure 7. The intrinsic fluorescence follows the distribution of the reflection signal although it is more intense at 30 μm depth. A decay of the signal is observed at a higher depth. Nevertheless, this indicates that the ZnO is not only present at the uttermost CuNi surface but it rather penetrates through the entire CuNi network and reaches the Au surface. Therefore, the obtained materials can be truly regarded as 3D porous composites. Interestingly, contrary to fluorescent dots, where a pronounced decrease in the PL intensity is observed during illumination with UV or visible light (photobleaching),[38] here only a decrease of 15% of PL intensity was observed after irradiation during 10 min (Figure S5). Due to this stability in the PL signal and the relatively large width of the observed PL peak, these novel ZnO@CuNi porous films could be appealing for optoelectronic devices.

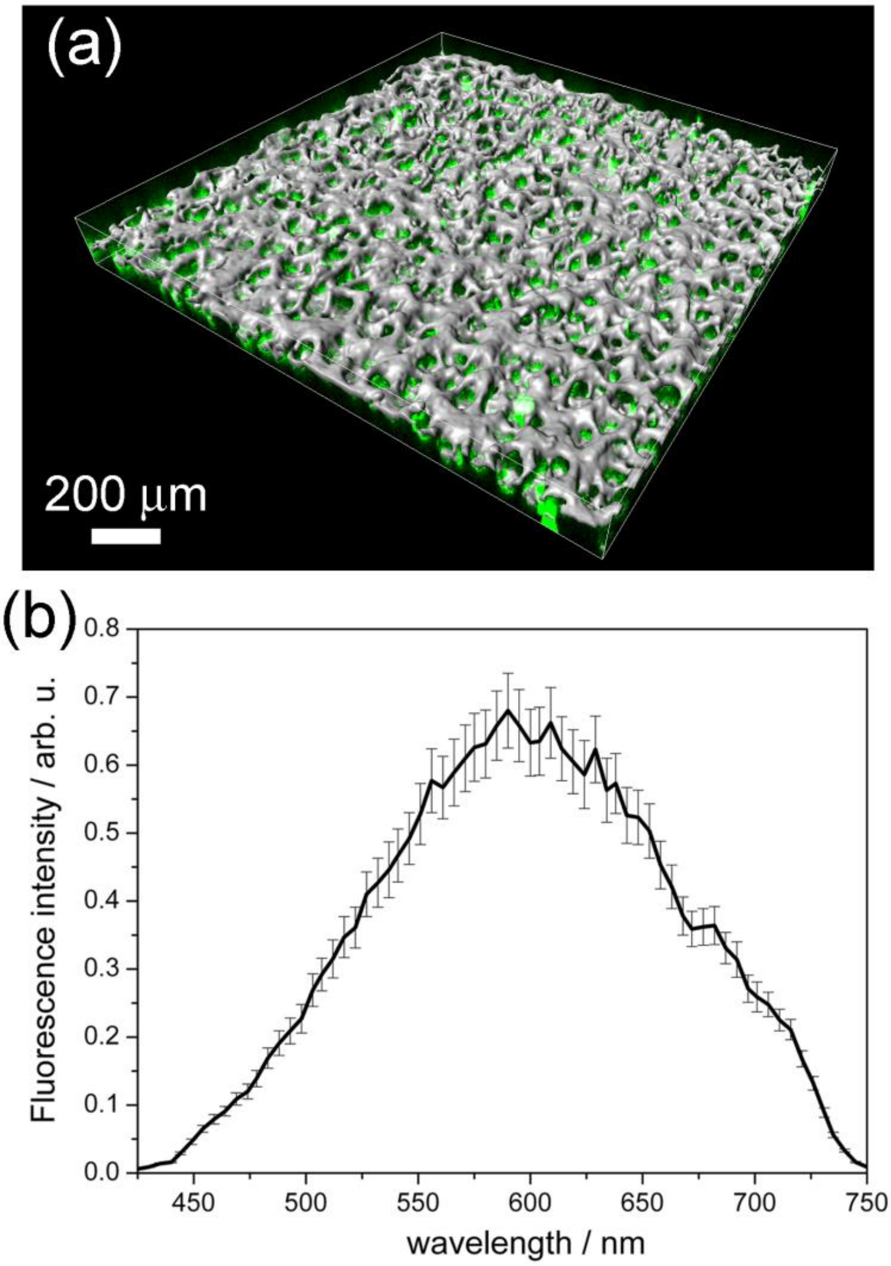

Figure 6. (a) 3D projection images of the hybrid ZnO@$Cu_{80}Ni_{20}$ nanocomposite isosurface view by Imaris v.6.2.0 software. The 3D representation was obtained from a 50-section stack in steps of 3 µm. CuNi MF shows as grey color (reflection mode) whereas the ZnO component shows as green color (fluorescence). (b) Fluorescence spectrum obtained with the Lambda scan module of CSLM using a 5 nm resolution. Abbreviation: au = arbitrary unit.

3.4 Photocatalytic degradation of RhB dye

The photocatalytic performance of the ZnO@$Cu_{80}Ni_{20}$ porous film was evaluated by assessing the degradation rate of RhB under UV-Vis irradiation ($320 < \lambda < 500$ nm) after the adsorption-desorption equilibrium was reached.

As can be observed in Figure 8, the control test without catalysts (blank) under UV-Vis light irradiation showed that the photolysis of RhB is negligible. On the other hand, for the uncoated CuNi MF the concentration of RhB decreased very slightly: only 2% of the original organic matter was degraded after 3 h of exposure time. Regarding the ZnO- coated CuNi, it can be observed that the relative concentration (C/C_0) of RhB dye markedly decreased with the increase of exposition time. The final C/C_0 value was a function of the ZnO amount. The RhB concentration in solution decreases by 10% and 15% after 3 h when ZnO@$Cu_{80}Ni_{20}$ with *middle* and *final* coverages, respectively, were used. As expected, the photoactivity of hybrid porous ZnO@CuNi thin films is higher than that of bare CuNi MF, and it increases with ZnO content. Furthermore, the activity of a ZnO-coated non-porous electroplated CuNi flat dense film is much lower. This puts forward the importance of a large specific surface area for efficient dye removal and suggests that the macropore sidewalls do contribute to the photocatalytic activity. According to the literature,[39] RhB dye degradation mechanism may proceed according to (1-5):

$$\boldsymbol{ZnO + h\nu \rightarrow e^-_{cb} + h^+_{vb}} \qquad (1)$$

$$\boldsymbol{O_2 + e^- \rightarrow\ O_2^{\cdot -} + H^+ \rightarrow HOO^{\cdot}} \qquad (2)$$

$$\boldsymbol{e^- + HOO^{\cdot} +\ H^+ \rightarrow\ H_2O_2} \qquad (3)$$

$$\boldsymbol{H_2O_2 + e^- \rightarrow\ OH^{\cdot} +\ OH^-} \qquad (4)$$

$$\text{RhB+}\ \boldsymbol{O_2/O_2^{\cdot -}/HOO^{\cdot}/OH^-} \rightarrow \text{ mineralized product} \qquad (5)$$

Upon illumination, the generation of electron–hole (e_{cb}^- and h_{vb}^+) pairs between conduction (CB) and valence bands (VB) of ZnO NPs occurs (Equation (1)). The generated e^- are then scavenged by the dissolved O_2 to generate superoxide anion $\boldsymbol{O_2^{\cdot -}}$ (Equation (2)), which, in turn, generate H_2O_2, OH ions and radicals

(Equation (3) and (4)). All the generated reactive species are able to degrade RhB and mineralize it (Equation (5)).

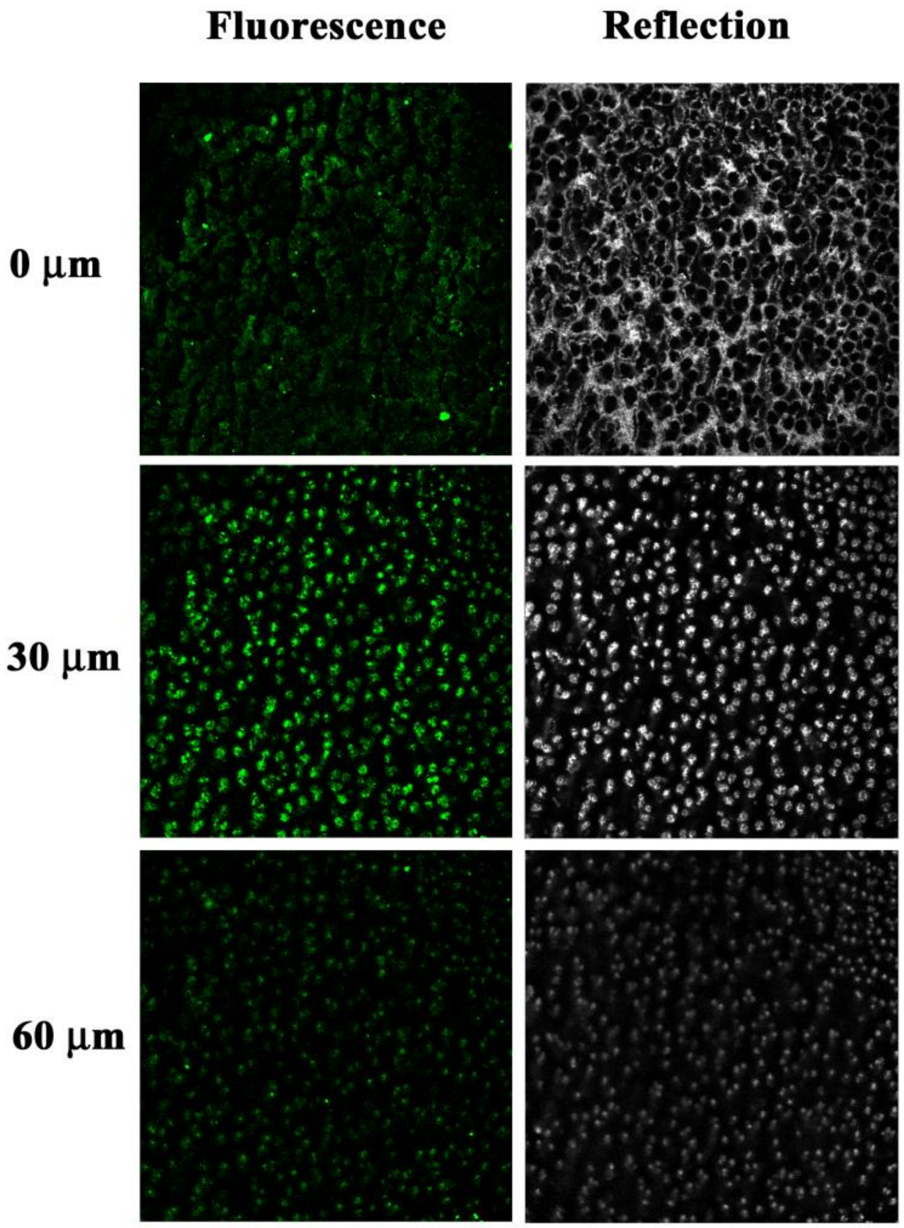

Figure 7. Fluorescence and reflection confocal micrographs (sample area: 621.21 µm x 621.21 µm) of the ZnO@$Cu_{80}Ni_{20}$ hybrid porous layer taken at different sections from the nanocomposite surface up to a total depth of 60 µm. Fluorescence microscopy was employed to visualize ZnO NP (in green). Reflection confocal microscopy was used to visualize the CuNi matrix (in grey).

Previous conditioning under dark conditions for 60 min in the presence of the ZnO@$Cu_{80}Ni_{20}$ did not bring any change in the RhB concentration, indicating that UV-Vis irradiation is indispensable for dye degradation. Upon several consecutive degradation tests under irradiation conditions, a decrease of the photocatalytic efficiency was observed (Figure S6), likely due to gradual deactivation of ZnO caused by the adsorption of species present in solution.[40] No apparent detachment of the ZnO NPs from the CuNi MF was observed though. The solution remained fully transparent (eventual turbidity arising from detached ZnO NPs was not noticed) and SEM images of the CuNi MF after the photocatalytic tests did not disclose appreciable changes in morphology. Compared to the literature dealing with ZnO-based materials, the photocatalytic activity of the here-developed hybrid composites is not particularly high. Different strategies could help improve the photocatalytic performance: through doping of ZnO with suitable cations/anions or by further increasing the specific surface area of the CuNi MF (e.g. via the creation of homogeneously distributed nanopores) and, hence, of the ZnO coating. Moreover, diffusion of the RhB dye through the 3D macroporous network is perhaps not fully efficient. Indeed, taking into account the mean pore diameter (several micrometers), it is expected that a non-negligible fraction of the inner part of the film contributes to the photocatalytic activity. If the pores were much narrower, diffusion of RhB through the pores would have been probably more challenging. Nevertheless, detailed studies are required to evaluate the efficiency of dye diffusion within the 3D network. Although the photocatalytic tests with ZnO-coated non-porous CuNi films do indicate that porosity is definitely beneficial, further work should be done in order to take full advantage of the macroporous architecture of the material. This also includes optimizing the way the material is irradiated so that the inner ZnO shells fully contributed to the catalytic response.

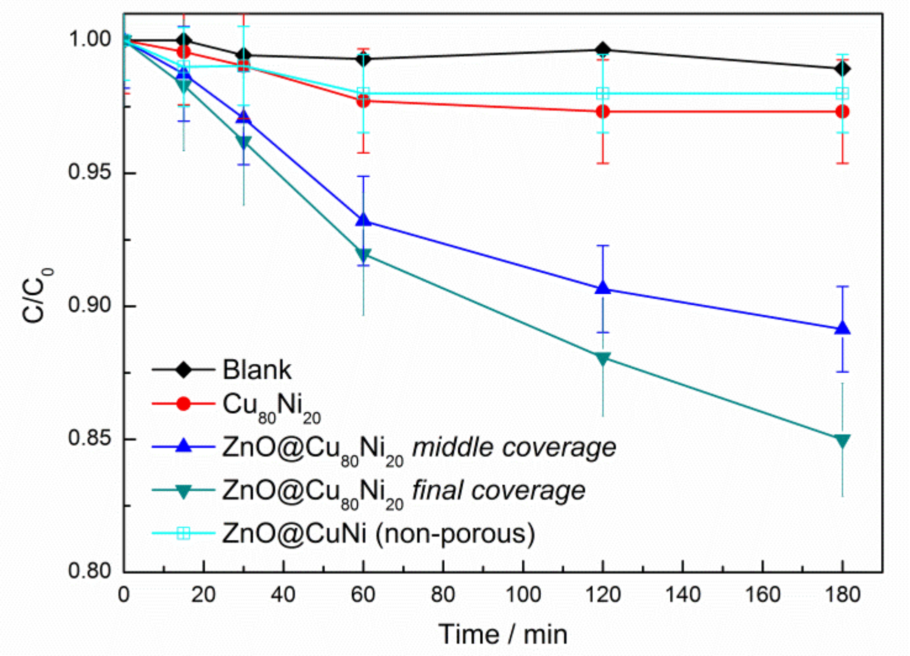

Figure 8. C/C_0 plot of the degradation of RhB in the blank, in the presence of $Cu_{80}Ni_{20}$ MF, and in the presence of $ZnO@Cu_{80}Ni_{20}$ photocatalysts with middle and final coverages. The RhB degradation profile for ZnO-coated non-porous Cu-rich flat layer is also shown for the aim of comparison.

4. Conclusions

In summary, a fast and inexpensive synthetic approach to obtain hybrid porous ZnO@CuNi films has been presented. First, two-phase CuNi porous magnetic films were grown by means of electrodeposition. Then, a suspension containing ZnO nanoparticles was dropwise added onto the CuNi framework, coating not only its outermost external surface but also the inner pores, as revealed by CLSM imaging, hence rendering truly 3D porous ZnO@CuNi hybrid films. This strategy overcomes the problems associated with high temperature post-synthesis heat treatments that can be deleterious from both morphological and compositional viewpoints. Indeed, thanks to the lack of annealing treatments, the inherent macro-porosity of the initial CuNi MFs as well as their ferromagnetic properties are preserved after coating with ZnO. The obtained ZnO@CuNi hybrid porous layers show some activity for the aqueous degradation of Rhodamine B under UV−vis light irradiation. When supported onto substrates, these materials could be handled as classical heterogeneous catalysts. If released from the substrate, the composite films could eventually be wirelessly manipulated using external magnetic fields, whilst being both photoluminescent and photocatalytic upon irradiation under UV-Vis light. This would be possible due to the combination of the various properties of the different phases comprising the hybrid composites. The reported synthetic strategy could also be extrapolated to other types of materials, paving the way for the preparation of hybrid materials in general, suitable for multifunctional solid-state devices.

Acknowledgements

This work has been funded by the Generalitat de Catalunya [project 2014-SGR-1015] and the Spanish Ministerio de Economía y Competitividad (MINECO) [project MAT2014-57960-C3-1-R and MAT2014-57960-C3-3-R]. Partial funding from the European Research Council (Consolidator Grant, project number 648454, SPIN-PORICS) is acknowledged. E. Pellicer is grateful to MINECO for the ‘Ramón y Cajal’ contract (RYC-2012-10839). J. Zhang is grateful to the China Scholarship Council (CSC) for the PhD grant. M. Guerrero acknowledges the support of the Secretary for Universities and Research of the Government of Catalonia and the COFUND Programme of the Marie Curie Actions of the 7th R&D Framework Programme of the European Union for the ‘Beatriu de Pinos’ contract (2013 BP-B 00077).

Supporting information

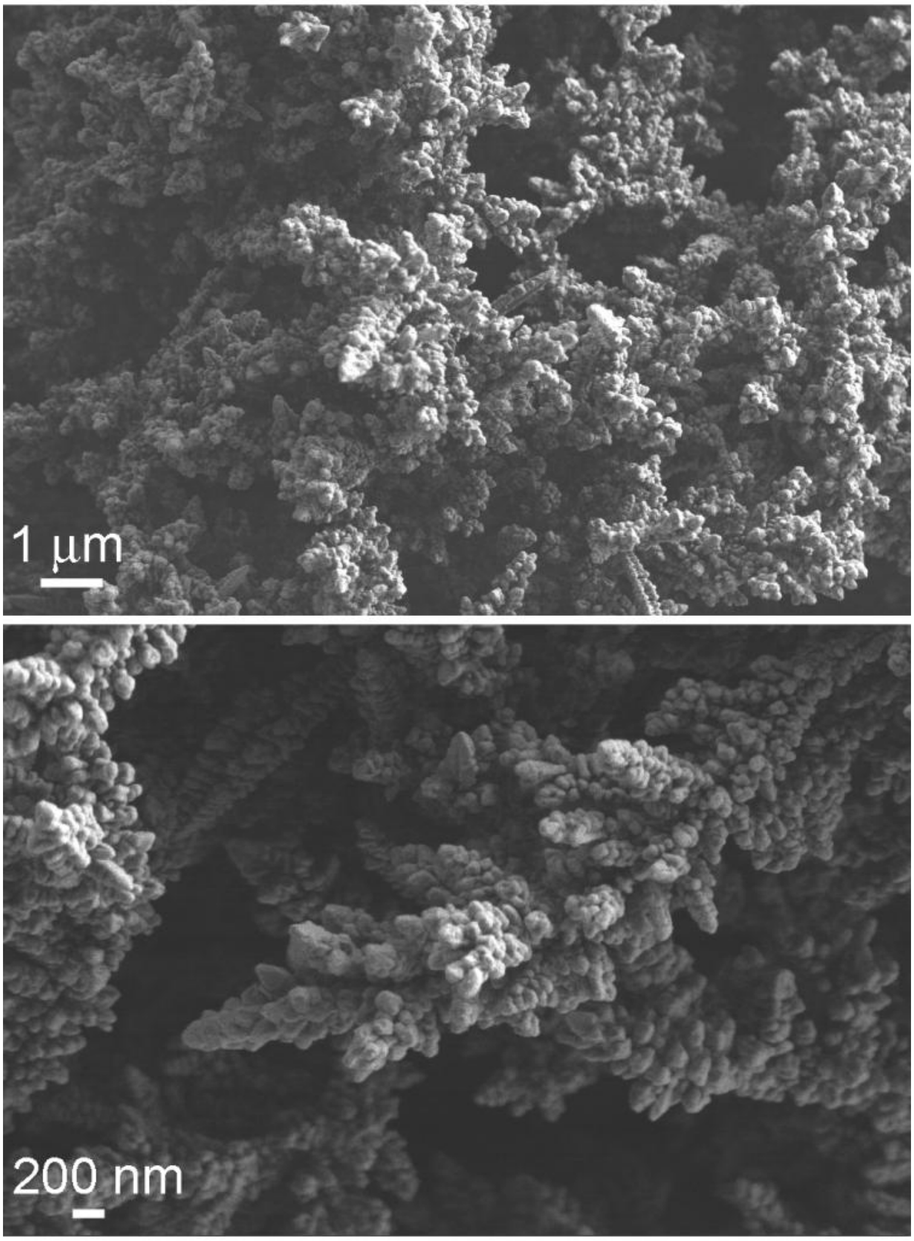

Figure S1. SEM images of the $Cu_{80}Ni_{20}$ walls showing the dendritic-like morphology.

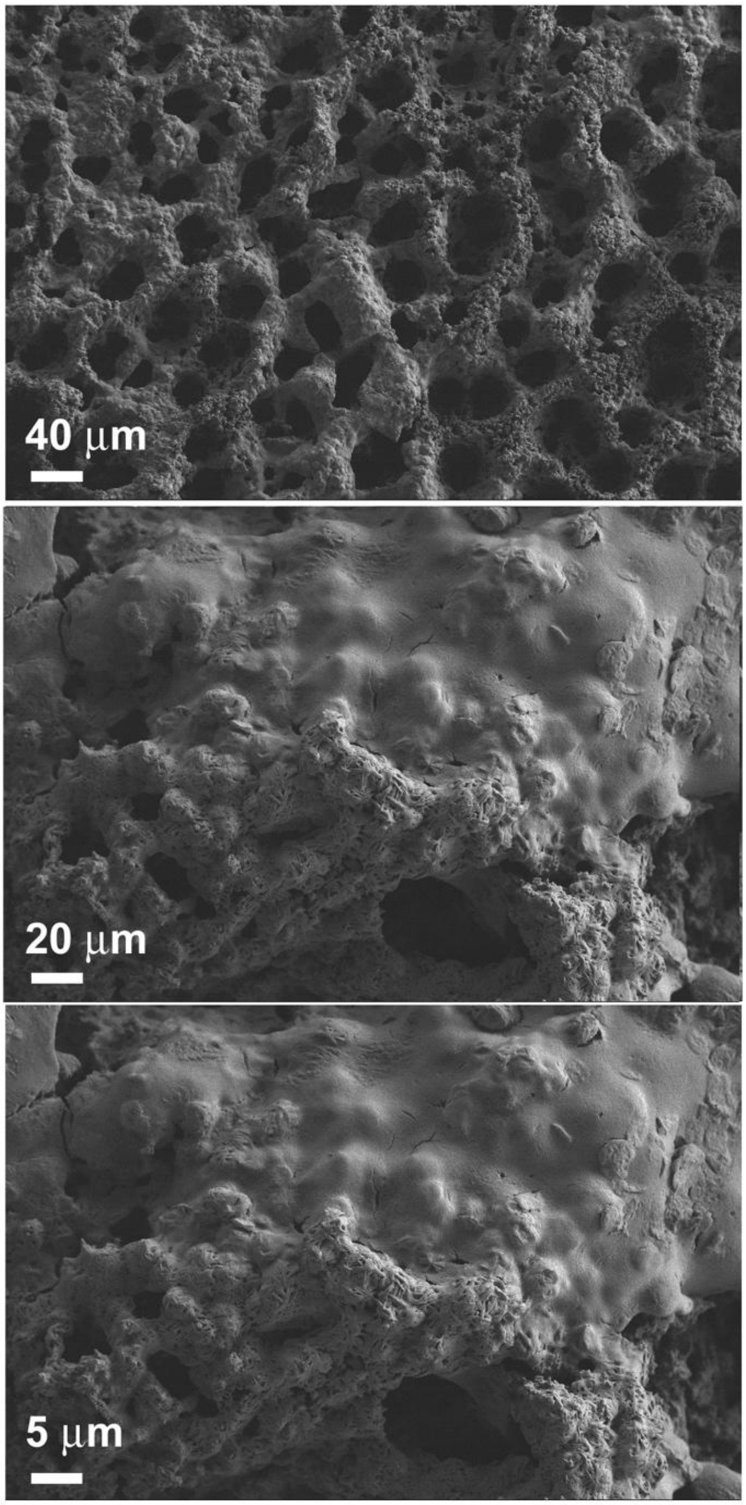

Figure S2. FE-SEM images at different magnifications of the ZnO-coated $Cu_{65}Ni_{35}$ porous layer (*final* coverage).

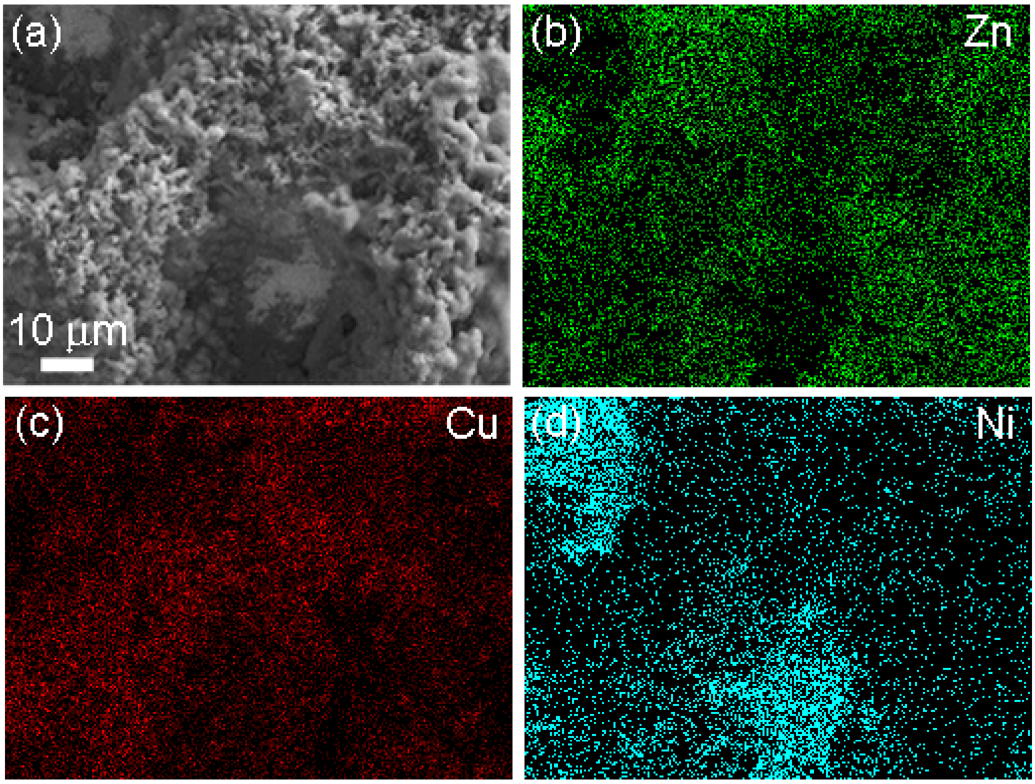

Figure S3. EDX mapping images of the middle coverage ZnO@$Cu_{80}Ni_{20}$ porous nanocomposite film. (a) SEM image, (b) Zn, (c) Cu and (d) Ni element distribution.

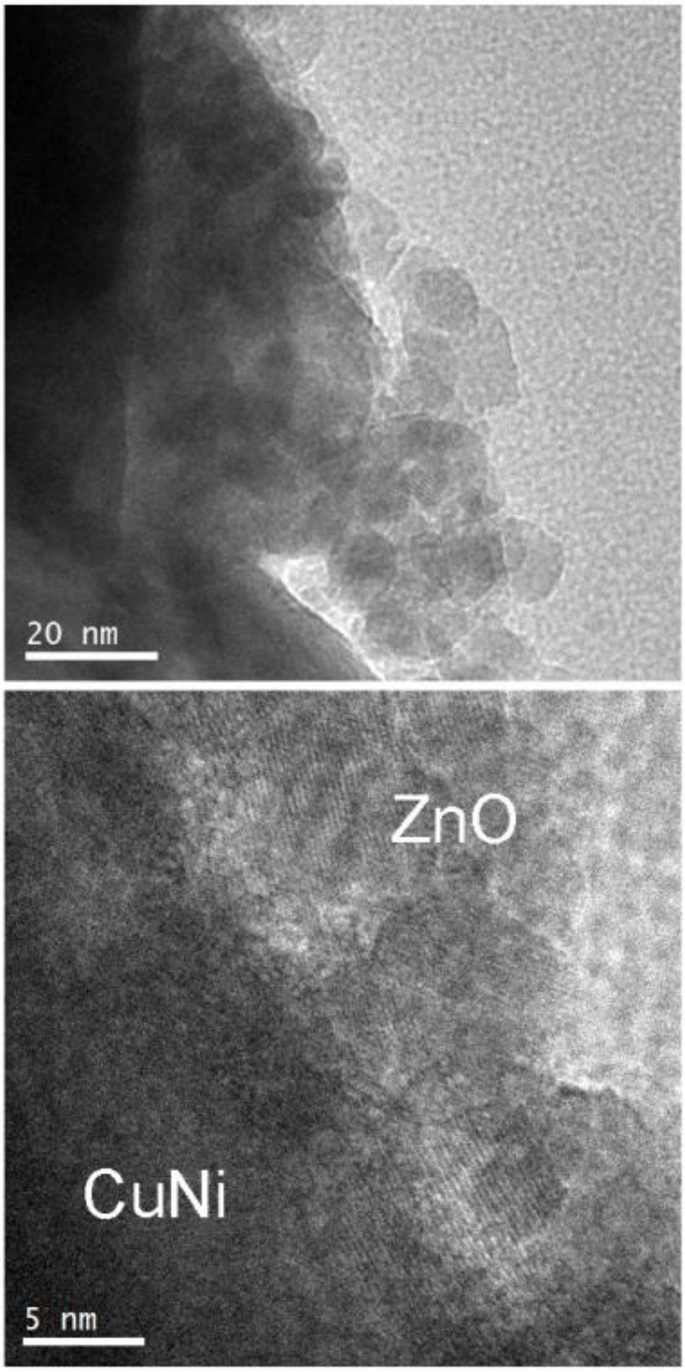

Figure S4. TEM images of the $Cu_{80}Ni_{20}$/ZnO interface, showing the ZnO NPs well stacked to the CuNi layer.

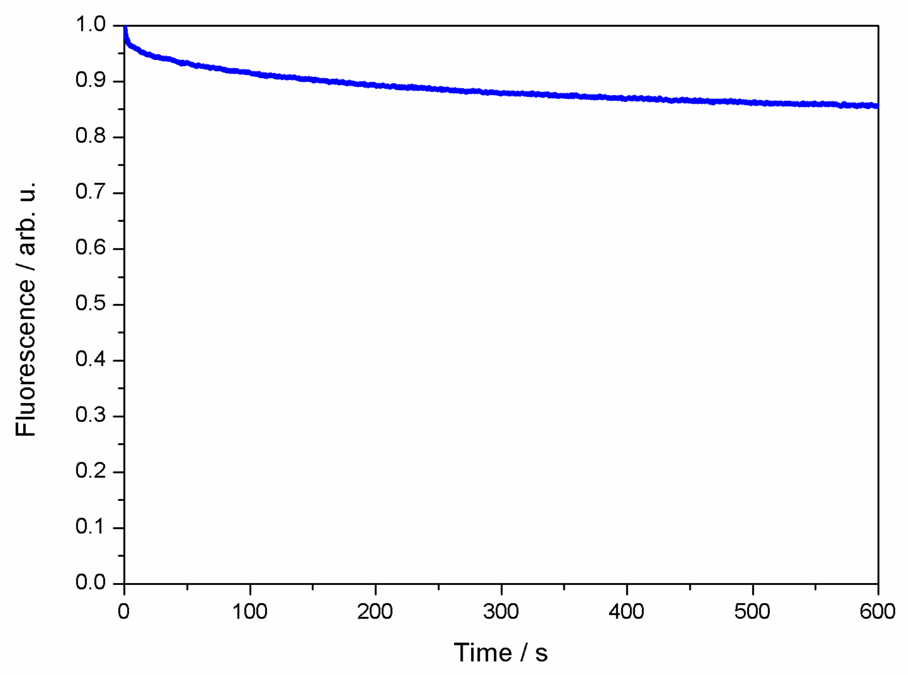

Figure S5. Photostability of the ZnO@$Cu_{80}Ni_{20}$ porous nanocomposite film upon irradiation at its excitation wavelength (405 nm).

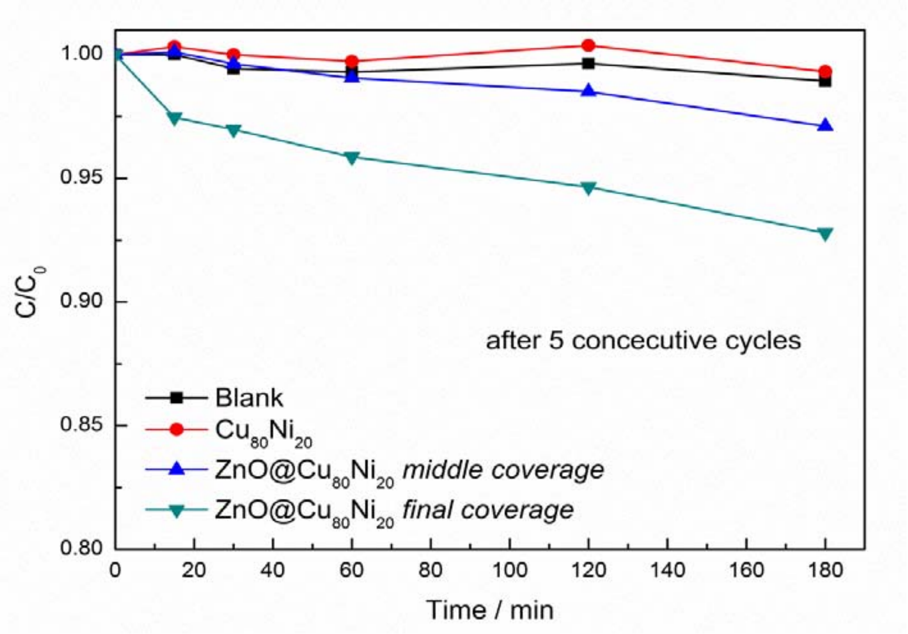

Figure S6. C/C_0 plot of the degradation of RhB in the blank, in the presence of $Cu_{80}Ni_{20}$ MF, and in the presence of ZnO@$Cu_{80}Ni_{20}$ photocatalysts with middle and final coverages at the 5th cycle.

Cu-Ni layer	Cu-rich phase	Ni-rich phase
$Cu_{80}Ni_{20}$	2θ = 43.39 (deg) *d* = 2.0839 (Å) *a* = 3.6094 (Å) at% Cu = 93.92 at% Ni = 6.08	2θ = 44.48 (deg) *d* = 2.0352 (Å) *a* = 3.5251 (Å) at% Cu = 1.19 at% Ni = 98.81
$Cu_{65}Ni_{35}$	2θ = 43.47 (deg) *d* = 2.0802 (Å) *a* = 3.6030 (Å) at% Cu = 86.91 at% Ni = 13.09	2θ = 44.43 (deg) *d* = 2.0374 (Å) *a* = 3.5289 (Å) at% Cu = 5.43 at% Ni = 94.57

Table S1. Composition of the Ni-rich and Cu-rich phases present in the two investigated porous films, as determined from XRD analyses (combining the Bragg's law with the Vegard's law).

Notes and references

1. L. Jiangtian and W. Nianqiang, *Catal. Sci. Technol*., 2015, 5, 1360.
2. T. Wagner, S. Haffer, C. Weinberger, D. Klaus and M. Tiemann, *Chem. Soc. Rev.*, 2013, 42, 4036.
3. A. Prim, E. Pellicer, E. Rossinyol, F. Peiró, A. Cornet and J. R. Morante, *Adv. Funct. Mater*., 2007, 17, 2957.
4. X. Hu, G. Li, and J. C. Yu, *Langmuir*, 2010, 26, 3031.
5. M. Zarei-Chaleshtori, V. Correa, N. López, M. Ramos, R. Edalatpour, N. Rondeau and R. R. Chianelli, *Catalysts*, 2014, 4, 346.
6. J. Lin, Y.-U. Heo, A. Nattestad, Z. Sun, L. Wang, J. H. Kim and S. X. Dou, *Sci. Rep.* 2014, 4, 5769, 1.
7. E. Pellicer, M. Cabo, A. López-Ortega, M. Estrader, L. Yedra, S. Estradé, F. Peiró, Z. Saghi, P. Midgley, E. Rossinyol, I. V.Golosovsky, A. Mayoral, J.D. Prades, S. Suriñach, M. D. Baró, J. Sort and J. Nogués, *Nanoscale*, 2013, 5, 5561.
8. T. Rodriguez-Suarez, J. F. Bartolomé and J. S. Moya, *J. Eur. Ceram. Soc.*, 2012, 32, 3887.
9. E. Menéndez, G. Salazar-Alvarez, A.P. Zhilyaev, S. Suriñach, M. D. Baró, J. Nogués and J. Sort, *Adv. Funct. Mater.*, 2008, 18, 3293.
10. J. Sort, J. Nogués, X. Amils, S. Suriñach, J. S. Muñoz and M. D. Baró, *Appl. Phys. Lett.*, 1999, 75, 3177.
11. O. D. Velev and E. W. Kaler, *Adv. Mater*., 2000, 12, 531.
12. A. Kołodziejczak-Radzimska and T. Jesionowski, *Materials* 2014, 7, 2833.
13. S. Nunomura, X. Che and S. R. Forrest, *Adv. Mater*., 2014, 26, 7555.
14. X. Zhang, J. Qin, Y. Xue, P. Yu, B. Zhang, L. Wang and R. Liu, *Sci. Rep*., 2014, 4, 1.

15. C. Tian, Q. Zhang, A. Wu, M. Jiang, Z. Liang, B. Jiang and H. Fu, *Chem. Commun.*, 2012, 48, 2858.

16. M. H. Huang, S. Mao, H. Feick, H. Q. Yan, Y. Y. Wu, H. Kind, E. Weber, R. Russo and P. D. Yang, *Science* 2001, 292, 1897.

17. R. M. Bashami, A. Hameed, M. Aslam, I. M. I. Ismail and M. T. Soomro, *Anal. Methods*, 2015, 7, 1794.

18. J. Shi, S. Grutzik and X. Wang, *ACS Nano*, 2009, 3, 1594.

19. X.-H. Xu, M. Zhang, J.-F. Wu, S.-J. Liu, B.-Z Fang and G.-H.Leng, *Chem. Res. Chin. Univ*., 2011, 32, 1703.

20. H. Fang, W. Wu and Z. Huang, *Adv. Mat. Res*., 2014, 881, 256.

21. J. Zhou, M. Zhang and Y. Zhu, *Phys. Chem. Chem. Phys.*, 2014, 16, 17627.

22. Y. Zhang, T. Guo, Y.-D. Luo, Y.-H. Lin and C.-W. Nan, *J. Am. Ceram. Soc*., 2013, 96, 361.

23. S. Chen, G. Carraro, D.Barreca and R. Binions, *Thin Solid Films*, 2015, 584, 316.

24. S. Vijayalakshmi, S. Venkataraj, M. Subramanian and R. Jayavel, *J. Phys. D: Appl. Phys*., 2008, 41, 1.

25. G. Poongodi, R.-M. Kumar and R. Jayavel, *Ceram. Int*., 2015, 41, 4169.

26. G. Nam, H. Yoon, B. Kim, D.-Y. Lee, J. S. Kim and J.-Y. Leem, *J. Nanosci. Nanotechnol*., 2014, 14, 8544.

27. E. Redel, S. Retrov, Ö. Dag, J. Moir, C. Huai, P. Mirtchev and G. A. Ozin, *Small*, 2012, **8**, 68.

28. S. Sokolov, B. Paul, E. Ortel, A. Fische and R. Kraehnert, *Langmuir*, 2011, 27, 1972.

29. R. Zhang, J. Liu, H. Guo, X. Tong, *Mater. Lett.*, 2014, 115, 208.

30. K. A. Eswar, J. Rouhi, H. F. Husairi, M. Rusop and S. Abdullah, *Adv. Mater. Sci. Eng.*, 2014, 796759, 1

31. L. Znaidi, *Mater. Sci. Eng. B - Adv. Funct. Solid - State Mater.*, 2010, 174, 18.

32. B. J. Plowman, L. A. Jones, and S. K. Bhargava, *Chem. Commun.*, 2015, 51, 4331-4346.

33. R. A. Young, Union of Crystallography, Oxford University Press: Oxford, U.K., 1995.

34. I. Bakonyi, E. Tóth-Kádár, J. Tóth, T. Becsei, T. Tarnóczi, and P. Kamasa, *J. Phys. Condens. Matter*, 1999, 11, 963-973.

35. J. Zhang, M. D. Baró, E. Pellicer and J. Sort, *Nanoscale,* 2014, 6, 12490.

36. A. Varea, S. Pané, S. Gerstl, M. A. Zeeshan, B. Özkale, B. J. Nelson, S. Suriñach, M. D. Baró, J. Nogués, J. Sort and E. Pellicer. *J. Mater. Chem. C*, 2013, 1, 7215.

37. A. B. Djurisic, W. C. H. Choy, V. A. L. Roy, Y. H. Leung, C. Y. Kwong, K. W. Cheah, T. K. G. Rao, W. K. Chan, H. T. Lui and C. Surya, *Adv. Funct. Mater.*, 2004, 14, 856.

38. T. Moyo, K. Maruyama and H. Endo, *J. Phys. Condens. Matter.*, 1992, 4, 5653.

39. Q. I. Rahman, M. Ahmad, S. K. Misra and M. Lohani, *Mater. Lett.*, 2013, 91, 170.

40. W.-J. Sun, J. Li, G. Mele, Z.-Q. Zhang, and F.-X. Zhang., *J. Mol. Catal. A: Chem.*, 2013, 366, 84-91.

3.3 Tailoring staircase-like hysteresis loops in electrodeposited tri-segmented magnetic nanowires: a strategy towards minimization of interwire interactions

In this article a novel strategy to reduce the interwire dipolar interactions in nanowires (NWs) that are to be dispersed in fluids, thereby minimizing their agglomeration, is reported. To this end, arrays of tri-segmented hard-magnetic(CoPt)/non-magnetic(Cu)/soft-magnetic(Ni) NWs with different segments lengths are prepared by electrodeposition in polycarbonate (PC) membranes. By XRD analyses, it is found that Ni and Cu segments crystallize in the face-centered cubic (*fcc*) structure. Meanwhile, the CoPt segment grows in the hexagonal closed-packed (*hcp*) structure. Variable segments lengths are achieved by adjusting the electrodeposition time. These NWs exhibit staircase-like hysteresis loops resulting from the two different coercivities of the soft (Ni) and hard (CoPt) ferromagnetic segments. The orientation of the two magnetic segments can be individually controlled to make them either parallel or antiparallel to each other. The magnetization amplitudes of the two ferromagnetic contributions are found to depend on the relative lengths of CoPt and Ni segments.

Antiparallel alignment between the two ferromagnetic segments can be settled after positive saturation by applying a negative magnetic field sufficient to switch the Ni magnetization but smaller than the CoPt coercivity. In such antiparallel alignment, proper adjustment of the Ni and CoPt segment lengths eventually leads to virtually zero remanent magnetization (fully compensated NWs). Since the saturation magnetization of Ni ($\mu_0 M_{s,Ni} = 0.6$ T) is approximately half that of CoPt ($\mu_0 M_{s,CoPt} \approx 1$-1.3 T), the compensated situation can occur when the length of the Ni segment is around twice the length of CoPt, i.e. $\mu_0 M_{s,Ni} \times l_{Ni} \times A \approx \mu_0 M_{s,CoPt} \times l_{CoPt} \times A$ (l is the length and A is the cross-sectional area of the segment).

Analytical calculations leaded by the Superconductivity Group (Physics Department, UAB) reveal that, once released from the template, the magnetic interaction energy between two fully-compensated tri-segmented NWs is reduced with respect to a single NW with the same length or the tri-segmented NWs with the two segments parallel to each other.

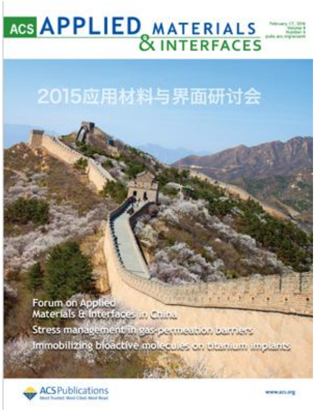

Tailoring Staircase-like Hysteresis Loops in Electrodeposited Tri-segmented Magnetic Nanowires: a Strategy towards Minimization of Interwire Interactions

Jin Zhang[†], *Sebastià Agramunt-Puig*[†], *Núria Del-Valle*[†], *Carles Navau*[†], *Maria D. Baró*[†], *Sònia Estradé*[‡], *Francesca Peiró*[‡], *Salvador Pané*[⊥], *Bradley Nelson*[⊥], *Alvaro Sanchez*[†], *Josep Nogués*[#,§], *Eva Pellicer**[,†], and *Jordi Sort**[,†,§]

[†]Departament de Física, Universitat Autònoma de Barcelona, E-08193 Bellaterra, Barcelona, Catalonia, Spain

[‡]LENS, MIND-IN2UB, Departament d'Electrònica, Universitat de Barcelona, Martí i Franquès 1, E-08028 Barcelona, Spain

[⊥]Institute of Robotics & Intelligent Systems (IRIS), ETH Zürich, CH-8092 Zurich, Switzerland

[#]Catalan Institute of Nanoscience and Nanotechnology (ICN2), CSIC and The Barcelona Institute of Science and Technology, Campus UAB, Bellaterra, 08193 Barcelona, Spain

[§]Institució Catalana de Recerca i Estudis Avaçats (ICREA), Barcelona, Catalonia, Spain

*To whom correspondence should be addressed:

Prof. Jordi Sort, Dr. Eva Pellicer

E-mail: Jordi.Sort@uab.cat, Eva.Pellicer@uab.cat

ABSTRACT

A new strategy to minimize magnetic interactions between nanowires (NWs) dispersed in a fluid is proposed. Such strategy consists in preparing tri-segmented NWs containing two antiparallel ferromagnetic segments with dissimilar coercivity separated by a non-magnetic spacer. The trisegmented NWs exhibit a staircase-like hysteresis loop with tunable shape that depends on the relative length of the soft- and hard-magnetic segments and the respective values of saturation magnetization. Such NWs are prepared by electrodepositing CoPt/Cu/Ni in a polycarbonate (PC) membrane. The antiparallel alignment is set by applying suitable magnetic fields while the NWs are still embedded in the PC membrane. Analytic calculations are used to demonstrate that the interaction magnetic energy from fully compensated trisegmented NWs with antiparallel alignment is reduced compared to a single-component NW with the same length or the trisegmented NWs with the two ferromagnetic counterparts parallel to each other. The proposed approach is appealing for the use of magnetic NWs in certain biological or catalytic applications where the aggregation of NWs is detrimental for optimized performance.

KEYWORDS: segmented nanowires, magnetic interactions, template-assisted electrodeposition, staircase hysteresis loops, nanomagnetism

1. INTRODUCTION

Owing to their unique physicochemical properties, materials structured in the form of one-dimensional nanoarchitectures, such as nanorods and nanowires (NWs), have found widespread applications in several technological areas, e.g. optoelectronics,[1] magnetism,[2,3] catalysis,[4] piezo- and thermo-electricity,[5,6] biosensing,[7,8] and micro-/nanoelectromechanical systems (MEMS/NEMS),[9] among others. Specifically, ferromagnetic NWs are being employed as components in information storage and logic devices,[3,10,11] spintronics,[12] magnetic sensors,[13] and also as platforms in the biomedical field (e.g., hyperthermia or drug delivery).[14]

For their range of applications to be expended further, the implementation of other materials with dissimilar nature within the NW architecture can provide additional and complementary functionalities. The resulting hybrid structures (i.e., core-shell NWs or segmented NWs) offer enhanced performance due either to the established synergy between the properties of each building block, or to interfacial interaction effects between them. Segmented NWs can be all-electrodeposited in a cost-effective manner,[15-18] whereas core-shell NW structures usually require a combination of different synthetic approaches (e.g., electrodeposition together with chemical vapor deposition).[19] In the field of magnetism, segmented NWs served as a model system for heterostructured junctions that exhibit various fascinating perpendicular spin transport phenomena, such as current-perpendicular-to-plane giant magnetoresistance (GMR)[20,21] or tunneling magnetoresistance (MR)[22], to name a couple. Likewise, core/shell NWs[23] combining several phases of distinct magnetic properties could generate additional effects, e.g., spintronic, multiferroic, magnetoplasmonic, and so forth. These outstanding properties have furnished hybrid NWs a host of applications in giant magnetoresistance sensors,[24] spring-magnets,[25] exchange bias systems,[26] nanomagnet microwave resonators,[27] and magneto-plasmonics devices.[28]

Once released from the template or detached from the substrate, self-standing magnetic NWs can be dispersed in fluids and subsequently manipulated using external magnetic fields and field gradients. Wireless magnetic actuation is crucial for the utilization of these NWs in certain biological or catalytic applications.[18,19,29-31] However, one of the most challenging issues in areas like drug delivery or biological labeling is to avoid the aggregation of NWs once the external magnetic field is removed. Agglomeration of NWs inside bodily fluids can cause obstruction of the vessels, eventually leading to thrombosis or even more serious health diseases.

The formation of NWs bundles is also a serious concern in applications that require the use of a single NW, for example when a single NW is intended to be bound to cells or proteins[32] or in NWs that need to be precisely attached to small components to build sophisticated miniaturized devices.[33] Also, aggregation of NWs has to be prevented to obtain high-quality homogeneous ferrofluids or to preserve the mechanical properties of composites containing magnetic NWs.[13]

Magnetic dipolar interactions between magnetic particles dispersed in liquids are directly responsible for their agglomeration. In the absence of a magnetic field, such interactions are proportional to the overall remanent magnetization of each particle. For this reason, superparamagnetic nanoparticles, with zero net remanent magnetization, are usually preferred in comparison to NWs for certain biological applications.[31] Nevertheless, their exceedingly small surface area limits their efficiency as drug carriers. An alternative approach is to use magnetic vortices,[34] also with virtually zero magnetic remanence, but disks of a few micrometers in diameter are needed to form such magnetic configurations. Hence, magnetic vortices can be rather impractical for most biological purposes.

Ferromagnetic NWs offer some advantages with respect to superparamagnetic nanoparticles or microstructured disks exhibiting magnetic vortices. However, a smart strategy to tailor (and, in particular, to reduce) the overall remanent magnetization of magnetic NWs is needed to control (and decrease) the strength of interwire dipolar interactions to minimize aggregation. It is well-known that some of the properties of magnetic NWs (e.g., the effective magnetic anisotropy direction or the coercivity) are strongly dependent on the diameter and aspect ratio as well as on the dipolar coupling between the ferromagnetic segments.[35] For example, Liu and coworkers[36] have electrodeposited Co/Cu multilayered NWs, in which the magnetic configurations can be tuned by adjusting the Co segment aspect ratio. In turn, the saturation magnetization depends mainly on the composition of the NWs.

In this work, the possibility to tune the remanent magnetization of NWs is demonstrated by synthesizing tri-segmented NWs in which the orientation of the different segments comprising the NWs is individually controlled, similarly to what has been successfully demonstrated in synthetic ferrimagnets,[37] patterned multilayers for multi-bit data storage[38] or recently proposed in core/shell nanoparticles.[39,40] To this end, arrays of tri-segmented CoPt/Cu/Ni NWs (i.e., hard- and soft-ferromagnetic segments separated by a non-magnetic Cu spacer) embedded in polycarbonate (PC) membranes have been prepared by electrodeposition. Magnetic measurements of the hybrid NWs, while still embedded in the PC templates, reveal the occurrence of staircase-like hysteresis loops, resulting from the two different coercivities of the soft and hard ferromagnetic segments. The overall shape of the hysteresis loops (i.e., the magnetization step sizes) can be tuned by varying the aspect ratio of the different segments. Antiparallel alignment between the CoPt and Ni segments can be established after saturation by applying a negative magnetic field larger than the coercivity exhibited by Ni but lower than the coercivity corresponding to CoPt. In such antiparallel alignment, proper adjustment of the Ni and CoPt segment length leads to either positive or negative remanent magnetization, eventually even resulting in zero remanent net magnetization (fully compensated NWs). The trisegmented NWs can be easily released from the PC membrane and satisfactorily dispersed in fluids. Analytical calculations are used to corroborate that the interaction magnetic energy between two fully-compensated tri-segmented NWs (with two antiparallel magnetic segments) is generally reduced with respect to a tri-segmented NW having the two segments parallel to each other.

2. EXPERIMENTAL SECTION

2.1. Synthesis of the Trisegmented NWs

Template-assisted electrodeposition was carried out in a typical single-compartment double-jacketed glass electrochemical cell. Track-etched PC membranes with 30 nm nominal pore size (Nuclepore, Whatman) were used as working electrodes (WE). PC membranes with well-separated pores were selected for two reasons: (i) these membranes can afford the basic pH values needed to grow CoPt, and (ii) the distance between neighboring NWs is sufficiently high to ensure that interwire dipolar magnetic interactions between NWs are negligible such that their behavior when still embedded in the PC membrane is essentially the same as that of an isolated non-interacting NW. The fabrication process of trisegmented NWs is illustrated in Scheme 1.

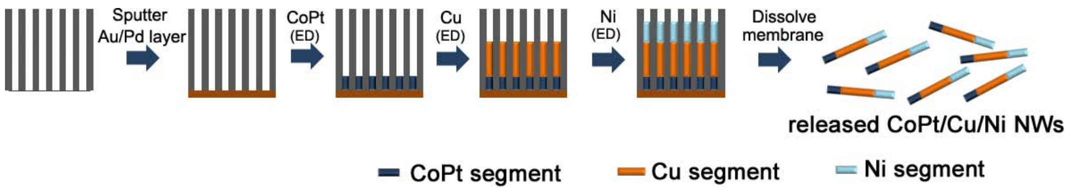

Scheme 1. Schematic picture of Trisegmented NWs Fabrication Process Using PC Template-Based Electrodeposition (ED).

First, a thin Au-Pd layer was sputtered onto one side of PCs to make them conductive. The Au-Pd surface was put in contact with a copper plate and held inside a plastic stationary holder, and a circular area of 3.14 cm^2 was exposed to the electrolyte for deposition. Before electrodeposition, the PC membrane was placed in an ultrasonicator for 3 min to remove the air inside the PC channels. In this way, the electroactive species can penetrate inside the channels and access the Au-Pd layer, thereby enabling the electrodeposition. A platinum wire was utilized as counter electrode, which was positioned vertically facing the WE. A double junction Ag|AgCl 3 M KCl electrode (E = + 0.210 V versus standard hydrogen electrode) was used as reference electrode to record the potential at the WE. The three electrodes were connected to a PGSTAT302N Autolab potentiostat/galvanostat (Ecochemie).

The tri-segmented NWs were prepared via sequential direct current electrodeposition of CoPt, Cu and Ni segments by changing the corresponding electrolytes. The deposition of the CoPt segments was performed galvanostatically at j = -10 mA cm^{-2}, pH = 8.5, T = 65°C. The electrolyte consisted of 30 mM $Co(SO_3NH_2)_2{\cdot}xH_2O$, 2 mM $Pt(NH_3)_2(NO_2)_2$, 0.1 M glycine, 0.1 M sulfamic acid, 5 mM saccharine, and 0.1 M sodium citrate. The electrodeposition of Cu segments was carried out potentiostatically at E = -1.0 V in an electrolyte containing 0.2 M $CuSO_4{\cdot}5H_2O$ and 0.1 M boric acid. The third segment (Ni) was grown galvanostatically at j = -10 mA cm^{-2} from an electrolyte consisting of 2 M NH_4Cl and 0.1 M $NiCl_2$. The deposition processes for Cu and Ni segments were carried out at 25°C and the pH was left unadjusted (i.e., preparation pH). All the electrolytes were deaerated before and during the experiments in order to get rid of dissolved oxygen and to ensure the homogeneity of the solution. For electron microscopy observations, the trisegmented NWs were released by dissolving the PC template in chloroform and washed several times afterwards. For the sake of comparison, single-component Ni, Cu and CoPt NWs were also electrodeposited using the same conditions as for the hybrid NWs.

2.2. Structural Characterization

Scanning electron microscopy (SEM) images and energy-dispersive X-ray spectroscopy (EDX) compositional analyses were acquired using a Merlin Zeiss microscope operated at 3 kV and 15 kV, respectively. Specimens for SEM and EDX measurements were prepared via drop-casting a droplet of NWs suspended in chloroform onto an aluminum foil and subsequent drying in air. A similar preparation method onto Cu grids was used for TEM observations. The structure and morphology of the NWs (length of the different segments, aspect ratio, etc.) were also investigated by high-resolution transmission electron microscopy (HRTEM) using a Jeol-JEM 2011 system with a field emission gun operating at 200 kV. Electron energy loss spectra (EELS) were acquired along the NWs. Spectra were taken in the 650-1150 eV energy loss range, where the Co L2,3, the Cu L2,3 and the Ni L2,3 edges were found, at 779, 931 and 855 eV, respectively. The quantitative analysis of the EELS spectra was performed using the homemade software package Oxide Wizard.[41] X-ray diffraction (XRD) patterns of the NWs were recorded on a Philips X'Pert diffractometer in the 30-100° 2θ range (step size = 0.026°, step time = 2000 s) using Cu K_α radiation (λ = 0.154178 nm). In this case, the PC membrane was not dissolved –the XRD patterns were acquired while the NWs were still embedded inside the membrane.

2.3. Magnetic Characterization

Hysteresis loops were collected on the single-component (CoPt and Ni) and trisegmented (CoPt/Cu/Ni) NWs at room temperature using a vibrating sample magnetometer (VSM) from Oxford Instruments with a maximum applied magnetic field of 0.5 T. An antiparallel alignment between the CoPt and Ni segments was settled by first saturating the NWs in the positive direction and then applying a negative magnetic field sufficient to reverse Ni but lower than the coercivity of the CoPt segment.

3. RESULTS AND DISCUSSION

3.1. Structure and Magnetic Behavior of Single-Component CoPt and Ni

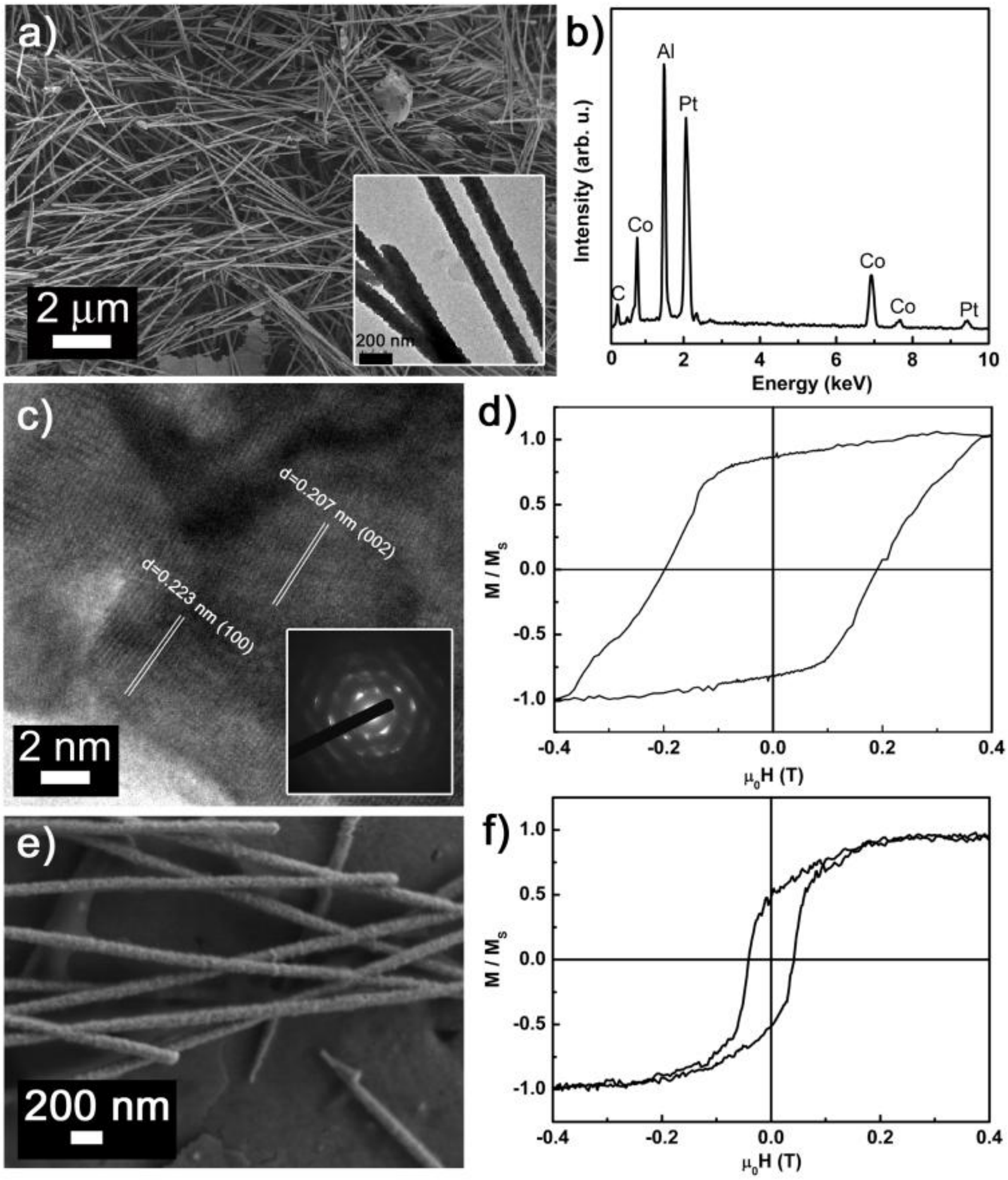

Figure 1. (a) SEM, (b) EDX spectrum and (c) HRTEM image of CoPt NWs released from the PC membrane, (d) room-temperature magnetic hysteresis loop of single-component CoPt NWs arrays (measured before PC removal, along the NWs axis), (e) SEM image of single-component Ni NWs released from the PC membrane, and (f) room temperature hysteresis loop of single-component Ni NWs arrays (embedded in the PC membrane). Insert in (a) shows a magnified view of a few CoPt NWs, whereas insert in (c) shows a SAED pattern of CoPt NWs.

All the investigated NWs were deposited inside the channels (i.e., pores) of PC membranes that are visible as black spots by SEM imaging (see Figure S1 in the Supplementary Information). These pores traverse the membranes completely, hence allowing the growth of the NWs by electrodeposition. The thickness of the PC membranes is approximately 5 µm, the average pore diameter (at the surface of the PC template) ranges from 40 to 60 nm, and there is an areal density of less than 10 pores µm^{-2}. Single-component NWs consisting of CoPt alloy, Cu and Ni were first deposited individually to estimate and optimize the growth rates.

As shown in Figure 1a, CoPt NWs can be obtained in high-yields with a length of around 5 µm and a diameter about 100 nm (see also the corresponding TEM image, inset of Figure 1a). The larger diameter of the NWs, as compared to the average pore diameter at the surface of the PC membranes, indicates that the channels inside the PC are probably not completely homogeneous in width. This is actually supported by previous works from the literature in which it has been suggested that the pores inside PC templates are not completely cylindrical (with a constant cross-section) but instead appear to be “cigar-like shaped”[42]. The NWs have all similar lengths, suggesting that their growth proceeds at the same rate over the whole PC area. This is an important feature for the subsequent fabrication of the trisegmented NWs. The EDX spectrum (Figure 1b) confirms that the NWs are composed of Pt and Co, with a mean atomic composition of $Co_{70}Pt_{30}$. The aluminum signal in Figure 1b comes from the aluminum foil onto which the NWs were drop-casted. The HRTEM and the associated SAED pattern (Figure 1c and inset) reveal that the CoPt NWs are polycrystalline (hexagonal closed-packed, hcp, phase) with clear lattice fringes. The obtained interplanar distances can be ascribed to the (100) and (002) planes of hcp structure. Representative SEM images of the Ni and Cu single-component NWs are shown in Figures 1e and S2, respectively. Similar to CoPt NWs, well-grown, continuous Cu and Ni NWs can be deposited with an approximate diameter of 100 nm.

Typical XRD patterns of the as-deposited CoPt, Cu and Ni NWs embedded in the PC membrane are shown in Figure 2. For both Cu and Ni single-component NWs, the (111), (200), (220) and (311) reflections of face-centered cubic (fcc) structure are detected. In addition, for Cu NWs, by comparing the tabulated and experimental relative peak intensities (*I*) of the (111) and (200) reflections, clear conclusions regarding the crystallographic texture can be drawn.

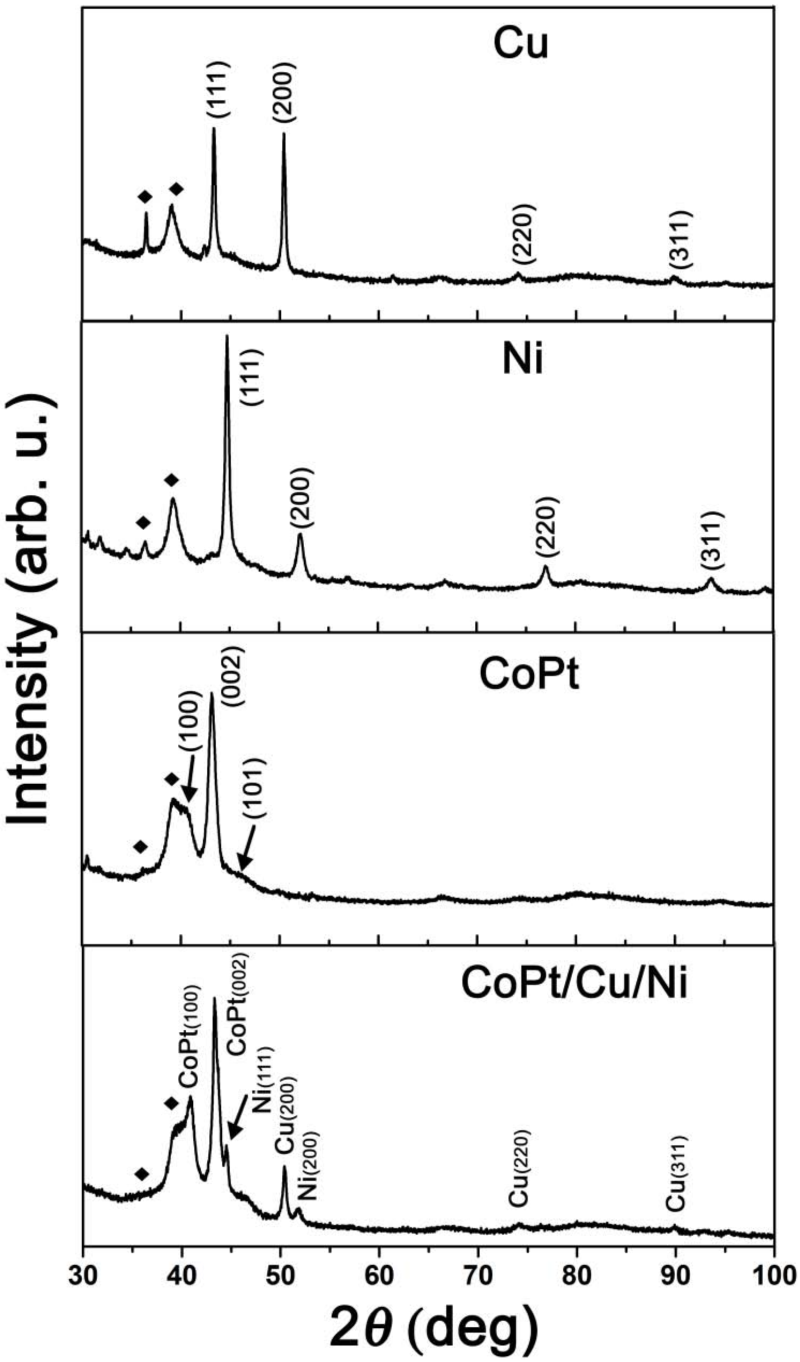

Figure 2. XRD patterns of single-component Cu, Ni and CoPt NWs and trisegmented CoPt/Cu/Ni NWs. Peaks denoted by ♦ belong to the sputtered Au-Pd conductive layer.

Namely, the experimental I_{200} / I_{111} ratio is 1.02, which is larger than the theoretical value (0.46) for randomly oriented Cu grains. This indicates the formation of [100] textured Cu NWs. Textures in electrodeposited materials are highly influenced by electrolyte composition and working conditions. Thus, either non-textured or textured materials can be readily obtained by simply changing the plating parameters.

The diffractogram of single-component CoPt NWs reveals that the strongest peak appears at $2\theta = 43.13°$. This position matches both hcp and fcc phases. However, the absence of any reflection at ~ 51.5° suggests that CoPt has crystallized in the hcp structure, as it corresponds to Co-rich NWs electrodeposited in basic pH conditions.[43] The intensity of the (101) reflection is dramatically reduced as compared to the standard powder pattern, which suggests that the hexagonal *c* axis lies preferentially along the long axis of the NWs.

The magnetic hysteresis loop of the single-component CoPt NW arrays measured with the applied field parallel ($H_{//}$) to the long axis of the NWs is shown in Figure 1d. The coercivity, H_c, is ~1950 Oe. Therefore, CoPt NWs show hard ferromagnetic behavior. The magnetic properties of single-component Ni NWs were measured under the same conditions as for CoPt NWs. As shown in Figure 1f, H_c is around 410 Oe in this case. According to these data, it is clear that hard magnetic/spacer/soft magnetic trisegmented CoPt/Cu/Ni NWs could be, in principle, successfully deposited into PC membranes by simply changing the electrolyte.

3.2. Structural Characterization of Trisegmented NWs

The XRD pattern of the as-deposited tri-segmented CoPt/Cu/Ni NW arrays embedded in the PC membrane is shown at the bottom of Figure 2. By comparing the XRD patterns of single-component and trisegmented CoPt/Cu/Ni NWs, all of the peaks corresponding to CoPt, Cu and Ni phases can be straightforwardly indexed. Hence, the sequential fabrication process did not introduce any extra phases or impurities. Therefore, CoPt/Cu/Ni tri-segmented NWs can be successfully synthesized through a template-based electrodeposition method.

The compositional variations along the NW axis were assessed by EDX (see Figure 3). A TEM image of a whole tri-segmented NW can be observed in the upper panel of Figure 3. NWs show a sharp needle-like end due to the narrowing of the PC pores near the surface, in agreement with the literature.[42] The darker and brighter contrast reveals the difference in atomic weight between the constituent phases with the electron dispersing capability of CoPt stronger than for both Cu and Ni. Because Cu and Ni have similar atomic weight, it is difficult to clearly distinguish them by TEM. Therefore, the brightest region stands for CoPt and the darker regions represent the Cu + Ni segments.

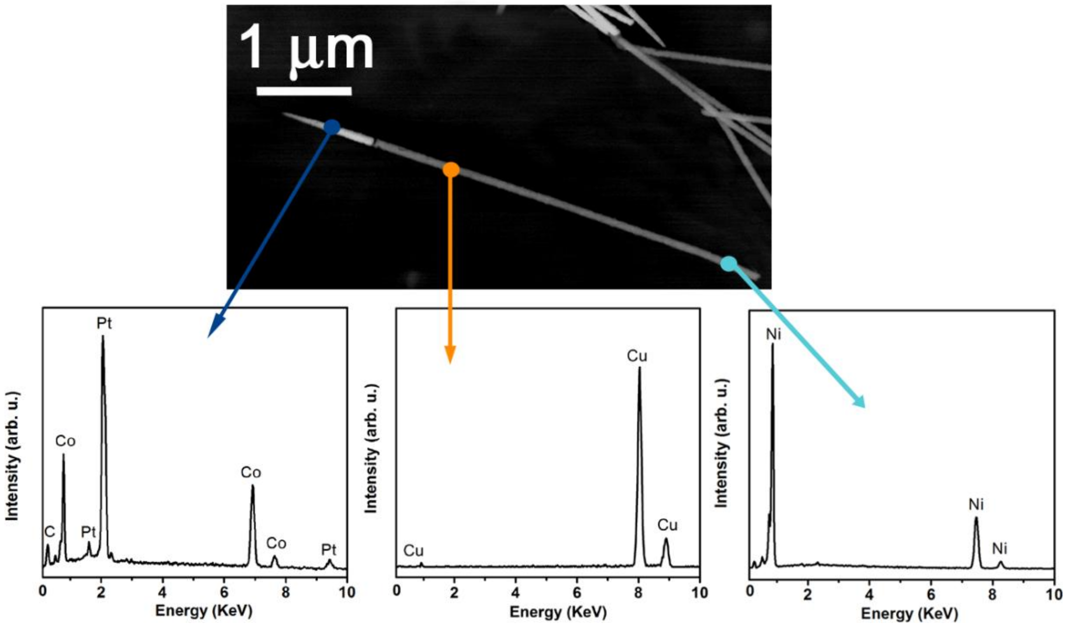

Figure 3. EDX spectra acquired in each of the segments of the tri-segmented NW shown in the upper TEM image. Note that no clear interface between Cu and Ni can be seen using standard TEM conditions.

For gaining further insight into the heterostructured architecture of the NWs, STEM-EELS analyses were performed (Figure 4). EELS analyses were actually necessary to distinguish between the Cu and Ni segments and, in turn, to determine their lengths. When the electron beam was spotting in “a”, Co was detected (Figure 4a). When the electron beam was directed to the middle part of the NW (point “b”), only Cu was visible (Figure 4b). Similarly, the EELS analysis on point “c” (Figure 4c) clearly confirms that the ending segment of the NW is made of pure Ni. EELS line-scan was used to determine the length of the different segments, as shown in Figures 4d and

4e. In this particular case (referred to as “sample D” in Section 3.3), the length of the CoPt segment, which now corresponds to the darker region, is 0.97 µm, whereas the Ni segment has a length of 1.74 µm. Finally, the Cu segment, with a length of 2.72 µm, is sandwiched between CoPt and Ni. In turn, EELS analysis performed in the NWs with shorter Ni segments (sample A in section 3.3) reveals that the CoPt, Cu and Ni segment lengths are 1.10, 2.63 and 0.61 µm, respectively.

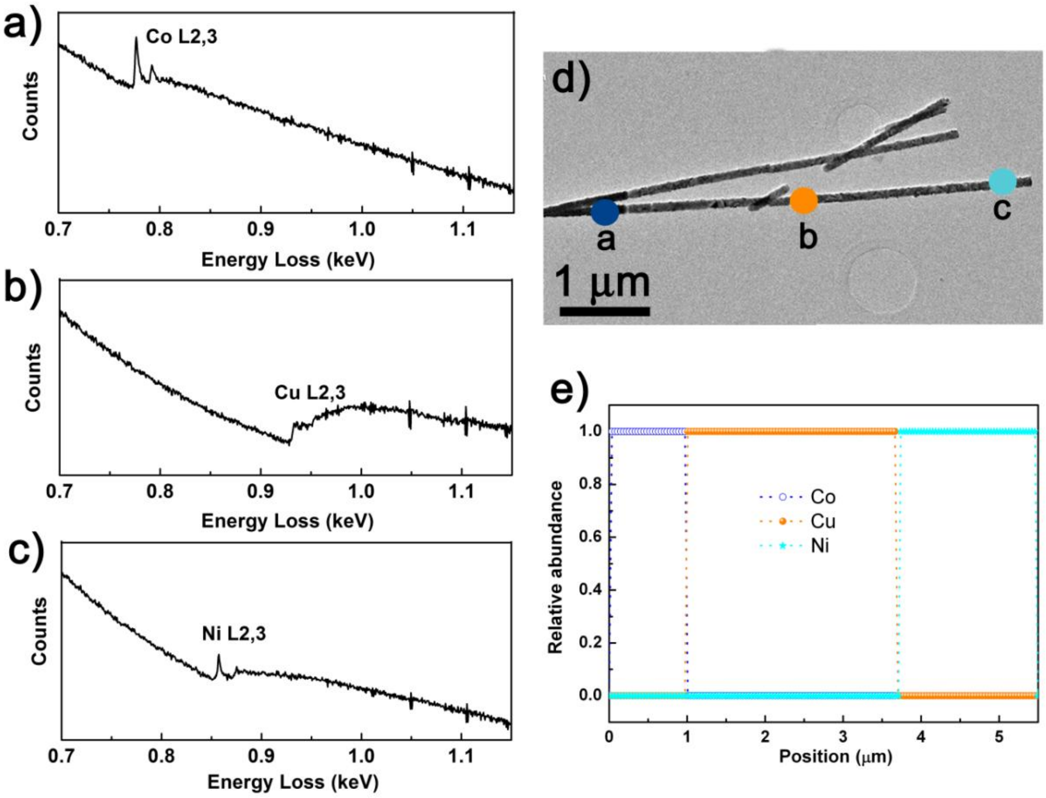

Figure 4. (a-c) EELS point spectra for CoPt/Cu/Ni trisegmented NWs [marked as a, b and c in (d)]. (d) STEM image of CoPt/Cu/Ni trisegmented NW for which an EELS line-scan was performed. (e) The corresponding element distribution as a function of NW length.

3.3. Magnetic Characterization of the Trisegmented NWs

Hysteresis loops from various arrays of CoPt/Cu/Ni trisegmented NWs embedded in the PC membrane, measured along the NWs axis, are shown in Figure 5. The loops exhibit a staircase-like shape with two well-differentiated coercivities corresponding to the magnetization reversal of Ni (soft segment) and CoPt (hard segment), respectively. These two switching events can be clearly seen because (i) the magnetic dipolar interactions between neighboring NWs in the PC membranes are small (due to the large interpore distance), and (ii) the segments in each nanowire are separated by the non-magnetic Cu spacer to avoid magnetic exchange interactions between CoPt and Ni. Otherwise, if the NWs were deposited close to each other (as in conventional anodized aluminum oxide templates), the loops would become tilted and the staircase shape would be lost.[44] Similarly, in the absence of the Cu segments, the interfacial coupling between Ni and CoPt would promote a simultaneous switching of the magnetization in both magnetic segments. Hence, this configuration of the tri-segmented NWs provides access to various magnetization states depending on the relative orientation of the magnetization in each segment, as indicated in Figure 5b.

Figure 5a reveals that altrhough the contribution of Ni to the overall magnetization is larger than that of CoPt in sample C (in which the Ni segment is much longer than CoPt), the opposite is observed in samples A and B. Remarkably, the hysteresis loop shown in Figure 5b (sample D) exhibits virtually equal magnetization amplitudes from Ni and CoPt. Such precise tailoring of the hysteresis loop shape can be accomplished by varying the relative lengths of the Ni and CoPt segments (see Table 1). Because the saturation magnetization of Ni ($\mu_0 M_{S,Ni}$ = 0.6 T)[45] is approximately half that of CoPt ($\mu_0 M_{S,CoPt} \approx 1 - 1.3$ T)[46,47], the compensated situation (Figure 5b) occurs when the length of the Ni segment is approximately twice the length of CoPt (Table 1). In other words, in sample D (which is the one that corresponds to the EELS results shown in Figure 4) one has: $\mu_0 M_{S,Ni} * l_{Ni} * A \approx \mu_0 M_{S,CoPt} * l_{CoPt} * A$ (where, l designates “length” and A is the cross-sectional area of the segments).

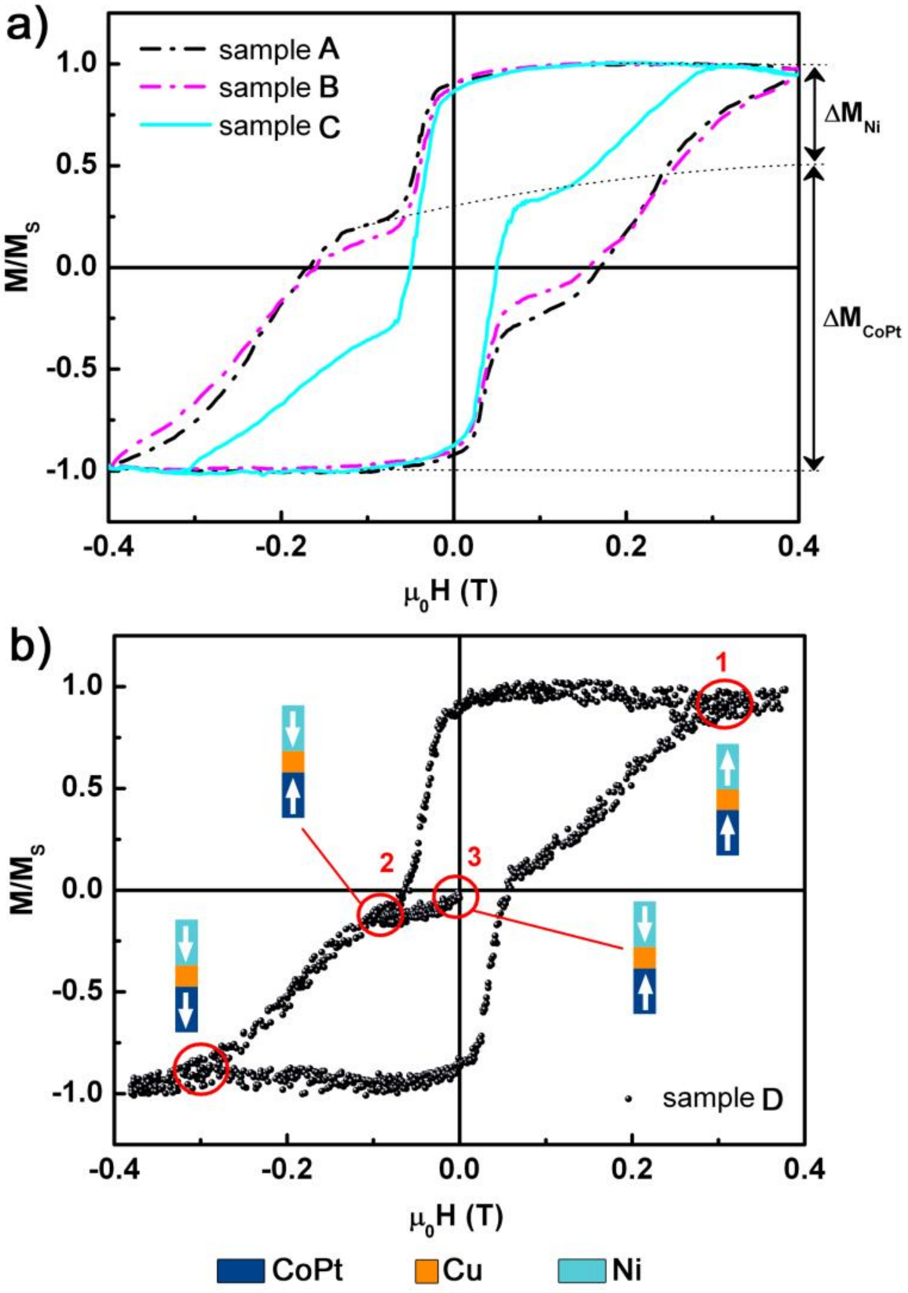

Figure 5. (a) Staircase-shaped hysteresis loops corresponding to tri-segmented CoPt/Cu/Ni NWs with variable relative length ratios of the soft (Ni) and hard (CoPt) segments (samples A, B and C; see Table 1). (b) Hysteresis loop corresponding to an array of tri-segmented CoPt/Cu/Ni NWs (sample D) where the magnetization amplitudes of the Ni (ΔM_{Ni}) and CoPt (ΔM_{CoPt}) segments are virtually equal to each other. Indications in (b) are the magnetic orientations of the two segments at different positions of the hysteresis loop.

Sample	$<l_{CoPt}>/<l_{Ni}>$	$\Delta M_{CoPt} / \Delta M_{Ni}$	$M_{r,minor}/M_S$
A	~ 1.8	~ 3.2	0.31
B	~ 1.1	~ 2.2	0.23
C	~ 0.3	~ 0.6	-0.20
D	~ 0.5	~ 1.0	0

Table 1. Dependence of the Relative Magnetization Amplitudes of the CoPt (ΔM_{CoPt}) and Ni (ΔM_{Ni}) segments, as well as the Resulting Remanent Magnetization once the two segments are oriented antiparallel to each other as depicted in Figure 5b as a function of the average relative lengths of the CoPt (l_{CoPt}) and Ni (l_{Ni}) segments[a].

[a] Note that $M_{r,minor}$ is not the overall remanence magnetization of the whole hysteresis loops (which is close to 1 in all cases) but instead denotes the remanent magnetization obtained when performing the minor loop sequence to set the antiparallel alignment between Ni and CoPt segments (i.e., when sweeping the field from positions 1 →2 →3 as indicated in Figure 5b. Samples A-D correspond to the ones whose hysteresis loops are shown in Figure 5.

3.4. Strategy to Minimize Interwire Interactions

As mentioned in the Introduction, magnetic NWs are appealing for various technological applications (biomedical, catalytic, MEMS/NEMS, etc.) but the strength of interwire magnetic interactions, once the NWs are dispersed in a fluid, needs to be controlled and minimized in order to attain optimized performance. By taking advantage of the staircase shape of the hysteresis loops, it is possible to engineer a protocol to set an antiparallel alignment between the soft and hard segments, and therefore reduce the overall remanent magnetization of the NWs when they are still embedded in the PC template. This can be done by first saturating the array of NWs using a strong positive magnetic field (position 1 in Figure 5b) and then applying a negative field sufficient to switch Ni to the negative orientation without reversing the magnetization of CoPt (position 2). Once the magnetic field is brought back to zero (position 3), the two segments remain antiparallel to each other and the resulting remanent magnetization ($M_{r,minor}$) will depend on the relative magnetization amplitudes of the Ni and CoPt segments (ΔM_{Ni} and ΔM_{CoPt}), i.e., on their length. The procedure is indicated in Figure 5b. Then, $M_{r,minor}/M_S$ can have either a positive value (samples A and B), negative value (sample C) or be virtually zero (sample D) (see Table 1). A comparative analytic calculation to show how the magnetic interaction energy outside the tri-segmented NW in sample D is reduced when the two segments are antiparallel to each other, with respect to the case of parallel alignment, is given in section 3.5. It is worth mentioning that such antiparallel alignment between the soft and hard segments will remain in the NWs dispersed in the fluid provided that the applied external magnetic fields used to manipulate them do not exceed the coercivity of the soft segment. Fortunately, wireless manipulation of magnetic NWs in low Reynolds number aqueous environments is actually possible under the action of external fields of only a few tens of Oe, if combined with suitable magnetic field gradients.[48]

3.5. Modeling the Magnetic Interaction Energy between Two Trisegmented NWs

For the sake of simplicity, we assume that each fully compensated trisegmented NW has a circular cross-section of diameter a and it is composed of a hard segment of length c and uniform magnetization $2M_S$, a soft segment of length $2c$ and uniform magnetization M_S, and a nonmagnetic segment represented by an empty space of length d between the two magnetic segments (left of Figure 6a). To some extent, this theoretical NW can be approximated as a set of pairs of point magnetic charges. That is, the hard segment is assumed equivalent to two charges of values $-2q$ and $2q$, where q would correspond to $M_S\pi a^2/4$, located at the center of the lower and upper surfaces of the segment, respectively. In the same way, the soft segment can be simplified as two charges of values q and $-q$ located at the center of the lower and upper surfaces, respectively (right of Figure 6a). The sign of each pair of charges changes depending on the orientation of the segment magnetization. For simulating the NWs of sample D, the dimensions of the NWs are $a = c/10$ and $d = 2.5c$.

Once the NWs are properly magnetized (with the two segments aligned parallel or antiparallel) and dispersed in the fluid, they can be oriented in any direction. The relative orientation between two NWs can cause some attractive or repulsive movements between them because of the magnetic interaction that can result in the agglomeration of NWs. Figure 6 shows the possible ways of attractive interaction between NWs with antiparallel magnetic segments (Figure 6c) or parallel magnetic segments (Figures 6b and d). The symbols +, ++, - and --represent the equivalent charges $+q$, $+2q$, $-q$, and $-2q$, respectively, in the point charge approximation. In the case of antiparallel segments the NWs would be mainly attracted by forming a T-shape (Figure 6c) and in the parallel case the NWs attracted by following an antiferromagnetic coupling (Figure 6b) or by aligning one along the other (Figure 6d). Other configurations of NWs interactions have weaker attractive interaction.

To analyze which NW configurations have lower magnetic attraction and thus, weaker possibility of agglomeration, we plot in Figure 7 a comparison of the energies of the three different arrangements sketched in Figure 6. The magnetic interaction energy (normalized to $\mu_0 q^2/c$) of two NWs is plotted as a function of their distance w (normalized to c) when $d = 2.5c$. The results reveal that for interwire distances $w < c$ the interaction between T-shape NWs with antiparallel segments (solid black line) is lower than the one obtained in the case of antiferromagnetic coupled NWs with parallel segments (dashed red line). In these results the size of the nonmagnetic segment is a relevant parameter because if $d < c$ the "T-shape" NWs configuration becomes the one with the largest interaction (not shown). Note that for interwire distances $w < 0.1c$ (that is $w < a$) the model of point charges is no longer valid. The inset of Figure 7 shows the case of large interwire distances, with the same interaction energies plotted in logarithmic scale (in absolute value). For comparison, the dependences $1/w^3$ (thin solid green line) that correspond to a dipole-dipole magnetic interaction, and $1/w^5$ (thin dashed orange line), that correspond to a quadrupole-quadrupole magnetic interaction are also plotted. These calculations reveal that for large interwire distances ($w > 50c$) the interaction between T-shape NWs is the lowest one and decays as $1/w^5$ (black line is parallel to the orange one), whereas for the configurations with parallel segment NWs, it decays as $1/w^3$ (red and blue lines are parallel to the green one).

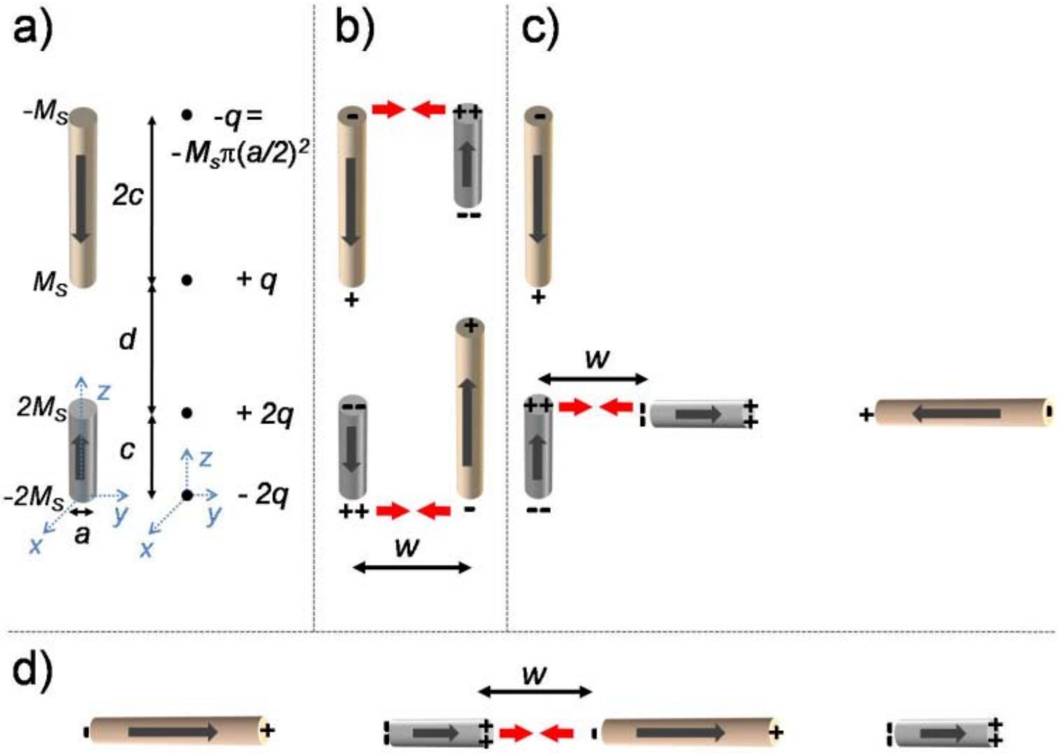

Figure 6. (a) (Left) Schematic portrayal of a trisegmented NW in antiferromagnetic (compensated) arrangement, where the hard segment (bottom) has length *c* and saturation magnetization 2 M_S and the soft segment (top) has length *c* and saturation magnetization M_S. The nonmagnetic segment is represented by the empty space of length *d* between the magnetic segments. The NW has diameter a. (right) Simplified representation of the NW as a set of point magnetic charges. (b-d) Different arrangements of NWs with attractive interactions (possibly leading to agglomeration) depending on the magnetization alignment between the magnetic segments, where *w* is the distance between wires. The symbols + and - indicate the sign of the equivalent charges and the red arrows represent an attractive interaction between NWs.

The results of this section demonstrate theoretically that the agglomeration power between NWs with parallel magnetic segments is always larger than for NWs with antiparallel segments. The results do not qualitatively change when considering charged surfaces instead of point charges.

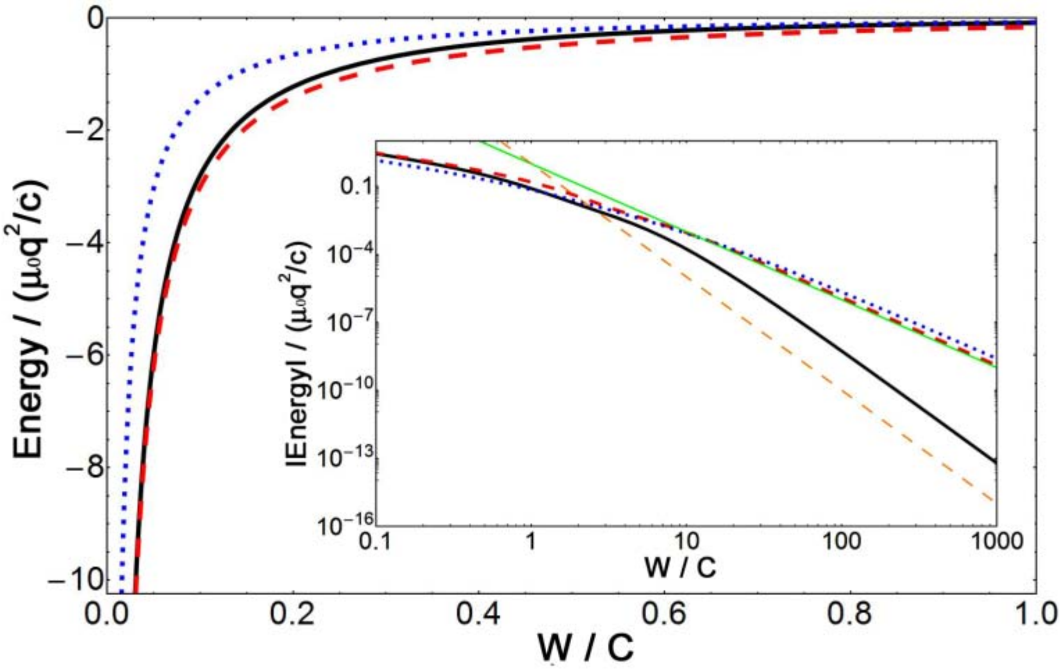

Figure 7. Interaction energy as a function of separation w between the NWs when *d* = 2.5*c* for the different NW configurations of Figure 6: parallel magnetization alignment of Figure 6b (dashed red line), antiparallel alignment of Figure 6c (solid black line) and parallel alignment of Figure 6d (dotted blue line). The inset shows the absolute value of the energy of the main plot in a logarithmic scale. For comparison the dependences $1/w^3$ (thin solid green line) and $1/w^5$ (thin dashed orange line) are also plotted in the inset.

4. CONCLUSIONS

In summary, arrays of tri-segmented CoPt/Cu/Ni NWs with tunable segment lengths have been satisfactorily electrodeposited inside the pores of PC membranes and subsequently further characterized both structurally and magnetically. These NWs exhibit staircase-like hysteresis loops resulting from the two different coercivities of the soft (Ni) and hard ferromagnetic (CoPt) segments. The magnetization amplitudes of the two ferromagnetic contributions depend on the relative lengths of CoPt and Ni. Antiparallel alignment between both ferromagnetic segments can be settled after positive saturation by applying a negative magnetic field sufficient to switch the Ni magnetization but smaller than the CoPt coercivity. In such antiparallel alignment, proper adjustment of the Ni and CoPt segment lengths eventually leads to virtually zero remanent magnetization (fully compensated NWs). The trisegmented NWs can be then released from the PC membrane and satisfactorily dispersed in fluids. Analytical calculations are employed to corroborate that the magnetic interaction energy between two fully compensated trisegmented NWs (with two antiparallel magnetic segments with the same overall magnetic moment) is reduced with respect to a single NW with the same length or the tri-segmented NW with the two segments parallel to each other. Hence, this strategy is suitable to decrease the strength of magnetic interactions between NWs dispersed in liquids and is thus very appealing in all applications requiring the utilization of well-isolated magnetic single NWs, as well as to minimize NWs agglomeration during/after usage.

ACKNOWLEDGEMENTS

This work has been partially funded by the 2014-SGR-1015, 2014-SGR-150 and 2014-PROD-00059 projects from the Generalitat de Catalunya, the MAT2014-57960-C3-1-R (co-funded by FEDER), MAT2012-35370, MAT2013-41506, and CSD2009-00013 projects from the Spanish Ministerio de Economía y Competitividad (MINECO) and the the MANAQA FET-Open Project from the European Commission (FP7) under the Grant Agreement 296679 and the ERS CoG 648454 SPIN-PORICS. J.Z. is grateful to the China Scholarship Council (CSC) for the PhD grant. E.P. is grateful to MINECO for the “Ramon y Cajal” contract (RYC-2012-10839). A.S. acknowledges a grant from ICREA Academia, funded by the Generalitat de Catalunya. ICN2 acknowledges support from the Severo Ochoa Program (MINECO, Grant No. SEV-2013-0295).

Supporting information

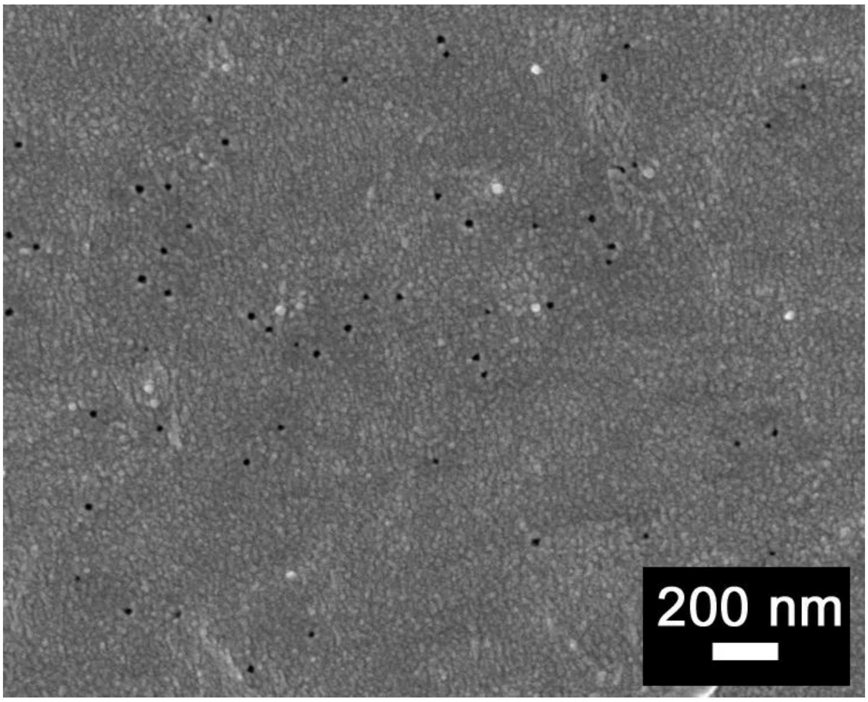

Figure S1. SEM image of polycarbonate (PC) membrane with an average pore size of 50 nm.

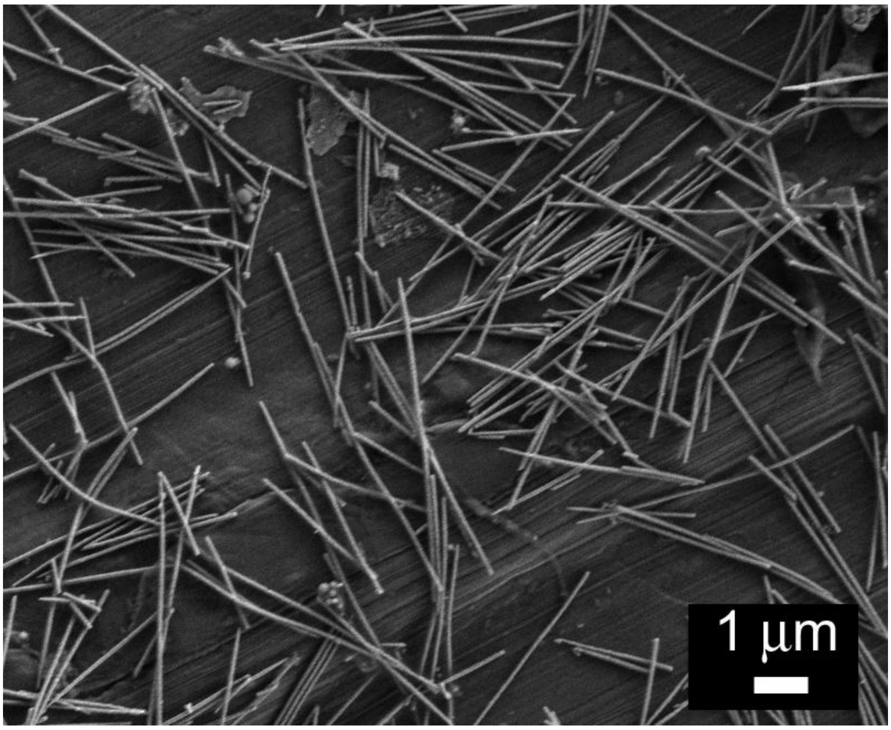

Figure S2. SEM image of single-segmented Cu nanowires released from the PC membrane.

REFERENCES

(1) Brambilla, G. Optical Fibre Nanowires and Microwires: A Review. *J. Opt.* **2010**, *12*, 043001–043020.

(2) O'Brien, L.; Petit, D.; Lewis, E. R.; Cowburn, R. P.; Read, D. E.; Sampaio, J.; Zeng, H. T.; Jausovec, A.-V. Tunable Remote Pinning of Domain Walls in Magnetic Nanowires. *Phys. Rev. Lett.* **2011**, *106*, 087204.

(3) Vázquez, M.; Vivas, L. G. Magnetization Reversal in Co-Base Nanowire Arrays. *Phys. Status. Solidi.* **2011**, *248*, 2368–2381.

(4) Sun, Y.; Zhang, F.; Xu, L.; Yin, Z.; Song, X. Roughness-Controlled Copper Nanowires and Cu nanowires–Ag Heterostructures: Synthesis and Their Enhanced Catalysis. *J. Mater. Chem. A* **2014**, *2*, 18583–18592.

(5) Espinosa, H. D.; Bernal, R. A; Minary-Jolandan, M. A Review of Mechanical and Electromechanical Properties of Piezoelectric Nanowires. *Adv. Mater.* **2012**, *24*, 4656–4675.

(6) Farhangfar, S. Size-Dependent Thermoelectricity in Nanowires. *J. Phys. D: Appl. Phys.* **2011**, *44*, 125403.

(7) Yogeswaran, U.; Chen, S. A Review on the Electrochemical Sensors and Biosensors Composed of Nanowires as Sensing Material. *Sensors* **2008**, *8*, 290–313.

(8) Zheng, G.; Patolsky, F.; Cui, Y.; Wang, W. U.; Lieber, C. M. Multiplexed Electrical Detection of Cancer Markers with Nanowire Sensor Arrays. *Nat. Biotechnol.* **2005**, *23*, 1294–1301.

(9) Fan, D. L.; Zhu, F. Q.; Cammarata, R. C.; Chien, C. L. Controllable High-Speed Rotation of Nanowires. *Phys. Rev. Lett.* **2005**, *94*, 247208.

(10) Kou, X.; Fan, X.; Dumas, R. K.; Lu, Q.; Zhang, Y.; Zhu, H.; Zhang, X.; Liu, K.; Xiao, J. Q. Memory Effect in Magnetic Nanowire Arrays. *Adv. Mater.* **2011**, *23*, 1393–1397.

(11) Parkin, S. S. P.; Hayashi, M.; Thomas, L. Magnetic Domain-Wall Racetrack Memory. *Science* **2008**, *320*, 190–194.

(12) Zhang, Z.; Dai, Y.; Yu, L.; Guo, M.; Huang, B.; Whangbo, M.-H. The Surface Termination Effect on the Quantum Confinement and Electron Affinities of 3C-SiC Quantum Dots: A First-Principles Study. *Nanoscale* **2012**, *4*, 1592–1597.

(13) Winkler, A.; Mühl, T.; Menzel, S.; Kozhuharova-Koseva, R.; Hampel, S.; Leonhardt, A.; Büchner, B. Magnetic Force Microscopy Sensors Using Iron-Filled Carbon Nanotubes. *J. Appl. Phys.* **2006**, *99*, 104905.

(14) Choi, D. S.; Park, J.; Kim, S.; Gracias, D. H.; Cho, M. K.; Kim, Y. K.; Fung, A.; Lee, S. E.; Chen, Y.; Khanal, S.; Baral, S.; Kim, J.-H. Hyperthermia with Magnetic Nanowires for Inactivating Living Cells. *J. Nanosci. Nanotechnol.* **2008**, *8*, 2323–2327.

(15) Prida, V. M.; García, J.; Iglesias, L.; Vega, V.; Görlitz, D.; Nielsch, K.; Barriga-Castro, E. D.; Mendoza-Reséndez, R.; Ponce, A.; Luna, C. Electroplating and Magnetostructural Characterization of Multisegmented $Co_{54}Ni_{46}/Co_{85}Ni_{15}$ Nanowires from Single Electrochemical Bath in Anodic Alumina Templates. *Nanoscale Res. Lett.* **2013**, *8*, 263.

(16) Choi, J.; Oh, S. J.; Ju, H.; Cheon, J. Massive Fabrication of Free-Standing One-Dimensional Co/Pt Nanostructures and Modulation of Ferromagnetism via a Programmable Barcode Layer Effect. *Nano lett*. **2005**, *5*, 2179-2183.

(17) Bangar, M. A.; Hangarter, C. M.; Yoo, B.; Rheem, Y.; Chen, W.; Mulchandani, A.; Myung, N. V. Magnetically Assembled Multisegmented Nanowires and Their Applications. *Electroanalysis* **2009**, *21*, 61–67.

(18) Özkale, B.; Shamsudhin, N.; Chatzipirpiridis, G.; Hoop, M.; Gramm, F.; Chen, X.; Martí, X.; Sort, J.; Pellicer, E.; Pané, S. Multisegmented FeCo/Cu Nanowires: Electrosynthesis, Characterization, and Magnetic Control of Biomolecule Desorption. *ACS Appl. Mater. Interfaces* **2015**, *7*, 7389–7396.

(19) Zeeshan, M. A.; Pané, S.; Youn, S. K.; Pellicer, E.; Schuerle, S.; Sort, J.; Fusco, S.; Lindo, A. M.; Park, H. G.; Nelson, B. J. Graphite Coating of Iron Nanowires for Nanorobotic Applications: Synthesis, Characterization and Magnetic Wireless Manipulation. *Adv. Funct. Mater.* **2013**, *23*, 823–831.

(20) Piraux, L.; George, J.M.; Despres J. F.; Leroy C.; Ferain, E.; Legras, R.; Ounadjela, K.; Fert, A. Giant Magnetoresistance in Magnetic Multilayered Nanowires. *Appl. Phys. Lett*. **1994**, *65*, 2484-2486.

(21) Liu, K.; Nagodawithana, K.; Searson, P. C.; Chien, C. L. Perpendicular Giant Magnetoresistance of Multilayered Co/Cu nanowires. *Phys. Rev. B* **1995**, *51*, 7381-7384.

(22) Doudin, B.; Redmond, G.; Gilbert, S. E.; Ansermet, J. –Ph. Magnetoresistance Governed by Fluctuations in Ultrasmall Ni/NiO/Co Junction. *Phys. Rev. Lett.* **1997**, *79*, 933-936.

(23) Chong, Y. T.; Görlitz, D.; Martens, S.; Yau, M. Y. E.; Allende, S.; Bachmann, J.; Nielsch, K. Multilayered Core/Shell Nanowires Displaying Two Distince Magnetic Switching Events. *Adv. Mater*. **2010**, *22*, 2435-2439.

(24) Piraux, L.; Renard, K.; Guillemet, R.; Mátéfi-Tempfli, S.; Mátéfi-Tempfli, M.; Antohe, V. A.; Fusil, S.; Bouzehouane, K.; Cros, V. Template-Grown NiFe/Cu/NiFe Nanowires for Spin Transfer Devices. *Nano lett*. **2007**, *7*, 2563-2567.

(25) Gapin, A. I.; Ye, X. R.; Chen, L. H.; Hong, D.; Jin, S. Patterned Media Based on Soft / Hard Composite Nanowire Array of Ni/CoPt. *IEEE Trans. Magn.* **2007**, *43*, 2151–2153.

(26) Salabas, E. L.; Rumplecker, A.; Kleitz, F.; Radu, F. Schuth, F. Exchange Anisotropy in Nanocasted Co_3O_4 Nanowires. *Nano lett*. **2006**, *6*, 2977–2981.

(27) Mourachkine, A.; Yazyev, O. V.; Ducati, C.; Ansermet, J. Template Nanowires for Spintronics Applications : Nanomagnet Microwave Resonators Functioning in Zero Applied. *Nano lett*. **2008**, *8*, 3683-3687.

(28) Zhang, Y.; Ashall, B.; Doyle, G.; Zerulla, D.; Lee, G. U. Highly Ordered Fe−Au Heterostructured Nanorod Arrays and Their Exceptional Near-Infrared Plasmonic Signature. *Langmiur* **2012**, *28*, 17101-17107.

(29) Su, Y.; Tang, J.; Yang, H.; Cheng, Z. Multifunctional Multisegmented Co/CoPt$_3$ Heterostructure Nanowires. *Nanoscale* **2013**, *5*, 9709-9713.

(30) Gao, W.; Manesh, K. M.; Hua, J.; Sattayasamitsathit, S.; Wang, J. Hybrid Nanomotor: A Catalytically/Magnetically Powered Adaptive Nanowire Swimmer. *Small* **2011**, *7*, 2047–2051.

(31) Alvarez-Lorenzo, C.; Concheiro, A. Smart Drug Delivery Systems: From Fundamentals to the Clinic. *Chem. Commun.* **2014**, *50*, 7743-7765.

(32) Reich, D. H.; Tanase, M.; Hultgren, A.; Bauer, L. A.; Chen, C. S.; Meyer, G. J. Biological Applications of Multifunctional Magnetic Nanowires (invited). *J. Appl. Phys.* **2003**, *93*, 7275-7280.

(33) Gao, F.; Gu, Z. Nano-Soldering of Magnetically Aligned Three-Dimensional Nanowire Networks. *Nanotechnology* **2010**, *21*, 115604.

(34) Kim, D.-H.; Rozhkova, E. A.; Ulasov, I. V.; Bader, S. D.; Rajh, T.; Lesniak, M. S.; Novosad, V. Biofunctionalized Magnetic-Vortex Microdiscs for Targeted Cancer-Cell Destruction. *Nat. Mater.* **2010**, *9*, 165–171.

(35) Chen, M.; Chien, C. L.; Searson P. C. Potential Modulated Multilayer Deposition of Multisegment Cu/Ni Nanowires with Tunable Magnetic Properties. *Chem. Mater*. **2006**, *18*, 1595-1601.

(36) Wong, J.; Greene, P.; Dumas, R. K.; Liu, K. Probing Magnetic Configurations in Co/Cu Multilayered Nanowires. *Appl. Phys. Lett*. **2009**, *94*, 032504.

(37) Sort, J.; Rodmacq, B.; Auffret, S.; Dieny, B. Pinned Synthetic Ferrimagnets with Perpendicular Anisotropy and Tuneable Exchange Bias. *Appl. Phys. Lett*. **2003**, *83*, 1800-1802.

(38) Baltz, V.; Rodmacq, B.; Bollero, A.; Ferré, J.; Landis, S.; Dieny, B. Balancing Interlayer Dipolar Interactions in Multilevel Patterned Media with Out-of-Plane Magnetic Anisotropy. *Appl. Phys. Lett*. **2009**, *94*, 052503.

(39) Estradé, S.; Arbiol, J.; Peiró, F.; Abad, L.; Laukhin, V.; Balcells, L.; Martínez, B. Cationic Diffusion in $La_{2/3}Ca_{1/3}MnO_3$ Thin Films Grown on $LaAlO_3$ (001) Substrates. *Appl. Phys. Lett*. **2007**, *91*, 252503.

(40) López-Ortega, A.; Estrader, M.; Salazar-Alvarez, G.; Roca, A. G.; Nogués, J. Applications of Exchange Coupled Bi-Magnetic Hard/soft and Soft/hard Magnetic Core/shell Nanoparticles. *Phys. Rep.* **2015**, *553*, 1–32

(41) Yedra, L.; Xuriguera, E.; Estrader, M.; López-Ortega, A.; Baró, M. D.; Nogués, J.; Roldan, M.; Varela, M.; Estradé, S.; Peiró, F. Oxide Wizard: An EELS Application to Characterize the White Lines of Transition Metal Edges. *Microsc. Microanal*. **2014**, *20*, 698–705.

(42) Schönenberger, C.; Van der Zande, B. M. I.; Fokkink, L. G. J.; Henny, M.; Schmid, C.; Krüger, M.; Bachtold, A.; Huber, R.; Birk, H.; Staufer, U. Template Synthesis of Nanowires in Porous Polycarbonate Membranes: Electrochemistry and Morphology. *J. Phys. Chem. B* **1997**, *5647*, 5497–5505.

(43) Jang, B.; Pellicer, E.; Guerrero, M.; Chen, X.; Choi, H.; Nelson, B. J.; Sort, J.; Pané, S. Fabrication of Segmented Au/Co/Au Nanowires : Insights in the Quality of Co/Au Junctions. *ACS Appl. Mater. Interf*aces **2014**, *6*, 14583-14589.

(44) Agramunt-Puig, S.; Del-Valle, N.; Pellicer, E.; Zhang, J.; Nogués, J.; Navau, C.; Sanchez, A.; Sort, J.; Modeling the Collective Magnetic Behavior of Highly-packed Arrays of Multi-segmented Nanowires. *New J. Phys.* **2016**, *18*, 013026.

(45) Ferré, R.; Ounadjela, K.; George, J. M.; Piraux, L.; Dubois, S. Magnetization Processes in Nickel and Cobalt Electrodeposited Nanowires. *Phys. Rev. B* **1997**, *56*, 14066–14075.

(46) Mitsuzuka, K.; Shimatsu, T.; Kikuchi, N.; Okamoto, S.; Aoi, H.; Kitakami, O. Remanence Coercivity of Dot Arrays of Hcp-CoPt Perpendicular Films. *J. Phys.: Conf. Ser.* **2010**, *200*, 102005.

(47) Mallet, J.; Yu-Zhang, K.; Chien, C.-L.; Eagleton, T. S.; Searson, P. C. Fabrication and Magnetic Properties of Fcc Co_XPt_{1-X} Nanowires. *Appl. Phys. Lett*. **2004**, *84*, 3900-3902.

(48) Zhang, L.; Petit, T.; Lu, Y.; Kratochvil, B. E.; Peyer, K. E.; Pei, R.; Lou, J.; Nelson, B. J. Controlled Propulsion and Cargo Transport of Rotating Nickel Nanowires Near a Patterned Solid Surface. *ACS Nano* **2010**, *4*, 6228–6234.

Table of Contents Graphic

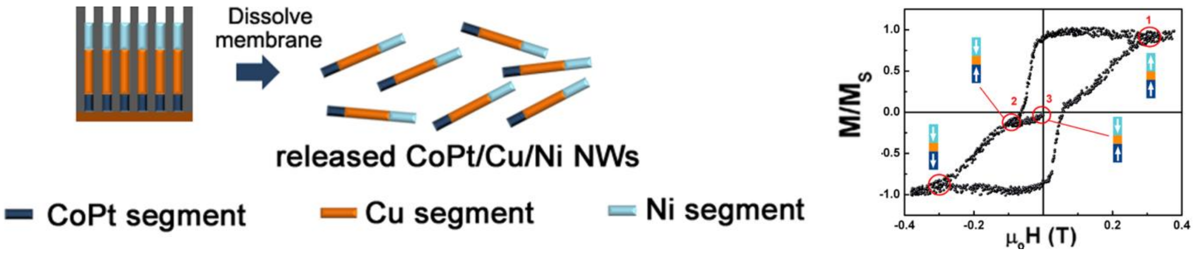

3.4 Modeling the collective magnetic behavior of highly-packed arrays of multi-segmented nanowires

In this article we report on a powerful model to calculate in a time-effective manner the collective magnetic response of large arrays of tri-segmented magnetic NWs (i.e., comprising two magnetic segments with different coercivity separated by a non-magnetic spacer). Simulations were run by the Superconductivity Group members from Autonomous University of Barcelona. Several meetings between this group and Gnm^3 group members (including myself) were carried out in the framework of this study in order to approach the theoretical findings with the experimental results. This work was performed in parallel with the study on CoPt/Cu/Ni NWs represented in section 3.2, and thereby it is included in the thesis.

The model is based on a coarse discretization of the NWs in which each box is considered as a single magnetic dipole. After validating the approximations by comparison with micromagnetic simulations, the magnetic response of large arrays of NWs is presented. The model predicts the distances over which NWs do not interact appreciably with their neighbors. At the same time, it is demonstrated that NWs made of segments of different coercivity and saturation magnetization can be used to attain antiparallel or parallel magnetic alignment, as required in magnetic sensors based on the GMR effect and other applications based on multiple magnetic states (e.g. multi-bit recording media).

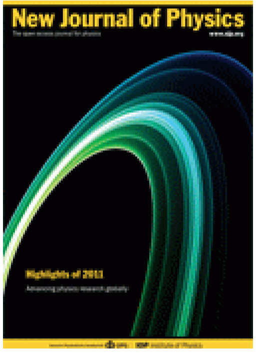

Modeling the Collective Magnetic Behavior of Highly-packed Arrays of Multi-Segmented Nanowires

S. Agramunt-Puig[1], *N. Del-Valle*[1], *E. Pellicer*[1], *J. Zhang*[1], *J. Nogués*[2,3], *C. Navau*[1], *A. Sanchez*[1,*], *J. Sort*[1,3]

[1]Departament de Física, Universitat Autònoma de Barcelona, 08193 Bellaterra, Barcelona, Catalonia, Spain

[2]Catalan Institute of Nanoscience and Nanotechnology (ICN2), CSIC and The Barcelona Institute of Science and Technology, Campus UAB, Bellaterra, 08193 Barcelona, Spain

[3]Institució Catalana de Recerca i Estudis Avaçats (ICREA), Barcelona, Catalonia, Spain

*To whom correspondence should be addressed:

Prof. Alvar Sanchez

Email: Alvar.Sanchez@uab.cat

Abstract

A powerful model to evaluate the collective magnetic response of large arrays of segmented nanowires comprising two magnetic segments of dissimilar coercivity separated by a non-magnetic spacer is introduced. The model captures the essential aspects of the underlying physics in these systems while being at the same time computationally tractable for relatively large arrays. The minimum lateral and vertical distances rendering densely packed weakly-interacting nanowires and segments are calculated for optimizing their performance in applications like magnetic sensors or recording media. The obtained results are appealing for the design of multifunctional miniaturized devices actuated by external magnetic fields, whose successful implementation relies on achieving a delicate balance between two opposing tec$_{hn}$ological demands: the need for an ultra-high density of nanowires per unit area and the minimization of inter-wire and inter-segment dipolar interactions.

Keywords: nanowires, micromagnetics, nanomagnetism

Owing to their anisotropic shape and reduced lateral sizes, one-dimensional nanostructures (e.g., nanowires, nanotubes or nanorods) have boosted a wealth of applications in diverse technological areas, such as electronics and optoelectronics, magnetic memory units, biological sensors, gas sensors, spintronic devices or micro-/nano-electro-mechanical systems, amongst others [1-3]. The elongated shape of these nano-objects promotes mutual interactions along preferential directions when these structures are arranged or assembled together to form an array, hence leading to physical properties that are highly anisotropic.

An additional advantage of nanowires with respect to isotropic nanoparticles is that it is relatively easy to sequentially grow and combine various segments of dissimilar materials, each exhibiting different physico-chemical properties, along the length of the nanowire [1,4,5]. This renders multifunctionality to the obtained hybrid materials. Without being exhaustive, some recent examples of this type of materials are: Au /polypyrrole/Ni nanowires that simultaneously contain a biofunctionalizable segment (Au) and a ferromagnetic segment (Ni) that allows magnetic alignment and wireless manipulation [6]; Co/Cu and FeCoNi/Cu multilayered (barcode) nanowires displaying giant magnetoresistance (GMR) effect, suitable for magnetic field sensors and spintronic nanodevices [7-10]; Ag/ZnO nanowires suitable for photocatalysis, photochemical conversion and hydrogen generation [11]; CdTe/Au/CdTe trilayered nanowires for detection of DNA molecules [12]; FeCo/Cu barcode nanowires for magnetic control of biomolecule desorption [13]; Ni/CoPt exchange coupled patterned media [14,15]; multilevel recording [16,17] and so on. The progress in all these applications has been possible due to the tremendous advancement in the various synthetic methods to fabricate hybrid nanowires, including electrodeposition inside the pores of hard templates, electrospinning, or one-dimensional conjugation of building blocks (e.g., nanoparticles) [1,5].

In terms of magnetic applications, the use of arrays of multisegmented nanowires instead of multilayered magnetic continuous films is appealing for several reasons: (i) GMR elements with current-perpendicular-to-plane geometry can be easily fabricated in high-aspect ratio structures (such as nanowires) [18], minimizing the variation of the intralayer thicknesses, which is detrimental for the GMR effect; (ii) a large number of segments with uniform thickness can be obtained in a fast and inexpensive way using pulse electrodeposition, thus enhancing the GMR effect by virtue of the increase in the number of magnetic layers with antiparallel orientation; (iii) a high areal density of multiplex sensors can be prepared for the simultaneous detection of several chemical agents, in the form of miniaturized devices. In all these cases, though, it is of upmost importance to be able to fully control the orientation of the different magnetic segments comprising the nanowires. This is possible by the use of external magnetic fields, provided that each magnetic segment exhibits a well-defined, sufficiently different, coercivity value. However, if the interwire lateral distance and/or the separation between the magnetic segments inside each nanowire are exceedingly small, then dipolar magnetic interactions are enhanced and can cause undesirable magnetic switching and concomitant loss in the functionality of the hybrid nanowires. Dipolar interactions are indeed detrimental for the magnetic stability of the multi-segmented nanowires, since the magnetic switching of one layer or nanowire may accidentally switch the neighboring ones.

Hence, a clear understanding of the effects of magnetic interactions as a function of the geometrical arrangement of the hybrid nanowires is indispensable to optimize their performance. However, this problem is difficult to be theoretically tackled by conventional micromagnetic simulations, because the computation time drastically rises as the number of simulated ferromagnetic elements is progressively increased [19]. Hence there is an increasing need to develop new, time-saving, models to simulate the collective behavior large arrays of complex nanowires.

In this article we introduce an efficient model to simulate the collective magnetic behavior of large arrays of multi-segmented nanowires with a high aspect-ratio (length-to-diameter ratio, c/a = 5). This model is based on a coarse discretization of the nanowires in boxes, each considered as a single magnetic dipole, interacting magnetostatically with the other boxes. After validating the approximations by comparison with more accurate calculations (i.e., analytic and micromagnetics), we study the magnetic response of large arrays of nanowires, including the case of segmented wires. The results show that stable, well-defined, magnetization states can be obtained, provided that the wires are approximately separated in the horizontal direction a distance 1.5-2 times their diameter and the segments are about one diameter apart in the vertical direction (depending on the anisotropy of the hard phase).

The reversal modes of single nanowires have been studied widely in the literature [20-25]. Analytical calculations evidence, depending on the relation between the exchange length (l_{ex}) and the length-to-diameter ratio, two main reversal modes, coherent rotation and curling, although more advanced analyses have shown the possibility of reversal by nucleation of transverse domain walls [26-28]. Moreover, micromagnetic simulations have demonstrated other reversal modes like nucleation, propagation and annihilation of 3D vortex states [29, 30].

In arrays of such nanowires the field at which the magnetization deviates from uniformity, H_{du}, is particularly complex to study since it must be calculated over each of them and taking into account the whole ensemble of nanowires. Analytic studies assuming hexagonal arrangement of nanowires have shown the need for adding an additional term to the H_{du} of a single nanowire [20, 31]. This term may be interpreted as an average of the magnetostatic field and thus it depends linearly on the saturation magnetization and the density of nanowires [32] (e.g., the porosity of the template used to fabricate them [33]). This magnetostatic field reduces the H_{du} predicted for coherent and curling modes in single nanowires [20]. Other methods involve calculating the field of neighboring nanowires using accurate methods, but describing the field of further wires as a continuum [34,35]. Micromagnetic calculations have been performed considering few nanowires [36] or applying periodic conditions to the algorithm [37]. In spite of these efforts, reliable tools to systematically scale up to a representative large number of nanowires are still lacking.

We first consider a nanowire with the shape of a prism with square base of side a and length c (see inset in figure. 1(a)). The nanowire is divided into cubic boxes of side a, with a dipole of magnitude $M_{\mathrm{S}}a^3$ in the middle of each box, where M_{S} is the saturation magnetization of the material. We assume that the whole nanowire is uniformly magnetized either in the positive or negative z direction (along the c direction) and we evaluate the total field at the center of each box, that is the sum of the applied field and magnetostatic fields created by all other boxes in the same nanowire and in neighboring nanowires. The magnetization of the nanowire switches when the maximum (in absolute value) of the z component of the total field is opposed to the overall nanowire magnetization and is larger than a certain threshold H_{crit}. This criterion can be mathematically formulated as follows. All boxes have the same magnetization $\vec{M} = \pm M_s\hat{z} = M\hat{z}$ and the field created by the j box at the center of the i box is $\vec{H}_{ij} = H_{ij}\hat{z} = \frac{Ma^3}{2\pi {d_{ij}}^3}\hat{z}$, where d_{ij} is the distance between the centers of boxes i and j. Since the applied field is $\vec{H}_a = H_a\hat{z}$, the total field at the center of the i box is

$$\vec{H}_i = \vec{H}_a + \textstyle\sum_{j\neq i}\vec{H}_{ij} = (H_a + \sum_{j\neq i} H_{ij})\hat{z} = H_i\hat{z}. \tag{1}$$

If k is the box where $|H_i|$ is maximum for all i, then the magnetization of the nanowire switches when $|H_k| > H_{\mathrm{crit}}$ and $\mathrm{sign}(H_k) = -\mathrm{sign}(M)$.

When this criterion is fulfilled, all the boxes of the nanowire switch together. The parameter H_{crit} takes implicitly into account the anisotropy of the involved materials. In the case of ideally soft (i.e., no magneto-crystalline anisotropy) nanowires, for simplicity, we assume $H_{\mathrm{crit}} = 0$. For the case of hard (large magneto-crystalline anisotropy) nanowires this threshold is taken of the order of saturation magnetization M_S, $H_{\mathrm{crit}} \sim M_S$ (similar to [38] for hard magnetic materials). One could choose Fe and CoPt as soft and hard ferromagnetic materials, respectively, as examples of actual materials.

The weaker magnetostatic field (in absolute value) is at the wire edges [39] (having less neighboring boxes), so H_{du} of an isolated soft nanowire is equal to the magnetostatic field at a box at the tip of the wire. This can be calculated as the sum of the magnetostatic fields that all the cells (with a magnetic dipole each one) create to the one at the edge, which can be analytically calculated as

$$\frac{H_{du}}{M_S} = \frac{H_1}{M_S} = \sum_{j=2}^{c/a} \frac{a^3}{2\pi {d_{1j}}^3} = \sum_{j=2}^{c/a} \frac{a^3}{2\pi \left|\vec{r_1} - \vec{r_j}\right|^3} = \sum_{j=2}^{c/a} \frac{a^3}{2\pi \left|z_1 - z_j\right|^3} = \sum_{j=2}^{c/a} \frac{a^3}{2\pi \left((j-1)a\right)^3} =$$

$$\frac{1}{2\pi} \sum_{j=2}^{c/a} \frac{1}{(j-1)^3} = \frac{1}{4\pi} [\ \ \left(\frac{c}{a}\right) + 2\ \ (3)] \,, \qquad (2)$$

where we have chosen the origin of coordinates at the center of the top box of the nanowire, so the each box is placed at $\vec{r_i} = z_i \hat{z} = -(i-1)a\hat{z}$ with i=1,...,c/a, and where (x) and (x) are Polygamma function of second order and the Riemann Zeta function, respectively. This expression can be obtained from Eq. 1 by setting H_a=0 and i=1, where 1 corresponds to the index of the edge box and c/a the number of the boxes in the NW. In figure 1 we analyze the case of an isolated nanowire. Figure 1a compares the results of this simple box model for soft nanowires ($H_{\mathrm{crit}} = 0$) having aspect ratio $c/a = 5$ with a micromagnetics simulation [40] (using $a = 4l_{\mathrm{ex}}$, where $l_{\mathrm{ex}} = \sqrt{\frac{2A}{\mu_0 M_S^2}}$ and A is the exchange stiffness constant). Note that, although we consider $H_{\mathrm{crit}} = 0$, the soft nanowire simulated by the box model has some coercivity due to the shape anisotropy. Namely, at zero-applied field, the total field (now only the magnetostatic field created by all the boxes of the nanowire) has the same direction as the magnetization of nanowire, thus there is no switching despite the $H_{\mathrm{crit}} = 0$.

Consequently, an extra field of opposite direction is required to overcome the dipolar field and hence induce the switching.

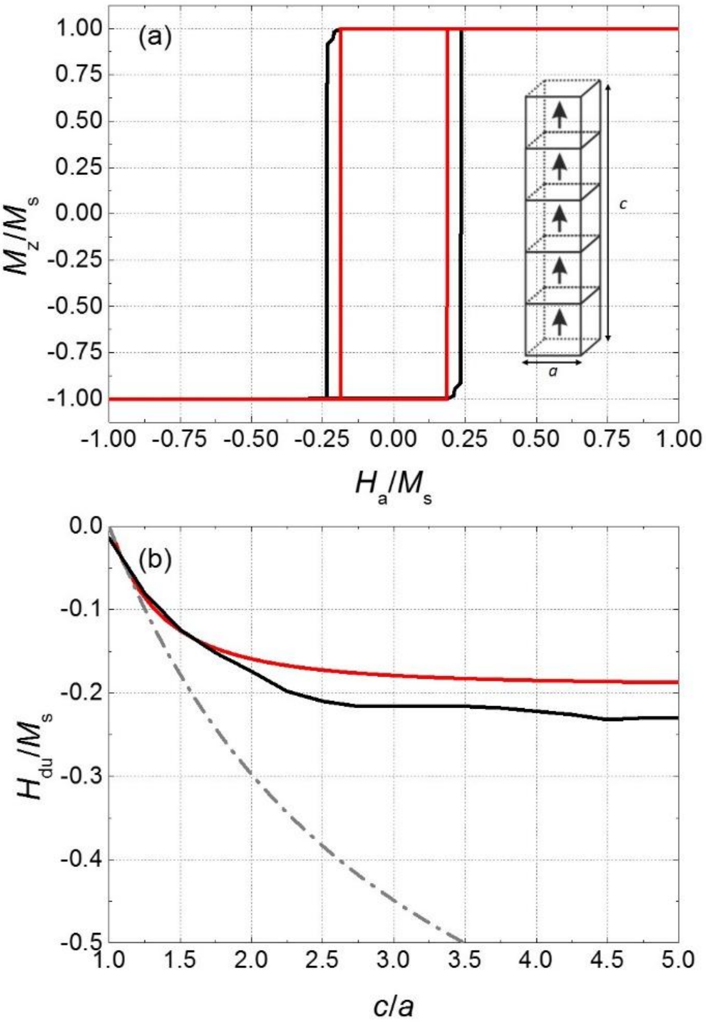

Figure 1 (a) Hysteresis loops for a single nanowire with aspect ratio *c/a*=5 using micromagnetic theory ($a = 4l_{ex}$) and our simplified box model with H_{crit}=0 (soft wires) in black and red curves, respectively. A schematic representation of a nanowire with *c/a*=5 is shown in the inset. (b) Normalized H_{du} as a function of the normalized length of the nanowire, *c*, for the cases: micromagnetic calculation for $a = 4l_{ex}$ (black curve), SW model for *a, c* << l_{ex} (grey dash-dotted curve), and the box model (solid red curve).

As seen in figure 1(a), the hysteresis loops calculated using micromagnetics and our simple box model are rather similar. Moreover, in the micromagnetics case, the deviation from uniformity field H_{du} and the switching field (field at which the magnetization switches its direction) are nearly the same. This allows considering only uniform states during the nanowire magnetization reversal in the box model, and therefore the only parameter that characterizes each hysteresis loop is H_{du}. To further verify the validity of our model, in figure 1(b) we plot the normalized deviation from uniformity field H_{du}/M_s as a function of the aspect ratio c/a of the nanowire using micromagnetics (assuming $a = 4l_{ex}$), and the box model using Eq. 2. For reference, we also plot the case c, $a \ll l_{ex}$, corresponding to the classical Stoner-Wohlfarth (SW) case [41], in which the magnetization remains uniform due to the large exchange interaction (only valid if the nanowire has very small dimensions). All calculations converge to the same $H_{du} = 0$ when the nanowire becomes a cube ($c = a$), because in this case the magnetostatic energy does not depend on the magnetization direction (i.e., no shape anisotropy). For larger c/a, H_{du} increases because of the difference in magnetostatic energy between the magnetization parallel and perpendicular to the wire, as predicted in [41]. For all aspect ratios, the largest (negative) H_{du} corresponds to the SW limit in which not only the magnetization is uniform, as in the box model, but also the demagnetizing field is. Micromagnetic calculations allow for small deviations of the magnetization (e.g., the formation of 3D flower states at the edges of the wires), therefore decreasing the magnetostatic energy of the nanowire (with respect to the uniform case). This results in a reduction of the switching field with respect to the SW model. Interestingly, the H_{du} obtained from the simpler box model roughly follows the trend of the micromagnetic calculations in the whole range of c/a, although it shows a slightly smaller H_{du} field since it only considers the field at the edges of the nanowires (where it is weaker). However, the predicted H_{du} is reasonably similar to the one calculated with micromagnetics for the whole c/a range. These results justify the use of our simple box model instead of tedious micromagnetic calculations to undertake the analysis of the switching behavior of large arrays of nanowires. Actually, the computation time of both models depends mainly on the evaluation of the magnetostatic field over all the elements and it is thus proportional to the square of their number. Micromagnetic boxes have a typical length ~l_{ex} (or smaller) [42,43]. Instead, our model assumes that each box is a cube with side $\Delta_{box} = a$. Therefore, there are $(a/l_{ex})^3$ more micromagnetic cells than boxes, and as a consequence the calculation time when using the box model is reduced by a factor $(a/l_{ex})^6$. This implies that while the box model can treat a very large number of wires, the same arrangements turn computationally impossible to be treated by micromagnetics.

Next, we consider regular square arrays of $N_x \times N_y$ nanowires, with $N_x = N_y = N$, separated by a distance d along x and y directions (see sketch in figure. 2(b)). Starting from large (positive) applied fields, all the nanowires are initially magnetized in the same direction. Each wire experiences a negative field along z due to the magnetostatic interaction with the rest of the wires, which will depend on the distance between them. In general, the overall magnetostatic field has a maximum (in absolute value) at the central nanowire (assuming N odd); therefore this wire is the one that switches first and determines H_{du} of the whole array. In figure 2(b) we show H_{du} for an $N = 20$ arrangement as a function of the inter-wire distance. When the nanowires get closer to each other ($d \rightarrow 0$) the switching field is large and positive, in the same direction as the initial magnetization. As the distance between nanowires is increased, their interaction becomes weaker and the deviation from uniformity field becomes negative, tending to the value for an isolated nanowire when d is large (see figure 1(b)). In particular, the magnetic interaction energy between two identical nanowires decreases with d and follows the dipole-dipole interaction dependence $1/d^3$ for $d > 2c$ ($d > 10a$) giving negligible long-range interaction values (see figure 2c) in agreement with figure 2b. Similar results were analytically predicted by Guslienko [44] in in-plane magnetized circular cylindrical dot arrays. Interestingly, the shape of the hysteresis loops of the arrays changes considerably with d compared to the one of isolated nanowires. The loops are no longer squared but tilted, as depicted in figure 2(a).

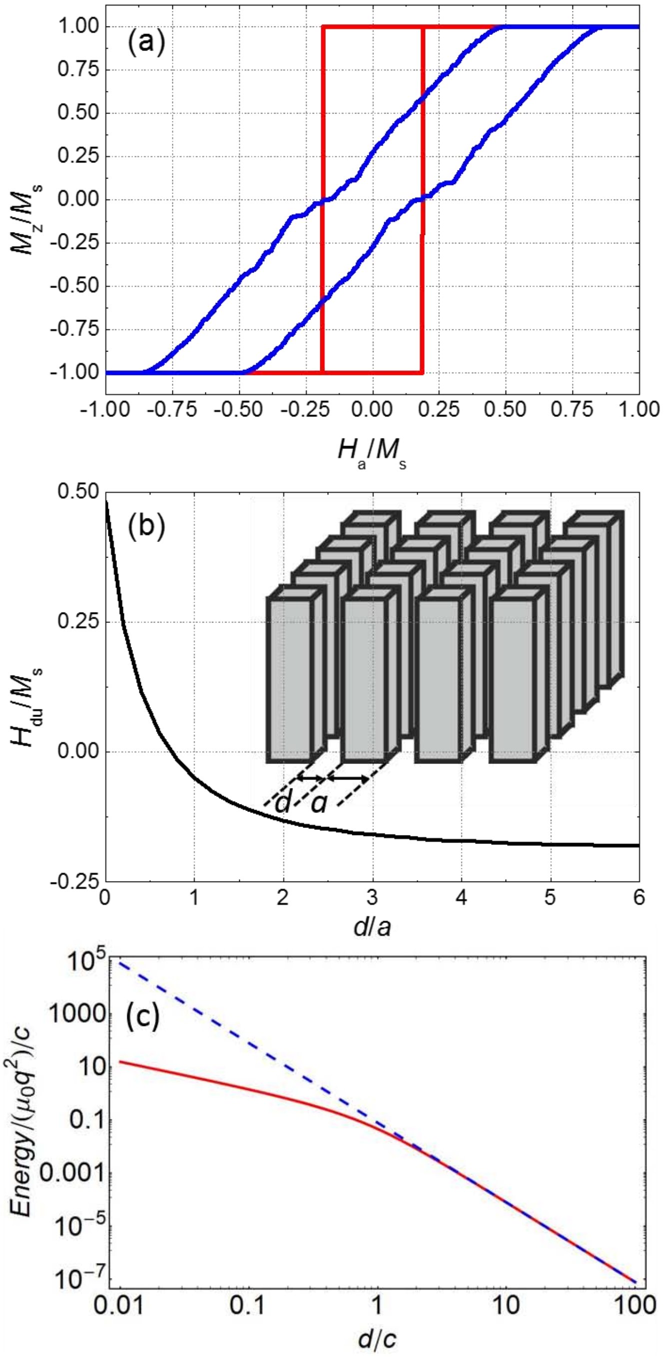

Figure 2 (a) Hysteresis loops for $d \to 0$ (blue) and $d \to \infty$ (red) for $N = 20$ with aspect ratio $c/a = 5$. (b) Normalized H_{du} for a sample with $N = 20$ as a function of the separation d. Shown in the inset is a schematic representation of the nanowire arrangement. (c) Normalized magnetic interaction energy as a function of the separation d for the cases of two identical uniformly z-magnetized nanowires with M_S (solid red), each one simulated as a pair of magnetic pointed charges of value $\pm q = \pm M_S a^2$ separated a vertical distance c, and two identical magnetic dipoles with magnetic moment $\overrightarrow{m_d} = M_S a^2 c\hat{z}$ (dashed blue).

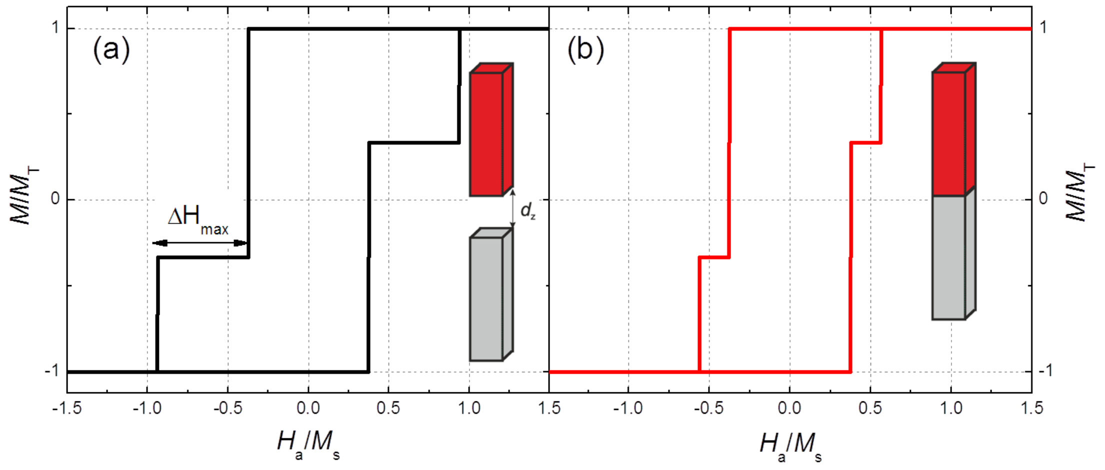

Figure 3 Hysteresis loops for a soft and a hard segment (see sketches) with c/a=5, separated (a) an infinite vertical distance ($d_z \rightarrow \infty$) and (b) at zero vertical distance ($d_z \rightarrow 0$).

We now consider segmented nanowires with a magnetically soft segment ($H_{crit} = 0$) and a hard segment ($H_{crit} = 3/4M_S$), both with aspect ratio $c/a = 5$. The saturation magnetization for the hard segment is M_S and for the soft one is $2M_S$, so when the whole nanowire is uniformly magnetized its overall saturation magnetization is $M_T = 3M_S/2$. Shown in figure 3(a) is the loop for a single segmented wire where two segments are infinitely separated along the wire ($d_z \rightarrow \infty$), so that they do not interact magnetostatically. The hysteresis loop is simply the weighted sum of their individual loops, where the first and second jumps correspond to the reversal of the soft and hard segments, respectively. As can be seen in figure 3(b), for a single segmented wire when the two segments are in close proximity but not in contact (i.e., $d_z \rightarrow 0$, interacting magnetostatically but neglecting exchange effects), the loop shows a very slightly increase in the switching field of the soft part and an appreciable decrease in the switching field of the hard part with respect to the non-interacting case ($d_z \rightarrow \infty$). In the interacting case, when saturated in a positive applied field the box that feels a weaker field in the soft part is the one away from the interface. Thus, the field at this cell determines the switching field, which increases only slightly because the field exerted by the hard segment over it is relatively weak and in the same direction as the magnetization. In contrast, once the soft segment has switched, the weaker magnetostatic field over the hard segment is in the interfacial box because of its proximity to the negatively magnetized soft segment, thus, the soft segment induces a field opposite to the magnetization of the hard segment therefore reducing its H_{du}.

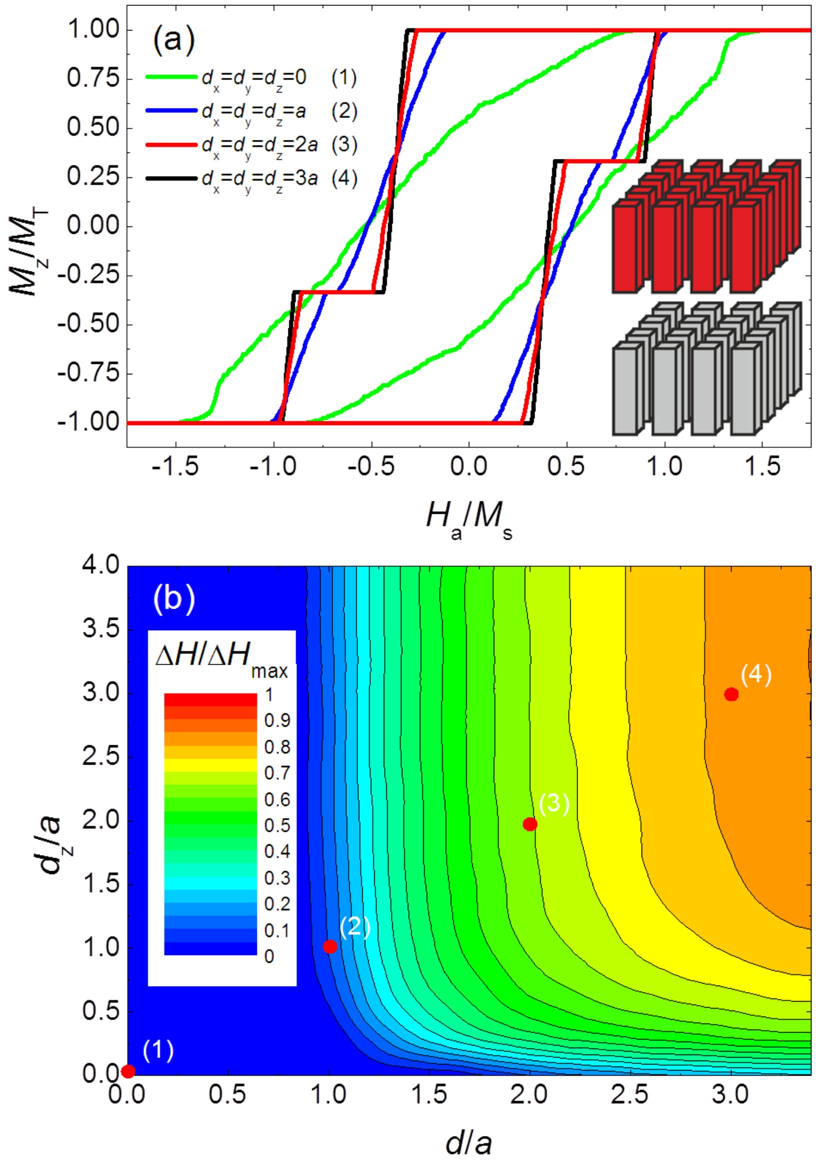

Figure 4 (a) Hysteresis loops for four arrangements of N = 20 arrays of hard/soft segmented nanowires, as shown schematically in the inset. The green curve corresponds to zero separation $d = d_z = 0$, blue to $d = d_z = a$, red to $d = d_z = 2a$, and black to $d = d_z = 3a$. (b) Normalized size of the field plateau, $\Delta H/\Delta H_{max}$, as a function of the normalized separation between nanowires in the horizontal direction, d, and vertical separation between soft and hard segments d_z in the vertical direction. Points (1)-(4) correspond to the cases plotted in (a).

To evaluate the feasibility to obtain multiple well-defined states using segmented wires, arrays of nanowires consisting of a soft and a hard segment (sketched in figure 4(a)) are considered. To optimize the design of the composite material, we analyze in a systematic way the effect of the in-plane distance of the wires in the array, d, and the distance between the soft and hard segments in each nanowire, d_z. As can be seen in figure 4(a), when their separation is large ($d \geq 2a$) the loop is almost the same as in figure 3(a), with well-established states, thus suitable for applications requiring multiple-states.

However, for very small distances the loop radically changes as a consequence of the interactions among the wires and their segments, leading to a rounded shape, not useful for most technological uses. To establish the boundary of d and d_z to attain two well-defined states in each hysteresis sub-loop we use the width of the plateau ΔH in the hysteresis loop as a quality parameter. To normalize it, we divide ΔH by its maximum possible value, ΔH_{max}, i.e., when all segments are completely isolated [see figure 3(a)]. In figure 4b we show $\Delta H/\Delta H_{max}$ for different in-plane (d) and out-of-plane (d_z) separations. It can be seen that for inter-wire distances below $d/a = 1$ the loop has no step, i.e., $\Delta H/\Delta H_{max} \sim 0$, thus, unusable for most purposes. If we set $\Delta H/\Delta H_{max} \sim 0.5$ as an indispensable requirement for a stable state, the minimum d suitable for applications would be about $1.5a$ (for moderate d_z). On the other hand, the system is less sensitive to the vertical separation d_z between wires. For example, for $d = 2a$ we would need only $d_z = 0.5a$ to fulfil the $\Delta H/\Delta H_{max} \sim 0.5$ criterion. These results indicate that the magnetostatic interaction from vertically separated segments is weaker than that for horizontal ones.

If the anisotropy of the hard segments is increased, for example by increasing the threshold to $H_{crit} = M_S$, we obtain a figure similar to figure 4(b) but with larger values of $\Delta H/\Delta H_{max}$ (not shown). The general trends are similar to figure. 4b although the data is shifted to the left and down, that is, for $d = 2a$ and $d_z = 0.5a$ we obtain $\Delta H/\Delta H_{max} \sim 0.7$. Consequently, to fulfil $\Delta H/\Delta H_{max} \sim 0.5$ criterion only $d = 1.5a$ and $d_z = 0.25a$ would be necessary for this higher anisotropy case. Hence, in principle, designing multi-level nanowires with higher anisotropies of the hard counterpart would be desirable to increase the magnetic stability while safely operating the system. However, the maxim field available from the electromagnetic coils to establish the orientation of the hard layer would set the limit for the maximum allowable anisotropy.

In conclusion, we have presented a simple but powerful model to describe the magnetization switching of large arrays of segmented nanowires. Our model is capable of predicting the distances over which nanowires do not interact appreciably with their neighbors (horizontal separation $d > a$). At the same time we demonstrate that nanowires made of segments of different coercivity and saturation magnetization can be used to attain antiparallel or parallel magnetic alignment, as required in magnetic sensors based on the GMR effect and other applications based on multiple-states. Thus, the model can become a useful tool to efficiently design future optimized spin-valve like sensors or even other applications, such as high-density multi-level recording media or magnetic encoders.

We acknowledge the support from the 2014-SGR-1015 and 2014-SGR-150 projects of the Generalitat de Catalunya, the MAT2012-35370 and MAT2014-57960-C3-1-R projects from the Spainish Ministerio de Economía y Competitividad (MINECO) -the latter cofinanced by the ´Fondo Europo de Desarrollo Regional´ (FEDER)-, the SPIN-PORICS 2014-Consolidator Grant (Grant Agreement 648454) from the European Research Countil (ERC), and the MANAQA project (grant agreement 296679) from European Community's Seventh Framework Programme (FET-Open/FP7/2007-2013). AS acknowledges funding from an ICREA Academia award. EP acknowledges the Spanish Ministerio de Economía y Competitividad (MINECO) for the 'Ramon y Cajal' contract (RYC-2012-10839). ICN2 acknowledges support from the Severo Ochoa Program (MINECO, Grant SEV-2013-0295).

References

[1] Yuan J, Xu Y and Müller A H E 2011 One-dimensional magnetic inorganic-organic hybrid nanomaterials *Chem. Soc. Rev.* **40** 640-655.

[2] Wanekaya A K, Chen W, Myung N V and Mulchandani A 2006 Nanowire-based electrochemical biosensors *Electroanalysis* **18** 533-550.

[3] Krahne R, Morello G, Figuerola A, George C, Deka S and Manna L 2011 Physical properties of elongated inorganic nanoparticles *Phys. Rep.* **501** 75.

[4] Lee W, Scholz R, Nielsch K and Gösele U 2005 A template-based electrochemical method for the synthesis of multisegmented metallic nanotubes *Angew. Chem.* **117** 6204-6208.

[5] Hurst S J, Payne E K, Qin L and Mirkin C A 2006 Multisegmented one-dimensional nanorods prepared by hard-template synthetic methods *Angew. Chem. Int. Ed.* **45** 2672-2692.

[6] Bangar M A, Hangarter C M, Yoo B, Rheem Y, Chen W, Mulchandani A and Myung N V 2009 Magnetically assembled multisegmented nanowires and their applications *Electroanalysis* **21** 61-67.

[7] Pullini D and Busquets-Mataix D 2011 Electrodeposition efficiency of Co and Cu in the fabrication of multilayer nanowires by polymeric track-etched templates *ACS Appl. Mater. Interf*. 3, 759- 764.

[8] Cox B, Davis D and Crews N 2013 Creating magnetic field sensors from GMR nanowire networks *Sens. Actuators A* **203**, 335-340.

[9] Piraux K, George J M, Despres J F, Leroy C, Ferain E, Legras R, Ounadjela K and Fert A 1994 Giant magnetoresistance in magnetic multilayered nanowires *Appl. Phys. Lett.* **65**, 2484-2486.

[10] Liu K, Nagodawithana K, Searson P C and Chien C L 1995 Perpendicular giant magnetoresistance of multilayered Co/Cu nanowires *Phys. Rev. B* **51** 7381(R)-7384(R).

[11] Maijenburg W, Rodijk E J B, Maas M G, Enculescu M, Blank D H A and ten Elshof J E 2011 Hydrogen generation from photocatalytic silver/zinc oxide nanowires: towards multifunctional multisegmented nanowire devices *Small* **7**, 2709-2713.

[12] Wang X and Ozkan C S 2008 Multisegment nanowire sensors for the detection of DNA molecules *Nano Lett.* **8** 398-404.

[13] Ozkale B *et al*. 2015 Multisegmented FeCo/Cu nanowires: electrosynthesis, characterization, and magnetic control of biomolecule desorption *ACS Appl. Mater. Interf*. 7, 7389-7396.

[14] Gapin A I, Ye X-R, Chen L-I , Hong D and Sungho J 2007 Patterned Media Based on Soft/Hard Composite Nanowire Array of Ni/CoPt *IEEE Trans. Magn.* **43** 2151-2153.

[15] Tanaka T, Matsuzaki J, Kurisu H and Yamamoto S 2008 Magnetization behavior of hard/soft-magnetic composite pillar *J. Magn. Magn. Mater.* **320** 3100-3103.

[16] Allende S, Vargas N M, Altbir D, Vega V, Görlitz D, and Nielsch K 2012 Magnetization reversal in multisegmented nanowires: Parallel and serial reversal modes *Appl. Phys. Lett.* **101** 122412.

[17] Cisternas E and Vogel E E 2015 Improving information storage by means of segmented magnetic nanowires *J. Magn. Magn. Mater.* **388** 35-39.

[18] Evans P R, Yi G, Schwarzacher W 2000 Current perpendicular to plane giant magnetoresistance of multilayered nanowires electrodeposited in anodic aluminum oxide membranes *Appl. Phys. Lett.* **76** 481-483.

[19] Miltat J E and Donahue M J 2007 Numerical Micromagnetics: Finite difference Methods. Handbook of Magnetism and Advanced Magnetic Materials (John Wiley & Sons, Ltd.).

[20] Vazquez M and Vivas, L G 2011 Magnetization reversal in Co-base nanowire arrays *Phys. Status Solidi B* **248** 2368-2381.

[21] Aharoni A 1996 *Introduction to the Theory of Ferromagnetism* (Oxford University Press, Oxford).

[22] Brown W F 1963 Thermal Fluctuations of a Single-Domain Particle *Phys. Rev.* **130** 1677-1686.

[23] Aharoni A 1997 Angular dependence of nucleation by curling in a prolate spheroid *J. Appl. Phys.* **82** 1281-1287.

[24] Frei E H, Shtrikman S and Treves D 1957 Critical size and nucleation field of ideal ferromagnetic particles *Phys Rev.* **106** 446-455.

[25] Kronmüller H and Fähnle M 2003 *Micromagnetism and the Microstructure of Ferromagnetic Solids* (Cambridge University Press, Cambridge).

[26] Lavín R, Denardin J C, Escrig J, Altbir D, Cortés A, and Gómez H 2009 Angular dependence of magnetic properties in Ni nanowire arrays *J. Appl. Phys.* **106** 103903.

[27] Landeros P, Allende S, Escrig J, Salcedo E, Altbira D, and Vogel E E 2007 Reversal modes in magnetic nanotubes *Appl. Phys. Lett.* **90** 102501.

[28] Escrig J, Bachmann J, Jing J, Daub M, Altbir D and Nielsch K 2008 Crossover between two different magnetization reversal modes in arrays of iron oxide nanotubes *Phys. Rev. B* **77**, 214421.

[29] Hertel R and Kirschner J 2004 Magnetization reversal dynamics in nickel nanowires *Phys. B* **343** 206-210.

[30] Forster H, Schrefl T, Scholz W, Suess D, Tsiantos V and J. Fidler 2002 Micromagnetic simulation of domain wall motion in magnetic nano-wires *J. Magn. Magn. Mat.* **249** 181-186.

[31] De La Torre J, Piraux L, Olais J M and Encinas A 2010 Double ferromagnetic resonance and configuration-dependent dipolar coupling in unsaturated arrays of bistable magnetic nanowires *Phys. Rev. B* **81** 144411.

[32] Kou X, Fan X, Dumas R K, Lu Q, Zhang Y, Zhu H, Zhang X, Liu K and Xiao J Q 2011 Memory Effect in Magnetic Nanowire Arrays *Adv. Mater*. **23** 1393-1397.

[33] Nielsch K, Choi J, Schwirn K, Wehrspohn R B and Gösele U 2002 Self-ordering regimes of porous alumina: the 10 porosity rule *Nano Lett.* **2** 677-680.

[34] Clime L, Ciureanu P, and Yelon A 2006 Magnetostatic interactions in dense nanowire arrays *J. Magn. Magn. Mat.* **297** 60-70.

[35] Clime L, Zhao S Y, Chen P, Normandin F, Roberge H and Veres T 2007 The interaction field in arrays of ferromagnetic barcode nanowires *Nanotech.* **18** 435709.

[36] Hertel R 2001 Micromagnetic simulations of magnetostatically coupled Nickel nanowires *J. Appl. Phys.* **90** 5752-5758.

[37] Zighem F, Mauer T, Ott F and Chaboussant G 2011 Dipolar interactions in arrays of ferromagnetic nanowires: a micromagnetic study *J. Appl. Phys.* **109** 013910.

[38] Navau C, Chen D-X, Sanchez A and Del-Valle N 2011 Demagnetizing effects in granular hard magnetic bodies *J. Appl. Phys.* **109** 093901.

[39] Ivanov Y P, Vázquez M and Chubykalo-Fesenko O 2013 Magnetic reversal modes in cylindrical nanowires *J. Phys. D: Appl. Phys.* **46**485001.

[40] Agramunt-Puig S, Del-Valle N, Navau C and Sanchez A 2014 Controlling vortex chirality and polarity by geometry in magnetic nanodots *Appl. Phys. Lett.* **104** 012407.

[41] Stoner E C and Wohlfarth E P 1948 A mechanism of magnetic hysteresis in heterogeneous alloys *Phil. Trans. Royal Soc. London A* **240** 599-642.

[42] Ravea W, Ramstöckb K and Hubert A 1998 Corners and nucleation in micromagnetics *J. Magn. Magn. Mater* **183** 329-333.

[43] Aharoni A 2001 Micromagnetics: past, present and future *Physica B* **306** 1-9.

[44] Guslienko K Yu 1999 Magnetostatic interdot coupling in two-dimensional magnetic dot arrays *Appl. Phys. Lett.* **75** 394-396.

Departament de Física

4. Further insights into nanowires and porous films

Chapter 4: Futher insights into nanowires and porous films

In the previous chapter, template-assisted electrodeposition in its three different modalities, namely dynamic, self-organized and restrictive template-assisted electrodeposition, is proposed. In section 3.1, we take advantage of hydrogen bubbles evolved during electrodeposition of Cu-Ni to prepare magnetic foam films. In section 3.2, it is demonstrated that porous Cu-Ni films can be decorated with ZnO nanoparticles previously synthesized by sol-gel, without causing any deterioration of the pristine Cu-Ni properties.The electrodeposition of nanowires comprising CoPt, Cu and Ni segments is presented in section 3.3, here using PC membranes as a restrictive template.

In this Chapter 4, supplementary works also dealing with template-assisted electrodeposition approaches and thematically connected with Chapter 3 are shown.

The influence of crystallographic texture on the robustness of interfaces in tri-segmented CoPt/Cu/Ni and bi-segmented CoPt/Ni magnetic NWs is shown in section 4.1. This study reveals that smooth and robust junctions are formed between CoPt and Ni in bi-segmented NWs. On the contrary, Cu, which deposits in the (200) textured *fcc* structure, cannot accommodate well on the c-axis oriented *hcp* CoPt. As a result, tri-segmented CoPt/Cu/Ni NWs often show defective junctions. Magnetic measurements reveal that staircase-like hysteresis loops also hold for the bi-segmented NWs, likely because interfacial exchange interactions between the Ni and CoPt counterparts are not sufficient to force a simultaneous magnetization reversal.

Apart from sol-gel deposition approaches, another harmless coating technique – atomic layer deposition (ALD) – is described in section 4.2. Different metal oxides (Al_2O_3, which is insulating, and Co_2FeO_4, which is ferrimagnetic) are conformally deposited by ALD onto 3D porous Ni films previously synthesized by hydrogen bubble-assisted electrodeposition. The thickness of the ALD nanolayers varies from 5 nm to 25 nm. Interestingly, the saturation magnetization of the material remains virtually the same after the ALD process and, simultaneously, the surface becomes slightly more polar.

Finally, nanoporous Ni films deposited using tri-block polymer P123 as a self-organizing template are presented in section 4.3. The growth of Ni follows a quasi-perfect layer-by-layer deposition, in which the pore size gradually varies along film thickness. A reduction of both the Young's modulus and the constraint factor are observed when the maximum applied load is decreased, while hardness remains constant. These results can be understood on the basis of the increase in porosity and the decrease of ligament size with film thickness. These results are jointly presented with the nanomechanical behavior of dealloyed Cu-Zn ribbons (this part of the work was conducted by Dr. Jordina Fornell from Gnm^3 group). Modeling of the nanomechanical behavior of both nanoporous electrodeposited Ni and dealloyed Cu materials was carried out by Dr. Daniel Esqué-de los Ojos from Gnm^3 group as well.

4.1 Toward robust segmented nanowires: Understanding the impact of crystallographic texture on the quality of segment interfaces in magnetic metallic nanowires

Segmented nanowires (NWs) have found a wealth of applications due to their multifuctionality, arising from complementarities and synergies among segments of different materials. However, to ensure a practical use of segmented NWs, high quality interfaces between dissimilar segments must be ensured. Herein, tri-segmented CoPt/Cu/Ni NWs and bi-segmented CoPt/Ni magnetic NWs are fabricated by means of template-assisted electrodeposition and the characteristics of their interfaces are investigated in detail. The presence of a Cu segment sandwiched between the CoPt and the Ni segments severely affects the integrity of the whole NW. Namely, Cu deposits in a (200) textured face-centered cubic (*fcc*) structure, which cannot accommodate well on the c-axis oriented hexagonal close-packed CoPt. Instead, when the Cu segment is absent, well-connected CoPt/Ni NWs with smooth interface are obtained. Unlike the Cu segment, Ni shows the (111) textured *fcc* structure, which holds good crystallographic matching with the underlying CoPt segment. Magnetic measurements reveal that CoPt/Ni NWs exhibit staircase-like hysteresis loops similar to the tri-segmented CoPt/Cu/Ni NWs. Such loop shape stems from the dissimilar coercivity between the hard (CoPt) and soft (Ni) segments. The bi-segmented NWs (with robust interfaces) are appealing for multi-bit recording media, magnetic nanoelectromechanical systems and magnetically-driven wireless drug delivery nanoplatforms.

4.1.1 Introduction

Owing to their unique chemical, size, shape and composition dependent properties, nanowires (NWs) have become appealing for a wide range of technological applications, including nanoelectronics,[1,2] optoelectronics,[3,4] catalysis,[5] sensing,[6] plasmonics,[7] and drug delivery.[8,9] Segmented NWs can be considered as an upgrade to single-component / single-phase NWs, as the combination of dissimilar materials within a nanoarchitecture leads to unique combined properties and synergies. Specifically, segmented NWs with magnetic properties have found several uses in devices such as giant magnetoresistance sensors,[10-12] or biomedical transducers,[13] among others. The ability to control the relative orientation of the magnetization between various magnetic segments in multi-component NWs can trigger new applications of these materials in multi-bit magnetic recording media[14,15] or as synthetic ferrimagnets with reduced dipolar interactions for spin-valve sensors.[15,16]

A major challenge in assembling building blocks, such as segments of different materials consists of securing a good quality interface at the junctions, not only for ensuring the mechanical robustness of the final ensemble, but also for enabling an effective synergy or combination of properties.[17-20] The occurrence of porous, wavy or cracked interfaces can severely affect or hinder the practical application of segmented NWs.

Electrodeposition inside the pores of anodized aluminum oxide (AAO) or polycarbonate (PC) membranes is frequently utilized to synthesize ordered arrays of segmented or layered magnetic NWs.[21-24] To date, segmentation is achieved mainly by two different means: (*i*) sequential electrodeposition by switching the working electrode between different electrolytes[25,26] or (*ii*) electrodeposition from a single bath by swapping the deposition potential or current density.[13,26-28 The former approach minimizes the co-deposition of different metals within the same segment and thus compositionally pure segments can be obtained.

In a previous work, the synthesis of tri-segmented CoPt/Cu/Ni NWs by template-assisted electrodeposition was demonstrated.[26] The possibility to tune the length of different segments in order to achieve room-temperature staircase-like hysteresis loops was proven. Full antiparallel alignment between hard (CoPt) and soft (Ni) segments and, hence, zero remanent net magnetization rendered NWs with very weak dipolar interactions, thus minimizing their agglomeration in eventual biological applications. However, the characteristics of the different interfaces were not explored in detail. This is a serious issue in applications for which the NWs need to be released from the template because if the junctions are not well-built, then NWs unavoidable break up across the interface.

Herein, we present a detailed characterization of the interfaces in segmented hard-ferromagnetic/soft-ferromagnetic CoPt/Ni NWs with and without the presence of a non-magnetic Cu spacer, obtained by sequential electrodeposition in PC membranes. Tri-segmented CoPt/Cu/Ni and bi-segmented CoPt/Ni NWs are taken as model systems for studying the characteristics of the CoPt/Cu, Cu/Ni, and CoPt/Ni interfaces. Contrary to the CoPt/Cu interface, smooth and robust junctions are formed between CoPt and Ni, thus ensuring a good adhesion between these two segments. The observed trends are rationalized on the basis of the different crystallographic features exhibited by CoPt, Cu, and Ni segments. Furthermore, magnetic measurements reveal that staircase-like hysteresis loops are obtained at room-temperature for both systems, even when Cu is absent between the two ferromagnetic segments. Our study highlights the importance of the interface quality in layered nanostructures in order to optimize their performance and guarantee a correct and reliable operation.

4.1.2 Experimental Section

4.1.2.1 Experimental details

Track-etched polycarbonate (PC, Nuclepore, Whatman) membranes with on-top pore diameter ranging from 40 nm to 60 nm were used for fabricating the segmented NWs. A thin layer of Au-Pd was sputter deposited onto one side of the PC to serve as working electrode. The PC membrane was sequentially mounted onto a Cu plate held inside a homemade plastic holder, leaving a circular area of 3.14 cm^2 exposed to the electrolyte. The mounted holder was firstly kept in ultrasonic cleaning for 3 min to get rid of the air entrapped inside the pores. All the experiments were performed on a PGSTAT302N Autolab potentiostat/galvanostat (Ecochemie). Platinum spiral was utilized as the counter electrode (CE), which was positioned vertically facing the working electrode (WE). A double junction Ag|AgCl

3M KCl electrode (*E*= + 0.210 V versus standard hydrogen electrode (SCE)) was used as the reference electrode (RE). All chemicals were of analytical grade and used as received without further purification. Electrolyte solutions were prepared from ultrapure water.

CoPt, Cu and Ni segments were prepared by direct current electrodeposition as follows. The CoPt electrolyte consisted of 30 mM $Co(SO_3NH_2)_2{\cdot}xH_2O$, 2 mM $Pt(NH_3)_2(NO_2)_2$, 0.1 M glycine, 0.1 M sulfamic acid, 5 mM saccharine and 0.1 M sodium citrate, and the deposition parameters were held constant with j = –10 mA/cm^2, pH = 8.5, T = 65 °C. Cu segment was grown potentiostatically at E = –1 V in a bath containing 0.2 M $CuSO_4{\cdot}5H_2O$ and 0.1 M boric acid. Ni segment was deposited under a constant current density of –10 mA/cm^2 and the bath contained 0.1 M $NiCl_2$ and 2 M NH_4Cl as buffer agent. The sequence for segmented NWs deposition was: CoPt segment, Cu segment and Ni segment (tri-segmented NWs) or CoPt segment and Ni segment (bi-segmented NWs). The deposition processes for Cu and Ni segments were carried out under 25 °C. Ar was purged through the solution so as to ensure the proper mixture of ions and to remove the gas bubbles from the sample surface. For electron microscopy observations, the segmented NWs were released by dissolving the PC template in chloroform and washed several times afterwards.

4.1.2.2 Characterization

Scanning electron microscopy (SEM) images and energy-dispersive X-ray spectroscopy (EDX) compositional analyses were acquired using a Merlin Zeiss microscope operated at 3 kV and 15 kV, respectively. Specimens were prepared via drop-casting a droplet of NWs suspended in chloroform onto an aluminum foil and subsequent drying in air. Transmission electron microscopy (TEM) analyses were done on a Jeol-JEM 2011 system with a field emission gun operating at 200 kV. STEM-EDX analyses were performed on a Tecnai F20 HRTEM / STEM microscope. For both TEM and STEM-EDX observations, a couple of drops of NWs suspended in chloroform were placed onto a carbon-coated TEM grid. X-ray diffraction patterns of the segmented NWs (before PC removal) were recorded on a Philips X'Pert diffractometer in the 30-100° 2θ range (step size = 0.026°, step time= 2000 s) using

Cu K_α radiation (λ=0.154178 nm). Hysteresis loops were recorded at room temperature using a vibrating sample magnetometer (VSM) from Oxford Instruments, with a maximum applied magnetic field of 0.5 Tesla.

4.1.3 Result and discussion

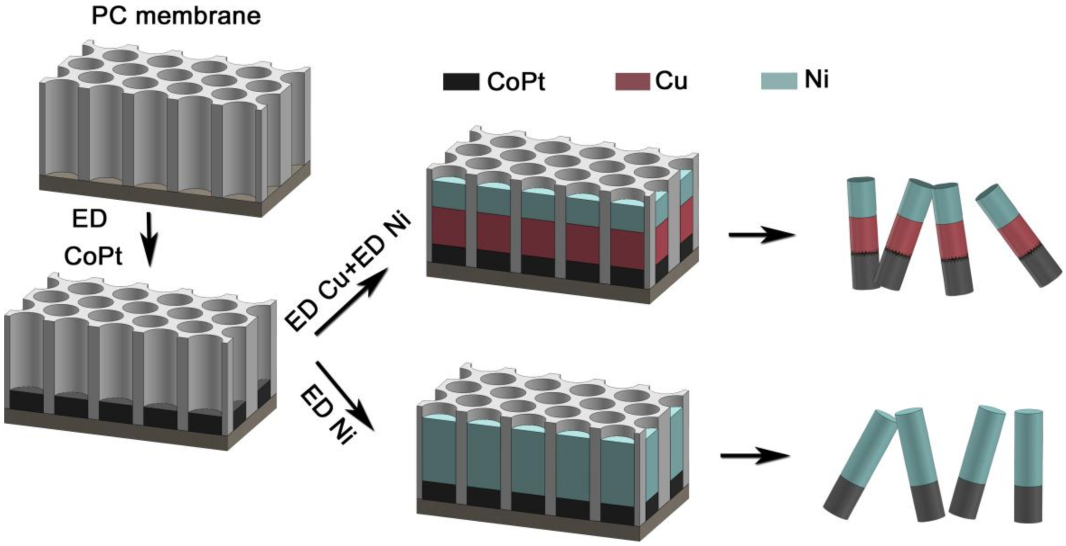

Figure 4.1: Scheme of the fabrication process of tri-segmented CoPt/Cu/Ni and bi-segmented CoPt/Ni NWs.

The NWs were deposited inside the channels of a PC membrane (Figure 4.1). The PC backside was sputter-coated with a Au-Pd layer to make it conductive. CoPt was first electrodeposited followed by Ni (CoPt/Ni NWs) or followed by Cu and later Ni (CoPt/Cu/Ni NWs). Details of different bath formulations and deposition parameters can be found elsewhere.[26] The PC membrane was selected over AAO because the former is particularly well suited for further assessing the magnetic behavior of individual NWs still embedded in the template, as the pores are separated enough from each other (see Figure 4.2). Assessing the magnetic behaviour of isolated NWs, rather than the collective behaviour of the array is important in devices such as nanoelectronic machinery or magnetically driven drug delivery nanocarriers. Such information is obtained provided that the NWs are sufficiently separated from each other, so that interwire dipolar interactions are minimized. Besides, PC can withstand the alkaline electrolyte needed to electrodeposit hard-magnetic CoPt.

According to several works on CoPt electrodeposition, hard-magnetic properties are easierly achieved in the as-deposited state when the alloy is plated from alkaline baths above room temperature, typically at 50-60 ℃.[29-31] Under these conditions, Co-rich alloys with hexagonal close-packed phase are frequently obtained. Unfortunately, AAO cannot tolerate pH values beyond 8.2 (at room temperature) and undergoes dissolution in the electroplating bath,[32] which is even exacerbated at higher temperatures. The NWs had a mean diameter of 100 nm and the overall length was ca. 3.6 μm for the bi-segmented and 5 μm for the tri-segmented NWs. For the CoPt segment, deposition conditions were optimized so that a Co-rich alloy with $Co_{70}Pt_{30}$ stoichiometry was obtained.[26]

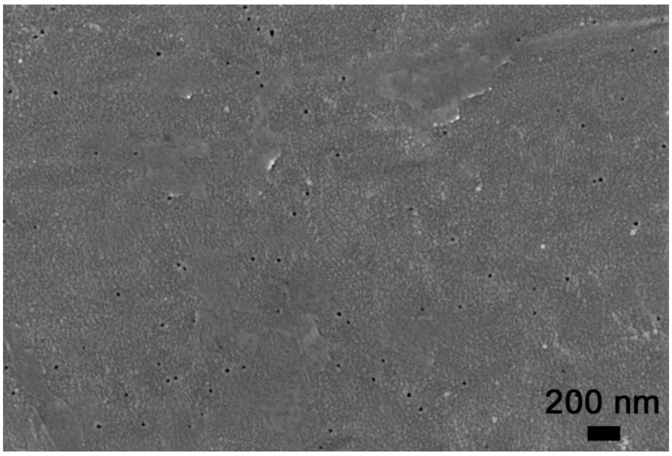

Figure 4.2: SEM image of polycarbonate (PC) membrane with an average pore size of 50 nm and rather large interpore distance.

A backscattered electrons SEM image of the tri-segmented CoPt/Cu/Ni NWs is shown in Figure 4.3a, in which CoPt and Cu segments can be easily distinguished thanks to their different contrast (CoPt looks bright while Cu looks dark). The CoPt/Cu junctions look rather discontinuous and some NWs have broken along the CoPt/Cu interface. On the contrary, it is difficult to locate the boundary between the Cu and the Ni segments because both elements possess similar atomic weights (*i.e.*, they have similar electron dispersing capability and, hence, contrast under SEM). Moreover, no defects such as cracks or pores, that could eventually reveal the location of the interface, were detected. Therefore, the interface between Cu and Ni is seemingly very smooth. A zoomed view of CoPt/Cu junction was further taken by

TEM. Figure 4.3b shows severely cracked and/or porous interfaces between the CoPt and the Cu segments. Notice that here the contrast is opposite to the SEM (CoPt looks darker than Cu). The occurrence of such defective junctions unavoidably leads to the detachment of many CoPt segments when the NWs are released from the PC membrane. As a result, multiple broken NWs are observed by both SEM and TEM. Figure 4.4a shows a representative SEM image of a bi-segmented CoPt/Ni NW. Unlike the tri-segmented case, detached CoPt segments are rarely observed by SEM. TEM imaging further reveals that the CoPt and the Ni segments are well attached (Figure 4.4b). The corresponding lengths can be straightforwardly determined thanks to the contrast. Under the applied electrodeposition conditions,[26] the CoPt segment is 0.9 µm long and the Ni segment has a length of 2.9 µm.

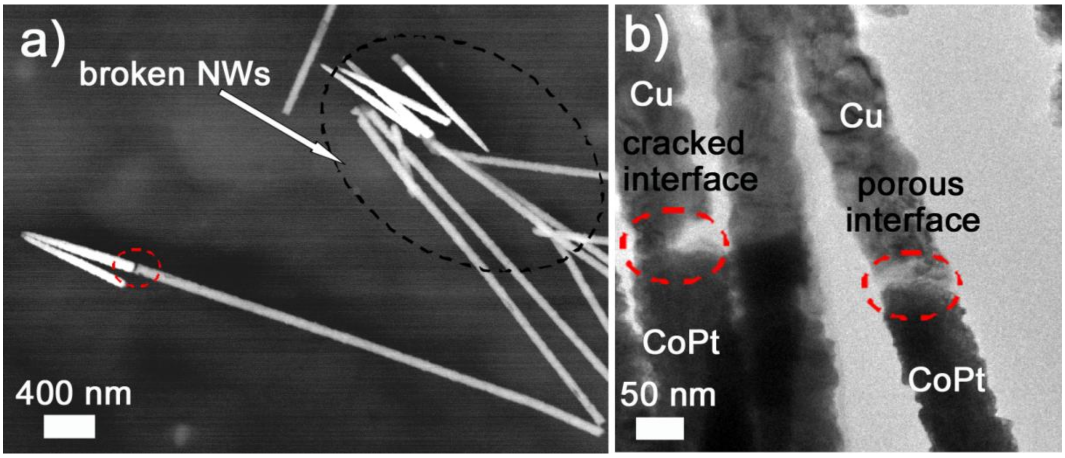

Figure 4.3: (a) Back-scattered electrons SEM image of tri-segmented CoPt/Cu/Ni NWs. The red dotted circle embraces the CoPt/Cu interface. The big black dotted circle and the arrow points to a group of broken NWs (b) TEM image of the CoPt/Cu interfaces in tri-segmented CoPt/Cu/Ni NWs.

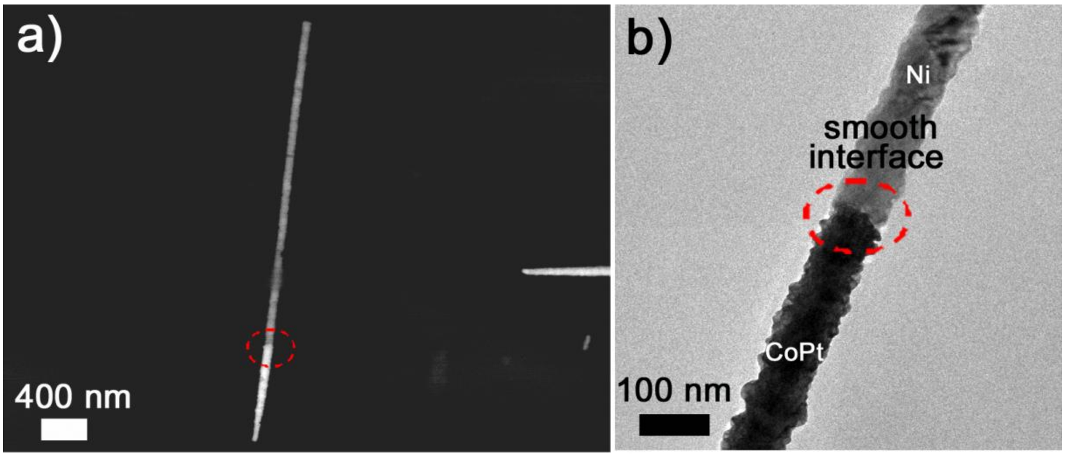

Figure 4.4: (a) Back-scattered electrons SEM and (b) TEM images of a bi-segmented CoPt /Ni NW. The red dotted circles embrace the CoPt/Ni interface.

It is known that the structure and properties of a deposit are greatly influenced by the piling layer upon which plating is carried out.[33] Besides, adhesion of deposits to the piling layer is greatly affected by texture. It is conjectured that the defective interface between the CoPt and the Cu segments is mainly due to lattice mismatch. To verify this hypothesis, NWs made of either CoPt, Ni or Cu were electrodeposited inside the PC membrane using the same baths and deposition parameters as for the segmented cases. X-ray diffraction (XRD) analyses of the individual (non-segmented) CoPt, Ni and Cu NWs embedded in the PC membrane were carried out and the results are presented in Figure 4.5. All the diffractograms show peaks arising from the Au-Pd conductive layer sputtered onto the PC backside before electrodeposition. In the case of Cu NWs, four diffraction peaks at 2θ = 43.3°, 50.4°, 74.1° and 89.9º, ascribed to the (111), (200), (220) and (311) reflections, respectively, of the face-centered cubic (fcc) phase, are observed. By comparing the tabulated and experimental peak intensities (I) of (111) and (200) reflections, some conclusions can be drawn. The ratio of the integral intensity of the (200) peak to that of the (111) peak, $I_{(200)}$ / $I_{(111)}$, is 1.02, which is larger than the tabulated value for randomly oriented Cu (0.46).[34] This indicates the growth of {100} textured Cu during the electrodeposition process. Duan et al.[35] have previously reported the occurrence of various textures in fcc-Cu films depending on the electrodeposition conditions (pH, applied potential and temperature). The {100} or {110} textures are obtained at relatively high H ions concentration in the bath, since H ions are prone to be adsorbed in the (100) and (110) high-surface-energy planes, causing a reduction of their surface energies to values even lower than for the {111} planes, thus promoting crystallographic texture along these directions. Hence, in our case, the rather acidic pH (3.93) could favor the {100} texture in Cu, at the expense of the most densely packed {111} planes. For Ni NWs, the fcc phase is also obtained. The experimental $I_{(200)}$ / $I_{(111)}$ ratio is 0.04, which in this case is much smaller than the theoretical ratio for randomly oriented Ni grains (0.42).[34] Hence, Ni shows the {111} texture. Again, the occurrence of texture in electrodeposited Ni coatings depends on the electrolyte composition and the operating conditions and typically there is not a sole origin. As observed by Amblard et al.,[36] the electrocrystallization of Ni is a highly inhibited process. Adsorbed hydrogen (H_{ads}) species generated during electrodeposition are regarded as inhibitors for Ni deposition. In acid plating baths, the concentration of protons (H^+) at the cathode neighborhood is large. They are discharged and immediately adsorbed onto the cathode, leading to its rapid depletion and a local increase of the pH at the Ni/electrolyte interface. This, in turn, promotes the precipitation of $Ni(OH)_2$, which is believed to be another inhibiting species for metallic Ni deposition and to ‘promote’ a given mode of growth. Namely, (111)-oriented Ni deposits become stabilized by $Ni(OH)_2$. The occurrence of texture can be also explained from the different growth rate of crystal facets.[37] Using a purely geometric argument, it can be demonstrated that fast growing faces grow out of existence whereas slow growing crystal faces survive. Densest faces have the slowest growth velocity. For the fcc, the velocity follows the order: {111} < {110} < {100} and, therefore, the (111) facet preferentially develops.

The diffractogram for CoPt NWs is also shown in Figure 4.5. The most intense peak at 43.1° matches the 2θ position expected for either (002) hexagonal-closed packed (*hcp*) or (111) fcc phase of Co. The absence of a diffraction peak at ca. 51.5° (which should match the angular position of the (200) peak for fcc-Co), suggests that CoPt has fully crystallized in the *hcp* structure.[38] Moreover, the intensity of the (101) reflection is dramatically reduced as compared to the standard powder pattern, which suggests that the hexagonal *c* axis lies preferentially along the long axis of the

NWs.[39,40] This means that PtCo is also crystallographically textured, here in the [002] direction.

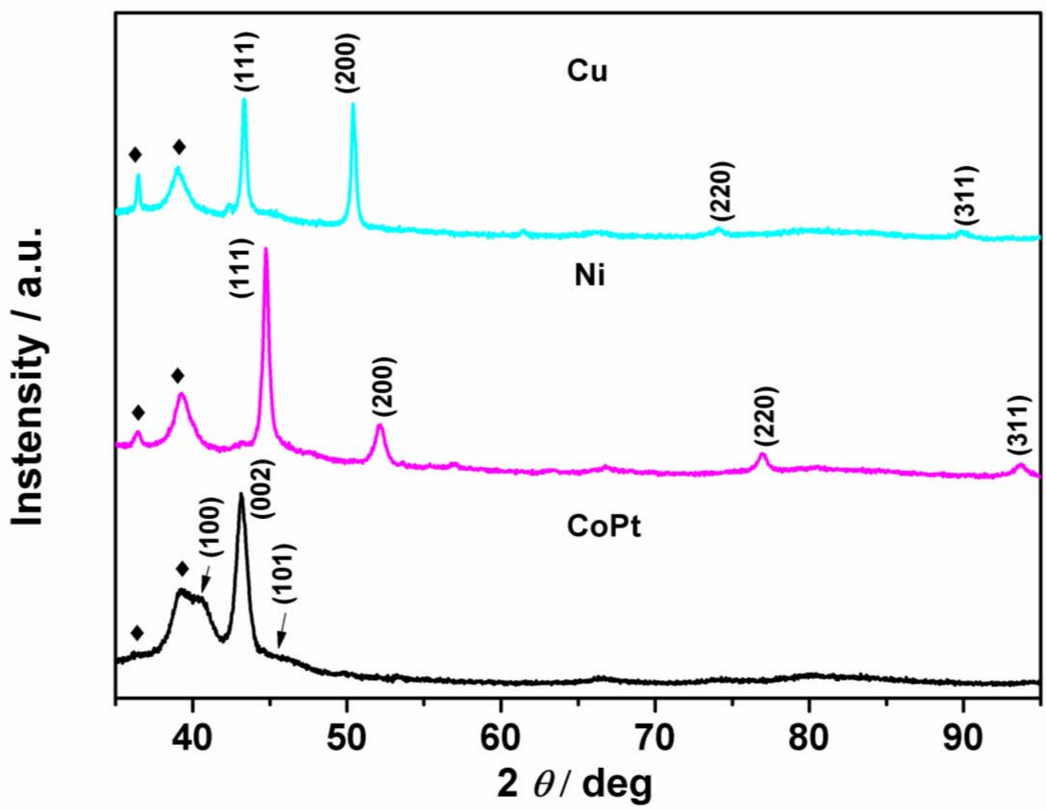

Figure 4.5: XRD patterns of non-segmented Cu, Ni and CoPt NW arrays. Peaks denoted by ♦ belong to the sputtered Au-Pd conductive layer onto the PC membrane.

In order to verify whether the observed textures were maintained for the bi- and the tri-segmented NWs, the XRD patterns of CoPt/Cu/Ni and CoPt/Ni NW arrays embedded in the PC membrane were recorded (Figure 4.6). On comparing the profiles with those of Figure 4.5, the peaks coming from CoPt, Cu and Ni phases can be straightforwardly identified in the tri-segmented CoPt/Cu/Ni NWs diffractogram. Likewise, the peaks corresponding to CoPt and Ni phases show up in the bi-segmented CoPt/Ni NWs pattern. CoPt maintains the (002) preferred orientation, as for the non-segmented case. This is predictable since CoPt is firstly deposited (i.e., it deposits onto the AuPd layer both in the non-segmented and segmented cases). Regarding the Ni segments, the relatively high intensity of the Ni (111) peak over the (200) suggests the occurrence of texture (both in the bi- and tri-segmented cases), similar to the non-segmented case. However, the $I_{(200)\text{-}Ni}$ / $I_{(111)\text{-}Ni}$ ratio cannot be precisely quantified due to partial overlapping of the Ni (111) with CoPt (002) peaks. Concerning the Cu signal in the CoPt/Cu/Ni diffractogram, although the (111) reflection is masked by the (002) peak from CoPt phase, the relatively large intensity of the Cu (200) reflection suggests the occurrence of {100} texture as for the non-segmented Cu NWs.

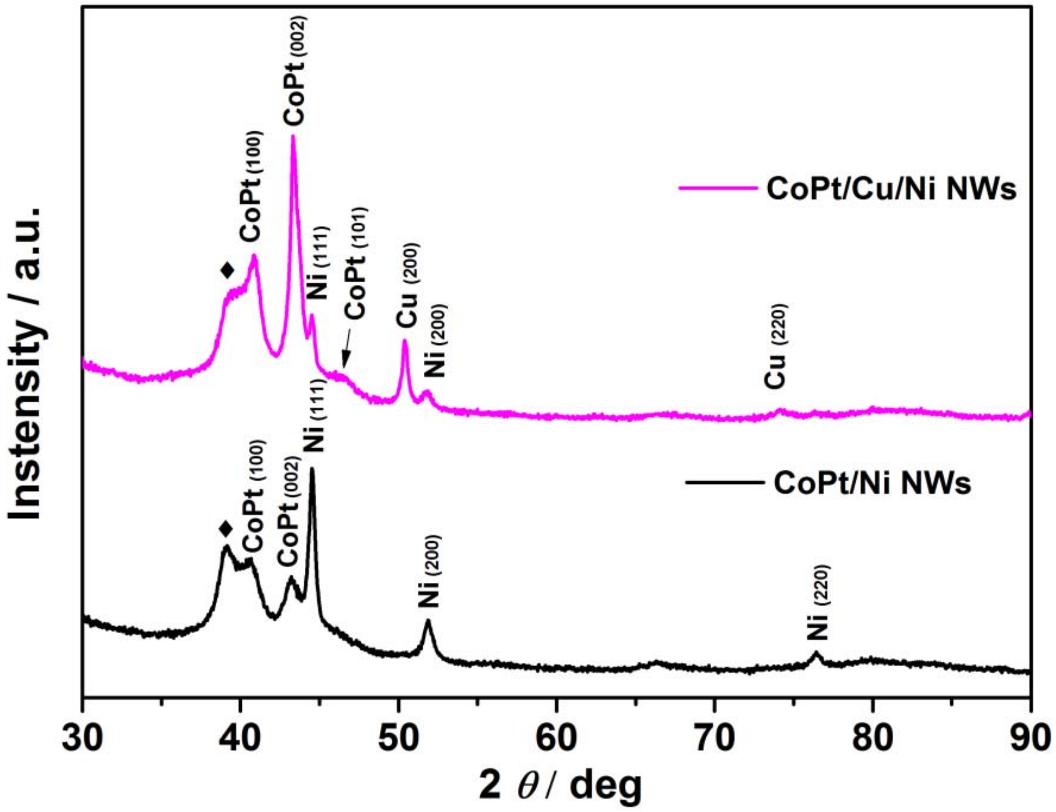

Figure 4.6: XRD patterns of tri-segmented CoPt/Cu/Ni and bi-segmented CoPt/Ni NWs. Peaks denoted by ◆ belong to the sputtered Au-Pd conductive layer.

Considering the aforementioned structural features, one can actually anticipate the rather poor adhesion between CoPt and Cu segments. Since they grow in different crystallographic phases (*hcp* versus *fcc*), cracked and porous interfaces develop due to severe lattice mismatch. Analogous results were previously observed between *hcp*-Co and fcc-Au in multi-segmented Au/Co/Au NWs.[41] Meanwhile, even though CoPt and Ni also grow in different crystallographic structures, the adhesion between the segments is reasonably good. This can be understood taking the textures previously observed by XRD into account. The (001) planes of *hcp*-CoPt and the (111) planes of fcc-Ni are planes of highest atomic packing (*i.e.*, densest possible arrangements of atoms in 2D). Both can be described as a compact hexagonal arrangement of atoms in 2D, being structurally analogous to each other.[42] Indeed, the densest packing fashion along the [111] orientation of fcc phase matches the [001] oriented *hcp* planes (Figure4.7). It is known that duplication of the structure of the piling layer favors good connection and therefore a smooth interface between the CoPt segment and the subsequent Ni segment builds up. Such structural equivalence does not hold between the (001) planes of *hcp*-CoPt and the (100) planes of fcc-Cu.

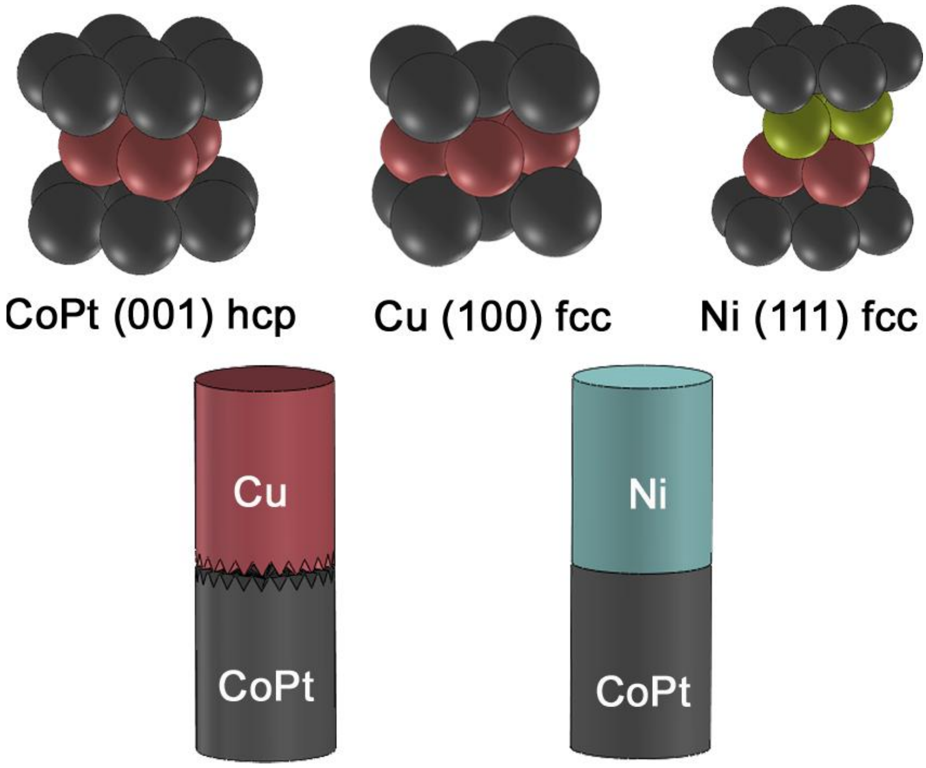

Figure 4.7: Putative densest packing of CoPt, Cu and Ni and schematic drawing of the interface in CoPt/Cu and CoPt/Ni.

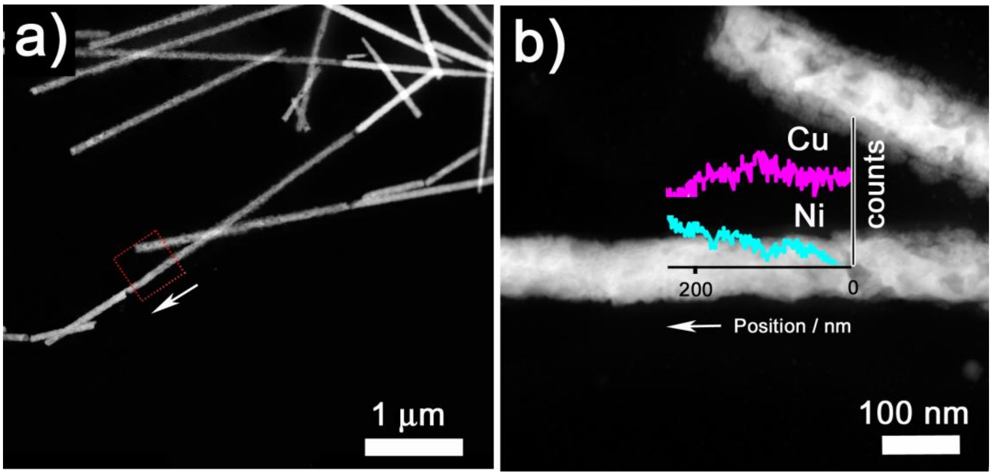

Figure 4.8: a) TEM image of the tri-segmented CoPt/Cu/Ni NWs. b) STEM-EDX line scan taken at the junction between Cu and Ni segments enclosed in the dotted square in a). Images were acquired on a FEI Tecnai G^2 F20 HR(S)TEM which features enhanced contrast with respect to Jeol-JEM 2011 microscope, thus enabling the location of the Cu/Ni junction to some extent.

Despite Cu and Ni segments possess a different fcc texture, the Cu/Ni junction is rather difficult to be distinguished by both SEM and TEM, as mentioned above. For this reason, STEM-EDX line scan analysis was performed on a scanning transmission electron microscope (STEM) in order to determine the composition profile at the interface. Figure 4.8 shows a TEM image featuring a whole tri-segmented NW at the center. The EDX line scan was done along the portion enclosed in the red box in Figure 4.8a, therefore capturing the Cu/Ni interface composition. It can be seen that this portion embraces a porous region (right) and a denser region featuring brighter contrast (left) (Figure 4.8a). Porosity in Cu can be attributed to the hydrogen co-evolution that accompanies cations discharge at the potential applied for Cu segment growth (E = −1 V vs. Ag/AgCl). As a result, deposits consisting of agglomerates of Cu grains are typically obtained.[43] As shown in Figure 4.8b, both Cu and Ni are detected within the analyzed portion. As the beam is scanning the NW toward the Ni segment, the Ni signal monotonically increases whereas the Cu signal starts to decrease. This proves that there is not an abrupt change in composition but rather Cu and Ni are present within a distance larger than 100 nm, thus rendering a relatively thick interface. It is conjectured that a small electrolyte volume remains entrapped inside the pores of the PC membrane after Cu deposition. Upon switching to the Ni bath, the residual Cu^{2+} ions mix with the Ni electrolyte constituents. As a result, Cu-Ni might get codeposited within the first stages of Ni segment deposition. Co-deposition is indeed thermodynamically favored at the current density applied for Ni deposition (-10 mA cm^{-2}).[44] Another possibility would be that Ni deposits in the upper voids left by the porous Cu segment until a flat Ni layer is formed. However, if this were the case one would expect greater fluctuation of the Cu and Ni signals along the EDX-line scan (*i.e.*, Cu and Ni signals would somehow alternate).

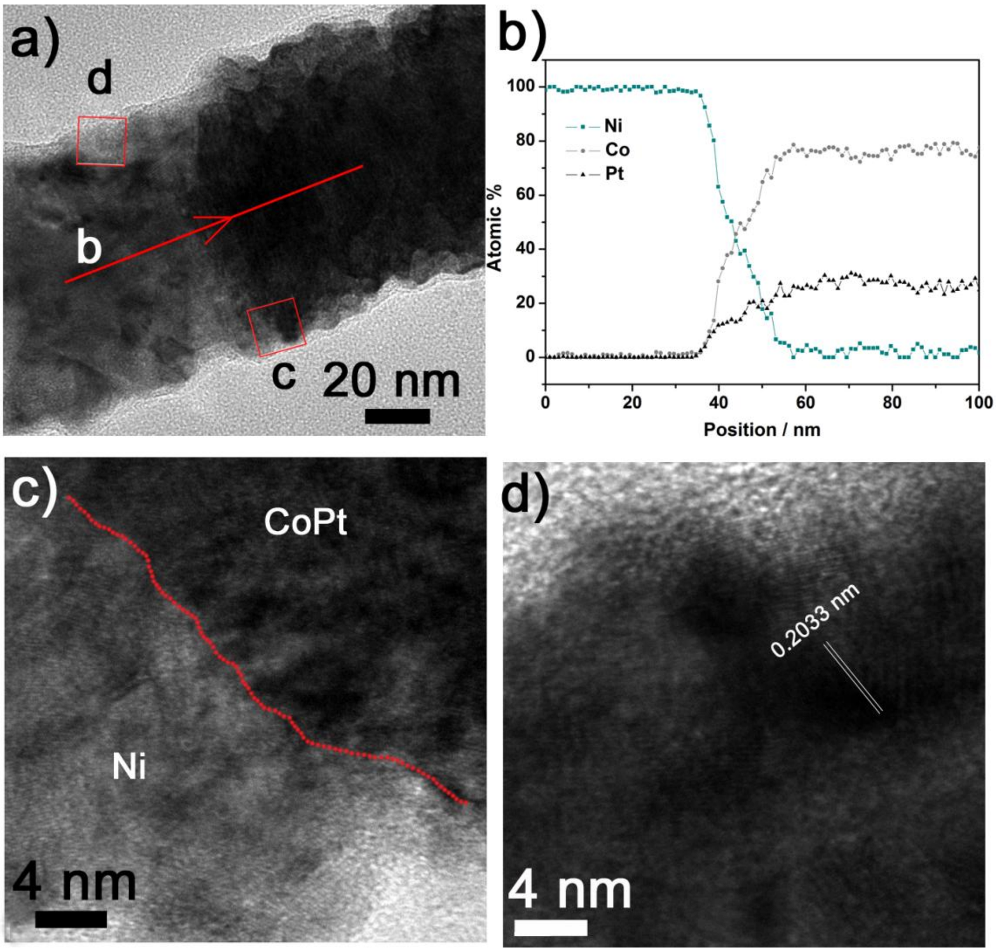

Figure 4.9: a) TEM image of the interface between Ni (left) and CoPt (right) segments in bi-segmented CoPt/Ni NWs. b) line-scan STEM-EDX analysis across the interface depicted with the red arrow in a), c) HRTEM image of the area enclosed with the red square labelled as ‘c’ in a), corresponding to the interface. d) HRTEM image of the area enclosed with the red square labelled as ‘d’ in a), corresponding to the Ni segment.

To get a better insight into the morphology of the well-formed CoPt/Ni interface, bi-segmented CoPt/Ni NWs were further examined by HRTEM and STEM-EDX line analyses. As shown in Figure 4.9a, (111) textured Ni exhibits excellent adhesion to the (002) oriented *hcp* CoPt segment. When the electron beam was spotted onto the bright region in Figure 4.9a, only Ni was detected. The Ni signal gradually decreases down to negligible levels as the electron beam is swept through the Ni/CoPt interface (Figures 4.9b and 4.9c). Meanwhile, Co and Pt signals simultaneously increase until a constant value, leading to a Co/Pt atomic ratio of 7:3. The change from pure Ni to pure CoPt is accomplished within 20 nm. The resulting interface is thus thinner than for Cu/Ni. Figure 4.9c shows an HRTEM image of the junction, which proves the fine adhesion of Ni onto CoPt. Although the Ni segment is in fact polycrystalline, as observed by HRTEM (Figure 4.9d), many of the lattice fringes perpendicular to the NWs long axis could be assigned to the interplanar distance of (111) fcc (d = 0.2033 nm). Therefore, the presence of a large population of (111) facets would favor a good connection to the CoPt segment

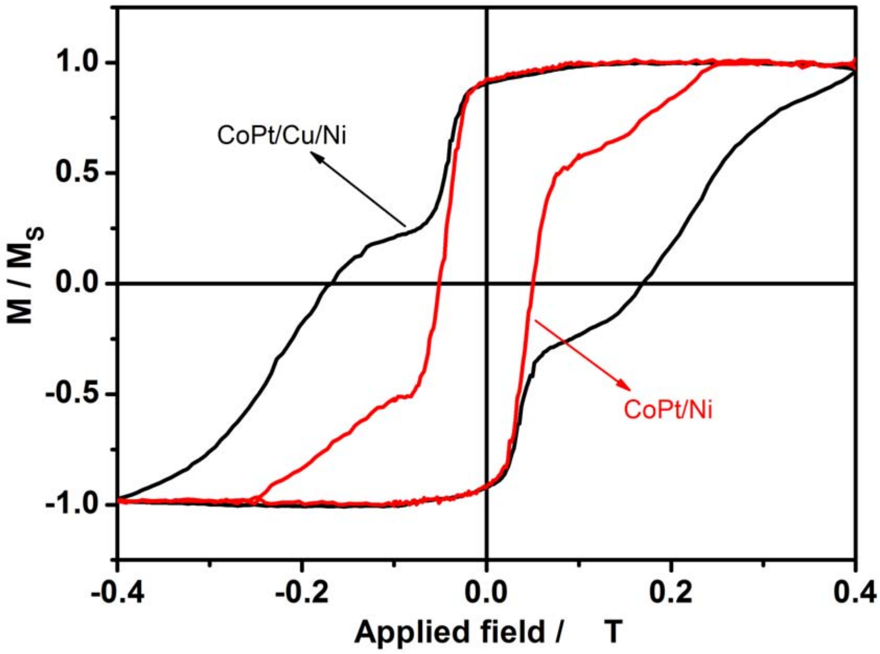

Figure 4.10: Room-temperature hysteresis loops of tri-segmented (CoPt (0.97 μm)/Cu (2.72 μm)/Ni (1.74 μm)) and bi-segmented (CoPt (0.9 μm)/Ni (2.9 μm)) NW arrays.

Hysteresis loops of segmented CoPt/Cu/Ni and CoPt/Ni NWs embedded inside the PC membrane were measured along the long axis of the NWs, as shown in Figure 4.10. The magnetic dipolar interactions between neighboring NWs in PC membranes can be neglected, owing to the relatively large interpore distance (much larger than the pore diameter, very often exceeding 200 nm). Hence, in a first approximation, the loops correspond to the behavior of isolated, non-interacting NWs. Interestingly, both hysteresis loops reveal the magnetization switching of CoPt and Ni, since the two segments have different values of coercivity.[26] Although clear staircase-like hysteresis loops were expected for the tri-segmented case, this was not necessarily the case for the bi-segmented NWs. In principle, magnetic exchange interactions between CoPt and Ni should take place in the absence of a non-magnetic spacer (Cu) and, therefore, non-stepped loops might be obtained if the reversal of Ni and CoPt occurred simultaneously. However, magnetic measurements reveal that exchange interactions between CoPt and Ni in the bi-segmented NWs are not sufficient to force such simultaneous reversal, probably due to the small interface area between the two segments (as compared to their overall volume). Consequently, the two switching events can be separately observed, similar to what typically occurs in many types of exchange-interacting spring-magnets.[45,46] Moreover, even if Ni spins close to the interface would be pinned to some extent by CoPt, the spins at the center of the soft segment would be free to follow the external field, given the much longer length of Ni segmentsas compared to CoPt ones.Once the applied magnetic field exceeds the exchange field, the spins in the Ni segment exhibit a continuous rotation, leading to a relatively steep magnetization reversal.[46] The different ratios between the relative magnetization of the Ni and CoPt segments in tri- and bi-segmented NWs are simply due to the dissimilar relative segment lengths in the two investigated systems, bearing in mind that the saturation magnetization of CoPt is approximately twice that of the Ni.[26] This difference in length of the Ni segments can also explain the difference in coercivity of the CoPt segments in the CoPt/Ni and CoPt/Cu/Ni NWs. Once the soft Ni segment is reversed, it exerts a dipolar stray field to the CoPt segment (tending to promote its reversal), which adds to the external applied field. Such dipolar stray field is higher for longer Ni segments, thus reducing the coercivity of CoPt.

4.1.4 Conclusion

Bi-segmented CoPt/Ni NWs and tri-segmented CoPt/Cu/Ni NWs can be fabricated by electrodeposition in PC membrane by switching between different electrolytes (sequential-electrodeposition mode). The crystallography of the different segments and the occurrence of texture greatly determine the quality of the resulting interfaces. The Cu segment cannot accommodate satisfactorily onto CoPt owing to lattice mismatch. As a result, CoPt segment undergoes detachment from the rest of the NW upon PC dissolution. Meanwhile, the structural equivalence existing between (002) *hcp* CoPt and (111) *fcc* Ni favors the construction of a good quality junction. Both systems (bi-segmented and tri-segmented NWs) exhibit staircase-like hysteresis loops at room temperature. For the Cu-free CoPt/Ni NWs, the occurrence of a staircase-like hysteresis loop indicates that interfacial exchange interactions between the soft and hard counterparts are not sufficient to force a simultaneous magnetization reversal of both segments. The current findings will likely contribute to the advancement in the field of segmented magnetic metallic NWs. In applications requiring the use of isolated NWs or, at least, removal of the template (AAO or PC) (*e.g.* in NEMS or biomedical applications), the presence of robust interfaces is an essential requirement that needs to be attained before any optimization of the physical, chemical or physicochemical properties of these systems is attempted.

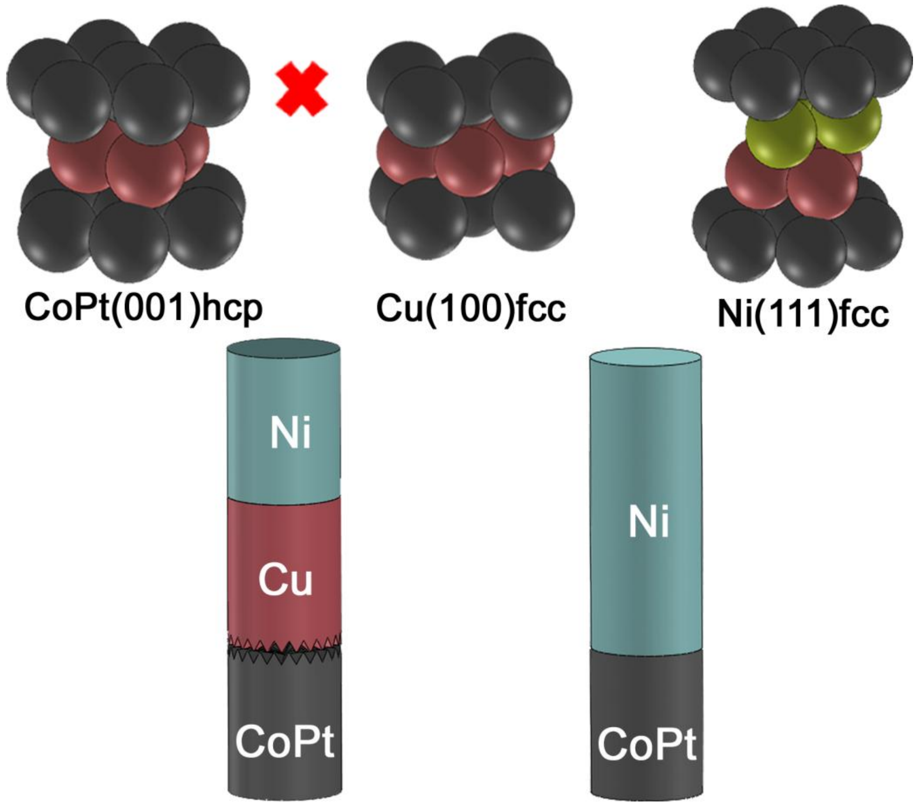

Figure 4.11: Table of contents graphic

4.2 Conformal oxide nanocoatings on electrodeposited 3D porous Ni films by atomic layer deposition

A versatile synthesis procedure to obtain Al_2O_3 and Co_2FeO_4 nanolayers conformally coating a three-dimensional (3D) porous Ni film is presented. First, porous Ni is grown by hydrogen bubble template-assisted electrodeposition. Subsequently, Al_2O_3 and Co_2FeO_4 layers, with thickness ranging from 5 nm to 25 nm, are directly deposited onto the pore walls by atomic layer deposition, while maintaining the porous architecture and magnetic properties of the Ni scaffold. The crystal structure, thickness and distribution of elements within the composite coatings are investigated in detail. The resulting magnetic properties are assessed. Furthermore, wettability tests reveal that 3D porous Ni films become more hydrophilic after coating with Al_2O_3 or Co_2FeO_4. From a technological point of view, the obtained composite porous films could be appealing for applications like magnetically-actuated micro/nano-electromechanical systems (MEMS/NEMS) or bio-MEMS/NEMS, among others.

Keywords: Atomic layer deposition, H_2 bubble template-assisted electrodeposition, conformal coating, 3D porous structure, magnetic properties, wettability

4.2.1 Introduction

During the last decades, much progress has been made towards the development of novel synthetic approaches to prepare nanocomposite materials with tunable composition and microstructure. Multiphase composite materials are interesting since they combine the properties of the different constituents, often in a synergetic manner. The generation of large amounts of interfaces (as it is the case in nanocomposites) allows exploring novel interfacial coupling effects. In turn, porous structures, with much larger surface area-to-volume ratio compared to their fully dense counterparts, are very appealing to enhance certain physico-chemical properties. In terms of applications, nanostructured porous materials have received considerable attention since they hold great promise in areas like drug delivery systems[47,48], batteries[49], electrocatalysis[50-52], supercapacitors[53] or magnetic micro/nano-electromechanical systems (MEMS/NEMS)[54]. Recently, coating porous surfaces with different organic and inorganic materials has become an important route to obtain functionalized multiphase nanocomposites[55,56]. Depositing an insulating layer can reduce electrical shorting in MEMS/NEMS, while bio-MEMS/NEMS can benefit from the coating with a hydrophilic layer, which allows greater wetting with aqueous biological fluids[57]. In turn, coating porous materials with a biocompatible layer makes them more amenable to be used *in vivo*, such as for drug delivery or diagnosis[58]. Moreover, besides its protective role, a coating can also serve as an integrated functional unit. For example, 3D porous Ni films can function as scaffolds to anchor $Co(OH)_2$[59] or Si[60] to produce nanoporous composites with superior supercapacitor performance. A magnetic porous film can also host second phases that could provide electrical insulation, biocompatible surfaces, hydrophilic/hydrophobic properties or even enhanced magnetic performance.

In general, the synthesis of porous nanocomposite films is accomplished by chemical or electro-chemical reactions that occur at surface level. Nanocasting procedures using suitable precursors allow the filling of parent templates with oxide second phase materials of interest[61]. Nanoporous ceramic or polymeric templates (e.g., alumina or polycarbonate) can be filled with certain metals and alloys by electrodeposition[62]. Contrary to these examples, the complete or partial filling or coating of metallic porous templates with oxide materials is more challenging. The preparation procedures usually involve some heating steps, which can easily deteriorate the properties of the porous metallic framework, from both morphological (collapse of the pore structure) and compositional (oxidation) points of view. This is certainly deleterious for the subsequent implementation of these materials into real devices. Thus, the choice of an appropriate technique to grow this type of composites is of paramount importance. Very recently, we have demonstrated that porous CuNi supported ZnO hybrid films can be successfully prepared at relatively low temperature by combining electrodeposition with sol-gel drop casting in which (i) the matrix or host and the coating can be chosen independently, and (ii) the ferromagnetic properties of CuNi are preserved[63]. However, sol-gel deposition methods and some physical vapor deposition techniques are not so convenient to obtain a fully-continuous conformal coating of the parent template. Actually, atomic layer deposition (ALD) is the most suitable deposition technique to conformally coat materials exhibiting gaps, cavities, pores, trenches, out-of-sight surface and high-aspect ratio structures. This technique is based on alternate surface-limited reactions from the gaseous reactant to produce thin films and overlayers with nanoscale control, independently of the substrate's geometric complexity[64,65]. Therefore, it is a powerful technique that allows precise control over the composition and physical properties of nanoscaled materials and novel nanostructures[66]. To date, ALD of magnetic nanotubes and nanowires inside anodized alumina templates has been reported[67,68]. Interestingly, Al_2O_3 ALD films were successfully grown on a variety of magnetic substrates, including Co, Ni, NiFe and NiMn[69]. The aforementioned studies have proved the potential of ALD to deposit a wide variety of materials into narrow and high-aspect ratio pores.

In this work, we propose the combination of electrodeposition and ALD to obtain Ni/Al_2O_3, and Ni/Co_2FeO_4 magnetic nanocomposite porous films. 3D porous Ni films are prepared by one-step hydrogen bubble assisted galvanostatic electrodeposition[70-72], while ALD is used to conformally coat the pores of the Ni scaffold with Al_2O_3 and Co_2FeO_4 nanolayers. Recent developments in the use of hydrogen bubble-templated method have led to the production of several magnetic porous films including Ni[59,60], CuNi[73,74] or phase-separated Cu-Ni[52]. These films typically show macropores and, depending on the synthetic conditions, nanoporous dendritic walls, hence exhibiting a hierarchical porosity. Both macro- and nanopores could in principle host materials grown by ALD. In this study, Al_2O_3 and Co ferrite were chosen to coat the Ni skeleton. Al_2O_3 has a high dielectric constant (of about 7-10[75]); meanwhile, Co_2FeO_4 is ferrimagnetic. For the latter, conformal coating could result in strong magnetic exchange coupling between the ferromagnetic metallic porous matrix and the guest metal oxide component. Remarkably, the porous structure of the Ni matrices is maintained after the ALD process, which demonstrates that ALD permits the deposition of different types of oxide nanocoatings at relatively low, non-damaging temperatures. Structural and magnetic characterization reveals that Ni is not severely oxidized during the process. In addition, the resulting nanocomposite may become either more hydrophilic or hydrophobic than the parent Ni film, depending on the applied nanocoating. The proposed synthetic protocol could be readily extended to fabricate other 3D porous metal supported composite nanostructures for a variety of technological applications.

4.2.2 Experimental section

4.2.2.1 Preparation of the 3D porous Ni film

All solvents and chemicals were of analytical grade and used without further purification. Deposition of 3D porous Ni film was carried out in a double-jacketed single-compartment cell with an electrolyte containing 2 M NH_4Cl and 0.1 M $NiCl_2$ at a pH value of 3.5. The working electrode (WE) was Si/Ti(25 nm)/Au(125 nm) with an active area of 0.25 cm^2 (Ti and Au were grown by evaporation). A platinum wire served as the counter electrode and a dual-junction Ag|AgCl 3M KCl (E = + 0.210 V versus standard hydrogen electrode) was used as the reference electrode. The electrolyte was bubbled with nitrogen to deaerate the solution before electrodeposition. Electrodeposition was performed galvanostatically at j = -1 A cm^{-2} for 150 s with a gentle stirring speed of 300 rpm at room temperature. The resulting porous Ni films were washed with Milli-Q water and dried in air.

4.2.2.2 Fabrication of Ni supported Al_2O_3/Co_2FeO_4 composite films

ALD nanolayers onto the previously grown porous Ni films were prepared in a Cambridge Nanotech Savannah 100 reactor in exposure mode. Al_2O_3 coating was produced by alternate pulsing of trimethylaluminum (TMA) and ozone (O_3) at a deposition temperature of 70-200℃. For Co_2FeO_4 films, deposition was performed by alternate pulsing of cobaltocene ($Co(Cp)_2$), ferrocene ($Fe(Cp)_2$) and O_3 at 250℃[76]. Pulse and purge times were optimized for each material, as described in Table 4.1.

4.2.2.3 Characterization of the structure and physical properties

Scanning electron microscopy (SEM) images and energy-dispersive X-ray spectroscopy (EDX) analyses were acquired using a Zeiss Merlin microscope operated at 3 kV and 15 kV, respectively. Transmission electron microscopy (TEM) and STEM-EDX analyses were performed on a Tecnai F20 HRTEM /STEM microscope operated at 200 kV. Cross sectional specimens were prepared by embedding the composites in EPON^{TM} epoxy resin. Subsequently, a very thin slide was cut using a microtome apparatus and placed onto a carbon-coated Cu TEM grid. X-ray diffraction (XRD) patterns of the different samples were recorded on a Philips X'Pert diffractometer with a pixel^{1D} detector in the 25-58° 2θ range (step size = 0.026°, total time = 1200 s) using Cu K_α radiation (λ = 0.154178 nm). Hysteresis loops were recorded at room temperature using a vibrating sample magnetometer (VSM) from Micro Sense, with a maximum applied magnetic field of 0.4 Tesla. Wettability properties of both uncoated and ALD-coated Ni samples were measured on a surface analyzer (Smartdrop, Femtofab) (sessile drop technique) at room temperature. 7 µL droplets of 5 wt% NaCl aqueous solution were deposited dropwise on the materials' surface using a microdispenser and the contact angle was determined.

4.2.3. Results and discussion

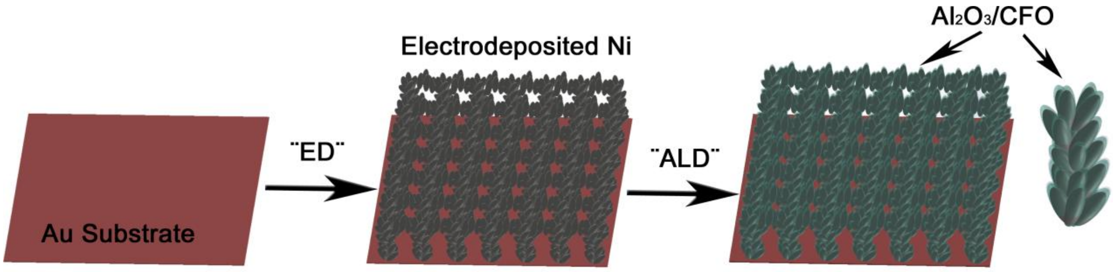

Figure 4.12: Schematic picture illustrating the fabrication of 3D porous Ni supported Al_2O_3/ Co_2FeO_4 nanolayers. CFO denotes Co_2FeO_4.

Figure 4.12 schematically shows the preparation process followed to obtain the porous composite films. First, a hierarchically porous Ni film is electrodeposited onto the Au surface at a sufficiently negative current density. Ni possesses a high overpotential toward hydrogen evolution during electrodeposition in acidic media[77]. The generated hydrogen bubbles are absorbed onto the WE and then are liberated from the freshly grown Ni deposit to the electrolyte-air interface, acting as a dynamic template during the deposition. Hence, metal electrodeposition occurs between the hydrogen bubbles, yielding a film with a 3D porous architecture. The porous Ni film acts as a backbone to deposit Al_2O_3 and Co_2FeO_4 by ALD.

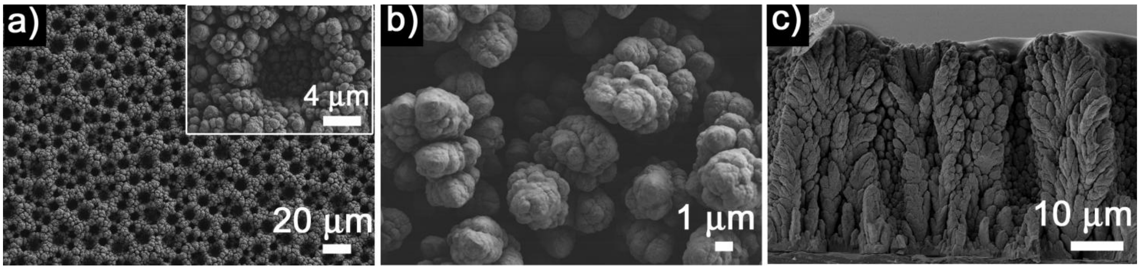

Figure 4.13: SEM images of the 3D porous Ni film: a) on-top general view of the material (inset shows a detail of a macropore); b) on-top zoomed detail of the pore wall; c) cross-sectional view of the Ni film.

Shown in Figure 4.13 are some representative SEM images of the as-deposited 3D porous Ni film. At low magnification (Figure 4.13a), pores with an on-top circular shape are seen all over the surface, whose sizes range from 5 µm to 15 µm. Higher magnification observations (Figure 4.13b) reveal that the pore walls consist of numerous tiny, interwoven, little protruding dendrites. The cross-sectional view of the deposits (Figure 4.13c) confirms the ramified nature of the pore walls. The deposited Ni thickness is approximately of 40 µm. Interestingly, the macropores extend from the outermost surface almost down to the substrate, having a depth of ~30 µm. This demonstrates the rather high aspect-ratio of the pores.

To obtain a smooth coating that perfectly replicates the template surface it is important to identify the deposition conditions to be within the ALD window. This window is a temperature region where the growth rate is constant and assures a tight control of the process and high reproducibility. Working outside this window means that undesired processes can occur, including decomposition or desorption of the precursor (temperature too high), precursor condensation or insufficient reactivity (temperature too low). As a result, the growth rate is modified and the level of impurities in the film can increase. For Al_2O_3, which is the most widely studied material in ALD because it has a behavior close to ideal (i.e., the ALD window is well established), the following reaction mechanism has been proposed[78]; 1) diffusion of the aluminum precursor ($Al(CH_3)_3$) into the near surface region of the host material, (2) reaction and saturation of the substrate surface with $Al\text{-}CH_3$ species and purge to eliminate reaction products and excess of the precursor (3) diffusion of the oxygen precursor into the $Al\text{-}CH_3$ surface, (4) reaction and saturation of the surface with Al-OH species followed by a purge to eliminate the reaction products. This is defined as the first ALD cycle and it is repeated as many times as required to obtain the desired thickness. This process allows the formation of a dense Al_2O_3 film that grows on top of the host material. According to the literature, the growth of a continuous thin layer of Al_2O_3 by ALD is possible at a temperature as low as 33℃[79] but the reaction kinetics is slow in this case (since the reaction is thermally activated) and hence higher temperatures are sometimes required[34]. The completion of the reaction, *i.e.* full coalescence of the Al_2O_3 clusters, needs longer time at lower temperatures.

Sample	A1	A2	A3	CFO/Ni
T	70℃	200℃	200℃	250℃
O source	H_2O	O_3	O_3	O_3
Precursor	TMA	TMA	TMA	$Co(Cp)_2$, $Fe(Cp)_2$
ALD mode	Pulse 0.3 s Exposure time 30 s	Pulse 0.3 s Exposure time 30 s	Pulse 0.7 s Exposure time 90 s	Fe: pulse 2s expos 30 s Co: pulse 1s expos 30 s

Table 4.1: ALD parameters used in this work. A1, A2 and A3 refer to Al_2O_3 coatings applied to Ni at the indicated experimental conditions. CFO/Ni stands for Co_2FeO_4 coating onto Ni.

It should be noted that, due to the precursor chemistry, such an ideal behavior is in many materials not easy to achieve. Here, as detailed in Table 4.1, several experiments have been performed varying the deposition temperature, oxygen source, precursor pulse and exposure time, to identify the optimal ALD conditions for both Al_2O_3 and Co_2FeO_4.

SEM images and the corresponding EDX mappings for A1, A2 and A3 composites are shown in Figure 4.14. Figure 4.14a reveals that the surface of A1 composite is rather rough, featuring small clusters instead of a continuous shell. Nevertheless, Al, O and Ni elements were homogeneously distributed in the corresponding EDX mapping image (Figure 4.14b) (note that shadowing effects during EDX analysis preclude detection of elements inside the pores). Thus, from the morphology observed in Figure 3a it is suggested that these deposition conditions are not optimal. It is likely that the reaction temperature is too low (precursor condensation-insufficient reactivity).

When the temperature is increased to 200℃ and, simultaneously, water is replaced by ozone (more reactive oxygen source), the Ni surface becomes smoother. An Al_2O_3 layer coating the Ni grains is apparently visible from Figure 4.14c and 4.14e. Remarkably, the porosity of the Ni matrix is preserved after the Al_2O_3 deposition, indicating that the oxide nanolayer is extremely conformal to the Ni skeleton. EDX elemental distribution images of A2 and A3 composites (Figure 4.14d, f) show that Al and O are distributed in a parallel way, which indicate that the relative Al_2O_3 coverage is completely uniform for reactant exposure times of 30 s. This finding is similar to that reported by George et al.[66] who also demonstrated that a reactant exposure of 30 s was sufficient to obtain a nearly conformal coating in high aspect-ratio structures.

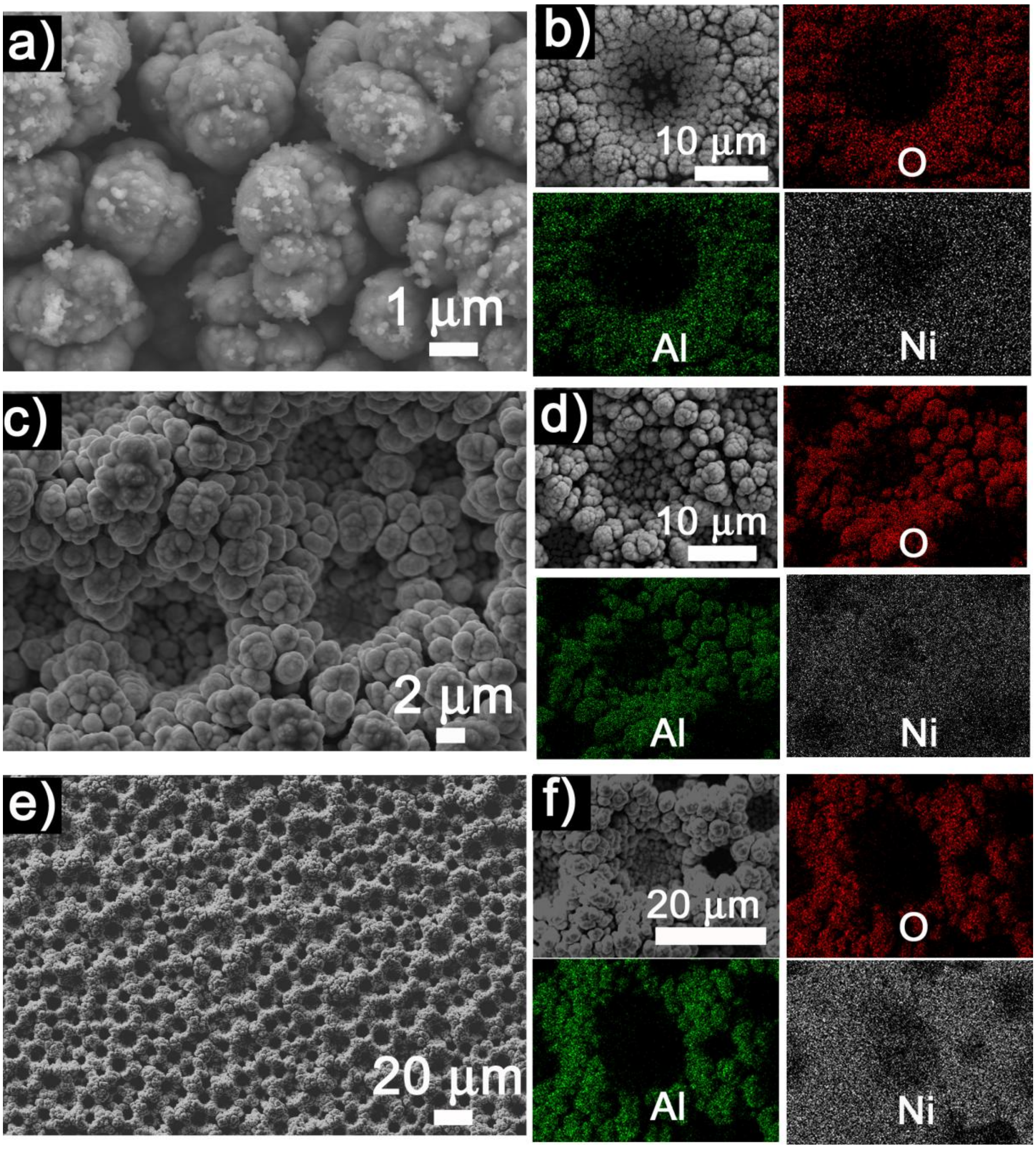

Figure 4.14: On-top SEM images of a) A1, c) A2 and e) A3 nanocomposites. EDX mapping distribution of Al, O, and Ni elements in b) A1, d) A2 and f) A3 composites, obtained from the zoomed SEM images shown on the left.

To further assess the conformal coating of Ni with Al_2O_3, sample A3 was embedded in resin and sliced in order to gain insight into Ni/Al_2O_3 interface. Sample preparation was very challenging since the material was prone to break into several pieces during the slicing owing to their 3D porous structure. Nevertheless, reasonably large isolated fragments of the material could be found by TEM, as shown in Figure 4.15a. These fragments, featuring a dark contrast, are surrounded by a brighter-contrast shell, as indicated with the solid orange line in Figure 4.15a.

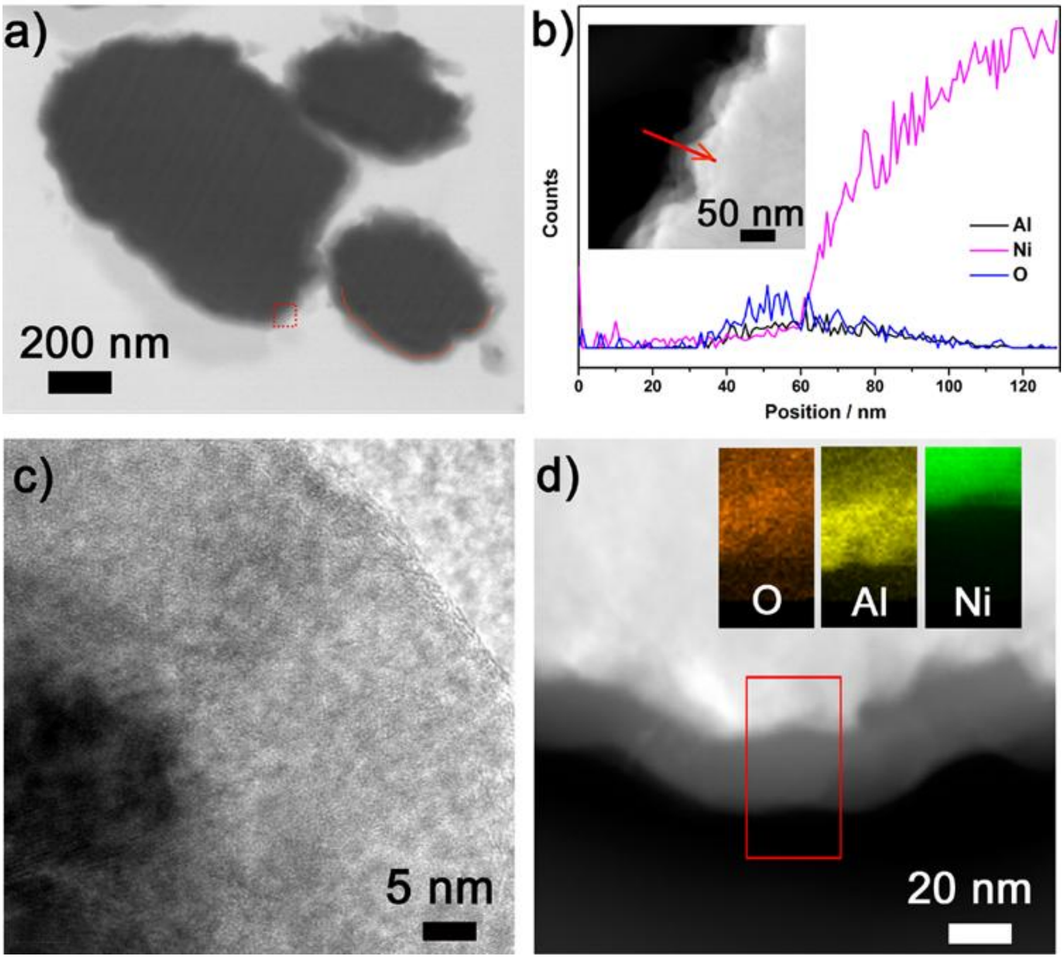

Figure 4.15: a) TEM image of A3 nanocomposite slice; b) line-scan STEM-EDX analysis across the interface between Ni and Al_2O_3, as indicated by the red arrow in the insert STEM image; c) HRTEM image of the area enclosed with the red dotted square in a); d) EDX elemental distribution of O, Al and Ni in the interfacial area enclosed within the red rectangle.

STEM-EDX line scan analysis was performed in order to determine the composition profile across the interface (Figure 4.15b). An EDX line scan was done along the red arrow depicted in the inset STEM image of Figure 4.15b, which embraces a translucent thin layer and a denser bright region. As the electron beam is scanned towards the Ni matrix, Al and O signals first appear at 35 nm from the initial scanning point and vanish at approximately 100 nm. Conversely, the Ni signal monotonically increases from around 60 nm, which indicates that the Al_2O_3 coating has a thickness of about 25 nm. Remarkably, there is no abrupt switching from Al and O signals to Ni signal but, instead, they coexist within a few nanometers interval.

This suggests the formation of a mixed Al/Ni oxide at the interface. This was further proved by STEM-EDX elemental distribution mapping (Figure 4.15d), *i.e.*, Ni-oxide or some mixed $(Al,Ni)_xO_y$ phases may exist at the interface region. Hence, the structure of the interface can be defined as $Al_2O_3/(Al,Ni)_xO_y/Ni$. Figure 4.15c actually corresponds to the HRTEM of the region enclosed in the small red box in Figure 4.15a. It is likely that the as-deposited Al_2O_3 layer is amorphous since lattice fringes were not detected. The amorphous nature of Al_2O_3 was further confirmed by θ-2θ scan X-ray diffraction (XRD) (Figure 4.16). For comparison, the XRD data of uncoated Ni is shown. Besides a peak coming from the Au surface, the diffraction peaks corresponding to Ni (111) and Ni (200) reflections of face-centered cubic (*fcc*) structure remain virtually unchanged after ALD coating of Ni scaffold with Al_2O_3. Hence, the 3D porous Ni withstands the ALD process both morphologically and crystallographically to a great extent. The typical peaks of crystalline Al_2O_3 in the range 25°-55° are not observed in the XRD pattern. Instead, two peaks at 33° and 37° were detected, which can be attributed to a Ni_xO_y phase. This result further confirms the hypothesis that the Ni outermost surface was slightly oxidized during ALD (i. e., the interface can be described as $Al_2O_3/(Al, Ni)_xO_y/Ni$). Based on these findings, 3D porous Ni supported cobalt ferrite composite films (Co_2FeO_4) were prepared using a similar protocol (Table 4.1). Metallocences are ideal precursors for ALD owing to their thermo stability, high volatility and reactivity toward oxidation to a certain degree[81].

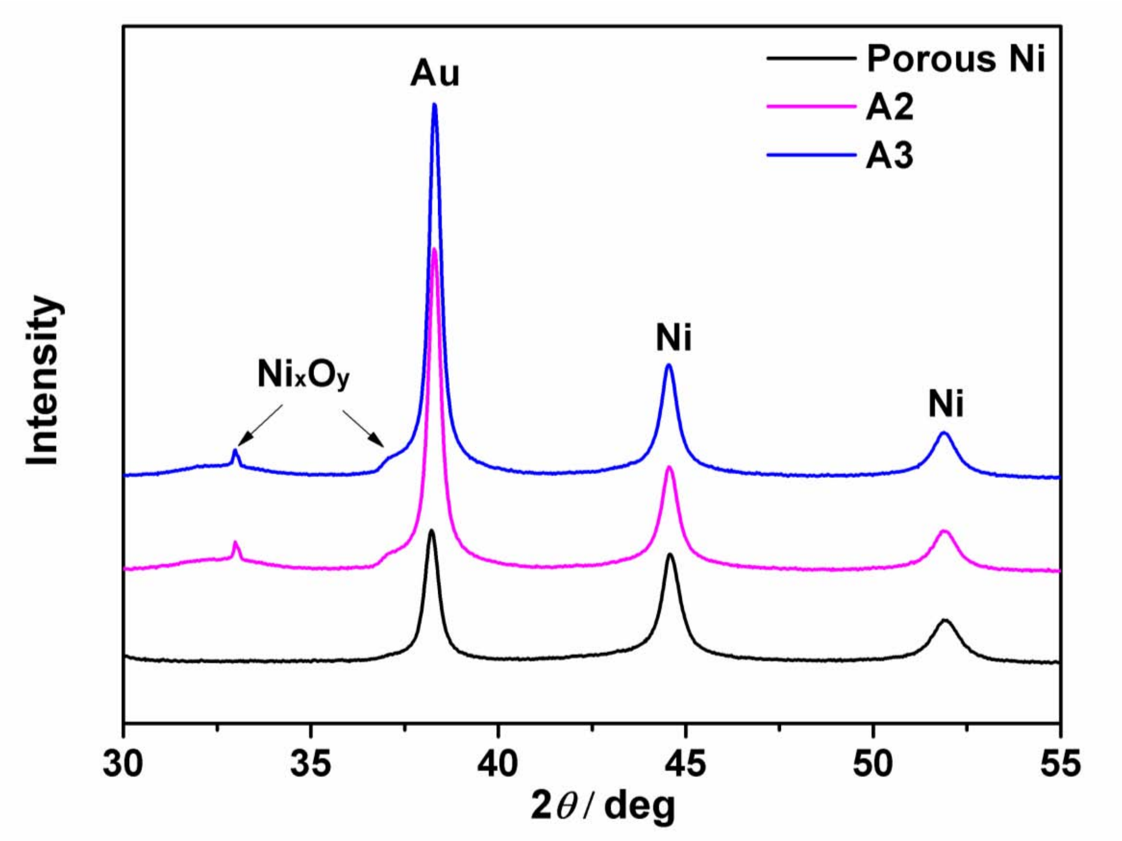

Figure 4.16: XRD patterns of porous uncoated Ni, and A2 and A3 composite samples.

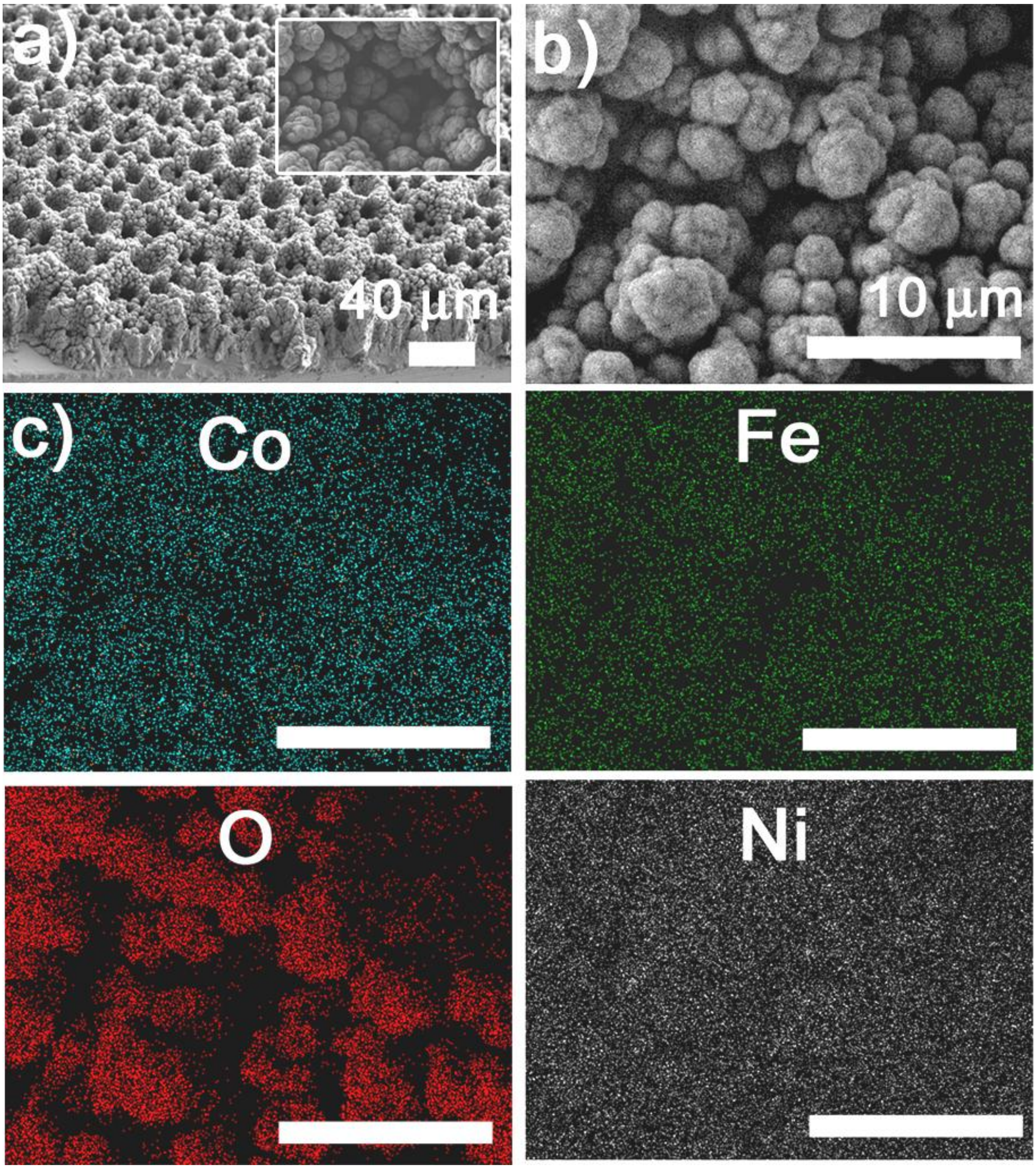

Figure 4.17: a) Oblique-sectional (insert, magnified) view of 3D porous Ni-supported cobalt ferrite; b) magnified SEM image; c) corresponding Co, Fe, O and Ni EDX mappings.

Figure 4.17 depicts typical SEM images of the as-prepared 3D porous Ni-supported cobalt ferrite. As for Al_2O_3 coating, the porous morphology provided by the Ni matrix remains unchanged (Figure 4.17a,b) and Co, Fe and O elements are evenly distributed (Figure 4.17c). A Ni/Co_2FeO_4 specimen for cross sectional view was also prepared to assess the quality of the oxide nanocoating. As displayed in the TEM image (Figure 4.18a), the sliced porous film shows a nanosheet morphology, being the interface between the metal and the oxide layer less defined compared to Al_2O_3 case. For this reason, a more detailed characterization was carried out near the edge. When the electron beam was spotted onto the red dot “b” in Figure 6a, Ni, Fe, Co and O signals appeared in the EDX spetrum (Figure 4.18b).The relative proportion between Co, Fe and O yielded a composition close to Co_2FeO_4, as expected. When the electron beam was swept from the body to the edge (red arrow in Figure 4.18a), the Ni signal gradually decreases down to negligible levels (Figure 4.18d). Meanwhile, Co, Fe and O signals simultaneously increase at the particle edge until a maxinum value, leading to a Co/Fe/O atomic ratio of 2:1:4. The atomic ratio of Co in the coating is larger than that of Fe, owing to the selected deposition conditions and the classic reactivity trend Co(II, d^7)>Fe(II, d^6), known for metallocenes[82]. The interface from pure Ni to Co_2FeO_4 is not well defined (as it was also the case for Ni/Al_2O_3), but rather a transition layer is formed which embraces the four elements. The thickness of this transition layer is around 5 nm.

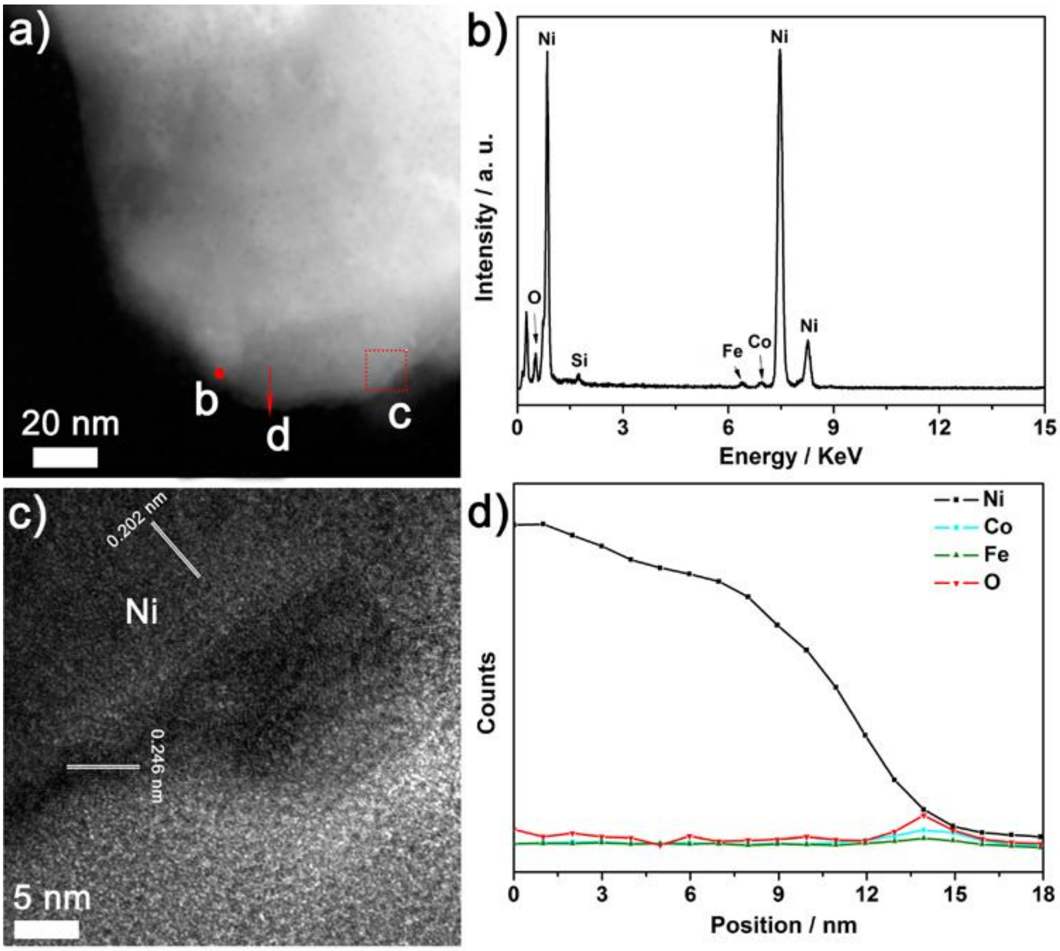

Figure 4.18: a) TEM image of the cross sectional view of Ni/Co_2FeO_4 sample; b) EDX spectrum corresponding to the red dot "b" in a); c) HRTEM image of the area enclosed with the red square labeled as "c" in panel a); d) line-scan STEM-EDX analysis across the edge depicted with the red arrow "d" in panel a).

Figure 4.18c shows a HRTEM image of the area enclosed in the red box in Figure 4.18a. The porous Ni template is slightly brighter than the Co_2FeO_4 nanocoating, which is about 5 nm thick. Both Ni and Co_2FeO_4 are polycrystalline with clear lattic fringes. The interplanar distance of d = 0.202 nm can be assigned to the (111) *fcc* phase of Ni, whereas d = 0.246 nm matches the (311) *fcc* of Co_2FeO_4. The formation of crystalline cobalt ferrite is also confirmed by the XRD pattern shown in Figure 4.19. Namely, the small peak at 36.02° after ALD can be ascribed to the (311) reflection of Co_2FeO_4.

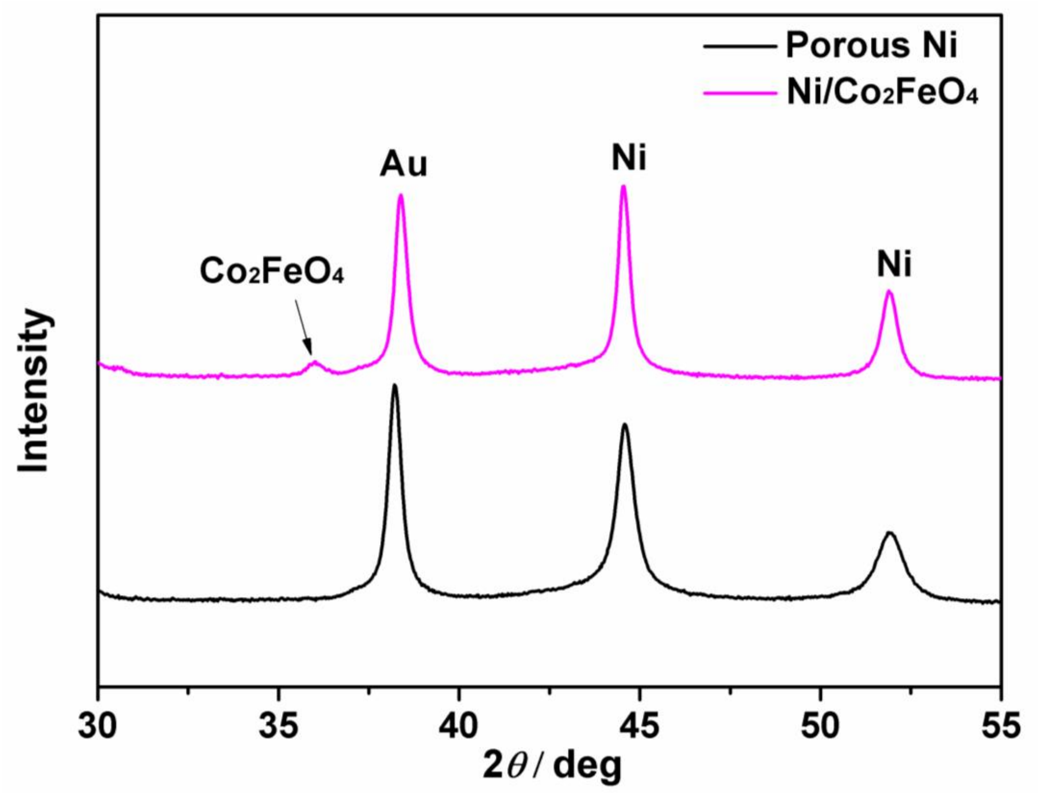

Figure 4.19: XRD patterns of porous uncoated Ni and Ni-supported CFO.

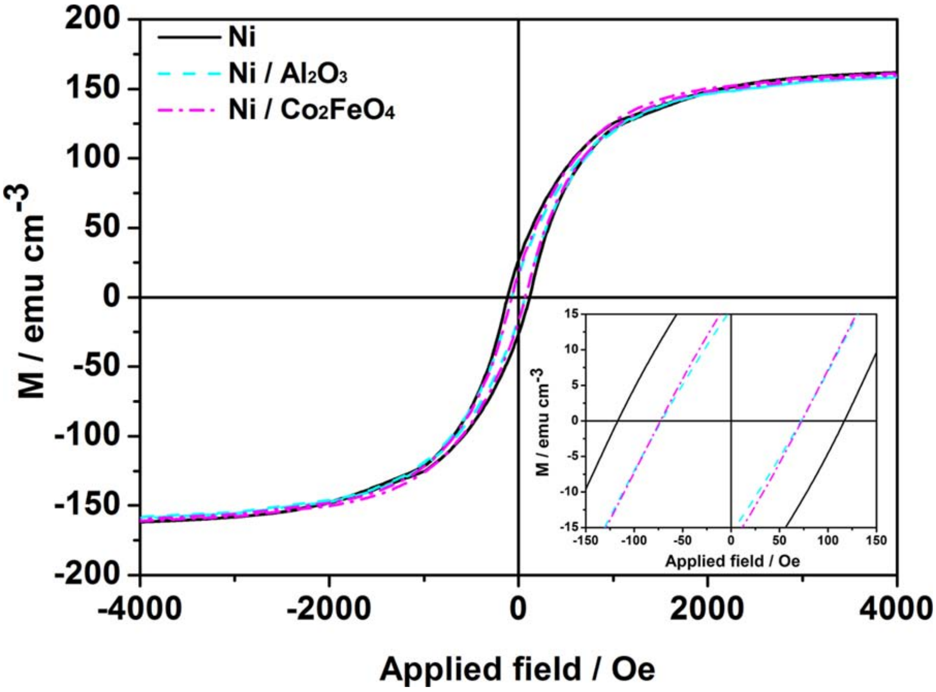

Figure 4.20: Room temperature hysteresis loops of uncoated Ni, Ni/Al_2O_3 and Ni/Co_2FeO_4 composite porous films.

Room-temperature magnetic hysteresis loops of the uncoated Ni, Ni/Al_2O_3 and Ni/Co_2FeO_4 porous films are shown in Figure 4.20. The saturation magnetization (M_s) for the Ni/Al_2O_3 nanocomposite films (159.1 emu cm^{-3}) is slightly lower than for pure Ni (162.02 emu cm^{-3}). This can be ascribed to the presence of a small amount of NiO (in agreement with the results from XRD and STEM-EDX), which is antiferromagnetic and hence exhibits virtually zero net magnetization. Note that the porosity degree is not taken into account in the magnetization (M) normalization; that is, the volume is calculated from the real "geometrical" thickness. When comparing the experimental and tabulated M_s value for pure Ni (491 emu cm^{-3}), it comes out that the porosity degree of the Ni layer is approximately 67 vol%. Although NiO is antiferromagnetic, no exchange bias effects (e.g., loop shift[83] or enhanced coercivity[84]) are observed, mainly because the relative amount of NiO is very low compared to that of Ni and exchange bias effects are known to be inversely proportional to the thickness of the ferromagnetic counterpart[83]. Similarly, because of the relatively low volume fraction of Co_2FeO_4, its contribution to the overall hysteresis loop of the Ni/Co_2FeO_4 film is also very small.

The hysteresis loops also reveal that the H_c values of the composite films (around 73 Oe) are smaller compared to H_c of uncoated Ni (118 Oe). This decrease of coercivity is probably related to thermally-induced microstructural changes that occur in metallic Ni during the ALD process. Actually, Figure 4.16 and 4.19 reveal that the width of the XRD peaks of Ni becomes narrower after ALD (particularly for Ni/Co_2FeO_4), which indicates that the crystallite size of Ni increases. The average crystallite size for Ni, estimated from XRD Rietveld refinements, increases from approximately 35 nm (for uncoated Ni) to 45 nm in the case of Ni/Al_2O_3 and 60 nm for Ni/ Co_2FeO_4 composites. In general, grain boundaries hinder and pin the propagation of magnetic domain walls. Hence, H_c, in polycrystalline magnetic alloys, is inversely proportional to the grain size[85]. Also the release of microstrains associated with the ALD thermal treatments also contributes to reduce the coercivity.

The wettability of Ni, Ni/Al_2O_3 and Ni/Co_2FeO_4 films was characterized by the sessile drop technique, using 7 µL of 5 wt% NaCl droplets. Figure 4.21 shows the shape of

NaCl droplets deposited onto the three different surfaces. The contact angle attains the highest value at the surface of uncoated Ni (138.8°) (Figure 8a). The contact angle values decrease to 119.2° and 102° for Ni/Al_2O_3 and Ni/Co_2FeO_4, respectively. Variations in surface roughness could account for the observed differences among the three samples. However, surface roughness is similar since both Al_2O_3 and Co_2FeO_4 coatings are really thin and conformal. In fact, variations of the contact angle in solids not only depend on surface roughness, but are also related to the surface energy of the investigated materials[86]. Metal oxides have lower surface energy than pure metals since the latter tend to react with the atoms (molecules) from the surrounding in an attempt to form a passive layer (e.g., metal oxide) with lower energy level. In general, most molecular liquids form lower contact angles on materials with a higher surface energy. However, this is opposite to what is observed here. Nonetheless, the wettability of a surface is also determined by the outermost chemical groups at the solid. Metal oxide surfaces are often fully or partly covered with OH groups which are usually formed by the interaction of water with the metal ions at the surface[87]. The surface-anchored hydroxyl groups participate in hydrogen bonding with the static aqueous droplets, thus increasing the wettability of the material.

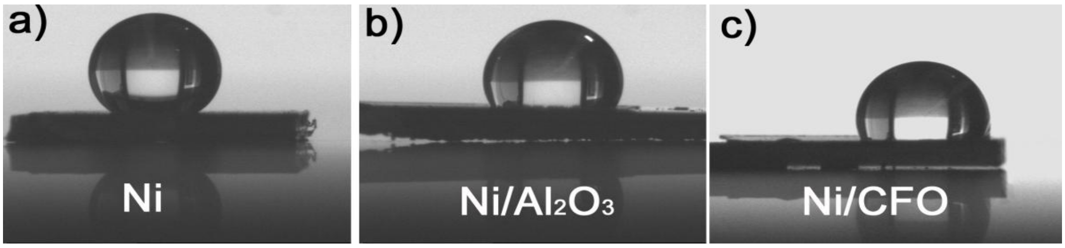

Figure 4.21: Optical photographs of an aqueous sodium chloride droplet (7 μm) onto the surface of (a) Ni, (b) Ni/Al_2O_3 and (c) Ni/Co_2FeO_4 porous films.

This combination of metals and oxides in a single 3D porous structure could be appealing as building blocks in MEMS/NEMS. In biological systems, relatively hydrophilic coatings allow the formation of tightly adherent layers of aqueous biological fluids with high lubricity to the material. Our results reveal that 3D porous Ni structures coated with metal oxide nanolayers are slightly more hydrophilic than the parent Ni template. Moreover, in biological applications, these oxide coatings would prevent from Ni ion leaching, which is a concern since Ni can pose cytotoxicity problems. In electronic devices, the use of Al_2O_3 would possibly reduce the tendency toward electrical shorting[75] since Al_2O_3 has a high dielectric constant (in the range of 7-10) and an electrical resistance of about 1015 Ω·cm. Likewise, Ni/Co_2FeO_4 is a material with potential applications in spintronics and as spring-magnet layered composites. Moreover, gas sensor based on cobalt ferrite showed high response, good selectivity to low concentration of ethanol[88], especially, it could detect 10 ppm ethanol. Yet the investigation on gas-sensing properties of cobalt ferrite is really limited, and further experimental proof is nevertheless still necessary.This indicates that the here-presented synthetic strategy of combining electrodeposition and ALD is very convenient to produce magnetic nanocomposite porous films with potential applications in a wide range of technological fields.

4.2.4 Conclusions

The possibility to combine electrodeposition with ALD to prepare 3D porous magnetic metals conformally coated with metal oxide nanolayers, namely Ni/Al_2O_3 and Ni/Co_2FeO_4, is demonstrated. Due to the nature of the presented approach the host (metal) and guest (metal oxide) materials can be chosen with certain degree of freedom. We demonstrate that both the hierarchical porosity and magnetic properties of the parent metallic Ni template are maintained after ALD step. Moreover, the presence of a nanometer-thick layer of Al_2O_3 or Co_2FeO_4 covering the Ni scaffold improves its hydrophilicity. The procedure could be extended to prepare other magnetic compositions obtained using the same protocol. Owing to the synergies emerged between the host and the guest components, these nanocomposite magnetic porous films are promising candidates for widespread technology areas, such as biological applications, magnetic sensors or magnetic micro/nano-electromechanical systems (MEMS/NEMS), amongst others.

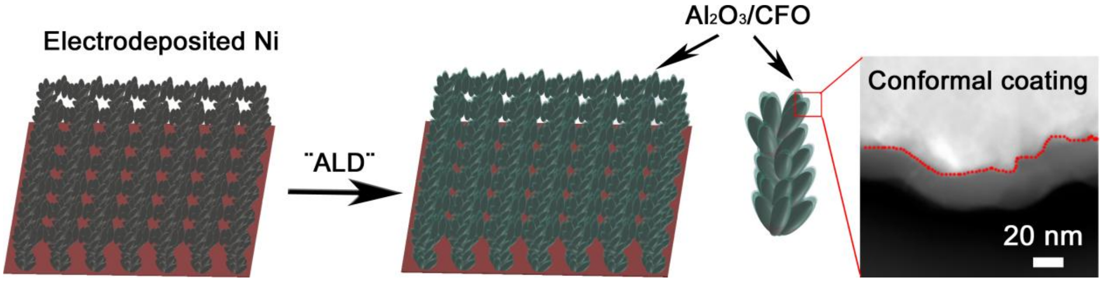

Figure 4.22: Table of contents graphic

4.3 Nanomechanical behaviour of open-cell nanoporous metals: homogeneous versus thickness-dependent porosity

Two different nanoporous materials, porous copper prepared by dealloying and porous nickel prepared by electrodeposition, have been studied by means of nanoindentation experiments at different maximum applied loads. While nanoporous Cu is homogeneous along its cross-section, the electrodeposited Ni films show a graded porosity, with smaller pores and thicker pore walls close to the film's surface. The mechanical properties of the two materials have been extracted using a methodology based on scaling laws and subsequent interpretation has been performed using finite element simulations. Two different deformation mechanisms are observed for nanoporous Cu and nanoporous Ni, respectively. Dealloyed porous copper behaves as an homogeneous material without evident effect of densification and with mechanical properties that are independent of the applied load. Given this homogeneity, it is possible to fit the entire loading -unloading curve for different maximum applied loads with a single set of mechanical properties. Conversely, electrodeposited porous nickel shows a decrease in the reduced Young's modulus, an increase in yield stress and a constant hardness when the maximum applied load during nanoindentation is increased. While the decrease in the reduced Young's modulus can be explained in the context of thickness inhomogeneity of the electrodeposited porous nickel (i.e., increase of porosity with depth), this cannot explain, and actually would go against, the observed increase in the yield stress, which is instead associated to the decrease in the ligament size.

Keywords: Dealloying; Electrodeposition; Finite element analysis (FEA) Mechancial properties; Nanoindentation; Porous materials; Size effects

4.3.1 Introduction

Owing to their extraordinarily high surface area, nanoporous materials have become ideal candidates for a widespread range of technological applications, both in chemistry[89,90], as well as in magnetic devices[91]. From a structural point of view, porous materials are being used for impact-energy absorption and in lightweight construction, as well as in various types of thermal insulation and acoustic damping[92].

Several strategies are currently being pursued for the preparation of nanoporous films. These include dealloying or electrodeposition[93,94] among others. Electrodeposition (either using hard templates -e.g. anodic aluminum oxide -or soft templates -e.g. block copolymers -in the electrolytic bath) and de-alloying are particularly suited for the preparation of metallic porous alloys (sometimes referred to as metallic foams). Selective de-alloying techniques typically produce materials with an open sponge-like structure of interconnecting ligaments and pore sizes of a few nm. During de-alloying, the least noble component in a solid solution is leached from the alloy, while the noblest elements undergo surface diffusion and agglomeration, forming the sponge-like metallic structure[93].

Irrespectively of the application, the mechanical properties of porous materials are of uppermost importance to ensure robustness and endurance of any device in which they are integrated. In fact, despite their extended utilization in industry, porous materials suffer from the drawback of being usually rather brittle. Therefore, the study of their mechanical properties by uniaxial tension, macroscopic compression or torsion experiments is often not possible. For this reason, nanoindentation has become one of the most appropriate methods to measure the mechanical properties of these materials since this technique keeps the induced deformation constrained into very local length scales. However, proper interpretation of the mechanical properties of porous materials using nanoindentation remains still rather challenging. First, a densified zone can form underneath the indenter during indentation, thus precluding a clear-cut assessment of the properties of the initially non-deformed material. Secondly, most of the models existing in the literature to correlate mechanical properties (i.e., hardness and Young's modulus) with the porosity degree are only applicable to some particular arrangements of porous networks (e.g., honeycomb-like geometries or close-cell pore structures)[95,96]. Remarkably, while the porosity degree is often taken into account in these models, the important role played by the pore size itself on the resulting mechanical performance is often overlooked. Furthermore, most mechanical studies so far have only focussed on fully homogeneous porous films or foams. The mechanical response of heterogeneous (i.e., thickness-dependent porosity) nanoporous alloys has essentially not been investigated.

In this work, the mechanical response during nanoindentation of homogenous nanoporous Cu films, prepared by dealloying, and that of heterogeneous nanoporous Ni (i.e., with graded porosity across thickness) directly grown by electrodeposition from a block polymer-containing solution, are compared. Interpretation of the experimental results is supported with finite element simulations. While the properties of homogeneous nanoporous Cu are found to be rather independent of the applied indentation load, the Young's modulus of porosity-graded nanoporous Ni decreases for higher loads, while the opposite trend is observed in the corresponding values of yield stress. Such results are ascribed to the structural evolution of nanoporous Ni with depth, i.e., to the interplay between the increase of the average pore size (and porosity degree) and the decrease of the ligament size as the distance from the film's surface increases.

4.3.2 Materials and Methods

4.3.2.1 Copper-Zinc dealloying

$Cu_{20}Zn_{80}$ 2 mm-thick sheets were purchased from Goodfellow. Nanoporous copper (Cu) samples were obtained by dealloying these sheets in 85 wt% H_3PO_4 for 4 days following the methodology described by Chung Cheng and coworkers[97]. Scanning Electron Microscopy (SEM) equipped with Energy-dispersive X-ray (EDX) was used to prove the Zn depletion. The morphology of the obtained nanoporous layer was observed by SEM. Further verification of Zn depletion was carried out by X-ray diffraction (XRD).

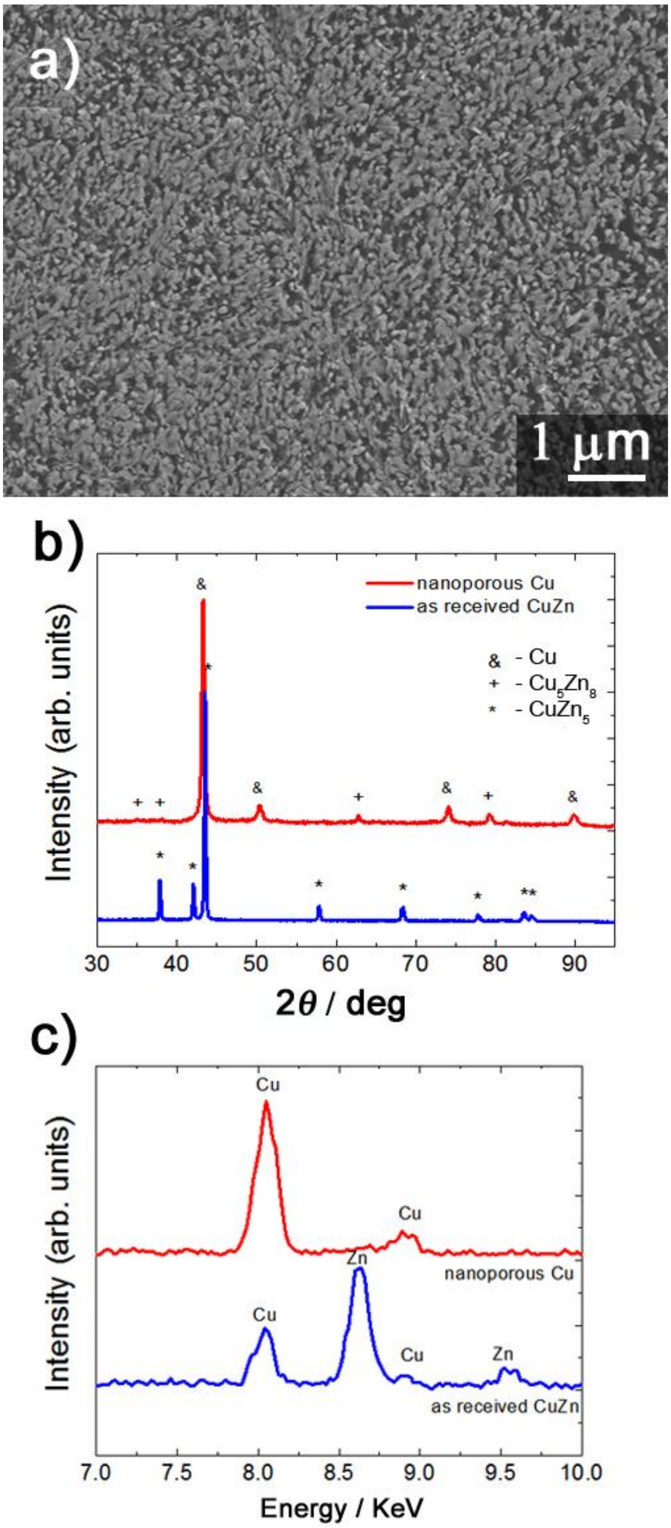

Figure 4.23: a) SEM image of the nanoporous Cu film (prepared by dealloying), observed along its cross section (notice the pore homogeneity across film thickness), b) XRD patterns corresponding to the as-cast $Cu_{20}Zn_{80}$ ribbon and the nanoporous Cu obtained by dealloying of the ribbon, c) EDX analyses of the as-received and dealloyed $Cu_{20}Zn_{80}$ ribbon.

Prior to indentation and SEM imaging, the sample was hot embedded in a conductive resin and polished with diamond suspension to mirror like appearance. Figure 4.23a corresponds to a cross-section SEM image of the dealloyed copper where a homogeneous microstructure across its depth can be observed. Figure 4.23b and c show the XRD patterns and EDX spectra of this sample before and after dealloying, respectively. While no Zn is detected by EDX (Figure 4.23c), low-intensity diffraction peaks from the intermetallic Cu_5Zn_8 phase are observed by XRD (Figure 4.23b). This apparent contradiction is due to the different penetration depths of X-rays and electrons in the two techniques. Namely, a small quantity of Zn seems to be still present in the sample but it is located well inside the central part of the ribbons. The mechanical properties are determined at the surface of the ribbons, which consists only of nanoporous Cu. In a first approximation, we thus neglected the minor amount of Zn in the analyses. Total thickness of the dealloyed porous Cu film was 50 ± 0.5 µm. AFM scans on the surface of the samples provided a roughness value of Ra = 10.5 nm.

4.3.2.2 Nickel electrodeposition

Nanoporous nickel (Ni) film was obtained by potentiostatic electrodeposition in a single compartment double-jacketed three-electrode cell. Si|Ti (25 nm)|Au (125 nm) substrate was used as cathode with working area of 0.25 cm^2 exposed to the electrolyte. A platinum spiral served as counter electrode, which was positioned vertically facing the working electrode. A double junction Ag|AgCl 3M KCl electrode (E = + 0.210 V versus standard hydrogen electrode) was utilized as reference electrode. Electrodeposition was conducted using a PGSTAT302N Autolab potentiostat/galvanostat (Ecochemie). Electrolyte was prepared by mixing the pluronic P123 amphiphilic block copolymer surfactant and aqueous solution of 0.4 M $NiSO_4$, 0.5 M $NaSO_4$, 0.2 M boric acid and 0.5 g/L saccharine. To prepare the mixture, 4 g of P123 was heated to 60℃ in a beaker prior to the addition of the aqueous phase and mixed manually for 5-10 min at constant heat. Then certain amount of ethanol was added to the mixture to assure a ratio of 0.2 g P123 per mL of ethanol. The resulting solution was subjected to vigorous magnetic stirring until it showed a turbid milky appearance. The nanoporous Ni was obtained at room temperature by applying a constant potential of -1.8 V for 1200 s.

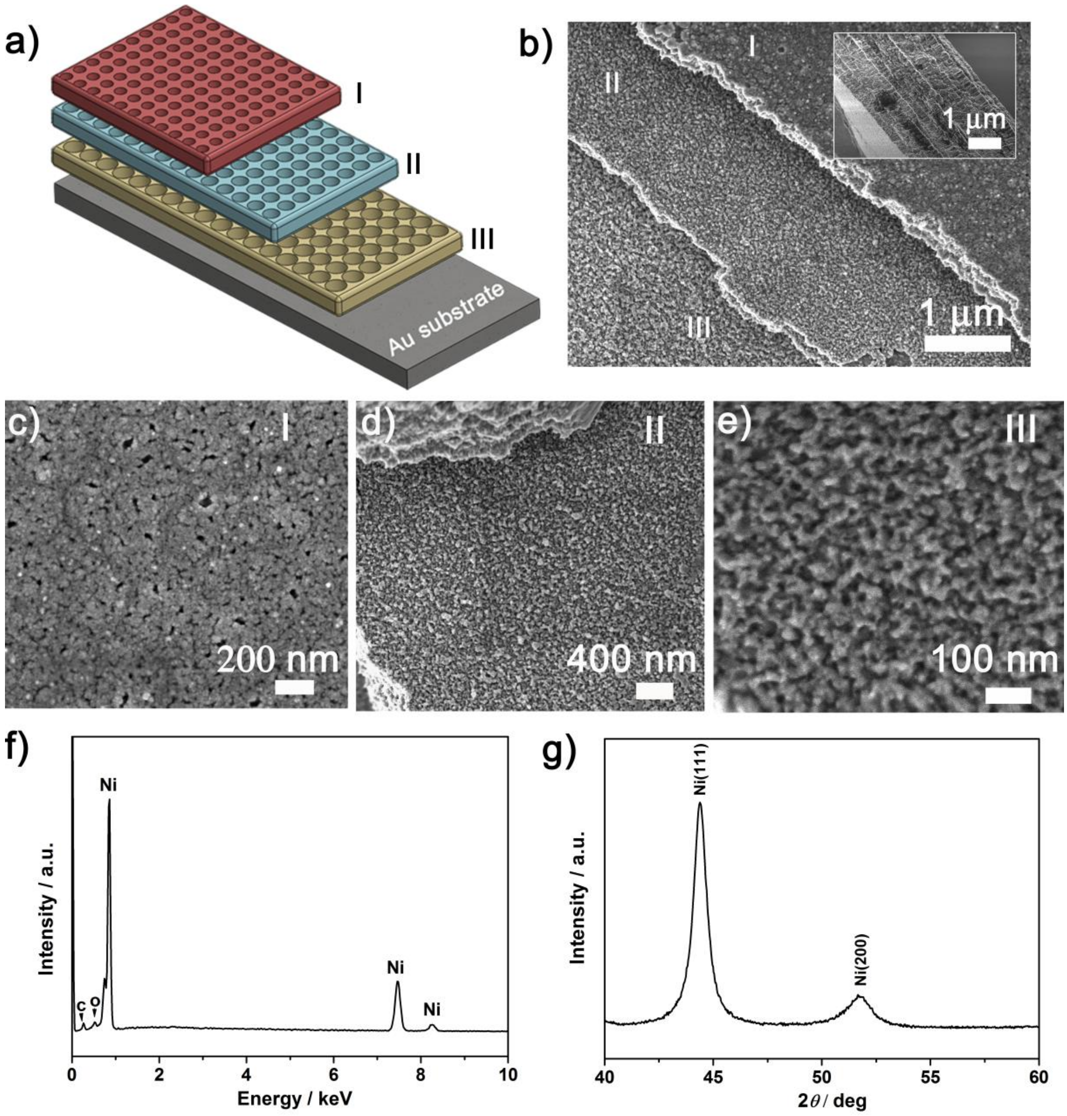

Figure 4.24: a) Schematic diagram showing the layer-by-layer growth of the electrodeposited nanoporous Ni film, where the pore size decreases and the ligament size increases as we move away from the substrate, b) top-view and cross sectional view (inset) SEM images of the nanoporous Ni, corroborating the layer-by-layer growth, inset: the thickness of the coating is 7 µm ± 0.5 µm. c), d) and e) correspond to zoomed SEM images of layer I, layer II and layer III in image b), respectively, (f) EDX spectrum of this sample, (g) XRD patctern of this sample. All the SEM images were collected in backscattered electrons mode.

The concentration of surfactant was set at 8 wt% which is above the critical micelle concentration of P123. The hydrophilic Au substrate serves as aggregation site for P123, as the surfactant gathers spontaneously at the solid-liquid interface. The surfactant micelle directs the Ni^{2+} ions towards the substrate and acts as structure-directing agent. As depicted in Figure 4.24a, the growth of Ni follows a quasi-perfect layer-by-layer process, in which the pore size de-creases gradually along the vertical direction. This layer-by-layer growth fashion is evident from the corresponding SEM picture, see Figure 4.24b. Layer III, which corresponds to the first stages of electrodeposition, exhibits the largest pore size. As deposition proceeds, a second Ni layer is formed on top of the first porous Ni. This second layer (II) features smaller pore size. Consequently, the uttermost layer (layer I) has the smallest pore size (around 10-20 nm). Contrary to the average pore size, the width of the pore walls (i.e., lateral size of the ligament) progressively increases with film thickness, from 20 ± 10 nm (layer III) to 70 ± 10 nm (layer I). Panels (c) to (d) in Figure 4.24 are HRSEM images from which the aforementioned evolution in the ligament size can be clearly observed. A representative EDX spectrum of the nanoporous Ni film is shown in Figure 4.24f. Only Ni, together with very low oxygen and carbon signal, are detected. This proves that the porous layers are almost entirely metallic. No P123 template remains in the porous matrix. Furthermore, the X-ray diffraction pattern in the 40°-60° 2θ range of the nanoporous Ni is also shown here (Figure 4.24g). Two diffraction peaks corresponding to Ni(111) and Ni(200) of face-centered cubic (*fcc*) structure are detected. Total thickness of the electrodeposited porous Ni films was 7.0 ± 0.5 µm. AFM scans on the surface of the samples provided a roughness value of Ra = 1.8 nm.

4.3.2.3 Nanoindentation experiments, extraction of mechanical properties and finite element simulations

Nanoindentation experiments were performed in load-control mode, using a UMIS instrument from Fischer-Cripps Laboratories equipped with a Berkovich pyramidal-shaped diamond tip. The maximum applied load ranged from 2 to 25 mN. The thermal drift was always kept below 0.05 nm s^{-1}. At least 10 indents were performed at each maximum applied load to verify the accuracy of the indentation data. The same protocol was followed for both porous Cu and Ni. For the extraction of mechanical properties, the hardness and the reduced indentation modulus values were evaluated at the beginning of the unloading segment by means of the method of Oliver and Pharr[98]. In order to estimate the yield stress, σ_{ys}, the methodology described in Alcalá and Casals group[99,100] has been used. It is well known that during sharp indentation of a homogenyeous material, the relation between the applied load and the displacement of the indenter can be expressed through[101]:

$$P = Kh_s^2 \qquad \text{[Eq. 4.1]}$$

being P the applied load, hs the indenter's displacement and K a constant that depends on the indented material. The unloading stage can be fitted using[98]:

$$P_u = B(h_s - h_r)^m \qquad \text{[Eq. 4.2]}$$

where B and m are fitting parameters and h_r is the remaining hs at $P = 0$. Additionally, the Sneddon's relation states that:

$$E_{eff} = \frac{}{\sqrt{A_{max}}} \frac{\mathrm{d}P}{\mathrm{d}h}\bigg|_{h_{max}} \qquad \text{[Eq. 4.3]}$$

being E_{eff} the effective indentation modulus, η is assumed to vary with the indenter's shape[102,103] and it is equal to 0.793 for a Berkovich indenter[99], and A_{max} is the projected contact area between the material and the indenter at (h_{max}, P_{max}). E_{eff} can be written as:

$$E_{eff} = \left(\frac{1}{E_r} + \frac{1 - v_i^2}{E_i}\right)^{-1} \qquad \text{[Eq. 4.4]}$$

where v_i and E_i are the Poisson's coefficient and Young's modulus of the indenter, respectively, and E_r the reduced indentation modulus of the material under indentation. The slope at (h_{max}, P_{max}) during unloading can be calculated through:

$$\frac{dP}{dh}\bigg|_{h_{max}} = \frac{P_{max}}{h_{max} - h_e} = \frac{P_{max}}{h_{\mathrm{max}}(1 - h_e/h_{max})} \qquad \text{[Eq. 4.5]}$$

where h_e is the penetration depth at which the tangent curve at (h_{max},P_{max}) crosses the hs axis. Figure 4.25 shows a schematic of a loading – unloading indentation curve including the expressions for the loading and unloading stages and the expression for the slope of the unloading stage.

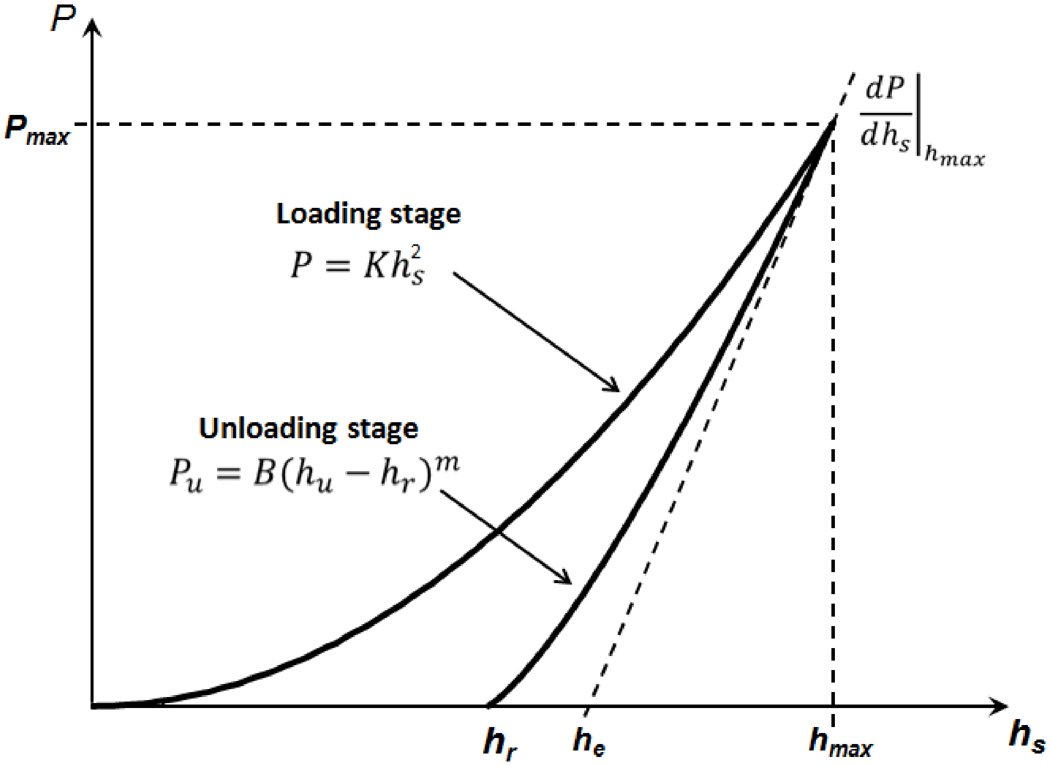

Figure 4.25: Schematic figure showing the loading and unloading stages during a sharp indentation test along with the expressions used to capture each stage. *P* is the applied load, h_s is the penetration depth, h_r is the remaining penetration depth after complete unloading and h_e is the penetration depth at $P = 0$ obtained from the slope (tangent) atthe upper part of the unloading stage.

Once parameters *B*, *m* and h_r in Eq. 4.2 are fitted, dP/dh evaluated at hmax can be obtained by differentiating Eq. 4.2 and he can be calculated through Eq. 4.5. Combining Eq. 4.1, Eq. 4.3 and Eq. 4.5 for (h_{max}, P_{max}) one can write:

$$E_{eff} = \sqrt{K\bar{p}}\,(1 - \frac{h_e}{h_{max}})^{-1} \qquad \text{[Eq. 4.6]}$$

being $\bar{p}$ = P/A the obtained hardness from nanoindentation experiments and A the projected contact area between the material and the indenter.

Finally, once having the values for E_{eff} and $\bar{p}$, one can use the expression[100]:

$$\frac{\bar{p}}{\sigma_{0.1}} = A_1 + A_2 \cdot \exp\left(\frac{-E_{eff}/\sigma_{0.1}}{A_3}\right) + A_4 \cdot \exp\left(\frac{-E_{eff}/\sigma_{0.1}}{A_5}\right) \qquad \text{[Eq. 4.7]}$$

to obtain $\sigma_{0.1}$, a characteristic stress corresponding to an uniaxial deformation of 0.1. Expressions for A_1, A_2, A_3, A_4 and A_5 can be found in Table 7 for Eq. (A.1) in the work of Casals and Alcalá[100]. Relation between $\sigma_{0.1}$ and σ_{ys} can be written as:

$$\sigma_{ys}^{n-1} = \frac{(0.1E)^n}{\sigma_{0.1}} \qquad \text{[Eq. 4.8]}$$

where *E* is the indentation modulus and *n* is the strain hardening coefficient during an uniaxial test.

With the extracted mechanical properties, we performed finite element (FE) simulations with the commercial ABAQUS finite element code under a full integration scheme. As the porous structure was not considered during simulations, the finite element mesh, constructed following a refining strategy, comprised two-dimensional 43,359 four-node axisymmetric quadrilateral elements and the Berkovich indenter was modelled using an equivalent conical indenter with an azimuthal angle equal to 65.3° . Simulations were performed under frictionless contact conditions and large-strain formulations. A linear elastic-perfectly plastic relation was assumed in the simulations with the Von Mises flow theory of plasticity, allowing to correlate directly $\sigma_{0.1}$ to σ_{ys}, as the strain hardening coefficient *n* was taken to be equal to zero. Here, it is worth mentioning that the presented FE model was intended to demonstrate that a unique set of mechanical properties was enough to roughly capture the overall indentation response of homogeneous porous Cu films. However, this was not the case for porous Ni films, given their heterogeneity. As a result, mechanical properties were strongly dependent on the penetration depth. In case one could be interested on the evolution of the porous structure during indentation, the approach by Jauffrès et al.[104] could be followed, where the concepts of Repeating Unit Cell (RUC) and Representative Volume Element (RVE) were used to introduce the geometry of the pores inside the model. This was beyond the scope of the present work.

4.3.3 Results and discussion

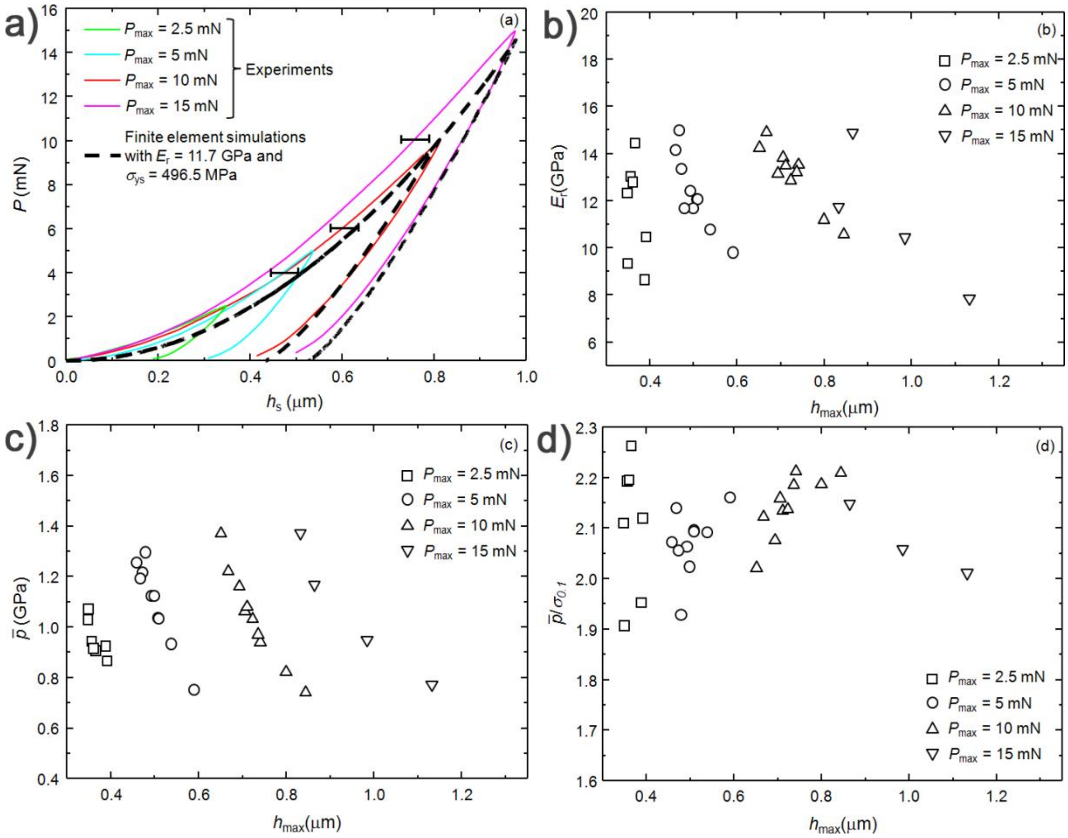

Figure 4.26: a) Applied load (P) – penetration depth (h_s) curves obtained through Berkovichnanoindentation on dealloyed porous Cu. Different curves correspond to different maximum applied loads (P_{max}). Discontinuous lines represent the P–h_s curves obtained through FE simulations using an elastic – perfectly plastic model. b) Evolution of the reduced Young's modulus (E_r) with maximum penetration depth (h_{max}) at different maximum applied loads (P_{max}) extracted as in reference [98]. c) Evolution of hardness ($\bar{p}$) with h_{max} for different P_{max}. d) Evolution of the constrain factor ($\bar{p}/\sigma_{0.1}$) with h_{max} for different P_{max}.

Figure 4.26 shows the nanoindentation curves at different maximum applied loads (Figure 4.26a) and the extracted mechanical properties (Figure 4.26b–d) for the dealloyed porous Cu. From Figure 4.26a it can be seen that the applied load (P) – penetration depth (h_s) curves at different maximum applied loads P_{max} are coherent with each other, i.e., the loading stages match rather well, except for P_{max} = 15 mN. It is also worthy to mention that, given the film thickness 50 ± 0.5 μm and maximum penetration depth h_s < 1 μm for P = 15 mN, no substrate effects are expected. Figure

4.26b,c show, respectively, the extracted values for the reduced indentation modulus (Er) and hardness $\bar{p}$, according to Oliver and Pharr[98], as a function of the maximum penetration depth h_{max} for the different P_{max}. Given the scattering, one can observe that the values for E_r and $\bar{p}$ do not show a significant tendency to increase, as one could expect on the event of a densification process. Analogously, Figure 4.26d shows the evolution of the scaled hardness ($\bar{p}/\sigma_{0.1}$) with h_{max} for different applied Pmax, being the value of $\bar{p}/\sigma_{0.1}$ practically constant. For a homogeneous bulk metal one can expect that the constraint factor C = $\bar{p}/\sigma_{0.1}$ = 2.6[100]. However, by introducing porosity, this value will be necessarily reduced due to reduction of hydrostatic pressure [105,106]. Figure 4.26a also includes FE simulations capturing the experimental P–h_s curves. Interestingly, a single set of mechanical properties was used for the simulations, namely E_r = 13.0 GPa and $\sigma_{0.1} = \sigma_{ys}$ = 478.9 MPa, supporting the idea that the present dealloyed porous Cu is homogeneous across the entire thickness. These values were obtained by averaging the extracted mechanical properties in Table 1 for P_{max} from 2.5 to 15 mN. The resulting simulated P–h_s curve was able to capture the experiments for the entire range of applied loads fairly well (here, just simulations for P_{max} = 10 mN and 15 mN are included for representation purposes). Most likely, simulations were not able to perfectly capture the loading stages due to slight structural changes in the dealloyed porous Cu during indentation. Table 4.2 summarizes the extracted mechanical properties according to what has been explained in Section 4.3.2.3 and also the relative density of the porous Cu, ρ^*/ρ_s, being ρ^* and ρ_s the densities of the porous and bulk materials respectively, calculated using Eq. 5.9[107]:

$$E_r = C_2 \, E_s \left(\frac{\rho^*}{\rho_s}\right)^n \qquad \text{[Eq. 4.9]}$$

where E_r is the reduced indentation modulus of the porous material. As the morphology of the dealloyed porous Cu approaches to an open-cell foam, the values C_2 = 1 and n = 2 can be assumed[107,108] giving as a result ρ^*/ρ_s = 0.33 (taking E_s = 120 GPa as the reduced indentation modulus of bulk Cu). This relative density is not far from the value of 0.20 that one could expect from the starting material ($Cu_{20}Zn_{80}$), if Zn was fully removed during the dealloying. The slight discrepancy could be due to:

(i) small amounts of Zn still present in the dealloyed Cu (although not easily detected by EDX) or (ii) C_2 and n not being exactly equal to 1 and 2, respectively. It is worth mentioning that to extract $\sigma_{0.1}$, as explained in Section 4.3.2.3, the used methodology was first thought for bulk-homogeneous materials. However, it has been proven that the dealloyed porous Cu can be understood as a homogeneous material, therefore this methodology can apply. A proof of that is the excellent agreement between experiments and simulations (using a single set of parameters) and also between the experiments and simulations (using a signle set of parameters) and also between the values of indentation moduli obtained through the method of Oliver and Pharr[56] and the presented methodology, as it can be seen in Table 4.2.

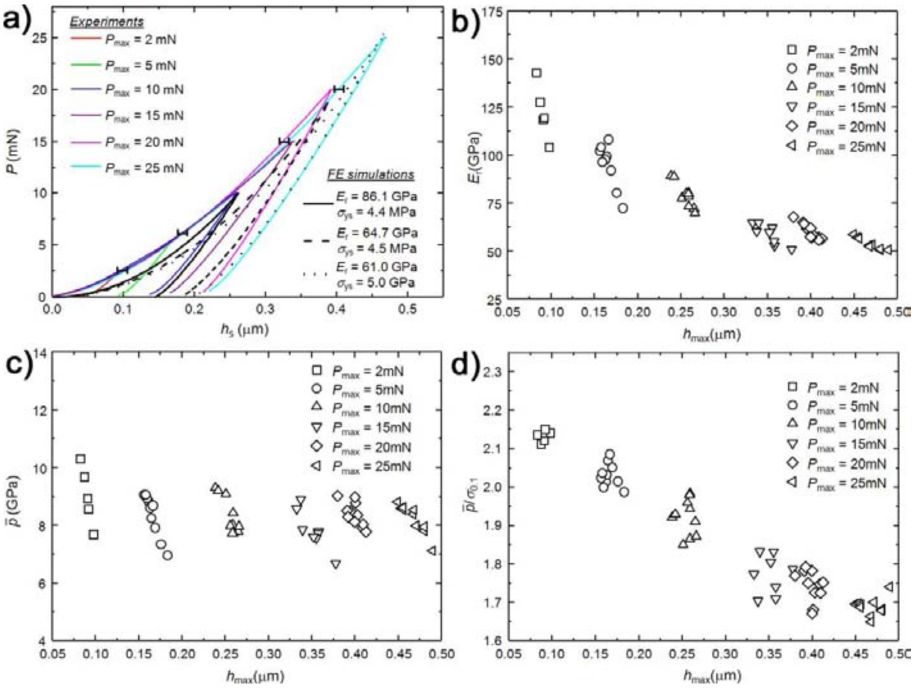

Figure 4.27: a) Applied load (P)–penetration depth (h_s) curves obtained through Berkovich nanoindentation on electrodeposited porous Ni. Different curves are for different maximum applied loads (P_{max}). Black lines represent the P–h_s curves obtained through FE simulations using an elastic–perfectly plastic model. b) Evolution of the reduced Young's modulus (E_r) with maximum penetration depth (h_{max}) at different maximum applied loads (P_{max}) extracted as in Oliver and Pharr[98]. c) Evolution of hardness ($\bar{p}$) with h_{max} for different P_{max}. d) Evolution of the constraint factor ($\bar{p}/\sigma_{0.1}$) with $h$max for different P_{max}, where $\bar{p}/\sigma_{0.1}$ clearly decreases with h_{max}.

$P_{\max}$ (mN)	E_r (GPa)		$\bar{p}$ (GPa)(1)	$\sigma_{0.1} = \sigma_{ys}$ (MPa)(2)	ρ^*/ρ_s(3)
	Methodology(1)	Experiments(2)			
2.5	13.1	11.6	0.95	450.7	0.33
5.0	13.4	12.3	1.07	515.2	0.33
10.0	14.2	12.6	1.04	487.0	0.34
15.0	11.4	10.3	1.06	462.7	0.31
Mean values	13.0	11.7	1.04	478.9	0.33

Table 4.2: Extracted mechanical properties for each maximum applied load ($P_{\max}$) for the dealloyed porous Cu. Values for relative density are also included.

(1) Mechanical properties extracted according to the method of Oliver and Pharr[98].

(2) Mechanical properties extracted according to the methodology described in Section 4.3.2.3 and in references [89] and [93]. See text for details.

(3) Relative densities calculated using Eq. 4.9 for an open-cell foam[107,108]. See text for details.

In the same fashion as for Cu, Figure 4.27 shows the $P - h_s$ curves (Figure 4.27a) and extracted mechanical properties (Figure 4.27b-d) for different P_{max} for electrodeposited Ni. As mentioned for the case of porous Cu indentation in Figure 4.26a, indentation curves in Figure 4.27a are not affected by sustrate effects given the total thickness of the porous Ni film, 7 ± 0.5 µm, and the maximum penetration depth, h_s < 0.5 µm for P = 25 mN. Contrary to what was observed in Figure 4.26a for Cu, here the loading stages for different P_{max} do not overlap so much with each other, anticipating heterogeneity across the electrodeposited porous Ni sample. Furthermore, Figure 4.27b shows that E_r decreases with h_{max} for different applied P_{max}, being this coherent with what was shown in Figure 4.24a and b, i.e., a material whose porosity increases with depth. Hence, if porosity increases it is natural to obtain a reduction in E_r, not considering, though, densification effects that, on the contrary, would increase E_r. However, this explanation seems to fail in Figure 4.27c and d that show, respectively, the variation of $\bar{p}$ and $\bar{p}/\sigma_{0.1}$ with h_{max}. From Figure 4.27c one can see that hardness remains approximately constant for the whole range of h_{max}. Instead, the constraint factor, $\bar{p}/\sigma_{0.1}$, decreases with hmax similar, to E_r. Then, since $\bar{p}/\sigma_{0.1}$ decreases while $\bar{p}$ remains constant with h_{max}, it is clear that the yield stress σys increases with P_{max}. Here, as for the dealloyed Cu, one can consider that $\sigma_{0.1} \sim \sigma_{ys}$, as it corresponds to a linear elastic–perfectly plastic material with no strain hardening, being this idea supported by Schwaiger et al[109]. The decrease of E_r and $\bar{p}/\sigma_{0.1}$ with h_{max} is rather straightforward to understand taking into account that the present porous electrodeposited Ni shows an increased porosity with depth. As h_{max} increases, the material experiences less hydrostatic pressure, resulting in a progressively lower constraint factor. However, this does not explain the increase of σ_{ys} with P_{max}. Actually, compaction of the material would certainly induce an increase of σ_{ys} but it would also increase E_r. Nonetheless, the work by Hodge et al[100] provided an answer for this apparent contradiction. These authors studied the yield strength of nanoporous open-cell Au foams for different relative densities (ρ^*/ρ_s). Although ρ^* was decreasing, indicating an increment of porosity, the yield strength increased, as in our study. The explanation for this phenomenon was that the ligaments' size was reduced as ρ^*became lower, leading to an effect analogous to the Hall-Petch relationship, where the characteristic length scale was, instead of the grain diameter, the ligament size:

$$\sigma^* = C_s\left[\sigma_o + k \cdot L^{-1/2}\right] \cdot \left(\frac{\rho^*}{\rho_s}\right)^{3/2} \qquad \text{[Eq. 4.10]}$$

where σ^* is the yield strength of the porous metal, C_s is a fitting parameter, σ_o is the yield strength of the bulk material, k is the Hall-Petch type coefficient for the theoretical yield strength of the metal, L is the ligament size and ρ^* and ρs the densities of the porous and bulk materials respectively. Eq. 4.10 is the result of combining a Hall-Petch type of relation:

$$\sigma_{yc} = \sigma_o + k \cdot L^{-1/2} \qquad \text{[Eq. 4.11]}$$

(being σ_{yc} the yield strength of a ligament with size L) with the Gibson and Ashby[107] scaling prediction for foams:

$$\sigma^* = C_2\sigma_s \cdot \left(\frac{\rho^*}{\rho_s}\right)^{3/2} \qquad \text{[Eq. 4.12]}$$

with coefficient $C_2 = 0.3$ according to Gibson and Ashby[107] and $\sigma_s \equiv \sigma_o$ is the yield strength of the bulk material. For the present nanoporous Ni, given its morphology, it was possible to estimate the ligament size at the top surface of the electrodeposited film (i.e., $L = 70 \pm 10$ nm) and the first layer (III), i.e., $L = 20 \pm 10$ nm. Table 2 summarizes the extracted mechanical properties according to Section 5.2.2.3 along with the different relative densities using Eq. 5.9 for open-cell porosity and $E_s = 200$ GPa. Taking $\sigma_{ys} = \sigma^* = 4.0$ GPa, the bulk value for Ni $\sigma_s = 21.8$ MPa[111], and $k_{Ni} = 7$ GPa$\sqrt{nm}$ [112] then, from Eq. 4.10 one can obtain $C_s = 3.2$ -4.0. Having the values of $\sigma_{ys} = \sigma^*$in Table 4.3 for different Pmax and the corresponding values of ρ^* / ρ_s along with the fitting value C_s, now one can calculate the corresponding ligament sizes that would produce the different values of σ_{ys}. These values are listed in Table 4.3 and they are in ather good agreement with the HRSEM observations (Figure 4.24c–e). As for the case of the porous dealloyed Cu, the extracted values for the indentation moduli with the method of Oliver and Pharr[98] and the present methodology are in excellent agreement. Also, this methodology was previously used in the framework of Cu single crystalline thin films on top of silica (Si) substrates (where the thin film/substrate interface acts as an inhomogeneity), with excellent results[113].

As in Figure 4.26a for the dealloyed porous Cu, here we also performed FE simulations of the indentation experiments on electrodeposited porous Ni, Figure 4.27a. Given the evolution on the mechanical properties shown in Figure 4.27b for the reduced indentation modulus and for the extracted yield stress in Table 4.3, in this case it was not possible to use a single set of parameters for the simulations, but different values of E_r and σ_{ys} were used for each P_{max}, in accordance with Table 4.3.

P_{max} (mN)	E_{r} (GPa)		$\bar{p}$ (GPa)(1)	$\sigma_{0.1} = \sigma_{ys}$ (GPa)(2)	ρ^*/ρ_s(3)	L (nm)(4)
	Methodology(1)	Experiments(2)				
2.0	134.1	133.3	8.70	4.0	0.78	50.0 – 60.0
5.0	103.8	102.8	8.36	4.2	0.72	34.9 – 42.9
10.0	85.6	86.1	8.53	4.4	0.66	24.3 – 29.9
15.0	64.0	64.7	8.02	4.5	0.57	14.9 – 18.3
20.0	63.0	67.6	8.33	4.8	0.58	13.8 – 16.9
25.0	59.2	61.0	8.35	5.0	0.55	10.8 – 13.2

Table 4.3: Extracted mechanical properties for each maximum applied load (P_{max}) for the electrodeposited porous Ni. Values for relative density and ligament size are also included.

(1) Mechanical properties extracted according to the method of Oliver and Pharr[98].

(2) Mechanical properties extracted according to the methodology described in Section 4.3.2.3 and in references [99] and [100]. See text for details.

(3) Relative densities calculated using Eq. 4.9 for open cell porosity[107,108]. See text for details.

(4) Ligament sizes calculated using Eq. 4.10[110]. See text for details.

4.3.4 Conclusions

Here we have studied the mechanical behaviour of porous Cu obtained by dealloying and porous Ni prepared by electrodeposition, combining nanoindentation experiments with finite element simulations. The following are the most remarkable conclusions reached during the present study.

- For dealloyed porous Cu it has been shown that, as a result of its homogeneous structure, mechanical properties such as the reduced indentation modulus, hardness and yield stress do not vary significantly with different maximum applied loads. This enables to capture the applied load–penetration depth experimental indentation curves with a single set of mechanical properties through finite element simulations. As no evolution of the mechanical properties was observed, densification effects could be essentially disregarded up to 15 mN maximum applied load.

- For electrodeposited porous Ni, the reduced indentation modulus and constraint factor decrease with the maximum applied load, while hardness stays constant. This variation of the mechanical properties precludes the use of a unique set of mechanical properties to fit the entire applied load–displacement indentation curves through finite element simulations. Actually, with each set of mechanical properties it is, at most, only possible to capture through finite element simulations the corresponding maximum load and the unloading stage, but not the loading stage. This is due to the inherent structure heterogeneity of the sample.

- Concerning the evolution in the mechanical properties of electrodeposited porous Ni, the reduction of the indentation modulus and constraint factor with Pmax can be understood from the increase of the porosity with depth, but this is in principle contradictory with the constancy of hardness and the increase of yield stress. To overcome this paradox, the critical role played by the ligament size was taken into account. The very small ligament sizes act similar to the small crystallite sizes in the Hall-Petch relation, in the sense that as the ligament size is reduced the yield stress increases. SEM images indeed reveal that while the porosity is increased, the ligament size is reduced across the electrodeposited porous Ni sample.

References

[1] D. K. Ferry, *Science* **2008**, *319*, 579.

[2] W. Zhou, X. Dai, T. M. Fu, C. Xie, J. Liu, C. M. Lieber, *Nano Lett.* **2014**, *14*, 1614.

[3] F. Zhang, T. Nyberg, O. Inganäs, *Nano Lett.* **2012**, *2*, 1373.

[4] H. Kind, H. Yan, B. Messer, M. Law, P. Yang, *Adv. Mater.* **2002**, 14, 158.

[5] Y. Sun, F. Zhang, L. Xu, Z. Yin, X. Song, *J. Mater. Chem. A* **2014**, *2*, 18583.

[6] F. Hernandez-Ramirez, J. D. Prades, A. Tarancon, S. Barth, O. Casals, R. Jimenez-Diaz, E. Pellicer, J. Rodriguez, J. R. Morante, M. A. Juli, S. Mathur, A. Romano-Rodriguez, *Adv. Funct. Mater.* **2008**, *18*, 2990.

[7] A. Casadei, E. F. Pecora, J. Trevino, C. Forestiere, D. Rüffer, E. Russo-Averchi, F. Matteini, G. Tutuncuoglu, M. Heiss, A. F. Morral, L. D. Negro, *Nano Lett.* **2014**, *14*, 2271.

[8] M. A. Zeeshan, S. Pané, S. K. Youn, E. Pellicer, S. Schuerle, J. Sort, S. Fusco, A. M. Lindo, H. G. Park, B. J. Nelson, *Adv. Funct. Mater*. **2013**, *23*, 823.

[9] D. Kagan, R. Laocharoensuk, M. Zimmerman, C. Clawson, S. Balasubramanian, D. Kang, D. Bishop, S. Sattayasamitsathit, L. Zhang, J. Wang, *Small* **2010**, *6*, 2741.

[10] K. Liu, K. Nagodawithana, P. C. Searson, C. L. Chien, *Phys. Rev. B* **1995**, *51*, 7381.

[11] B. Doudin, G. Redmond, S. E. Gilbert, J. Ph. Ansermet, *Phys. Rev. Lett*. **1997**, *79*, 933.

[12] L. Piraux, J. M. George, J. F. Despres, C. Leroy, E. Ferain, R. Legras, K. Ounadjela, A. Fert, *Appl. Phys. Lett*. **1994**, *65*, 2484.

[13] B. Özkale, N. Shamsudhin, G. Chatzipirpiridis, M. Hoop, F. Gramm, X. Chen, X. Martí, J. Sort, E. Pellicer, S. Pané, *ACS Appl. Mater. Interf.* **2015**, *7*, 7389.

[14] V. Baltz, B. Rodmacq, A. Bollero, J. Ferré, S. Landis, B. Dieny, *Appl. Phys. Lett*. **2009**, *94*, 052503.

[15] S. A. Puig. N. D. Valle, E. Pellicer, J. Zhang, J. Nogués, C. Navau, A. Sanchez, J. Sort, *New J. Phys*. 2016, *18*, 013026. [16] J. Sort, B. Rodmacq, S. Auffret, B. Dieny, *Appl. Phys. Lett.* **2003**, *83*, 1800.

[17] T. S. Ramulu, R. Venu, B. Sinha, S. S. Yoon, C. G. Kim, *Int. J. Electrochem. Sci*. **2012**, *7*, 7762.

[18] Y. Su, J. Tang, H. Yang, Z. Cheng, *Nanoscale* **2013**, *5*, 9709.

[19] D. J. Peña, J. K. N. Mbindyo, A. J. Carado, T. E. Mallouk, C. D. Keating, B. Razavi, T. S. Mayer, *J. Phys. Chem. B* **2002**, *106*, 7458.

[20] C. J. Roy, N. Chorine, B. G. De Geest, S. De Smedt, A. M. Jonas, S. D. Champagne, *Chem. Mater*. **2012**, *24*, 1562.

[21] Y. K. Su, D. H. Qin, H. L. Zhang, H. Li, H. L. Li, *Chem. Phys. Lett*. **2004**, *388*, 406.

[22] A. I. Gapin, X. R. Ye, L. H. Chen, D. Hong, S. Jin, *IEEE Trans. Magn*. **2007**, *43*, 2151.

[23] K. Y. Kok, C. M. Hangarter, B. Goldsmith, I. K. Ng, N. B. Saidin, N. V. Myung, *J. Magn. Magn. Mater*. **2010**, *322*, 3876.

[24] V. M. Pride, J. García, L. Iglesia, V. Vega, D. Görlitz, K. Nielsch, E. D. B. Castro, R. M. Reséndez, A. Ponce, C. Luna, *Nanoscale Res. Lett*. **2013**, *8*, 263.

[25] D. S. Xue, H. G. Shi, M. S. Si, *J. Phys. : Condens. Matter*. **2004**, *16*, 8775.

[26] J. Zhang, S. A. Puig, N. D. Valle, C. Navau, M. D. Baró, S. Estradé, F. Peiró, S. Pané, B. J. Nelson, A. Sanchez, J. Nogués, E. Pellicer, J. Sort, *ACS Appl. Mater. Interfaces* **2016**, *8*, 4109.

[27] J. H. Lee, J. H. Wu, H. L. Liu, J. U. Cho, M. K. Cho, B. H. An, J. H. Min, S. J. Noh, Y. K. Kim, *Angew. Chem. Int. Ed*. **2007**, *46,* 3663.

[28] J. U. Cho, Q. X. Liu, J. H. Min, S. P. Ko, Y. K. Kim, *J. Magn. Magn. Mater*. **2006**, *304*, e213.

[29] O. Berkh, Y. Shacham-Diamand, E. Gileadi, *J. Appl. Electrochem.* **2008**, *38*, 1275.

[30] K. Žužek Rožman, A. Krause, K. Leistner, S. Fähler, L. Schultz, H. Schlörb, *J. Magn. Magn. Mater.* **2007**, *314*, 116.

[31] I. Zana, G. Zangari, *J. Appl. Phys.* **2002**, *91*, 7320.

[32] P. P. Mardilovich, A. N. Govyadinoy, N. I. Mazurenko, R. Paterson, *J. Membrane Sci.* **1995**, *98*, 143.

[33] R. Weil, *Annu. Rev. Mater. Sci*. **1989**, *19*, 165.

[34] B. D. Cuillity, *Elements of X-ray Diffraction*, Addison-Wesley Publishing, Reading, MA, **1978**.

[35] J. Duan, J. Liu, D. Mo, H. Yao, K. Maaz, Y. Chen, Y. Sun, M. Ho, X. Qu, L. Zhang, Y. Chen, *Nanotechnology* **2010**, *21*, 365605.

[36] J. Amblard, I. Epelboin, M. Froment, G. Maurin, *J. Appl. Electrochem*. **1979**, *9*, 233.

[37] C. B. Nielsen, A. Horsewell, M. J. L. Ostergard, *J. Appl. Electrochem*. **1997**, *27*, 839.

[38] F. Li, T. Wang, L. Ren, J. Sun, *J. Phys. : Condens. Matter*. **2004**, *16*, 8053.

[39] A. K. M. Bantu, J. Rivas, G. Zaragoza, M. A. L. Quintela, M. C. Blanco, *J. Appl. Phys*. **2001**, *89*, 3393.

[40] K. Ounadjela, R. Ferré, L. Louail, J. M. George, J. L. Maurice, L. Piraux, S. Dubois, *J. Appl. Phys*. **1997**. *81*, 5455.

[41] B. Jang, E. Pellicer, M. Guerrero, X. Chen, H. Choi, B. J. Nelson, J. Sort, S. Pané, *ACS Appl. Mater. Interfaces* **2014**, *6*, 14583.

[42] W. D. Callister, Jr, *Materials Science and Engineering, An Introduction*, 5th edition, John Wiley & Sons, Inc., New York, **2000**.

[43] N. D. Nikolic, K. I. Popov, L. J. Pavlovic, M. G. Pavlovic, *Surf. Coat. Technol*. **2006**, *201*, 560.

[44] E. Pellicer, A. Varea, S. Pané, B. J. Nelson, E. Menéndez, M. Estrader, S. Suriñach, M. D. Baró, J. Nogués, J. Sort, *Adv. Funct. Mater.* **2010**, *20*, 983.

[45] J. E. Davies, O. Hellwig, E. E. Fullerton, J. S. Jiang, S. D. Bader, G. T. Zimányi, K. Liu, *Appl. Phys. Lett.* **2005**, *86*, 262503.

[46] E. E. Fullerton, J. S. Jiang, S. D. Bader, *J. Magn. Magn. Mater*. **1999**, *200*, 392.

[47] M. A. Shahbazi, B. Herranz, H. A. Santos, *Biomatter* **2012**, *2*, 1.

[48] M. Mustapic, M. S. A. Hossain, J. Horvat, P. Wagner, D. R. G. Mitchell, J. H. Kim, G. Alici, Y. Nakayama, B. Martinac, *Microporous Mesoporous Mater*. **2016**, *226*, 243.

[49] Q. Q. Xiong, J. P. Tu, Y. Lu, J. Chen, Y. X. Yu, X. L. Wang, C. D. Gu, *J. Mater. Chem*. **2012**, *22*, 18639.

[50] F. Yang, K. Cheng, X. Xue, J. Yin, G. Wang, D. Gao, *Electrochim. Acta* **2013**, *107*, 194.

[51] X. Qian, T. Hang, S. Shanmugam, M. Li, *ACS Appl. Mater. Interfaces* **2015**, *7*, 15716.

[52] J. Zhang, M. D. Baró, E. Pellicer, J. Sort, *Nanoscale* **2014**, *6*, 12490.

[53] G. Wang, H. Liu, J. Horvat, B. Wang, S. Qiao, J. Park, H. Ahn, *Chem. Eur. J.* **2010**, *16*, 11020.

[54] E. Pellicer, S. Pané, V. Panagiotopoulou, S. Fusco, K. M. Sivaraman, S. Suriñach, M. D. Baró, B. J. Nelson, J. Sort, *Int. J. Electrochem. Sci*. **2012**, *7*, 4014.

[55] W. Wang, M. Tian, A. Abdulagatov, S. M. George, Y. C. Lee, R. Yang, *Nano Lett.* **2012**, 12, 655.

[56] D. Li, Q. Zhang, Y. Wang, H. Chen, *Polym. Chem.* **2014**, 5, 14.

[57] V. S. Sundram, S. Nesappan, *Int. J. Nano Biomater.* **2014**, 5, 243.

[58] B. Sahoo, K. S. P. Devi, S. Dutta, T. K. Maiti, P. Pramanik, D. Dhara, *J. Colloid. Interf. Sci.* **2014**, 431, 31.

[59] X. H. Xia, J. P. Tu, Y. Q. Zhang, Y. J. Mai, X. L. Wang, C. D. Gu, X. B. Zhao, *J. Phys. Chem. C* **2011**, *115*, 22662.

[60] Y. Q. Zhang, X. H. Xia, X. L. Wang, Y. J. Mai, S. J. Shi, Y. Y. Tang, C. G. Gu, J. P. Tu, *J. Power Source* **2012**, *213*, 106.

[61] E. Pellicer, M. Cabo, A. López-Ortega, M. Estrader, L. Yedra, S. Estradé, F. Peiró, Z. Saghi, P. Midgley, E. Rossinyol, I. V. Golosovsky, A. Mayoral, J. D. Prades, S. Suriñach, M. D. Baró, J. Sort, J. Nogués, *Nanoscale* **2013**, 5, 5561.

[62] J. Zhang, S. Agramunt-Puig, N. Del-Valle, C. Navau, M. D. Baró, S. Estradé, F. Peiró, S. Pané, B. J. Nelson, A. Sánchez, J. Nogués, E. Pellicer, J. Sort, *ACS Appl. Mater. Interf*. **2016**, 8, 4109.

[63] M. Guerroro, J. Zhang, A. Altube, E. G. Lecina, M. Roldan, M. D. Baró, E. Pellicer, J. Sort, *Sci. Technol. Adv. Mater*. **2016**, 17, 177.

[64] C. Bae, H. Shin, K. Nielsch, *MRS Bulletin* **2011**, 36, 887.

[65] R. W. Johnson, A. Hultqvist, S. F. Bent, *Mater. Today* **2014**, 17, 236.

[66] M. Knez, K. Nielsch, L. Niinistö, *Adv. Mater*. **2007**, *19*, 3425.

[67] J. W. Elam, D. Routkevitch, P. P. Mardilovich, S. M. George, *Chem. Mater*. **2003**, *15*, 3507.

[68] M. Daub, M. Knez, U. Goesele, K. Nielsch, *J. Appl. Phys*. **2007**, *101*, 09J111.

[69] M. D. Groner, J. W. Elam, F. H. Fabreguette, S. M. George, *Thin Solid Films* **2002**, *413*, 186.

[70] H. C. Shin, J. Dong, M. Liu, *Adv. Mater*. **2003**, *15*, 1610.

[71] Y. Liu, W. Z. Jia, Y. Y. Song, X. H. Xia, *Chem. Mater*. **2007**, *19*, 5758.

[72] S. Cherevko, X. Xing, C. Chung, *Electrochem. Commun*. **2010**, *12*, 467.

[73] L. Mattarozzi, S. Cattarin, N. Comisson, R. Gerbasi, P. Guerriero, M. Musiani, L. V. Gómez, E. Verlato, *ESC Electrochem. Lett*. **2013**, *2*, D58.

[74] S. Eugénio, T. M. Silva, M. J. Carmezim, R. G. Duarte, M. F. Montemor, *J. Appl. Electrochem*. **2014**, *44*, 455.

[75] S. M. George, C. F. Herrmann, Al_2O_3 Atomic Layer Deposition to Enhance the Deposition of Hydrophilic Coating on Micro-Electromechanical Devices. US 20050012975 A1, January 20, **2005**.

[76] M. Coll, J. M. Montero Moreno, J. Gázquez, K. Nielschm X. Obradors, T. Puig, *Adv. Funct. Mater.* **2014**, 24, 5368.

[77] J. Lu, T. Xiong, W. Zhou, L. Yang, Z. Tang, S. Chen, *ACS Appl. Mater. Interfaces* **2016**, *8*, 5065.

[78] C. A. Wilson, R. K. Grubbs, S. M. George, *Chem. Mater*. **2005**, *17*, 5625.

[79] M. D. Groner, F. H. Fabreguette, J. W. Elam, S. M. George, *Chem. Mater*. **2004**, *16*, 639.

[80] A. C. Dillon, A. W. Ott, J. D. Way, S. M. George, *Surf. Sci*. **1995**, *322*, 230.

[81] Y. T. Chong, E. M. Y. Yau, K. Nielsch, J. Bachmann, *Chem. Mater*. **2010**, *22*, 6506.

[82] R. H. Grabtree, The Organometallic Chemistry of the Transition Metals, 2nd ed.; Wiley: New York, **1994**.

[83] J. Nogués, I. K. Schuller, *J. Magn. Magn. Mater.* **1999**, 192, 203.

[84] J. Sort, S. Suriñach, J. S. Muñoz, M. D. Baró, J. Nogués, G. Chouteau, V. Skumryev, G. C. Hadjipanayis, *Phys. Rev. B* **2002**, 65, 174420.

[85] R. Ramesh, G. Thomas, B. M. Ma, *J. Appl. Phys.* **1988**, 64, 6416.

[86] M. Ma, R. M. Hill, *Curr. Opin. Colloid Interface Sci*. **2006**, *11*, 193.

[87] D. Cappus, C. Xu, D. Ehrilich, B. Dillman, C. A. Jr. Ventnce, K. A1 Shamery, H. Kuhlenbeck, H. J. Freund, *Chem. Phys.***1993**, 177, 533.

[88] X. Chu, D. Jiang, Y. Guo, C. Zheng, *Sens. Actuators B* **2006**, *120*, 177.

[89] K. Otsubo, T. Haraguchi, O. Sakata, A. Fujiwara, H. Kitagawa, *J. Am. Chem. Soc*. **2012**, *134*, 9605.

[90] Q. Xiong, J. Tu, Y. Lu, J. Chen, Y. Yu, X. Wang, C. Gu, *J. Mater. Chem*. **2012**, *22*, 18639.

[91] E. Pellicer, M. Cabo, E. Rossinyol, P. Solsona, S. Suriñach, M. D. Baró, J. Sort, *Adv. Funct. Mater.* **2013**, *23*, 900.

[92] E. Linul, L. Marsavina, T. Voiconi, T. Sadowski*, J. Phys. Conf. Ser*. **2013**, *451*, 012002.

[93] V. Malgras, H. Ataee-Esfahani, H. Wang, B. Jiang, C. Li, K. C. W. Wu, J. Ho Kim, Y. Yamauchi, *Adv. Mater*. **2016**, *28*, 993.

[94] F. Scaglione, P. Rizzi, L. Battezzati, *J. Alloys Compd*. **2012**, *536*, S60.

[95] E. Pellicer, S. Pané, V. Panagiotopoulou, S. Fusco, K. M. Sivaraman, S. Suriñach, M. D. Baró, B. J. Nelson, J. Sort, *Int. J. Electrochem. Sci*. **2012**, *7*, 4014.

[96] N. Ramakrishnan, V. S. Arunachalam, *J. Am. Ceram. Soc*. **1993**, *76*, 2745.

[97] I. C. Cheng, A. M. Hodge*, Adv. Eng. Mater*. **2012**, *14*, 219.

[98] W. C. Oliver, G. M. Pharr, *J. Mater. Res*. **1992***, 7*, 1564.

[99] J. Alcalá, D. Esqué-de los Ojos, S. A. Rodríguez, *J. Mat. Res*. **2009**, *24,* 1235.

[100] O. Casals, J. Alcalá, *Acta Mater*. **2005**, *53*, 3545.

[101] Y. T. Cheng, C. M. Cheng, *Int. J. Solids and Struct*. **1999**, *36*, 1231.

[102] J. M. Meza, F. Abbes, M. Troyon*, J. Mater. Res*. **2008**, *23*, 725.

[103] Z. H. Xu, X. D. Li, *Acta Mater*. **2008**, *56*, 1399.

[104] D. Jauffrès, Y. Christelle, M. Verdier, R. Dendievel, A. Ayral, *Microporous and Mesoporous Mater.* **2011**, *140*, 120.

[105] R. Domingo-Roca, D. Esquè-de los Ojos, M. Guerrero, E. Pellicer, M. D. Baró, S. Suriñach, J. Sort*, Mater. Sci. Eng. A* **2015**, *626*, 150.

[106] M. A. Zeeshan, D. Esqué-de los Ojos, P. Castro-Hartman, M. Guerrero, J. Nogués, S. Suriñach, M. D. Baró, B. J. Nelson, S. Pané, E. Pellicer, J. Sort, *Nanoscale* **2016**, *8,* 1344.

[107] L. J. Gibson, M. F. Ashby, Cellular solids: structures and properties. 2nd ed. Cambridge: Cambridge University Press. **1997**.

[108] R. E. Williford, X. S. Li, R. S. Addleman, G. E. Fryxell, S. Baskaran, J. C. Birnbaum, C. Coyle, T. S. Zemanian, C. Wang, A. R. Courtney, *Microporous and Mesoporous Mater*. **2005**, *85*, 260.

[109] R. Schwaiger, B. Moser, M. Dao, N. Chollacoop, S. Suresh, *Acta Mater*. **2003**, *51*, 5159.

[110] A. M. Hodge, J. Biene, J. R. Hayes, P. M. Bythrow, C. A. Volkert, A. V. Hamza, *Acta Mater*. **2007**, *55*, 1343.

[111] C. E. Carlton, P. J. Ferreira, *Acta Mater*. **2007**, *55*, 3749.

[112] A. M. El-Sherik, U. Erb, G. Palumbo, K. T. Aust, *Scripta Metall. et Mater*. **1992**, *27*, 1185.

[113] D. Esqué-de los Ojos, J. Očenášek, J. Alcalá, *Comp. Mater. Sci*. **2014**, *86*, 186.

Departament de Física

5. General discussion

Chapter 5: General discussion

In this thesis relatively-thick Cu-Ni foam films were prepared by electrodeposition taking advantage of hydrogen co-evolution as a source of porosity. Strictly speaking, the term “foam” applies to a special class of cellular metals that originate from liquid-gas mixtures (typically aluminum). Closed-cell foams consist of trapped gas bubbles formed during the foam's expansion and cure. In open-cell foams, the blowing agent gas is not trapped by the forming cells but instead is released to the atmosphere during foam expansion and curing. The foam cells have "holes" in their walls, enabling them to interlock and interconnect. The spaces within the cells are filled with atmospheric air, much like a sponge. The term “foam” has nowadays expanded its meaning and it is used to refer to highly porous metallic materials processed using different approaches. The here-synthesized Cu-Ni films are close to the open-cell foams type. The micron-sized spherical pores form as a result of hydrogen bubbles continuously evolving during electrodeposition. Contact angle measurements showed that the Cu-Ni foams are superhydrophobic, featuring contact angle values larger than 150°. Although hydrophilic surfaces typically show enhanced HER properties compared to their hydrophobic counterparts, we have shown that the Cu-Ni films did exhibit remarkable HER properties. It is conjectured that the large surface area arising from their spongy morphology overcomes the possible negative effects due to their superhydrophobic character. The formation of bi-phase deposits instead of a solid solution (i.e., an alloy) afforded room-temperature ferromagnetic properties to the material in spite of the large Cu contents (ranging from 65 at% to 85 at%).

These porous Cu-Ni films were coated with a continuous shell of ZnO nanoparticles. In this way, the metallic films serve as scaffolds. The coating procedure is facile and simply consists in depositing dropwise a dispersion of the ZnO nanoparticles previously synthesized by sol-gel onto the Cu-Ni scaffolds. Since no thermal annealing is required to obtain the composites and, hence, possible oxidation of the Cu-Ni matrices is avoided, their magnetic properties were preserved. Furthermore, annealing often causes collapse of porous networks. Depending on the properties one wishes to exploit, different transition metal oxide nanoparticles could be synthesized by sol-gel or similar methods. In our case, ZnO was chosen in order to confer photoluminescent and photocatalytic properties to the material. The higher the number of successive depositions, the thicker the coating is. Although the Cu-Ni walls became covered by a ZnO skin and, therefore, the nanopores forming the walls were no longer visible, the spherical micropores remained. As a result, 3D porous ZnO@CuNi semiconductor-metal films were straightforwardly obtained. The method could be improved by implementing a sophisticated set-up to deposit the ZnO nanoparticles suspension onto the Cu-Ni films in order to avoid manual dosage, which always increases uncertainty.

A more conformal, much thinner coating (5 nm – 25 nm) was achieved by atomic layer deposition (ALD). In this case, electrodeposited Ni films instead of Cu-Ni films were used as porous scaffolds. Compared to the ZnO-coated Cu-Ni films, the hierarchical porosity of the Ni films was preserved. Two different metal oxides, namely Al_2O_3 and Co_2FeO_4, were deposited on the 3D porous Ni films. ALD conditions were optimized so that the nanolayers finely covered the metallic matrix in a conformal manner while its eventual oxidation was minimized. The work was conceived more as a proof-of-concept of the capabilities of the electrodeposition-ALD tandem, rather than as a means to trigger new or improved properties for the resulting composites. Nevertheless, the versatility of the combined synthetic approach in terms of materials composition suggests that multifunctional exotic porous composites could be readily fabricated.

The possibility to detach the composite porous films from the substrate for certain applications remains an open issue. Mechanical detachment of the layers from the substrate is usually unfavorable. Although not attempted in this Thesis, Cu-Ni and Ni porous films could in principle be prepared by electroforming. In electroforming, a thick layer of material is electroplated until the material itself is strong enough to be self-supporting.

Nanoporous (or more specifically mesoporous) Ni films were obtained from aqueous electrolytes containing Pluronic P123 amount above its critical micellar concentration. Compared to Ni films obtained from the hydrogen bubble template-assisted electrodeposition, the pore size was much smaller, falling in the mesoscale domain. Pore size was not homogeneous, though, but pores were smaller and pore wall (i.e., ligament size) was thicker close to the film's surface. Hence, films showed a graded mesoporosity. By combining nanoindentation experiments at different maximum applied loads with finite element simulations, it was observed that films showed a decrease in the reduced Young's modulus and constraint factor, an increase in yield stress and a constant hardness when the maximum applied load during nanoindentation was increased. The reduction of both the Young's modulus and constraint factor was related to the increase of the porosity with depth. The trends in hardness and yield stress were interpreted in terms of ligament size. The very small ligament sizes act similar to the small crystallite sizes in the Hall-Petch relationship, in the sense that as the ligament size is reduced the yield stress increases.

Besides porous films, the possibility to produce 1D nanostructures by electrodeposition was also considered in this Thesis. Tri-segmented nanowires (NWs) containing two ferromagnetic segments (CoPt and Ni) with dissimilar coercivity separated by a non-magnetic spacer (Cu) were deposited inside the channels of a polycarbonate (PC) membrane. The tri-segmented CoPt/Cu/Ni NWs exhibited a staircase-like hysteresis loop with tunable shape that depended on the relative length of the Ni and CoPt segments and the respective values of saturation magnetization. A new strategy based on an antiparallel alignment of segments' magnetization was proposed to minimize magnetic interactions between NWs dispersed in a fluid. Note that aggregation can be a serious shortcoming in biological or catalytic applications since it might worsen overall performance of the NWs. The antiparallel alignment was achieved by applying suitable magnetic fields while the NWs were still embedded in the PC membrane. In such antiparallel alignment, zero remanent magnetization (fully compensated NWs) is achieved provided that the lengths of the CoPt and Ni segments are accurately tuned. Analytic calculations demonstrated that the interaction magnetic energy from fully-compensated tri-segmented NWs with antiparallel alignment is reduced compared to a single-component NW with the same length or the tri-segmented NWs with the two ferromagnetic counterparts parallel to each other.

A simple and powerful model to calculate in a time-effective manner the collective magnetic response of large arrays of tri-segmented magnetic NWs was devised. The model is based on a coarse discretization of the NWs in which each box is considered as a single magnetic dipole. The model is capable of predicting the distances over which nanowires do not interact appreciably with their neighbors. In addition, it proves that NWs made of segments of different coercivity and saturation magnetization can be used to attain antiparallel or parallel magnetic alignment, in agreement with the experimental findings in CoPt/Cu/Ni NWs. These results are interesting in applications like magnetic sensors based on the GMR effect and other applications based on multiple magnetic states (e.g. multi-bit recording media).

Further experimental work on the segmented NWs highlighted the importance of the crystallographic structure and the texture for the formation of robust segment interfaces. Under our electrodeposition conditions, Cu was deposited in the face-centered cubic (*fcc*) structure and showed a strong (200) texture. As a result, Cu segments did not accommodate well on the CoPt ones, which showed the c-axis oriented hexagonal close-packed structure. Instead, when the Cu segment was absent, well-connected CoPt/Ni NWs with smooth interfaces were obtained. In this case, a structural equivalence holds between (002) *hcp* CoPt and (111) *fcc* Ni, which results in good quality junctions. When the PC template was removed, some of the CoPt/Cu/Ni NWs broke up through the defective CoPt/Cu interfaces, whereas the CoPt/Ni NWs remained intact. Surprisingly, magnetic measurements reveale that CoPt/Ni NWs also exhibit staircase-like hysteresis loops similar to the tri-segmented CoPt/Cu/Ni NWs. The occurrence of staircase-like hysteresis loops indicates that interfacial exchange interactions between the soft and hard counterparts are not sufficient to force a simultaneous magnetization reversal of both segments.

From a very general perspective, this Thesis tackles different synthetic approaches to obtain multi-phase composite materials with very controlled geometry based on the use of parent templates to be subsequently filled (or coated) with second phases of interest, in view of widespread functional applications. On the one hand, porous metallic frameworks, prepared by electrodeposition, are used as parent templates and filled/coated with different types of oxide materials. On the other hand, electrodeposition is used to fill the pores of a non-metallic parent template with metals, to obtain multi-segmented nanowires. Thus, the use of porous materials and electrodeposition is at the heart of all the studies presented in this Thesis. Also, all studies have in common the presence of Cu and Ni, utilized in very dissimilar morphologies and for very different purposes.

Departament de Física

6. Conclusions

Chapter 6: Conclusions

A diagram of the overall work conducted in this Thesis is shown below.

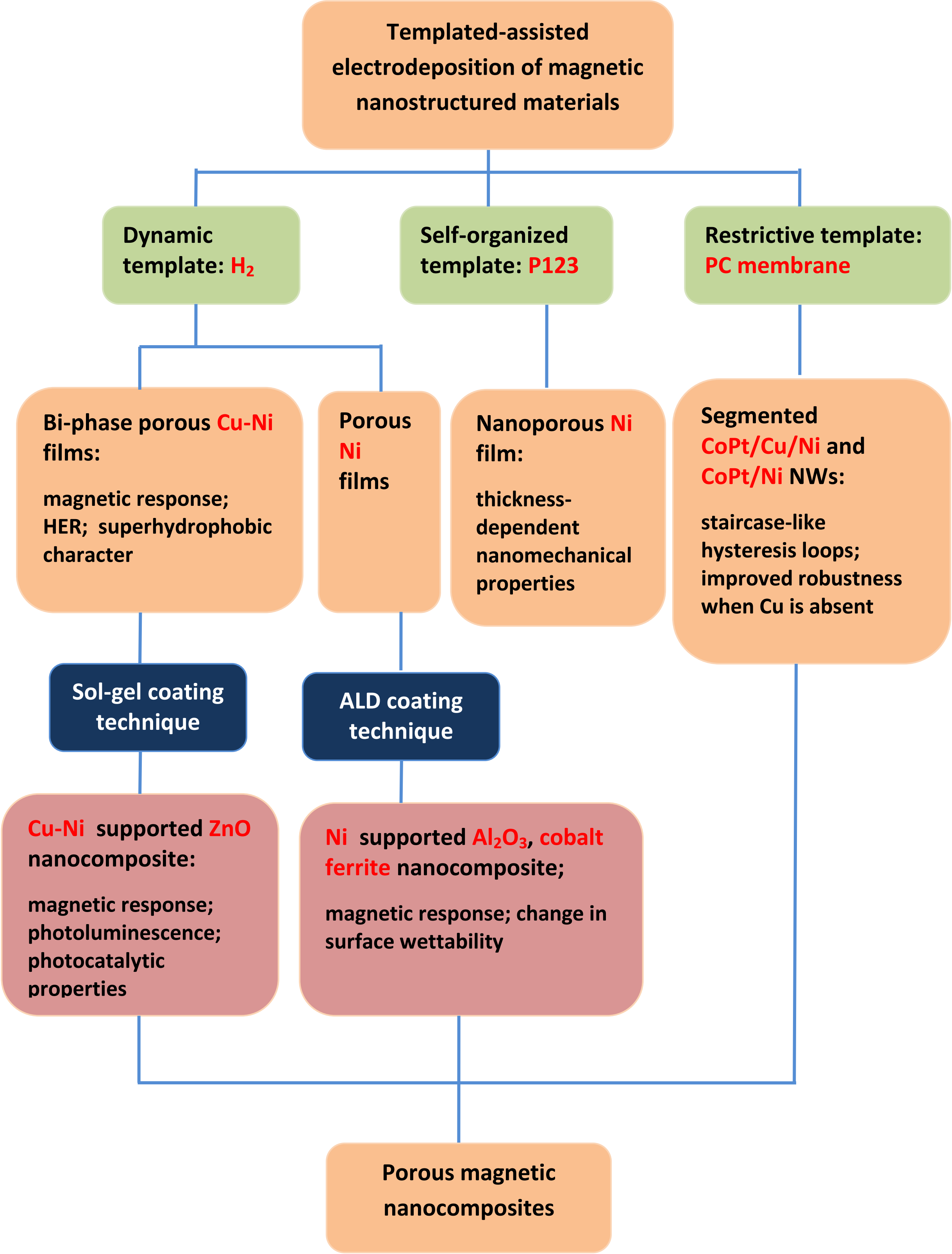

1. Bi-phase Cu-rich Cu-Ni magnetic metallic foam films (MMFs) have been fabricated by one-step galvanostatic electrodeposition from acidic electrolyte containing Cu (II) and Ni (II) sulfate salts and acetic acid as hydrogen bubble stabilizer. The hydrogen bubble template is found to confine nucleation events resulting in films exhibiting phase separation. The synthesized Cu-Ni MMFs display ferromagnetic behavior at even large Cu contents thanks to the occurrence of phase-separation.
2. The Cu-rich Cu-Ni MMFs display enhanced composition-dependent electrocatalytic activity towards hydrogen evolution reaction (HER) over pure Cu and Ni porous films. In particular, the $Cu_{85}Ni_{15}$ MMF shows the highest specific activity.
3. The Cu-Ni MMFs have been infiltrated with a suspension containing ZnO nanoparticles previously synthesized by sol-gel. The synthesized hybrid porous layers exhibit an interesting combination of ferromagnetic (arising from Cu-Ni scaffold) and photoluminescent (arising from ZnO) properties. The ZnO@CuNi hybrid films are active towards the photodegradation of Rhodamine B under UV-vis light irradiation.
4. Hydrogen bubble template-assisted electrodeposition has been also utilized to synthesize porous Ni films. The hierarchically porous Ni films have been conformally coated with Al_2O_3 and Co_2FeO_4 nanolayers by atomic layer deposition (ALD). The as-deposited Al_2O_3 layer is amorphous, while Co_2FeO_4 is polycrystalline with *fcc* structure. The applied ALD coatings make the material surfaces slightly more polar.
5. In both cases, ZnO@CuNi and Ni supported Al_2O_3 and Co_2FeO_4, the inherent porosity of the initial Cu-Ni and Ni films, as well as their ferromagnetic properties, are preserved. Hence, both sol-gel coating and ALD can be used as post-treatment coating methods of porous metallic scaffolds.
6. Arrays of tri-segmented CoPt/Cu/Ni nanowires are synthesized by sequential electrodeposition in PC membranes. Magnetic measurements reveal the occurrence of stair-case-like hysteresis loops, resulting from the two different coercivities of the hard (CoPt) and soft (Ni) ferromagnetic segments. Antiparallel magnetization alignment of CoPt and Ni segments can be achieved

by applying a suitable magnetic field while the nanowires are still embedded in the PC membrane. In this way, the magnetic interaction between nanowires should be effectively reduced when released from the membranes.

7. Theoretical studies have been used to predict the optimum aspect ratio of the different segments in the multi-segmented NWs in order to circumvent dipolar interactions in multi-state magnetic recording applications.
8. The impact of the crystallographic texture of Cu and Ni on the quality of segment interfaces in CoPt/Cu/Ni and CoPt/Ni NWs is remarkable. The as-deposited (200) textured *fcc* structure of Cu cannot accommodate well on the *c*-axis oriented hexagonal close-packed CoPt. As a result, defective CoPt/Cu junctions are observed. Meanwhile, Ni shows the (111) *fcc* structure, which crystallographically matches with CoPt. In particular, the densest packing fashion along [111] orientation of *fcc* phase matches the [001] oriented *hcp* planes.
9. Nanoporous Ni film with graded porosity has been deposited by potentiostatic electrodeposition using P123 as a structure direct agent. The films show different nanomechanical response as a function of the maximum applied load during nanoindentation. Namely, the reduced Young´s modulus is found to decrease and the yield stress to increase as the maximum applied load is increased. However, hardness remains constant.

Departament de Física

7. Future perspectives

Chapter 7: Future perspectives

New exciting perspectives are envisaged on the basis of the results achieved in this Thesis. In the following, issues which deserve more attention and directions for future research are briefly overviewed:

- P123 template-assisted electrodepositon method has been successfully applied only to the synthesis of mesoporous metallic layers consisting of a single element (Pt, Bi, Ni, Sn, Au, Cu, Zn…[1-6]) or alloys comprising two noble metals (in fact, PtRu is the only example reported so far[7]). Little is known about the synthesis of mesoporous alloys made of non-noble metals using this strategy. Currently, the fabrication of pseudo-ordered mesoporous CuNi alloy films by electrodeposition from P123 surfactant containing electrolytes is under progress. From the properties viewpoint, a comparison on the hydrogen evolution reaction (HER) performance between mesoporous CuNi, mesoporous Ni (section 4.3), macroporous Cu-Ni (section 3.1) and fully-dense Ni films could be drawn. Such comparison would provide useful information on the influence of the textural properties of deposits (surface area, pore size and volume) on the HER properties.
- The work on the atomic layer deposition (ALD) as a means to conformally coat the macroporous Cu-Ni films with transition metal oxides could be exploited to the full. For example, ALD could be applied to the nanoporous Ni films presented in section 4.3 and to other metallic frameworks in order to produce novel metal-ceramic nanocomposites. The thickness of the ALD coating could be systematically varied in order to study its influence on the properties of the material.
- The possibility to use multisegmented nanowires (NWs) for multi-bit magnetic storage could be implemented from an experimental point of view, based on the predictions of the theoretical modeling presented in this Thesis. The main challenge is to increase the areal density of NWs while preserving a small NW diameter, thus minimizing dipolar magnetic interactions and

allowing for an enhanced areal density of information. For this purpose, the polycarbonate templates should be replaced by other types of templates (for example anodized aluminum oxide membranes), which in turn should stand the electrodeposition conditions needed for the growth of the different segments. The obtained NWs could consist of as many segments as possible, provided that the coercivity of each segment is different than in the others, rendering staircase-like hysteresis loops with multiple steps. The amount of magnetic states that could be stored per NW would be directly proportional to the number of ferromagnetic segments.

- The growth of porous segmented NWs by template-assisted electrodeposition is also very appealing. Although much work has been done for dense segmented NWs of porous single-phase (i.e., non-segmented) NWs, the possibility to produce segmented porous 1D architectures would certainly be a huge step forward. For example, porous CoPt/Ni and CoPt/Cu/Ni NWs could be electrochemically synthesized from solutions containing non-ionic surfactants and afterwards an antiparallel alignment of the magnetization could be set for their magnetic CoPt and Ni segments. In this way, the resulting structures could host several drugs in their nanoporous skeleton. The NWs could be efficiently used as nanorobotics platforms in biomedical applications. In particular, they could be maneuvered toward the targeted tissue using external magnetic fields and release their cargo at the site. Thanks to the antiparallel alignment of their segments, eventual agglomeration in the body fluid would be precluded. Cytotoxicity analyses should be carried out owing to the potential toxicity of cobalt, copper and nickel ions.

References:

[1] H. Wang, L. Wang, T. Sato, Y. Sakamoto, S. Tominaka, K. Miyasaka, N. Miyamoto, Y. Nemoto, O. Terasaki, Y. Yamauchi, *Chem. Mater*. **2012**, *29*, 1591.

[2] F. Bender, R. J. Mankelow, D. B. Hibbert, J. J. Gooding, *Electroanalysis* **2006**, *18*, 1558.

[3] H. Luo, L. Sun, Y. Lu, Y. Yan, *Langmuir*, **2004**, *20*, 10218.

[4] G. S. Attard, C. G. Goltner, J. M. Corker, S. Henke, R. H. Templer, *Angew. Chem. In. Ed. Engl*. **1997**, *36*, 1315.

[5] A. H. Whitehead, J. M. Elliott, J. R. Owen, G. S. Attard, *Chem. Commun*. **1999**, 331.

[6] P. A. Nelson, J. M. Elliott, G. S. Attard, J. R. Owen, *Chem Mater*. **2002**, *14*, 524.

[7] H. Wang, M. Imura, Y. Nemoto, L. Wang, H. Y. Jeong, T. Yokoshima, O. Terasaki, Y. Yamauchi, *Chem. Eur. J.* **2012**, *18*, 13142.

Chronogram and scientific curriculum

A chronogram of the work is shown as follows:

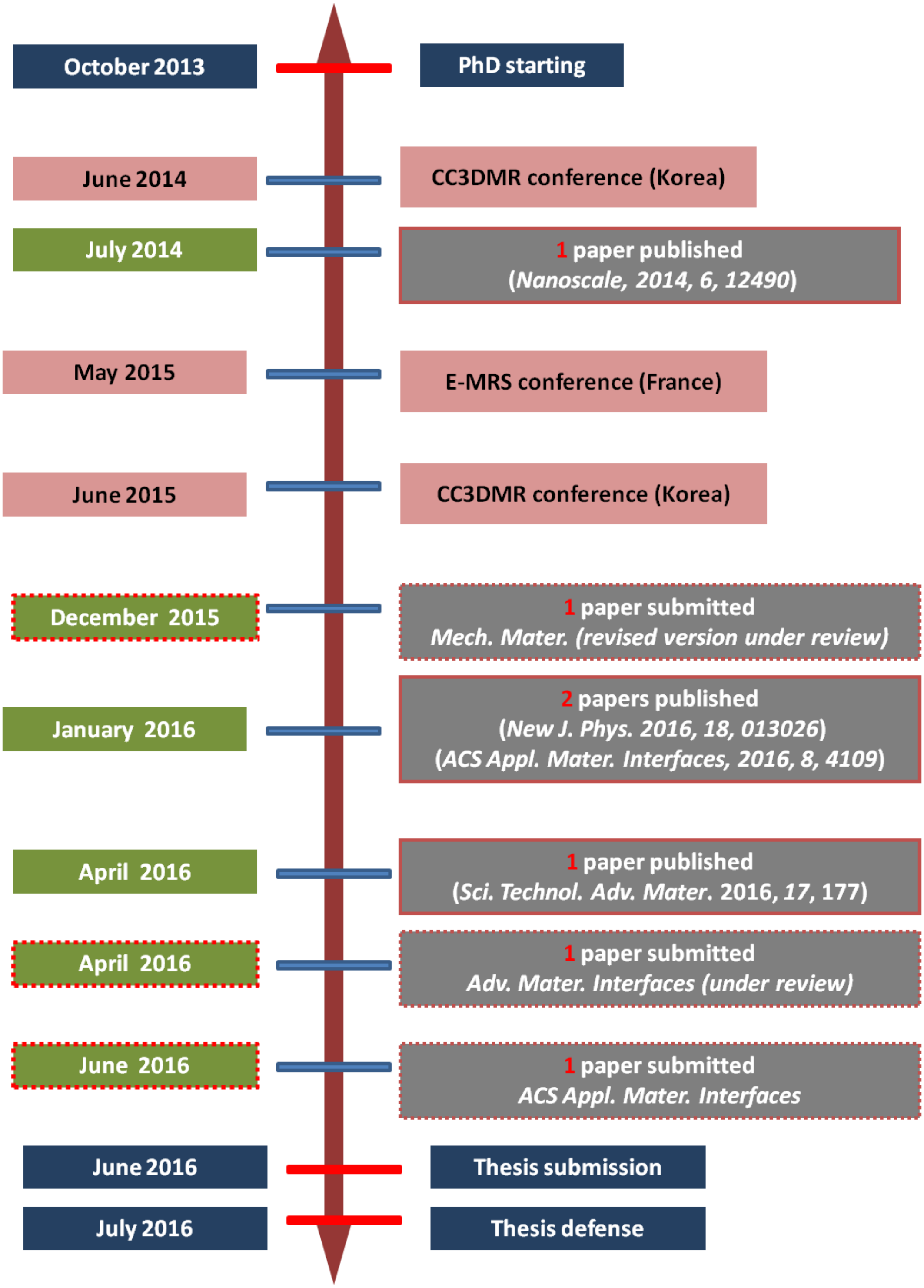

October 2013	PhD starting
June 2014	CC3DMR conference (Korea)
July 2014	1 paper published (*Nanoscale, 2014, 6, 12490*)
May 2015	E-MRS conference (France)
June 2015	CC3DMR conference (Korea)
December 2015	1 paper submitted *Mech. Mater. (revised version under review)*
January 2016	2 papers published (*New J. Phys. 2016, 18, 013026*) (*ACS Appl. Mater. Interfaces, 2016, 8, 4109*)
April 2016	1 paper published (*Sci. Technol. Adv. Mater.* 2016, 17, 177)
April 2016	1 paper submitted *Adv. Mater. Interfaces (under review)*
June 2016	1 paper submitted *ACS Appl. Mater. Interfaces*
June 2016	Thesis submission
July 2016	Thesis defense

Publications

1. Y. Yu†, J. Zhang†, X. Wu, W. Zhao, B. Zhang*.

Nanoporous Single-Crystal-Like $Cd_xZn_{1-x}S$ Nanosheets Fabricated by the Cation-Exchang Reaction of Inorganic-Organic Hybrid ZnS-Amine with Cadmium Ions

Angew. Chem. **2012**, 124, 921; *Angew. Chem. Int. Ed.* **2012**, 51, 897. (Cover paper) (Hot paper)

† Equally contributing authors

2. S. Zhuo, Y. Xu, W. Zhao, J. Zhang, B. Zhang*.

Hierarchical Nanosheet-Based MoS_2 Nanotubes Fabricated by an Anion-Exchange Reaction of MoO_3–Amine Hybrid Nanowires

Angew. Chem. Int. Ed. **2013,** *125*, 8764.

3. J. Zhang, W. Zhao, Y. Xu, H. Xu, B. Zhang*.

In-situ Photo-reducing Graphene Oxide to Create $Zn_{0.5}Cd_{0.5}S$ Porous Nanosheets/RGO Composites as Highly Stable and Efficient Photoelectrocatalysts for Visible-light-driven Water Splitting

Int. J. Hydrogen Energy **2014**, *39*, 702.

4. J. Zhang, M. D. Baró, E. Pellicer*, J. Sort*.

Electrodeposition of Magnetic, Superhydrophoboc Non-stick, Two-phase Cu-Ni Foam Films and Their Ehanced Performance for Hydrogen Evolution Reaction in Alkaline Water Media

Nanoscale, **2014**, *6*, 12490.

5. Y. Huang, Y. Xu, J. Zhang, X. Yin, Y. Guo, B. Zhang*.

Hierarchical Ultrathin-branched CdS Nanowire Arrays with Enhanced Photocatalytic Performance

J. Mater. Chem. A **2015**, *3*, 19507.

6. J. Zhang, S. A. Puig, N. D. Valle, C. Navau, M. D. Baró, S. Estradé, F. Peiró, S. Pané, B. Nelson, A. Sanchez, J. Noqués, E. Pellicer*, J. Sort*.

Tailoring Staircase-like Hysteresis Loops in Electrodeposited Trisegmented Magnetic Nanowires: a Strategy toward Minimization of Interwire Interactions

ACS Appl. Mater. Interfaces, **2016**, *8*, 4109.

7. M. Guerrero*†, J. Zhang†, A. Altube, E. G. Lecina, M. Roldan, M. D. Baró, E. Pellicer*, J. Sort.

Room-temperature Synthesis of Three-dimensional Porous ZnO@CuNi Hybrid Magnetic Layers with Photoluminescent and Photocatalytic Properties

Sci. Technol. Adv. Mater. **2016**, *17*, 177.

† Equally contributing authors

8. S. A. Puig, N. D. Valle, E. Pellicer, J. Zhang, J. Nogués, C. Navau, A. Sanchez*, J. Sort.

Modeling the Collective Magnetic Behavior of Highly-packed Arrays of Multi-segmented Nanowires

New J. Phys. **2016**, *18*, 013026.

9. J. Zhang, S. Pané, J. Sort*, E. Pellicer*.

Toward Robust Segmented Nanowires: Understanding the Impact of Crystallographic Texture on the Quality of Segment Interfaces in Magnetic Metallic Nanowires

Submitted to *Adv. Mater. Interfaces.* (under review)

10. D. Esqué-de los Ojos*, J. Zhang, J. Fornell, E. Pellicer, J. Sort.

Nanomechanical Behaviour of Open-cell Nanoporous Metal: Homogeneous Versus Thickness-dependent Porosity

Submitted to *Mech. Mater.* (revised version under review)

11. J. Zhang, M. Coll*, T. Puig, J. Sort*, E. Pellicer*.

Conformal oxide nanocoatings on electrodeposited 3D porous Ni films by atomic layer deposition

Submitted to *ACS Appl. Mater. Interfaces.*

Book chapter

J. Zhang, E. Pellicer, J. Sort*.

Towards voltage-driven nano-spintronics: a review in 'Commercialization of Nanotechnologies - A case study approach'

Springer(Ed. D. Brabazon), **2016** in press

Patents

1. Bin Zhang*, Jin Zhang, Jian-Hua Cui, Hua Zhang, Shuang-Xia Hou, You Xu.

A generalized one-step approach to synthesize 3D porous network-like noble-metal nanoelectrocatalysts,

Patent (China) **CN102166518A**.

2. Bin Zhang*, Jian-Hua Cui, Jin Zhang, Xuan Wu, Wei-Wei Zhao, Huan Wang.

A generalized one-step approach to synthesize 3D porous network-like noble-metal and alloy nanomaterials,

Patent (China) **CN102151840A**.

3. I. Chávez, J. Zhang, M. D. Baró, E. Pellicer, J. Sort, Magnetic-Electrocatalytic, pseudo-ordered mesoporous alloy films, a method for making them and their use.

Patent (Europe) **T-2015-040UK**, **GB 1607416.3**.

Contributions to Conferences

*** Presenting Author**

1. J. Zhang*, J. Sort, E. Pellicer, Ferromagnetic electrodeposited porous Cu-Ni films: tunable wettability and improved electrocatalytic performace towards hydrogen evolution, *Collaborative Conference on Materials Research (CCMR)*, June 23-27, **2014**. ***Oral presentation.***

2. J. Zhang*, S. Agramunt, S. Pané, S. Estradé, F. Peiró. N. del Valle, M. D. Baró, C. Navau, A. Sánchez, J. Nogués, E. Pellicer, J. Sort, Controlled electrodeposition and magnetic properties of hard ferromagnetic (FM)/spacer/soft FM multi-segmented nanowires, *European Materials Research Society (E-MRS)*, May 11-15, **2015**. ***Oral presentation***.

3. J. Zhang*, S. Agramunt, S. Pané, S. Estradé, F. Peiró. N. del Valle, M. D. Baró, C. Navau, A. Sánchez, J. Nogués, E. Pellicer, J. Sort, Template-assisted electrodeposition and magnetic properties of multi-segmented hard ferromagnetic (FM)/spacer/soft FM PtCo/Cu/Ni nanowires, *Collaborative Conference on Materials Research (CCMR)*, June 15-19, **2015**. ***Invited presentation***.